University of Alberta

Development of LCF Life Prediction Model for Wrinkled Steel Pipes

by

Jianmin Zhang

A thesis submitted to the Faculty of Graduate Studies and Research
in partial fulfillment of the requirements for the degree of

Doctor of Philosophy
in
Structural Engineering

Department of Civil & Environmental Engineering

Spring 2010
Edmonton, Alberta

Examining Committee

J.J. Roger Cheng, Civil and Environmental Engineering

Alaa E. Elwi, Civil and Environmental Engineering

Samer Adeeb, Civil and Environmental Engineering

Weixing Chen, Chemical and Materials Engineering

Leon D. Wegner, Civil and Geological Engineering, University of Saskatchewan

ABSTRACT

This research program focused on the behaviour of low cycle fatigue (LCF) of wrinkled pipes, and was designed to develop the LCF life prediction models for the wrinkled pipes. It consisted of three phases of work, which are strip tests, full-scale pipe tests, and finite element analysis (FEA).

In strip tests, 39 strip specimens were tested by a complete-reversed stroke-controlled method to investigate the effects of bend angle, bend radius, and stroke range on the low-cycle fatigue (LCF) life. Also, the LCF behaviour was explored by viewing the spectra of key variables and their corresponding hysteresis loops. The failure mechanism was discussed by examining the fracture surfaces. Two LCF life prediction models, life-based and deterioration rate-based, were developed and their prediction results were evaluated.

In full-scale pipe tests, two specimens were tested according to a complicated loading procedure. The loading was a combination of axial load, bending moment, and internal pressure; and it consisted of monotonic loading stage and cyclic loading stage. Based on those two tests, the global and local behaviour were investigated, the failure mechanism was studied and the application of the developed LCF life prediction models was discussed.

In FEA, three numerical models were developed and they were the strip model, the half-pipe model and the full-scale pipe model. In the strip model, the residual stresses and strains were analyzed and discussed. In the half-pipe model, the effects of pipe geometry, internal pressure, and global deformation on the wrinkle geometry were studied and discussed. In the full-scale pipe model, the full-scale pipe tests were simulated and both the global behaviour and local behaviour were discussed.

From this research program, some important conclusions were obtained. The wrinkle geometry is found to be greatly related to the pipe geometry, internal pressure, and global deformation. The global deformation has become localized after the wrinkle is fully developed. The opening deformation cycle is more

detrimental to wrinkled pipes than the closing deformation cycle. The test results also show that the seam weld governs the failure of wrinkled pipes if the pipes are subjected to cyclic axial deformation. The LCF life prediction models developed from this research program demonstrate good prediction capacity when they are applied to both strip tests and full-scale pipe tests.

ACKNOWLEDGEMENTS

Firstly, I would like to thank my supervisor, Dr. J. J. Roger Cheng. He not only gave me consistent and precious guidance but also left enough freedom when I did this research, and that made this research a complete success and made the education the best one in my life. In addition, the support, encouragement and friendship I have received from him have made me happy and confident at the U of A and I will benefit from it in my future life.

Secondly, I would like to thank TransCanada Pipelines Ltd. and Tokyo Gas Co. for financial assistance to this research program. Specific acknowledgement also goes to Dr. Z. (Joe) Zhou, Keith Adams and Dr. S. Adeeb. They made the fabrication and weld of the specimens successful.

Thirdly, I would like to thank the technicians Mr. Richard Helfrich and Larry Burden from I. F. Morrison Laboratory of Department of Civil and Environmental Engineering for their help with the experimental portion of this project. I would also like to thank technician Tina Barker from the Department of Chemical and Materials Engineering for their assistance with SEM.

Fourthly, I would like thank Dr. N. Khattak for his help in the strip tests, and Dr. M. Behbahanifard for checking the design of the full-scale pipe test set-up. Thanks also extended to Master student Mohmet Aydin who fabricated the full-scale pipe test set-up and Mr. Zoulong Zhou who helped me during the full-scale pipe tests.

Lastly, and most of all importantly, I want to thank my wife, Anne (Jiangyan) and my daughter, Quan. In particular, my wife is the source of support and my daughter is the source of courage in the long journey to pursue my degree.

TABLE OF CONTENTS

LIST OF TABLES

LIST OF FIGURES

LIST OF SYMBOLS AND ABBREVIATIONS

Latin Symbols

A	current or nominal cross-sectional area
A_o	initial cross-sectional area
a	constant
B	correction factor
b	fatigue strength exponent; constant
C	constant
C_1	constant
c	fatigue ductility exponent; constant
D	nominal outside diameter of pipe; damage
D_c	damage due to cyclic loading or LCF damage
D_f	damage at failure
D_i	damage caused by loading level i; inside diameter of pipe
D_m	damage due to monotonic loading or ductile damage
D_I	damage caused by microcrack initiation
D_{II}	damage caused by microcrack propagation
D_{ci}	LCF damage caused by loading level i
d	dimensionless damage ratio
du/dN_d	deterioration rate of HLE of an actual strip specimen
du/dN_v	deterioration rate of HLE of a pseudo strip specimen
E	Young's modulus
e	loading eccentricity
e_o	initial loading eccentricity
e_s	standard loading eccentricity
e_{cl}	loading eccentricity of a closed strip specimen or pipe wrinkle
e_{op}	loading eccentricity of a opened strip specimen or pipe wrinkle
e_{scl}	standard loading eccentricity of a closed strip specimen or pipe wrinkle

e_{sop}	standard loading eccentricity of a opened strip specimen or pipe wrinkle
f	constant
$g(N_{fi})$	constant related to N_{fi}
$g(\Omega;p)$	constant related to Ω and p
H	distance between pivots after pipe being deformed; current loading height
H_o	distance between pivots before pipe being deformed; initial loading height
H_{cl}	distance between the two loading hinges when the strip specimen is totally closed
H_{op}	distance between the two loading hinges when the strip specimen is totally opened
H_{so}	equivalent distance between pivots before pipe being deformed; equivalent initial loading height
H_{scl}	equivalent distance between the two pseudo loading hinges when the strip specimen is totally closed
H_{sop}	equivalent distance between the two pseudo loading hinges when the strip specimen is totally opened
h	distance from top pivot to the center of a cross section
h_p	distance from a pivot to its nearest end cross section of pipe
h_{bs}	distance from the bottom hinge to the pivot line
h_{ts}	distance from the top hinge to the pivot line
K_{RM}	bending moment required to attain a unit rotation in a strip specimen
K_{SM}	bending moment required to produce a unit stroke in a strip specimen
K_{SP}	axial load required to produce a unit stroke in a strip specimen
k	empirical material constant
L	pipe length
L_o	initial pipe length
L_c	chord length of pipe on concave side
L_w	deformed gauge length of the whole wrinkle

L_{wo}	initial gauge length of the whole wrinkle
L_{oij}	initial length of pipe segment between RVDT ‘Ri’ and ‘Rj’
l_{ma}	length of bending moment arm
l_w	undeformed wrinkle length
l_{wf}	sum of the undeformed length of the two wrinkle feet
l_{wh}	undeformed length of the wrinkle head
M	bending moment
M_y	initial yield bending moment of a cross section
M_u	ultimate moment capacity
M_{bp}	bending moment at bottom pivot
M_{tp}	bending moment at top pivot
M_{1po}	peak opening bending moment in the first cycle
M_{1vc}	valley closing bending moment in the first cycle
M_{cri}	critical bending moment
M_{ipo}	peak opening bending moment in the i^{th} cycle
M_{ivc}	valley closing bending moment in the i^{th} cycle
m	normalized bending moment on a cross section; constant
m_1	normalized bending moment on a cross section when primary yielding occurs
m_2	normalized bending moment on a cross section when secondary yielding occurs
m_c	constant
m_m	constant
m_{br}	empirical constant
m_{pc}	normalized bending moment on a cross section when full plasticity occurs
m_{po}	normalized peak opening bending moment
m_{vc}	normalized valley closing bending moment
N	normal force on a cross section
N_f	fatigue life
N_y	yield normal force of a cross section

N_{bp}	bottom pivot axial load
N_{di}	number of cycles to failure of a actual strip specimen or pipe wrinkle with respect to cyclic loading level i
N_{df}	number of cycles to failure of a strip specimen or a wrinkled pipe
N_{fi}	number of cycles to failure with respect to cyclic loading level i
N_{vf}	number of cycles to failure of a pseudo or virgin strip specimen
N_{NN}	nominal net axial load in pipe wall
N_{tp}	top pivot axial load
N_{Ii}	life of microcrack initiation under loading level i
N_{IIi}	life of microcrack propagation under loading level i
N_{vfi}	number of cycles to failure of a pseudo strip specimen or pipe wrinkle with respect to cyclic loading level i
n	normalized normal force on a cross section; size of sample
n_i	numbers of cycles consumed during cyclic loading level i
P	MTS load; axial load
P_j	jack load
P_p	load caused by Poisson's effect
P_w	load caused by water pushing the end plate
P_{bt}	resulting load in the bottom four tie rods
P_{tt}	resulting load in the top four tie rods
P_{1po}	peak opening load in the first cycle
P_{1vc}	valley closing load in the first cycle
P_{MTS}	MTS load
P_{ipo}	peak opening load in the i^{th} cycle
P_{ivc}	valley closing load in the i^{th} cycle
p	a constant related to material properties; internal pressure
p_i	predicted value
p_y	specified minimum yield strength (SMYS)
p_{po}	normalized peak opening load
p_{vc}	normalized valley closing load
R	bend radius

R^2	coefficient of multiple determinations
R_W	wrinkle radius at wrinkle crest
r_w	ratio of wrinkle length to pipe diameter
r_{wf}	ratio of length of wrinkle feet to pipe diameter
r_{wh}	ratio of length of wrinkle head to pipe diameter
S	stroke, RAD between pivots, or elastic sectional modulus
S_a	stroke amplitude
S_m	mean stroke
S_{cl}	stroke range caused by closing strip specimen or pipe wrinkle
S_{op}	stroke range caused by opening strip specimen or pipe wrinkle
S_{ecl}	equivalent stroke range caused by closing strip specimen or pipe wrinkle
S_{eop}	equivalent stroke range caused by opening strip specimen or pipe wrinkle
S_{max}	maximum stroke or maximum opening stroke
S_{min}	minimum stroke or maximum closing stroke
s	standard deviation
t	thickness of a strip specimen or pipe wall
U	total energy-absorption capacity in engineering scale
U_c	consumed energy-absorption capacity in engineering scale
U_t	total energy-absorption capacity in true scale
U_{tc}	consumed energy-absorption capacity in true scale
U_{1LS}	LS HLE in the first cycle
U_{1MR}	MR HLE in the first cycle
U_{iLS}	LS HLE in the i^{th} cycle
U_{iMR}	MR HLE in the i^{th} cycle
u_{MR}	normalized MR HLE
u_{LS}	normalized LS HLE
V	shear force
V_{bp}	shear force at bottom pivot
V_{tp}	shear force at top pivot

x_i	x value of sample
x_m	mean of x value of sample
y	height of elastic core of a cross section
y_i	y value of sample
y_m	mean of y value of sample
Z	plastic sectional modulus or nominal plastic sectional modulus

Greek Symbols

β	ratio of water pressure and SMYS
Δ	lateral deflection of the center of a cross section
$\Delta\alpha$	sum of rotation of both pivots
Δe	difference between loading eccentricity and standard loading eccentricity
$\Delta\varepsilon$	recovered strain due to unloading; total strain range
ΔS	stroke range
$\Delta\varepsilon^p$	plastic strain range
ΔS_e	equivalent stroke range
ΔS_i	stroke range of pipe wrinkle with respect to cyclic loading level i
ΔS_{ei}	equivalent stroke range of pipe wrinkle with respect to cyclic loading level i
$\Delta\theta$	rotation range
$\Delta\theta_{sl}$	rotation range of a strip specimen
δe	change of loading eccentricity
δL_w	RAD over a gauge length of whole wrinkle
δL_{cg}	RAD of concave side
$\delta\theta_{al}$	actual leg rotation of a strip specimen
$\delta\theta_{sl}$	pseudo leg rotation of a strip specimen
$\delta\theta_{sla}$	rotation amplitude of a strip specimen
$\delta\theta_{slm}$	mean rotation of a strip specimen

$\delta\theta_{alcl}$	closing rotation of actual strip legs
$\delta\theta_{alop}$	opening rotation of actual strip legs
$\delta\theta_{slcl}$	closing rotation of pseudo strip legs
$\delta\theta_{slop}$	opening rotation of pseudo strip legs
$\delta\theta_{slmax}$	maximum pseudo leg rotation or maximum rotation of a strip specimen
$\delta\theta_{slmin}$	minimum pseudo leg rotation or minimum rotation of a strip specimen
ε	engineering strain
ε_e	engineering strain on exterior fiber
ε_f	static fracture ductility
ε_i	engineering strain on interior fiber
ε_r	residual engineering strain
ε_t	true strain
ε_y	yield engineering strain
ε_f'	fatigue ductility coefficient
ε_t^e	true elastic strain
ε_t^p	true plastic strain
ε_{fR}	residual static fracture ductility
ε_{te}	true strain on exterior fiber
ε_{tf}	static true fracture ductility
ε_{ti}	true strain on interior fiber
ε_{tr}	residual true strain
ε_{ty}	true yield strain
ε_{pre}	prestrain
Φ_g	global curvature
Φ_y	global curvature at initial yielding of pipe
Φ_w	wrinkle curvature at wrinkle crest
Φ_{lij}	local curvature of pipe segment between RVDT ‘Ri’ and ‘Rj’

ϕ	normalized global curvature
ϕ_1	value of ϕ when primary yielding occurs
ϕ_2	value of ϕ when secondary yielding occurs
μ	Poisson's ratio
θ	inclination angle of a cross section;
θ_b	slope angle of bottom moment arm
θ_j	inclination angle of jack
θ_t	slope angle of top moment arm
θ_{Ri}	reading of RVDT 'Ri' where i = 1, 2, 3, 4 and 5
θ_{al}	internal angle between actual strip legs or 'actual leg angle'
θ_{sl}	internal angle between pseudo strip legs or 'pseudo leg angle'
θ_{alo}	initial actual leg angle
θ_{slo}	initial pseudo leg angle
θ_{alcl}	internal angle between the closed actual strip legs
θ_{alop}	internal angle between the opened actual strip legs
θ_{slcl}	internal angle between the closed pseudo strip legs
θ_{slop}	internal angle between the opened pseudo strip legs
Ω	damage parameter
ρ	correlation coefficient
σ	engineering stress
σ_h	hoop stress
σ_p	proportional limit
σ_r	residual engineering stress
σ_t	true stress
σ_u	static ultimate stress of material
σ_y	static yield stress of material
σ_f'	fatigue strength coefficient
σ_{ay}	axial stress that makes the material yield with the presence of hoop stress

σ_{tB}	corrected true stress
σ_{tf}	true fracture stress
σ_{tr}	residual true stress
σ_{ty}	true yield stress
σ_{ud}	dynamic ultimate stress of material
σ_{yd}	dynamic yield stress of material

Abbreviations

D/t	outside diameter to thickness ratio
TG	Tokyo Gas Co.
CDM	continuum damage mechanics
DAR	damage accumulation rule
DCA	damage curve approach
FDP	fast deterioration period
FEA	finite element analyses
HCF	high cycle fatigue
HLD	hysteresis loop diagram
HLE	hysteresis loop energy
LCF	low cycle fatigue
RAD	relative axial displacement
SDP	slow deterioration period
SEM	scanning electron microscope
DLDR	double linear damage rule
ELCF	extremely low cycle fatigue
LDAR	linear damage accumulation rule
LSHL	load vs. stroke hysteresis loop
LVDT	linear variable differential transducer
MRHL	moment vs. rotation hysteresis loop
NNAL	nominal net axial load

RVDT	rotational variable differential transformer
SMYS	specified minimum yield strength
TCPL	TransCanada Pipelines Ltd.
LS HLE	hysteresis loop energy obtained from load and stroke hysteresis loops
MR HLE	hysteresis loop energy obtained from moment and rotation hysteresis loops
SRSDAR	square root and square damage accumulation rule
SSRDAR	square and square root damage accumulation rule
U of A	University of Alberta

1 INTRODUCTION

1.1 PROBLEM STATEMENT

Buried pipelines are usually subjected to a combination of large axial deformations and rotations because of environmental and geotechnical effects, which may cause the pipes to buckle. As these effects increase, some buckling waves will grow and experience plastic deformations and, consequently, wrinkles mature in the pipe wall. The formation of a wrinkle can be accelerated by the presence of geometric imperfections, which can be caused by manufacturing errors, dents, corrosion, etc. The wrinkles are formed by large plastic deformations, which are irrecoverable, thus they permanently form softening regions along the pipelines and change the geometry of the pipe. Consequently, the safety and integrity of the pipelines become in question. In order to avoid undesirable accidents and environmental damage, the pipeline operators usually dig up the buckled pipe and replace the wrinkled portions, even though such remedial action may cost millions of dollars and may not always be necessary.

The subjects of buckling and post-buckling dominated the research of buried pipelines in past decades. The topics covered the structural behaviour of pipelines, the wrinkling of pipe walls, the buckling resistance of pipes, the critical buckling strain, and the ultimate rupture/fracture of pipes. The parameters investigated included different loading combinations, which included axial load or deformation, bending moment or curvature, shear force or lateral deflection, varied internal pressure, pipe geometry (outside diameter to thickness (D/t) ratio), pipe material, and the presence of girth weld in the buckled region. Significant findings and conclusions were obtained from those works. Among them, the most important one is that the occurrence of buckling or wrinkling does not necessarily affect the safety and integrity of pipelines if the pipes possess sufficient ductility against fracture. For example, all pipe segments tested at the University of Alberta (U of A), such as Mohareb et al. (1993), Yoosef-Ghodsi et al. (1995), Souza and Murray (1999), Dorey et al. (2001), Myrholm (2001), and Das (2002), developed

large deformations localized in a single wrinkle or multiple wrinkles without loss of containment integrity. Other researchers from outside of the U of A have drawn the same conclusion (Bouwkamp et al. 1973 and Schneider 1998).

For the wrinkled pipes, there are two principal fracture limit states: one is the tearing failure mode caused by very large deformation and/or curvature, and the other one is the low cycle fatigue (LCF) failure mode. Bouwkamp et al. (1973) fractured large diameter pipes (1219 mm diameter and 11.73 mm wall thickness) by applying very large curvatures. They concluded that the failure mode was the tearing shear failure of pipe wall. Das et al. (2002) successfully reproduced a field fracture, which was the tearing failure, in an NPS12 pipe (304.8 mm diameter and 6.84 mm wall thickness) by continuously increasing the axial deformation. Aydin (2006) investigated the tearing failure by applying axial deformation in two types of pipe with different D/t ratios and material grades under the condition of varied internal pressures and assorted locked curvatures. All of them found that the tearing failure can be one of the possible ultimate states of wrinkled pipes. However, the tearing type failure happens only when the applied curvature and/or axial deformation are very large, that greatly exceed normal service conditions. Therefore, the safety and the integrity of wrinkled pipes may not be a problem for line pipes with good ductility under normal service conditions.

Normally pipelines in service are subjected to cyclic load/deformation. Cyclic load/deformation may come from the operation of pipelines, the thermal effect of transporting media, the environment (such as frost heave and thaw settlement), and the seismic movement if they are located in seismic regions. These actions can fracture the pipelines in the mode of LCF. Das et al. (2001) and Myrholm (2001) found that the wrinkled pipes could be fractured by the strain reversal at the crest of wrinkle under the condition of cyclic loading. After identification of this limit state, the question is that how long those wrinkled pipes can be continued for further service. It is not easy to carry out a LCF evaluation on wrinkled pipes because of two major challenges. First, test specimens cannot be cut from the actual wrinkled pipelines directly because those wrinkled pipes are expected to provide further service. Therefore, the specimens have to be able to

properly replicate the current status of the wrinkled pipes, especially their overall and local (wrinkle) geometries. Secondly, it requires significant experimental data to develop a model to predict their LCF lives. It will be not only costly but also time consuming. To date, only the U of A has focused its research on this problem. Das et al. (2001) firstly conducted 10 full-scale pipe tests to investigate the LCF behaviour of wrinkled pipes. Myrholm (2001) developed a so-called strip test after observing the similar fracture shape between a pipe wrinkle and a strip specimen, and employed it to study the LCF behaviour of a pipe wrinkle. He tested eight pieces of strip specimen and eight segments of full-scale pipe specimen. Das (2002) conducted 16 more strip tests and developed a fracture model based on hysteresis loop energy (HLE) of the first cycle to predict the remaining fatigue lives of wrinkled pipes.

It is Myrholm (2001) and Das (2002), especially the latter, who started an investigation into the LCF of wrinkled pipes. However, by reviewing their work, it is clear that many questions still need to be answered. First, actual wrinkles can have diverse shapes and can come from different materials, so more test parameters need to be investigated. Second, the LCF lives of all previous strip tests were less than 20 cycles except one with a fatigue life of 32 cycles, and the LCF lives of all full-scale pipes were lower than 10 cycles. In field conditions, however, the actual loading on pipelines varies greatly with different operating, environmental and geotechnical conditions, thus those wrinkled pipes have wide fatigue life spans. Therefore, more strip specimens and full-scale pipe specimens with longer LCF lives should be tested. Third, the LCF failure mechanisms of wrinkled pipes, which are important for the development of fracture control plan and further improvement of pipe design, are not well researched and understood. Finally, the model developed by Das (2002) needs to be verified by more experimental data to determine its application range, and to be improved or developed afresh. All of those concerns motivate this research program.

1.2 OBJECTIVES AND SCOPE

This research program is designed to develop models to predict the LCF lives of wrinkled pipes. It consists of three phases of work, which are strip tests, full-scale pipe tests and finite element analyses (FEA).

In strip tests, a total of 39 pieces of specimen, which included three sets of thickness, two grades of material from two different suppliers, two types of bend radius, and two categories of bend angle, were tested by six levels of stroke range. Those strip tests plus the previous strip tests by Myrholm (2001) and Das (2002) formed a complete data base to develop LCF life prediction models.

In full-scale pipe tests, a total of two specimens, supplied by two different suppliers with different D/t ratios and material grades, were tested by varied stroke ranges. Those two pipe tests were used to test the accuracy of the developed LCF life prediction models based on strip tests.

In FEA, three models, a strip model, a half-pipe model and a full-scale pipe model, were developed . These three models were developed to simulate bending strip specimens and full-scale pipe tests and to perform parametric studies.

Specifically, the following objectives are expected to be achieved:

- To implement and expand the existing database of strip tests by testing specimens with expanded test parameters and extended LCF lives.
- To develop FEA models to investigate the behaviour of strip specimens and full-scale pipe specimens.
- To study the failure mechanisms of strip specimens and wrinkled pipes under the condition of LCF.
- To improve Das' HLE model (Das 2002) or develop totally new models based on the expanded database of strip test for predicting the LCF lives of wrinkled pipes.
- To bridge the gap between strip tests and full-scale pipe tests, thus make the application of LCF models possible.

1.3 ORGANIZATION OF THESIS

The thesis consists of five major chapters and two smaller chapters, the introduction chapter (Chapter 1) and the summary and conclusions chapter (Chapter 7). Chapter 2 briefly reviews some important background knowledge and the major achievements relevant to this research program. Chapter 3 introduces the strip tests, test results, and discussions. Chapter 4 presents the full-scale pipe tests, test results, and discussions. Chapter 5 discusses FEA models, analytical results, and discussions. Chapter 6 deals with the LCF life prediction models and their application in full-scale pipes.

2 LITERATURE REVIEW

This review will cover four topics: fatigue failure criteria, damage accumulation rules (DARs), LCF life prediction models, and past related work. The objective is to review some necessary information to guide this research program. The emphasis will be on summarizing the important background knowledge and main achievements relevant to this research program.

2.1 FATIGUE FAILURE CRITERIA

When conducting a fatigue test, the first important thing is to select an appropriate failure criterion so that fatigue lives can be determined. Although there are a lot of failure criteria, they can be classified into four main categories according to the engineering concerns: deterioration-based, crack-size based, function-based, and other criteria.

2.1.1 DETERIORATION-BASED CRITERIA

This type of criterion concerns the deterioration of load carrying-capacity or energy-absorption capacity of a specimen or a component. It defines fatigue failure as the moment when the load-carrying capacity or the energy-absorption capacity drops to a specific level. In a typical fatigue test, the load can be directly measured and the energy dissipation can be indirectly calculated, so this type of criterion can be easily used. Miyazaki et al. (2002), Hasegawa et al. (2002) and Ahn et al. (2002) defined the number of cycles to failure as the number corresponding to a 25% drop from the initial load or displacement when they studied extremely low cycle fatigue (ELCF) behaviour of steel pipe with local wall thinning. Calado and Azevedo (1989) treated fatigue failure as the moment when the normalized hysteretic energy drops to 50% of its initial amplitude when they investigated the failure of structural steel elements subjected to cyclic loading. Daali and Korol (1995) used both deterioration of strength and deterioration of energy dissipation as their failure criteria when they assessed the damage in steel beams by LCF. Yoon et al. (2003) defined the failure as the

starting point of fast decreasing of stress amplitude when they conducted LCF testing of stainless steel pipes. Gotoh and Berge (2004) employed two failure criteria: the first one defined failure by a 50% load drop of its initial level when they tested LCF strength of X65 pipes with girth welds, the other one used a critical crack size of 2 mm, which will be discussed in section 2.1.2.

On the extreme, the fatigue failure can be treated as the moment when a specimen or a component completely loses its load-carrying capacity or energy-absorption capacity, i.e. the two fractured portions are totally separated. This type of criterion can be also called rupture-based criteria. Because the criterion concerns only the final moment of rupture, it can bring two benefits. The first benefit is that the test becomes very simple because there is no need to pay specific attention to what happens during the test. Because of this benefit, this type of criterion has been most widely employed by traditional fatigue tests. The second benefit is that the error caused by determining fatigue life is minimized because the criterion used for determining fatigue life is very clear and definite. There are a lot of examples adopting this criterion, such as Park et al. (2004), Iida (1987), Libertiny et al. (1977), Uemura (1998), Mander et al. (1994), and Ballio et al. (1997).

2.1.2 CRACK SIZE-BASED CRITERIA

This type of criterion focuses on the crack size and defines fatigue failure as the point when the crack propagates to a specific length. This is very popular when the LCF life prediction model is formulated by using fracture mechanics, because this type of model is based on the rate of crack growth. If a structure can be periodically inspected, then the failure criteria can be defined by the so-called ‘detectable crack size’. As discussed before, Gotoh and Berge (2004) used a crack size equal to 2 mm. Miyazaki et al. (2002) defined fatigue failure as the propagation of the initiated circumferential crack at the maximum eroded part in their load-controlled tests when they studied the fatigue strength of pipes with flaws. Radziminski and Azizinamini (1986) and Sakano et al. (1994) defined the fatigue failure as the moment when the longest fatigue crack extended over

approximately three-quarters of the width of the flange angle when they investigated LCF of steel beam-column connections.

2.1.3 FUNCTION-BASED CRITERIA

This type criterion defines fatigue failure as the moment at which a structure or a component loses one of its design functions. In the pipeline industry, one of the popular failure criteria is the leakage or the crack penetration (Ogiso et al. 1993, Scavuzzo et al. 1992, and Hasegawa et al. 2000).

2.1.4 OTHER CRITERIA

All criteria that cannot be included in the above three categories can be put under this category, and generally this type of criterion is arbitrarily defined to some extent. For example, Hasegawa et al. (2000) defined the cycles to failure as the cycle at which 25% change from the initial displacement occurred in their load controlled tests when they studied the LCF strength for pipes with small cracks.

2.2 DAMAGE ACCUMULATION RULES

Generally, fatigue life prediction models can only handle problems with constant amplitude of cyclic load or deformation. Therefore, if a specimen or a component is subjected to variable amplitudes of cyclic load or deformation or multi-level cyclic load or deformation, a proper DAR has to be adopted.

Halford (1997) presented a good review of DAR, which included the linear damage accumulation rule (LDAR), the damage curve approach (DCA), and double linear damage rule (DLDR). The following gives a brief description of these rules.

A) The first one is the classical LDAR, which is the well known and most applied DAR. LDAR was first proposed by Palmgren in 1924. Some 15 years later, Langer independently proposed a similar linear rule for steel pressure vessel and steel piping components. In 1945, Miner built upon Langer's work and applied the LDAR to tension-tension axial fatigue data for an aircraft skin material (Halford 1997). Miner demonstrated excellent agreement

between the LDAR predictions and his experimental results. His success gave rise to a specific name to LDAR as the Miner's rule. This rule can be expressed as follows:

$$\sum D_i = \sum \frac{n_i}{N_{f_i}} = 1 \tag{2.1}$$

where D_i is the damage caused by loading level i; n_i denotes the numbers of cycles consumed during loading level i; and N_{f_i} represents the number of cycles to failure with respect to loading level i.

B) The DCA was postulated by Lewis in 1981 (Halford 1997). The DCA recognizes the following observations: in the regime of LCF, damage in the form of cracking of initially smooth specimens begins very early in the life, whereas in the regime of high cycle fatigue (HCF), cracking damage is not detectable until very late in life. This rule can be presented as follows:

$$\sum D_i = \sum \left(\frac{n_i}{N_{f_i}} \right)^{g(N_{f_i})} = 1 \tag{2.2}$$

where $g(N_{f_i})$ is a constant and it increases as N_{f_i} increases; generally, $g(N_{f_i})>1$.

In both Equations (2.1) and (2.2), the damage D_i could be interpreted physically as a dimensionless crack length, which cannot be negative, nor can it decrease.

C) The idea of DLDR is to approximate DCA by a bi-linear line (Halford 1997). Once the damage accumulation curves have been bi-linearized, it becomes a simple matter to describe the fatigue process in term of the two distinct phases: phase I is called 'microcrack initiation', phase II is termed as 'microcrack propagation'. The failure is defined when the two linear damage accumulation rules have been satisfied in sequence:

$$\sum D_I = \sum \left(n_i / N_{I_i} \right) = 1.0 \tag{2.3.1}$$

and

$$\sum D_{II} = \sum \left(n_i / N_{II_i} \right) = 1.0 \tag{2.3.2}$$

where D_I and D_{II} are the damage caused by microcrack initiation and by microcrack propagation, respectively; N_{I_i} and N_{II_i} are the life of microcrack initiation and the life of microcrack propagation under loading level i, respectively.

In addition, Ellyin (1997) introduced a dimensionless damage ratio as follows:

$$d = D \diagup D_f \tag{2.4.1}$$

where D is the damage; D_f the damage at failure; d = 0 for virgin material and d = 1 at failure. The damage D can be taken arbitrarily, but the following conditions should be satisfied: D = 0 for virgin material and D = D_f at failure for any fatigure process.

He then generalized the DAR for multi-level cyclic loading as follows:

$$\left\{\left[\left(\frac{n_1}{N_{f_1}}\right)^{g(\Omega_1;p)/g(\Omega_2;p)} + \frac{n_2}{N_{f_2}}\right]^{g(\Omega_2;p)/g(\Omega_3;p)} + \cdots + \frac{n_{i-1}}{N_{f_{i-1}}}\right\}^{g(\Omega_{i-1};p)/g(\Omega_i;p)} + \frac{n_i}{N_{f_i}} = 1 \tag{2.4.2}$$

where, n_j and N_{fj} (j=1, 2,…, i) are the same as defined in Equation (2.1); Ω is the damage parameter, and it is constant for a specific loading level; p is a constant related to material properties; and g(Ω;p) is a function of Ω and p, and it is constant for a specific loading level. On above, it is assumed that macro-mechanical properties are not affected by the damage process.

It can be observed that Equation (2.4.2) becomes Miner's rule, Equation (2.1), when $g(\Omega_1; p)$, $g(\Omega_2; p)$, …, $g(\Omega_{i-1}; p)$ and $g(\Omega_i; p)$ are equal to each other.

2.3 LCF LIFE PREDICTION MODELS

Based on the approach used to develop LCF life prediction models, Reemsnyder (1982) classified the fatigue life prediction models into two categories: analytical models, which include stress-life, local strain, and fracture mechanics models, and experimental models. Chen (2004) classified those models into two different

types: one is based on empirical correlation, which includes stress-based models, strain-based models and energy-based models, and the other is based on fracture mechanics.

Based on the damage parameter employed in models, Ellyin (1997) and Das (2002) classified fatigue life prediction models into four categories: stress-based models, strain-based models, energy-based models and other models. They did not include the models based on the fracture mechanics.

This research program focuses on the LCF of strip specimens and wrinkled pipes, so only the models related to this subject are introduced. They are strain-based models, energy-based models and other models.

2.3.1 STRAIN-BASED MODELS

In the field of LCF, strain-based models are the most widely used models. They were developed by Coffin (1954) and Manson (1954) independently. Based on the realization that LCF failure is the result of plastic strain reversal, they presented a power-law relationship, which has been known as the Coffin-Manson equation, between cycles to failure and plastic strain amplitude:

$$\Delta\varepsilon^{p}/2 = \varepsilon_f'\left(2N_f\right)^{c} \tag{2.5.1}$$

where $\Delta\varepsilon^{p}$ is the plastic strain range; ε_f' is the fatigue ductility coefficient which corresponds to the plastic strain at one reversal ($2N_f = 1$); and c is the fatigue ductility exponent.

For engineering applications, it is much easier to measure the total strain than to measure the plastic strain, so it is natural to develop an expression to relate the total strain range and the fatigue life. Manson (1960) originally proposed a model relating fatigue life to the total strain range by two separate power-law terms as follows:

$$\Delta\varepsilon/2 = \sigma_f^{'}\left(2N_f\right)^{b}/E + \varepsilon_f^{'}\left(2N_f\right)^{c} \tag{2.5.2}$$

where $\Delta\varepsilon$ is the total strain range; $\sigma_f^{'}$ is the fatigue strength coefficient; b is the fatigue strength exponent, E is the Young's modulus, and other parameters are the same as before.

This model is widely used in fatigue tests of smooth specimens and notched specimens where the strain range can be measured exactly (Iida 1987, Kuroda et al. 1999, Huang et al. 2001, and Gotoh and Berge 2004). This model has also been used in other specimens where strains are determined analytically (Scavuzzo et al. 1992, Sakano et al. 1993, Uemura 1998, Kuroda 2001, and Sleczka 2004).

2.3.2 ENERGY-BASED MODELS

If a specimen or a component experiences cyclic plastic deformation, then strain energy will be dissipated in each loading cycle. Based on the recognition of this dissipated strain energy (or a portion of it) being a main contributor to the fatigue damage process, it is natural to take it as the damage parameter.

Ellyin (1997) classified this model into three types based on what kind of energy being selected as the damage parameter. These are hysteresis energy-based models, plastic strain energy-based models and total strain energy-based models. For engineering applications, the first one has been widely used (Mander 1994, Azizinamini et al. 1989, and Radziminski et al. 1986, and Das 2002). An example of using plastic strain energy was given by Lefebvre and Ellyin (1984). Chen (2004) used both plastic strain energy and total strain energy as the damage parameter in her models.

Since the energy accounts for the effects of both stress and strain, so it is not surprising that it can unify HCF and LCF. Chan and Miller (1982) and Sarihan (1994) demonstrated that the energy-based models can handle test data from various sources, such as different specimens and different loading methods. Because of those benefits, this model has become more popular.

2.3.3 OTHER MODELS

In some cases, especially for LCF of some specific structural details, the aforementioned damage parameters cannot be obtained either directly by measurement or indirectly by analysis, or they cannot be kept constant during the test. Other specific damage parameters have to be identified to formulate LCF life prediction models. The following will give a brief introduction about those methods.

Radziminski and Azizinamini (1986) investigated the performance of semi-rigid steel beam-to-column connections under cyclic loadings and they used a non-dimensionalized nominal flange angle chord rotation index, which accounts for the effects of all major geometric parameters, for formulating LCF life prediction models. The comparison between the predicted results and test results exhibited very good agreement.

Ballio et al. (1997) studied the LCF behaviour of structural steel members and connections, and developed LCF life prediction models based on the damage parameter of so-called the effective stress range. But this parameter was related to the generalized displacement component, so in effect their model was based on the global displacement.

Mander et al. (1994) studied the LCF behaviour of semi-rigid top-and-seat angle connections. They used the plastic connection rotation as the damage parameter. They also found that a power-relation existed between the plastic connection rotation and hysteresis energy.

Daali and Korol (1995) assessed the LCF damage in steel beams, and they used the plastic rotation range as the damage parameter in their LCF life prediction model.

2.4 PREVIOUS WORK

To date, only the U of A has focused its research on the LCF of wrinkled pipes. Das et al. (2001) conducted twelve full-scale pipe tests from wrinkle to fracture. From the first two tests, they found that the wrinkled pipes could not be fractured

by only monotonically increasing the axial load under the condition of constant internal pressure. So they employed the cyclic loading after the initial wrinkle, and successfully fractured the other ten wrinkled pipes. They used two types of cyclic load, one was cyclic axial load only and the other was a combination of cyclic axial load and cyclic bending moment. The tested pipes were grade X52 NPS12 pipes. The pipes were tested by stroke-controlled method and the fatigue lives were from three to nine cycles only.

Based on the work of Das et al. (2001), Myrholm (2001) conducted eight more full-scale pipe tests. The pipes had a diameter of 508 mm and had two sets of thickness, 6.0 mm and 8.2 mm. The pipes were tested by a global curvature controlled method under three internal pressure levels, which were 0%, 40% and, 80% of the specified minimum yield strength (SYMS) in pipe walls. The maximum curvature was controlled by bending the pipe and the minimum curvature was generated by increasing the internal pressure under the absence of the bending moment and the axial load. In addition, the cyclic loading was applied at different global curvature levels; and at each level three repetitive cycles were applied. The obtained fatigue lives were from 3.5 to 12 cycles, in which six out of eight tests were below 10 cycles. In addition to the pipe tests, a so-called “strip test” was firstly conducted in his research based on the observation that the strip specimen had the similar fracture shape as the wrinkle of full-scale pipe, as shown in Figure 2.1. A strip specimen has a size of 57 mm by 535 mm. It was cut from a pipe, and then bent to a specific shape (refer to Chapter 3). He conducted 10 strip specimens, but only eight were valid tests. All the specimens were 6.8 mm thick and had a bend angle of 45°. The investigated parameters included two sets of bend radius, one was 15 mm and the other was 20 mm, five levels of stroke range, which were 50 mm, 60 mm, 70 mm, 80 mm, and 90 mm. The fatigue lives of these strip specimens ranged from 3 cycles to 17 cycles, but eight of them were less than 10 cycles.

From the work of Myrholm (2001), Das (2002) felt that more strip tests were needed to develop a fracture model, so he conducted 16 more strip tests. All the

specimens had the same bend angle of 45°, but eight were 6.0 mm thick and eight were 8.3 mm thick. Each thickness set was divided into two groups: one had a bend radius of 15 mm and the other had a bend radius of 20 mm. Each group was tested by four stroke levels and they were 50 mm, 60 mm, 70 mm and 80 mm. The obtained fatigue lives ranged from 4 to 32 cycles, specifically one was 32 cycles, three were about 15 cycles and the others were less than 10 cycles. Based on the data of strip tests, he developed a LCF life prediction model by employing the HLE in the first cycle as the damage parameter. Using the notation of this research program, his model can be expressed as follows:

$$\ln(N_{fd}) = -5.3654 - 2.58\ln(U_{1MR}) + 0.1642 \times t \qquad (2.6.1)$$

where U_{1MR} is the HLE defined as a measure of unit cycle energy absorbed by the crest of a strip specimen during the first cycle of loading and unloading (in kN·m); N_{fd} is the cycles to failure or the fatigue life; and t is the thickness of the specimen (in mm).

Because the actual U_{1MR} is difficult to be exactly computed from the hysteresis loop diagram (HLD) and is also impractical to get the HLD in field, Das (2002) simplified the computation of U_{1MR} as follows:

$$U_{1MR} = M_u \Delta\theta = \sigma_u Z \Delta\theta \qquad (2.6.2)$$

where, M_u is the ultimate moment capacity in kN·m; Z is the plastic sectional modulus in mm^3; σ_u is the ultimate stress in MPa; and $\Delta\theta$ is the rotation range of the specimen in radian.

Although this model works well in the case of the fatigue life being very short and exhibits good agreement with the results from full-scale pipe tests, there are still some questions about this model. Because the fatigue lives are so short, the hysteresis loop shrinks as loading cycles proceed. This makes taking HLE of the first cycle as the damage parameter questionable. Generally, a parameter with constant amplitude is chosen as the damage parameter in the fatigue life prediction model and this principle also works in the traditional fatigue regime. It is clear that the model obtained from fatigue tests with constant amplitude can easily be applied to the fatigue problems with varied amplitude by employing

DAR, such as Miner's rule. Secondly, can this model be applied in other cases? For example, other thickness, other bend angles and longer fatigue lives. The third one comes from the simplification. When the rotation range is large, the induced plastic deformation will be very large, and then the elastic deformation can be neglected. In this case, U_{1MR} can be approximated by Equation (2.6.2). But if the rotation range is small, the elastic deformation can not be neglected compared with the plastic deformation. Consequently, U_{1MR} can not be approximated by Equation (2.6.2). This is illustrated in Figure 2.2, where A_1 = the approximate U_{1MR} obtained by Equation (2.6.2) and A_2 = the actual U_{1MR} obtained from the actual hysteresis loop**,** and it is very clear that A_1 is much larger than A_2. Moreover, when selecting the approximate U_{1MR} as the damage parameter, the model should be re-regressed by using the selected parameter instead of by replacing the exact U_{1MR} with the approximate U_{1MR} in Equation (2.6.1). So it can be expected that this model will cause considerable errors if the fatigue life is longer. By further investigating Equation (2.6.2), it can be found that both of Z and σ_u are constants for a given type material and for a specific cross section, so in actual Equations (2.6.1) and (2.6.2) together reflect the relation between the rotation range and the cycles to failure. This observation makes an improvement of this model possible if rotation range is chosen as the damage parameter when establishing the life prediction model and this will be discussed later.

2.5 SUMMARY

By reviewing the relevant literatures, it can be found that the research on LCF has been the topic of interest for a long time and a lot of achievements have been obtained, but the research on the LCF of wrinkled pipes has only been conducted recently at the U of A. By reviewing the previous work that was completed at the U of A, it can be concluded that there are still parameters that need to be investigated, the existing model needs be improved, and new models may need to be developed based on the expanded parameters and extended fatigue lives.

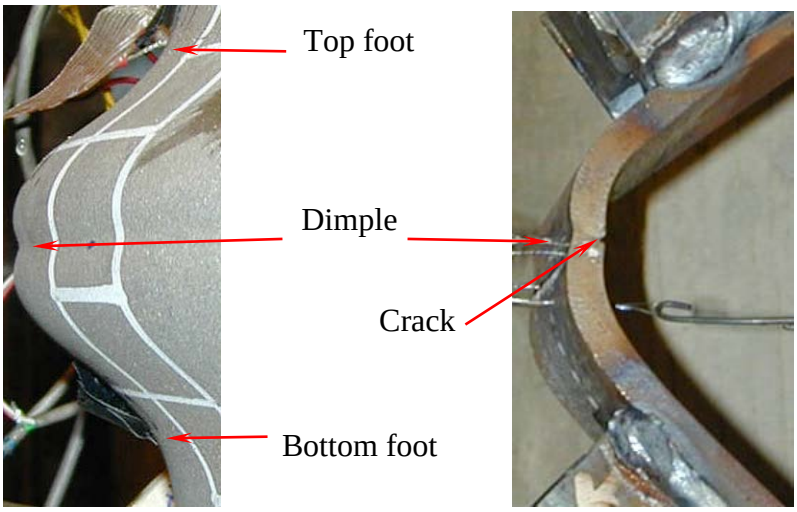

Figure 2.1: Comparison of a pipe wrinkle with a strip specimen
(Reprinted from S. Das (2002))

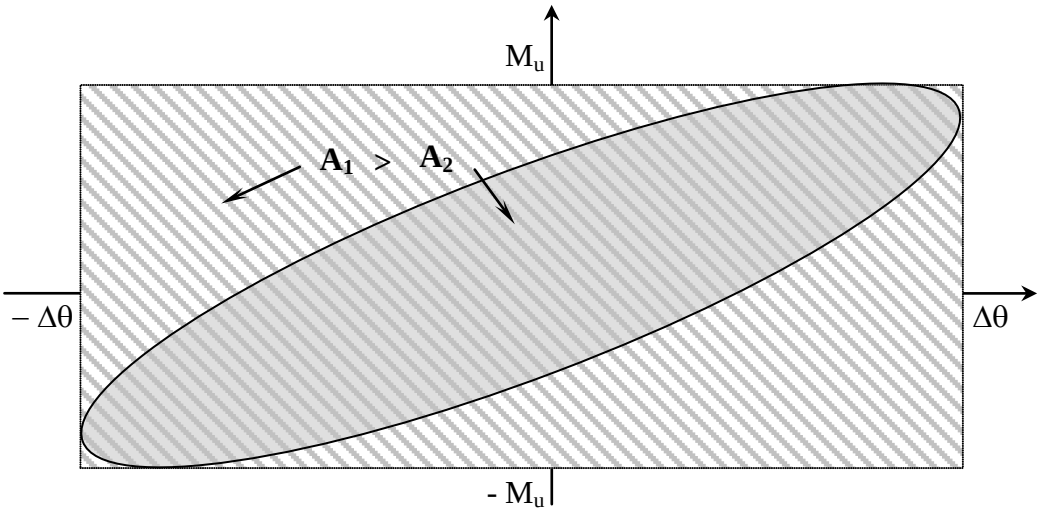

Note:
A_1 = Area of the whole square, is the approximate U_{1MR}, and
A_2 = Area of the loop, is the actual U_{1MR}.

Figure 2.2: Illustration of actual U_{1MR} and approximate U_{1MR} in Das' model

3 STRIP TEST PROGRAM

The LCF life prediction models for wrinkled pipes, which will be developed in Chapter 6, are based on the strip test results obtained from this program. In this chapter, a brief description will be given to the strip test program, and the test results will be presented and discussed.

3.1 TEST PROGRAM

This section consists of four parts: the specimens, the test set-up, the measurements and instrumentation, and the test procedures.

3.1.1 SPECIMENS

A total of 40 specimens were designed for this research program. These specimens were cut from three different full-scale pipes. One was 6 mm thick, 508 mm diameter X65 pipe, the second was 8.3 mm thick, 508 mm diameter X65 pipe, the last one was 11.9 mm thick, 406 mm diameter X 60 pipe. The 6 mm thick and 11.9 mm thick pipes were also used in full-scale pipe tests, which will be discussed in Chapter 4.

3.1.1.1 MECHANICAL PROPERTIES OF MATERIALS

Three different thicknesses (6.0 mm, 8.3 mm, and 11.9 mm) were used in the strip specimens. Therefore, three sets of tension coupons were prepared and tested correspondingly, and each set consisted of three specimens. The coupon specimens were cut from the same pipe segment as the strip specimens and were manufactured according to the requirements of Steel Pipe, CAN/CSA Z245.1-02 (CSA 2002) and ASTM A370-05 (ASTM 2005).

The tension coupons were tested by using the MTS1000 universal testing machine according to the procedure defined by SSRC Technical Memorandum No. 7 and No. 8 (T. V. Galambos 1998). A 50mm extensometer, i.e. 50 mm gauge length, was used over the middle cross section to measure strains and elongations.

The average results of each set are given in Table 3.1. In this table, the reduction of area was obtained by fitting the fractured surfaces together and measuring the dimensions of the smallest cross section. It has to be mentioned that the so-obtained value was just an approximate reduction of area because the fractured cross-section was not a perfect rectangular. It can be observed that all materials had exhibited significant elongations, which varied from 29.9 % to 33.5%. This indicated that all materials had great ductility. In addition, the variation of reduction of area from 54.6% to 63.0% also revealed the high ductility of those materials. Furthermore, the thickest material, 11.9 mm nominal thickness, had the highest ductility and the possible reason was that it had the lowest nominal grade.

3.1.1.2 SPECIMEN DESIGN

The strip specimens were designed to investigate the LCF behaviour of the wrinkled pipes in the field and further to develop the LCF life prediction model for those pipes. Therefore, similar bend shapes in the strip specimens as the wrinkle shape in the actual pipes were used, as shown in Figure 3.1. Generally, a pipe wrinkle can be divided into three parts: one wrinkle head (crest) and two wrinkle feet (see Figure 3.1). A wrinkle foot can be taken as the half of a reversed wrinkle head although their curvatures are generally different. Field and test observations (Das 2002) show the fracture usually occurs in the wrinkle head. So the strip specimen replicates only the features of a wrinkle head. Generally, different material thicknesses will have different ductility, so three sets of nominal thickness, 6 mm, 8.3 mm, and 11.9 mm, were chosen in this test program to study the influence of the material thickness. In the field, the pipelines are operated under varied loading conditions, which will result in wrinkles with different shapes. Previous test results (Das 2002) show that the wrinkle waveform or geometry is closely related to the operating pressure and the deforming stage. So in this research program, the bend angle and the bend radius were used to simulate the wrinkle geometry. A small bend angle indicated a large wrinkle and while a large bend angle revealed a small wrinkle; similarly, a small bend radius displayed a sharp wrinkle and a large bend radius demonstrated a blunt wrinkle.

Specifically, two different nominal bend radii, 15 mm and 20 mm, were chosen to simulate two types of wrinkle sharpness; and two nominal bend angles, 45° and 60°, were adopted to replicate two wrinkle sizes. In addition, six levels of stroke range, 12 mm, 20 mm, 30 mm, 50 mm, 70 mm and 80 mm, were used to represent different LCF loading amplitudes that wrinkled pipes encountered during operation.

3.1.1.3 SPECIMEN FABRICATION

The fabrication of a strip specimen consisted of three processes: cutting, bending and welding. Firstly, a straight strip with a size of 535 mm × 57 mm was cut from a pipe along its longitudinal direction by using high pressure water jets, which was called cold-cut. The reason to use this cutting method was to prevent forming residual strains and residual stresses in the strips. The considerations in determining the strip size were: on one hand, the strip had to be long enough to form a simulated wrinkle head and to weld the loading strips or plates; and on the other hand, the strip width had to be sufficiently wide to accommodate two rows of loading strip or loading plate and in the meantime be small enough to minimize the effect of the curvature of the pipe. Figure 3.2 shows a schematic of such a strip.

This straight strip was then bent by a rebar bending machine as shown in Figure 3.3. Firstly, the strip was fixed on the support by a clamp; and then the driving wheel, which could freely revolve about its own axis, rotated about the axis of the guide rod by a desired angle. After this bending operation, a strip bend, which simulated the wrinkle head, was formed in the central region of the strip. Because the elastic deformation was much smaller than the plastic deformation in this case, the bend radius could be approximated by the radius of guide rod, and the bend angle could be approached by the difference between 360 degree and the rotation of driving wheel.

Finally, two pieces of strips or plates (3 mm or 12 mm thick, respectively), called loading strips or plates, were welded on each of the strip legs and they were used to connect the specimen with the two custom-made loading mounts, as shown in

Figure 3.4. The 3 mm thick loading strips were used for the thin specimens (6 mm and 8.3 mm) and the thick specimens (11.9 mm) tested by small levels of stroke range (12 mm, 20 mm, and 30 mm). The 12 mm thick loading plates were used for the thick specimens (11.9 mm) tested by large levels of stroke range (50 mm, 70 mm, and 80 mm). The loading strips or plates were located on the strip legs by the distance between the center of the welded edge of a loading strip or plate to the center of the strip crest. For convenience, this distance is hereafter called the positioning distance, which is illustrated in Figure 3.4. The positioning distance was 105 mm for the loading plates and 110 mm for the loading strips, and was kept constant for all specimens based on two considerations. First, it had to be consistent with that used in the previous test programs (Myrholm 2001 and Das 2002). Second, it had to be large enough to prevent the strip bend, especially at the crest, from being affected by the welding of loading strips or plates, and at the same time, it had to be short enough to make the strip legs work as rigid bodies. It has to be mentioned that keeping the positioning distance constant had two side effects. The negative one was that it made the loading eccentricity, which is defined in Figure 3.1, varied with the bend angle, and the positive one was that it made the positioning of the loading strips or plates on strip legs easier and faster.

3.1.1.4 SPECIMEN DESIGNATION AND TEST MATRIX

A special designation system was introduced in this research program to label each strip specimen so that its physical parameters could be easily identified. In this designation system, T6, T8, and T12 were used to represent the nominal wall thickness of 6 mm, 8.3 mm, and 11.9 mm, respectively, and Rxx, Axx and Sxx were adopted to depict the magnitude of nominal bend radius (in mm), nominal bend angle (in degree), and nominal stroke range (in mm), respectively. For instance, T6R15A45S30 indicates a strip specimen of a nominal wall thickness of 6 mm, a nominal bend radius of 15 mm, a nominal bend angle of 45 degree, and being subjected to a nominal stroke range of 30 mm.

In this research program, a total of 40 strip specimens were planned to be tested, but a specimen designated by T6A45R15S50 was twisted during fabrication and

could not be tested, so 39 specimens were tested. The complete specimen matrix and their corresponding nominal parameters are shown in Table 3.2.

3.1.2 TEST SET-UP

Two types of loading mounts were used in this test program, as shown in Figure 3.5. The loading mount shown in Figure 3.5a was the same as that used in the previous test programs (Myrholm 2001 and Das 2002), and the other shown in Figure 3.5b was a gripping plate used for 11.9 mm thick specimens tested by nominal stroke ranges of 50 mm, 70 mm, and 80 mm.

The loading mounts were firstly bolted to the loading strips or pinned to the loading plates, and then were gripped by the hydraulic grips of the MTS1000 universal testing machine. As shown in Figure 3.6, the loading mounts had hinges that allowed the specimen subjected a vertical load only and this was similar to the loading of the wrinkled pipe wall.

As the loading heads moved up and down, the specimen was pried open and pushed close and finally it was fractured by this cyclically reversed movements of loading head.

3.1.3 MEASUREMENTS AND INSTRUMENTATION

In this test program, a series of parameters had to be measured and recorded to capture the behaviour of the test specimens. The following sections will describe those issues according to the parameters measured.

3.1.3.1 RESIDUAL STRAINS

The residual strains after monotonic bending had to be measured or evaluated properly because it was needed in both evaluating the damage due to this monotonic bending and calculating the cyclic strain induced by cyclic loading. Generally the electronic strain gauge is the first choice to measure strain because of its high preciseness and convenience, but it was excluded from the instrumentation list in this test based on two fatal limitations. The first one was the strain caused by monotonic bending, which was more than 15%, was far

beyond the measurement range of a strain gauge; the second one came from the bending process. The squeezing between the guide rod and the driving wheel during bending made it impossible to put the strain gauges on the surfaces of the strip specimen. Therefore, the approximate method used by Myrholm (2001) and Das (2002) was adopted and is briefly described as follows.

Firstly, two rows of tiny marks were punched on both outside surface and inside surface of a straight strip around its central portion, and the layout of such punch marks are shown in Figure 3.2. The distance between those two rows was 10 mm, and the gauge between any two adjacent marks was about 5 mm. When evaluating the residual strain, a gauge length of 15 mm (instead of 5 mm) was used because of two reasons: first, it had to be consistent with the clip gauge length which was employed later during cyclic loading, and, at the same time, it had to be large enough to make the errors caused by punch marks negligible. Because only the crest of strip bend, where cracks formed, was concerned, only three gauges of each row nearest to the crest of the bend were used to estimate the residual strains. The gauge length was carefully measured by an electronic caliper before the straight strip was bent, and this length was called the initial gauge length. After the specimen was bent, a strip of transparent adhesive tape was put over those punch marks carefully to avoid any voids between the tape and the strip surface, and then the locations of those marks were replicated on the tape by a pen. Next, this tape was taken away from the strip surface and put on a flat plate, so the deformed gauge length could be measured by the same electronic caliper. Then the change of gauge length, therefore the residual strain, could be obtained by calculation. The average of residual strains obtained from two rows on the same surface was taken as the final residual strain for that surface.

3.1.3.2 LOADING ECCENTRICITY

The loading eccentricity is the shortest distance from the center of strip crest to the loading line and it is shown in Figure 3.1. The loading eccentricity had to be measured because it was essential in determining the bending moment applied on the strip crest.

Before the cyclic load was applied, the loading eccentricity had to be measured firstly. This loading eccentricity was called the initial loading eccentricity and was denoted as e_o.

During the cyclic loading stage, the loading eccentricity, e, was reduced as the specimen was pried open and increased as the specimen was pushed close. It can be expressed as follows:

$$e = e_o + \delta_e \tag{3.1}$$

where δ_e is the change of loading eccentricity and is measured by a cable transducer. It is negative when the specimen is opened and positive when the specimen is closed.

3.1.3.3 ROTATIONS

Two kinds of internal angle were used in this test program. One was the internal angle between the two actual strip legs, it was call the 'actual leg angle', θ_{al}; the other one was the angle between the two pseudo legs, which were defined as the imaginary legs connecting the rotating hinges and the crest of the bend, and was termed as the 'pseudo leg angle', θ_{sl}. Correspondingly, there were two sets of rotational angle changes: one was the 'actual leg rotation', $\delta\theta_{al}$, and the other one was the 'pseudo leg rotation', $\delta\theta_{sl}$. All of those parameters are illustrated in Figure 3.7. In addition, the relations between the internal angles and rotations can be expressed as follows:

$$\delta\theta_{al} = \theta_{al} - \theta_{alo} \tag{3.2.1}$$

$$\delta\theta_{sl} = \theta_{sl} - \theta_{slo} \tag{3.2.2}$$

where θ_{alo} and θ_{slo} are the initial actual leg angle, which is the initial bend angle, and the initial pseudo leg angle, respectively (see Figure 3.7).

The reason to adopt the aforementioned rotations was based on the speculation that the difference between those two types of rotation would reveal the effect of plastic zone size to some extent. Furthermore, by investigating this effect, an approximate method could be obtained to estimate the rotation during cyclic loading, which will be introduced later.

θ_{alo} was measured right after the monotonic bending and θ_{slo} was measured just before the cyclic loading. $\delta\theta_{al}$ was measured directly by two RVDTs (rotational variable differential transformers). For some specimens, RVDTs were bolted to the loading mounts (as shown in Figure 3.6a), but it was found not to work well because the bolts could revolve about their own axes even if the nuts were snug tight. Hereafter they were clamped on the legs of specimen directly (as shown in Figure 3.6b). It was found that they worked very well. However, $\delta\theta_{sl}$ could not be measured directly, so an indirect method was introduced. This method uses the geometric relationship among the rotation, stroke, and loading eccentricity, and this relation can be expressed as follows:

$$\delta\theta_{sl} = 2 \times \tan^{-1}\left(\frac{H_o + S}{2(e_o + \delta_e)}\right) - \theta_{slo} \tag{3.3}$$

where e_o, δ_e and θ_{slo} were introduced previously, H_o is the initial loading height as shown in Figure 3.7 and S is the stroke of the loading machine.

3.1.3.4 CYCLIC STRAINS

Unlike the stroke and the rotation, which are global variables, the strain is a local variable. It is the most important parameter in the traditional LCF research because it is the requisite variable to determine the cyclic strain range and to develop the LCF life prediction model. Unfortunately, the actual strain could not be measured in this test because of the limitation of current measuring techniques. Experience from the test program of Myrholm (2001) showed that the electronic strain gauge on the strip crest was liable to debond from the specimen surface because of the very large and cyclically reversed bending deformation at the crest. So in this test program, only a clip gauge of 15 mm gauge length was installed on the outside surface of the strip crest to measure the strain history, as shown in Figure 3.6, during the cyclic loading.

It has to be emphasized here that the measured value by the clip gauge was not the strain of the extreme fiber on the outside surface of the strip crest according to the traditional definition of engineering strain, where it is defined as the length change of a unit line segment. For the clip gauge, its two feet stood on a curve

(strip bend), so what it measured was the strain of the straight line connected by the two points where it stood instead of the curve it mounted. For distinguishing this strain from the traditional engineering strain, it was termed as ‘clip strain’ in this test program.

3.1.3.5 OTHERS

The magnitudes of MTS load and MTS stroke were measured directly by the sensors in the MTS1000 machine and recorded automatically by an automatic data acquisition system at a pre-set frequency.

3.1.4 TEST PROCEDURES

Generally, the strain-controlled method is used to conduct the LCF test for two reasons. First, when the material becomes plasticized, the load increase can be quite small while the material went through strain hardening, and this makes the load control impossible in the LCF regime. Second, crack initiation is generally induced by the local plastic deformation around the defects and other imperfections. Coffin (1984) and Manson (2006) believed that the failure of LCF is basically caused by cyclic plastic strains. But for this test program, a totally reversed stroke-controlled, instead of strain-controlled, loading method was employed because of the difficulty in measuring the strain on the strip bend crest. The characteristics of the stroke spectra will be described and discussed in the next section.

For LCF, the loading rate has to be properly controlled. A too fast loading rate will cause significant heat loss and a too slow loading rate will induce creep (Wang and Chen 2001 and 2002, Wang et al. 2001). In this test program, the loading rates were chosen according to past experience, and the details of the loading program are shown in Table 3.3. The average loading rate was 8.57 mm/min for 12 mm stroke range, 11.45 mm/min for 20 mm stroke range, 11.19 mm/min for 30 mm stroke range (except for specimen T6R20A45S30 an average loading rate of 8.11 mm/min was used), 10.64 mm/min for 50 mm stroke range, 8.33 mm/min for 70 mm stroke range, and 8.07 mm/min for 80 mm stroke range.

These loading rates were programmed in the controller of the MTS1000 universal testing machine to automatically load the strip specimens.

The cyclic stroke was applied to the specimen by the MTS1000 universal testing machine. The test was terminated when the crack was totally developed across the cross section and the two parts were almost totally separated.

3.2 TEST RESULTS AND DISSCUSSION

In this section, the spectra and the hysteresis loops of MTS stroke and MTS load will be presented, followed by those of rotation and moment, and completed with those of clip strain and nominal stress. The fatigue lives and failure mechanism will also be presented and discussed.

3.2.1 MTS LOAD AND MTS STROKE

Usually, the controlled variable is called ‘input’ and the uncontrolled variable is called ‘output’. In this test program, the input was the MTS stroke and the output was the MTS load. And both of them were related to the MTS universal testing machine and they were global variables.

3.2.1.1 TERMINOLOGIES

Before giving the spectra and the hysteresis loops, the following terminologies are introduced firstly.

- Maximum stroke: the maximum opening stroke in each cycle and it is denoted as S_{max}. The opening stroke is positive.
- Minimum stroke: the maximum closing stroke in each cycle and it is denoted as S_{min}. The closing stroke is negtive.
- Stroke range: $\Delta S = S_{max} - S_{min}$.
- Stroke amplitude: $S_a = \Delta S/2$.
- Mean stroke: $S_m = (S_{max} + S_{min})/2$.

3.2.1.2 QUALITATIVE ANALYSIS

A qualitative analysis is conducted firstly to help in understanding the characteristics of axial load spectra and hysteresis loops. By deformation analysis, as shown in Figure 3.8, it can be found that two types of deformation contribute to the stroke: one is the elongation and contraction of the specimen and the other is the rotation of the specimen. For the specimen subjected to MTS load only, this load could be decomposed into two components, i.e. the parallel and vertical components with respect to the specimen leg. It was the parallel component that made the specimen elongation or contraction and it was the vertical component that caused the specimen legs to rotate. Therefore, the stroke can be symbolically described by the following equation:

$$S = \frac{P \sin \theta_{al}}{K_{SP}} + \frac{Pe}{K_{SM}} \tag{3.4}$$

where, S is the stroke, K_{SP} is the required axial load to produce a unit stroke (not a constant), K_{SM} is the required bending moment to generate a unit stroke (not a constant), P is the MTS load and e is the loading eccentricity.

Because of the strong constraints from the loading strips or plates, the specimen legs can be treated as ‘rigid bodies’. However, the strip bend is deformable and this makes the rigid strip legs translate and rotate. So in Equation (3.4), K_{SP} and K_{SM} are the properties of strip bend instead of sectional properties, and, virtually, they are directly related to both the bend geometry and the cross section size. For simplification, the strip bend can be treated as a hinge approximately when the specimen rotation is the concern, so the specimen rotation will be solely determined by the cross section properties and the bending moment applied at the strip crest.

For the strip specimen, since it has a very flat cross section, so it has much stronger axial rigidity to resist tension or compression than bending rigidity to resist rotation. In other words, the specimen is much easier to be bent than to be stretched or shortened. As the specimen is closed, the loading eccentricity increases, and the actual leg angle decreases, so the contribution of specimen

contraction to the stroke is small and can be neglected; but when the specimen is excessively opened, the loading eccentricity can be decreased near to zero, and the actual leg angle will become large, then the contribution of specimen elongation to the stroke will be large and cannot be neglected.

3.2.1.3 SPECTRA

GENERAL

The MTS stroke spectrum is the curve which exhibits the variation of MTS stroke with time and similarly the MTS load spectrum is the curve that shows the variation of MTS load with time. The characteristic parameters of MTS stroke spectra employed in this test program are summarized and given in Table 3.4. From this table, it can be found that the MTS stroke spectra can be categorized into six groups according to the corresponding MTS stroke ranges.

A better way to understand the difference between the MTS stroke spectra and the MTS load spectra is by direct comparison. Figure 3.9 shows both the MTS stroke spectra and the MTS load spectra, where four sets of typical spectra are chosen from specimens T12R15A45S20, T12R15A45S30, T12R15A45S50 and T12R20A45S70. It is noted that T12R20A45S70 instead of T12R15A45S70 was chosen because the test data could not be recorded properly for the latter. From Figure 3.9, the following observations can be obtained.

First, the MTS stroke amplitude was constant during the test, but the MTS load amplitude was not and it decreased as the test progressed. This phenomenon can be referred to as ‘stroke softening’, which is analogous with ‘strain softening’ observed in the traditional fatigue regime. In others words, the MTS load decreased as more cyclic MTS strokes were accomplished. Actually this drop of MTS load was due to the formation and propagation of cracks, which on one hand reduced the net area of the cross section and consequently decreased the required load to attain the designated stroke range, and on the other hand caused heavy stress concentration around the crack tips and made the cross section plasticized gradually. Second, the degree of ‘stroke softening’ was related to the MTS stroke

amplitude directly, it became worse as the MTS stroke amplitude increased. Third, all MTS stroke spectra had or nearly had the forms of sine waves, but the axial load spectra were not guaranteed to have the same wave forms as the MTS stroke spectra. When the MTS stroke amplitude was small, they showed the almost same wave forms, e.g. T12R15A45S20; but the MTS load spectra looked more like sine waves being chopped peaks and bottoms when the MTS stroke amplitude was large, e.g. specimen T12R20A45S70. This behaviour can be explained by the amplitude of plastic deformation. The MTS load near linearly varied with the MTS stroke if there was no plastic deformation, but this linear relation did not hold anymore when the cross section became plasticized and as a result, the increase of MTS load would be retarded. Finally, the MTS stroke was totally reversed, i.e. the mean MTS stroke was zero, and this indicated that the input was well controlled; but the MTS load was not totally reversed and the opening load was significantly larger than the closing load.

SOME ABNORMAL SPECTRA

Due to negligence or some unexpected reasons, some specimens were not tested by their designated stroke spectra. For those specimens, the following will give a brief description and their corresponding MTS stroke spectra.

For 6 mm and 8.3 mm thick specimens that were tested by a stroke range of 50 mm, the actual MTS stroke spectra consisted of two sets of form: one was the sine wave with a range of 50 mm and the other was the triangle form with a range of 42.8 mm, and they applied to the specimens alternatively. This fluctuation was due to a program error and was modified in testing 11.9 mm thick specimens. A portion of the loading spectrum is shown in Figure 3.10a.

The actual stroke range of specimen T6R15A60S80* was 60 mm instead of 80 mm. This specimen had a small initial eccentricity of 57.1 mm, so the opening load became so large when the MTS stroke approached the maximum stroke (i.e. 40 mm) that the spot-welds between the loading strips and the specimen legs were broken. Hence, the stroke range was reduced to 60 mm to finish this test. A part of the actual MTS stroke history is shown in Figure 3.10b.

Because a wrong loading program was employed, the specimen T6R15A45S30* was heavily overloaded and the maximum MTS stroke reached 46.7 mm in the second cycle. However, the stroke range was set back to 30 mm hereafter. A part of the actual MTS stroke history is shown in Figure 3.10c.

Because of the yield of the loading strips at the first cycle, the stroke range of specimen T12R15A60S50* was decreased to 40 mm (Figure 3.10d).

3.2.1.4 HYSTERESIS LOOPS

In this test, the MTS load and MTS stroke hysteresis loops could be obtained directly because both of them were recorded automatically. For convenience, hereafter those loops will be referred to as LSHLs (load vs. stroke hysteresis loops). LSHLs reflect the relation between the MTS load and the MTS stroke and moreover, the area enclosed by each loop indicates the dissipated energy during that cycle and is referred to as the HLE.

DESCRIPTION OF A TYPICAL LSHL

Based on the intrinsic features of LSHLs, a typical single loop, as shown in Figure 3.11, can be described in three different ways.

Because this test was stroke controlled, the ‘loading’ in this test meant increasing stroke from the minimum level to the maximum level and conversely, the ‘unloading’ denoted decreasing stroke from the maximum level to the minimum level. Based on this concept, the shown loop exactly recorded a cycle of loading and unloading paths: the unloading path of ‘ABCDEFG’ and the loading path of ‘GHIJKLA’.

Second, when the MTS load was positive, the specimen was being pulled; and when the MTS load was negative, the specimen was being pushed. So the presented loop precisely formed a cycle of pulling and pushing paths: the pulling path of ‘IJKLABC’ and the pushing path of ‘CDEFGHI’.

Third, from the initial position, i.e. before the cyclic loading was applied, the specimen was opened if the stroke was positive and it was closed if the stroke was

negative. So the given loop faithfully specified a cycle by the closing path of 'FGHIJKL' and the opening path of 'LABCDEF'.

Finally, the loop was also obviously characterized by six points: points 'L' and 'F' are called 'zero-stroke' points because the strokes are zero at those moments; points 'C' and 'I' are termed 'zero-load' points because the MTS loads are zero at those points; and points 'A' and 'G' are obviously corner points and they are named the upper corner point and the lower corner point, respectively.

GENERAL OBSERVATION AND DISCUSSION

Figure 3.12 shows some typical LSHLs from four specimens and based on them, some general observations can be made as follows.

First, the loops gradually became flat as the test advanced and this corresponded to the phenomenon of 'stroke softening', which was discussed previously. Furthermore, the flattening of loops showed that the energy absorption capacity was decreased as the test progressed. This was the direct result of the initiation and propagation of cracks.

Second, the loop peaks were exactly the upper corner points of loops, but the loop nadirs were not guaranteed to be the lower corner points of loops. They were the same when the stroke range was very small, e.g. specimen T12R15A45S20, and they were not when the stroke range was large, e.g. specimen T12R20A45S70. This can be attributed to the loading eccentricity, and it will be discussed further later.

Third, for the specimens tested by small stroke range, a very dark and thick 'loop', which was termed 'dark loop' in this program for convenience, could be identified in this figure; but for the specimens tested by large stroke range, there was no such 'dark loop'. Actually, the dark loop was a band of loops and it was the result of the slow decrease rate of the MTS load.

Fourth, for the specimens tested by large stroke range, the loop became steeper when the stroke approached the maximum level during the first few cycles. As discussed in the section 3.2.1.2, when the specimen was heavily opened, the

contribution of specimen elongation to stroke increased and at the same time, that of specimen rotation to stroke decreased, so more MTS load was needed to acquire the designated stroke. The reason will be given later.

The final observation is that there was an abrupt increase of pushing load when the stroke approached the minimum level at the very late stage of the test. This phenomenon corresponded to the closure of a very wide and deep crack on the inside of the specimen.

FURTHER OBSERVATION AND DISCUSSION

To fully understand the characteristics of LSHLs, Figure 3.11 has to be reviewed again and the following observations and discussion can be made.

First, the very short paths ‘AB’ and ‘GH’ were nearly vertical, which indicated the phenomenon of load relaxation due to the hold of the maximum stroke and the minimum stroke.

Second, along paths ‘BCD’ and ‘HIJ’, near linear relations existed between the MTS load and MTS stroke. This indicated that the specimen behaved elastically. But the unloading path ‘BCD’ was much steeper than the loading path ‘HIJ’ and this can be attributed to the loading eccentricity. The loading eccentricity increased along the unloading path that made the unloading accelerated, so this phenomenon can be termed as ‘unloading acceleration’. On the contrary, the loading eccentricity decreased along the loading path and this made the loading retarded, so this phenomenon can be called ‘loading retardation’.

Third, following path ‘BCD’, path ‘DE’ showed a gradually decreased unloading rate and this indicated the cross section at crest was gradually plasticized or ‘softened’. The point ‘E’ was the nadir of the whole unloading path. Similarly, path ‘JK’ exhibited a gradually decreased loading rate and this indicated the cross section at crest was gradually plasticized or ‘softened’. But point ‘K’ was not the summit of the loading path.

Fourth, path ‘EFG’ showed a negative unloading rate, which was very small; but path ‘KLA’ still exhibited a visible positive loading rate. The difference between

them can be explained by the loading eccentricity again. Along the path 'KLA', the cross-section at crest was totally plasticized and it reached its maximum moment resistant capacity, M_p, which was the product of the maximum MTS load and the corresponding loading eccentricity. As the specimen was loaded, the loading eccentricity was decreased, so the MTS load had to be increased to keep M_p constant at crest. On the contrary, as the specimen was unloaded, the loading eccentricity was increased, so the MTS load had to be decreased to keep M_p unchanged at crest. Moreover, the increase of loading eccentricity during unloading along path 'EFG' was much smaller than the decrease of loading eccentricity along path 'KLA', so this made the former being a near plateau and the latter being a slope.

Finally, significant strokes were left at the zero-load points 'C' and 'I', so the specimen could not go back to its initial position. This was because considerable plastic deformation accumulated in the strip bend. Similarly, zero-stroke points 'F' and 'L' exhibited that considerable MTS loads were needed to make the specimen back to its initial position.

3.2.2 MOMENT AND ROTATION

Henceforward, the moment refers to the moment at the cross section of strip crest, and the rotation can be either the actual leg rotation or the pseudo leg rotation, which were defined in section 3.1.3.3. For evaluating the difference between those two types of rotation, specimen T12R15A45S50 is taken as an example and the results are shown in Figure 3.13. From this figure, it is found that they have the same wave form and are synchronal, but their amplitudes are unequal and the actual leg rotation, $\delta\theta_{al}$, is bigger than the pseudo leg rotation, $\delta\theta_{sl}$. This difference indicates the impact of plastic zone on the rotation, and it can be expected that the difference becomes greater when the bend angle is small, which indicates a large plastic zone. From the engineering point of view, the difference is small enough to be ignored, so the pseudo leg rotation instead of the actual leg rotation is used in this test program to do the analysis. The other two reasons using $\delta\theta_{sl}$ instead of $\delta\theta_{al}$ in analyses are: first, some RVDTs did not work well in

the test program, so the actual leg rotations could not be applied to all specimens; second, the previous tests conducted by Myrholm (2001) and Das (2002) employed the pseudo leg rotations, so it was more convenient to use the pseudo leg rotations to make a comparison among them.

3.2.2.1 TERMINOLOGIES

Some terminologies, which are similar to those used in stroke spectra, can be introduced as follows:

- Maximum rotation: the maximum opening rotation in each cycle and it is denoted as $\delta\theta_{slmax}$. The opening rotation is considered positive.
- Minimum rotation: the maximum closing rotation in each cycle and it is denoted as $\delta\theta_{slmin}$. The closing rotation is considered negtive.
- Rotation range: $\Delta\theta_{sl} = \delta\theta_{slmax} - \delta\theta_{slmin}$.
- Rotation amplitude: $\delta\theta_{sla} = \Delta\theta_{sl}/2$.
- Mean rotation: $\delta\theta_{slm} = (\delta\theta_{slmax} + \delta\theta_{slmin})/2$.

3.2.2.2 QUALITATIVE ANALYSIS

As discussed in section 3.2.1.2, the relation between rotation and bending moment can be symbolically expressed as follows:

$$\delta\theta_{sl} = \frac{M}{K_{RM}} \tag{3.5}$$

where $\delta\theta_{sl}$ is the pseudo leg rotation, $M = P \times e$ is the bending moment, and K_{RM} is the required bending moment to attain a unit rotation (not a constant).

From this equation, it can be expected that the rotation can increase without the increase of the bending moment when the cross section is totally plasticized.

3.2.2.3 SPECTRA

Similarly, the rotation spectrum indicates the variation of rotation with time and the moment spectrum exhibits the variation of moment with time. And the characteristic parameters of rotation spectra are given in Table 3.5.

Some typical bending moment spectra and rotation spectra are shown in Figure 3.14. From this figure, some observations can be made. The first and most important one is that $\Delta\theta_{sl}$ is nearly constant during the whole loading period and this feature is the same as that of stroke spectra, so it can be treated as an input or controlled variable. Second, the maximum bending moment decreases as count number goes up and this phenomenon can be referred to as 'rotation softening', which is similar to 'stroke softening' in the MTS load spectra. Finally, the couple of rotation and moment spectra are similar to that of MTS stroke and MTS load spectra, so the similar observations can be made as those in MTS stroke and MTS load spectra.

3.2.2.4 HYSTERESIS LOOPS

Similarly, the bending moment and pseudo leg rotation hysteresis loops are denoted as MRHLs (moment vs. rotation hysteresis loops), henceforth just for convenience.

DESCRIPTION OF A TYPICAL MRHL

Based on the intrinsic features of MRHLs, a typical single loop, as shown in Figure 3.15, can be described in the same three different ways as were used in Figure 3.11, so no more details will be given.

GENERAL OBSERVATION AND DISCUSSION

Four typical MRHLs and their corresponding typical loops are shown in Figure 3.16. Compared with Figure 3.12, a couple of observations can be made as follows.

The first one, also the most important one, is that the loading path and the unloading path are approximately antisymmetric about the diagonal connected by the upper corner point and the lower corner point. This feature is different from that of Figure 3.12 and can be explained based on Equation (3.5). The relation between the rotation and the bending moment is totally determined by its bending moment resistance and rigidity, so the loops show the antisymmetric feature if the opening moment resistance and rigidity is similar to those of the closing. But,

based on Equation (3.4), the stroke depends not only on the MTS load and its corresponding resistance and rigidity but also on the bending moment and its corresponding resistance and rigidity. In addition, the pulling path and the pushing path are also nearly antisymmetric about the abscissa, and the opening path and the closing path are antisymmetric about a vertical line, which is parallel to the ordinate.

Second, the maximum opening rotation is bigger than the closing rotation and the degree of this bias goes up as the stroke range is increased. This can be easily explained from Equation (3.3).

Third, the maximum opening moment is almost the same as the closing moment, and they correspond to the maximum pseudo leg rotation and the minimum pseudo leg rotation, respectively. Specifically, a near plateau occurred when the pseudo leg rotation is large and the size of this plateau becomes larger as the pseudo leg rotation range is widened. Based on Equation (3.5), before the moment reaches M_p, the moment goes up as the specimen is being opened or closed; when the moment reaches M_p, the moment can not goes up any more, so the plateau forms.

FURTHER OBSERVATION AND DISCUSSION

Further observations and discussion will focus on Figure 3.15 and they are as follows.

First, similar with Figure 3.11, the very short paths ‘AB’ and ‘GH’ were nearly vertical, which corresponds to the phenomenon of load relaxation due to the hold of the maximum stroke and the minimum stroke.

Second, similar with Figure 3.11, near linear relations existed between the bending moment and the pseudo leg rotation along paths ‘BCD’ and ‘HIJ’ and this indicated that the specimen behaved elastically. Different to Figure 3.11, the unloading rate of path ‘BCD’ is almost same as the loading rate of path ‘HIJ’ and this indicated that the pseudo leg rotation is directly and almost only related to the bending moment, and vise verse.

Third, as for paths ‘DE’ and ‘JK’, the characteristics are the same as Figure 3.11 except that the point ‘E’ is not the nadir of the whole unloading path.

Fourth, path ‘EFG’ and path ‘KLA’ were nearly straight lines and their slopes were so small that they could be treated as plateaus. Along those paths, the cross-section at strip crest was totally plasticized and it reached its maximum moment resistance capacity, M_p, so the bending moment could not be increased anymore.

Finally, points ‘C’ and ‘I’ showed that significant pseudo leg rotations are left when bending moments decrease to zero and this was because considerable plastic deformation accumulated in the strip bend. Following this concept, points ‘F’ and ‘L’ exhibited that considerable bending moments were needed to make pseudo leg rotations back to zero.

3.2.3 STRESS AND STRAIN

As introduced previously, a straight strip was firstly bent to a desired shape. The whole loading history consisted of two stages: one was the monotonic bending stage and the other was the cyclic loading stage. The following sub-sections will discuss the stress and strain according to these two loading stages.

3.2.3.1 MONOTONIC BENDING STAGE

During the monotonic bending stage, the strip was heavily deformed and as a result the residual strain and residual stress were permanently left in the cross section in the strip bend when the bending load was totally removed.

RESIDUAL STRAIN

The residual strain can be measured by the method described in the previous section and the results are presented in Table 3.6. It can also be obtained by theoretical analysis and is discussed as follows.

To obtain the theoretical residual strain, the traditional hypotheses of plane section are assumed to be valid, i.e. the plane section remains plane after deformation and the neutral axis is normal to the plane section. Also three approximations have to be made for simplifying the analysis, i.e. the cross section

is a perfect rectangular, the material is elastic and perfectly plastic (as shown in Figure 3.17), and only bending moment acts on the specimen. Then the residual strain can be obtained by employing the principles of superposition and elastic recovery, the results can be found in most "Mechanics of Materials" books, such as Hibbeler (2003) and Dowling (2007). For this typical problem, the residual strain can be derived in the following forms (refer to Figure 3.17):

$$\varepsilon_r = \varepsilon - \Delta\varepsilon \tag{3.6.1}$$

where ε is the strain before unloading and $\Delta\varepsilon$ is the recovered strain due to unloading and they can be obtained according to the following equations. Specifically, these two parameters can be determined as follows (refer to Figure 3.18):

$$\varepsilon = 1 \Big/ (1 + 2R/t) \tag{3.6.2}$$

$$\Delta\varepsilon = \frac{\varepsilon_y}{2}\left[3 - \left(\frac{\varepsilon_y}{\varepsilon}\right)^2\right] \tag{3.6.3}$$

where

R = inside radius (or bend radius), in mm,

t = wall thickness, in mm,

ε_y = yield strain = σ_y/E,

y = elastic core size= $t \times \varepsilon_y / \varepsilon$.

In this test program, two types of bend radius, 15 mm and 20 mm, and three sets of nominal thickness, 6 mm, 8.3 mm and 11.9 mm, were used; and their corresponding mechanical properties were obtained from coupon tests (shown in Table 3.1); and then the residual strain can be calculated according to the above equations.

For the strip specimen, because the maximum bend radius is 20 mm and the minimum thickness is 6 mm, Equation (3.6.2) gives a minimum ε of 13.04%. And from Equation (3.6.3), the maximum $\Delta\varepsilon$ is 1.5 ε_y or 0.75%. It can be seen that $\Delta\varepsilon$

is so small compared with ε that it can be neglected. Thus ε_r can be approximate by ε, or by:

$$\varepsilon_r \approx \frac{1}{1+2R/t} \tag{3.7}$$

From this equation, two conclusions can be derived. First, the residual strain is mainly determined by the bend radius and the wall thickness. Second, the residual strain increases as the ratio of bend radius to wall thickness decreases. It also can be seen that the bend angle has no contribution to the residual strain.

For comparing with the measured values, those theoretical residual strains are also included in Table 3.6. From this table, some observations can be made as follows.

First, the residual strains are very large and the measured absolute values varied from 11.70% to 18.59% for the thinnest specimens, from 13.31% to 26.99% for the medium thick specimens, and from 21.03% to 35.59% for the thickest specimens. The residual strain increases as the thickness increases and/or as the bend radius decreases. This observation is consistent with the conclusion derived from Equation (3.7).

Second, the differences between the measured and calculated residual strains are small in the engineering point of view and both of them can be used to estimate the residual strain. But it is difficult to tell which one is better because both of them have their error sources. In the measurement method, errors mainly come from the method itself, e.g. the contact status between the transparent tape and the strip surface, the size of punch marks, and the coincidence of the tips of electronic caliper with those punch marks etc. In the theoretical method, errors come from the hypotheses, and idealized dimensions, which were usually different from their actual conditions.

The amplitudes of measured strains on the outside surface are all larger than those on the inside surface, but this observation is different from the conclusion of Equation (3.7), which concludes that they have the same amplitude. Consequently, the differences are all negative on the outside surface and all positive on the inside surface. This observation can be explained as follows:

Equation (3.7) assumes that the cross section is a perfect rectangular, but in actual it is a curved quadrangle. This will make the neutral axis move inward, i.e. toward the inside surface, so the strain on the outside surface will be larger than that on the inside surface.

RESIDUAL STRESS

The residual stress cannot be measured directly, but it can be analytically determined by using the measured residual strain and the assumed stress-strain relationship. An illustration of residual stress distribution is schematically shown in Figure 3.18.

Based on the conclusion that the yield strain can be neglected compared with the strain evaluated from Equation (3.7), the following characteristic values can be obtained:

$$\sigma_r \approx \begin{cases} -0.5\sigma_y & \text{on outside surface} \\ 0.5\sigma_y & \text{on inside surface} \end{cases} \tag{3.8}$$

where σ_r is the residual stress and σ_y is the yield stress of material.

The residual stress distribution is also schematically shown in Figure 3.18. It can be seen that a compressive residual stress is left on the outside surface while a tensile residual stress on the inside surface.

3.2.3.2 CYCLIC LOADING STAGE

Because only the cyclic strain on the outside surface of the cross section at strip crest was measured by the clip gauge, the following will only discuss this strain and its corresponding cyclic nominal stress.

CYCLIC STRAIN

When cyclic load was applied, the action of cyclic opening and cyclic closing made the strain cyclically increase and decrease. Because the deformation was so large that the specimens went far into the plastic region, the strain was accumulated gradually on both inside and outside surfaces at the strip crest.

It is difficult to measure this accumulated strain accurately because of the reasons discussed previously. In this test, a clip gauge was installed to record the so-called clip strain during cyclic loading on the outside surface at strip crest.

Figure 3.19 shows a clip gauge strain spectra of specimen T8R15A45S50 caused by cyclic loading. From it, three observations can be made. The first one is that the maximum strain reached as high as 34.8%, which was greatly over the static fracture strain (i.e. 30.5%) obtained from coupon test. One possible reason is that the clip strain is different from the strain defined in coupon test. Another possible reason is that the static fracture strain is less than the cyclic fracture strain. The second observation is that the mean clip strain was very high and increased steadily as the test progressed, and this steady increase of mean clip strain resulted in a phenomenon of 'ratching' in the clip strain spectrum. The last one is that the clip strain range increased as the number of cycles increased from the beginning to the near end, and this was due to the accumulation of plastic strain in the strip bend. But when the specimen was near to be fractured, the clip strain range decreased as more cycles were consumed, this is because the heavily fractured section on the inside, which made neutral axis greatly moved toward the outside and consequently only a very small strain was needed to obtain a given opening stroke.

CYCLIC STRESS

During the cyclic loading stage, the stress on the cross section of strip crest was induced by the combined action of axial load and bending moment. Two main reasons make obtaining the cyclic stress impossible. First, the specimen was in an elasto-plastic stress state and the cyclic stress-strain relation was unknown. Second, when the cracks occurred in the specimen, it was difficult to evaluate the actual cross section area and section modulus. So in this test program, no effort was made to obtain the cyclic stress on the cross section at the strip crest.

However, the cyclic stress can be obtained conceptually by analysis. It is known that the cyclic strain is beyond the yield strain, so the cyclic stress varies approximately from $-\sigma_y$ to $+\sigma_y$.

HYSTERESIS LOOPS

As stated above, the cyclic stress can not be measured, so the stress and strain hysteresis loops are not presented.

3.2.4 CYCLES TO FAILURE

3.2.4.1 RESULTS AND DISCUSSION

A specimen was considered to be failed when the two fractured portions were totally or near totally separated. The cycles to failure were determined based on the following two principles:

- Dividing a single loading cycle into four parts, which are $0 \rightarrow S_{max} \rightarrow 0 \rightarrow S_{min} \rightarrow 0$, so the minimum counting unit is 1/4 cycle.
- Taking 2% of the maximum opening load and 2% of the maximum closing load as the criteria of failure.

The results are given in Table 3.7. The cycles in the table also include the initial 1/4 cycle, in which the stroke goes from zero to the maximum opening stroke. From the table, it is obvious that the cycles to failure depends on the selected test parameters of material thickness, bend angle, bend radius, and stroke range. Increasing the stroke range, material thickness and bend angle will shorten the LCF life, but the reasons are different. For the stroke range, it is obvious that a big stroke range produces more reversed deformation in the strip bend than a small stroke range. For the material thickness, thick specimens have more residual strain before cyclic loading and experience more reversed deformation during cyclic loading in the strip bend than thin specimens. As for the bend angle, a specimen with big bend angle has a small loading eccentricity, so it experiences a big cyclic deformation in its strip bend. On the contrary, increasing bend radius will lengthen the LCF life. It is sure that a specimen with small radius has big residual strain, and this decreases the energy absorption ability of the specimen. But it is not sure how the bend radius impacts the cyclic deformation, and this needs to be investigated in the future.

3.2.4.2 COMPARISON AND DISCUSSION

Table 3.8 shows the cycles to failure obtained by Das (2002) and Myrholm (2001). From this table, the same observations as above can be made. Some tests performed by Das (2002) were repeated in this test program. Those tests were the specimens with nominal material thickness of 6 mm and 8.3 mm, bend angle of 45^{o} and stroke ranges of 50 mm and 80 mm, as shown in Tables 3.7 and 3.8. By comparing the results of the corresponding specimens it can be found that the difference between these two test series is within the error tolerance from the fatigue life point of view. The possible sources of the difference are the difference in failure criterion and the difference in bend angle, which could not be exactly controlled.

3.3 FAILURE MECHANISM

Because the strip specimens were subjected to cyclic loading, the fatigue failure is taken as their failure mechanism. However, in order to understand the failure mechanism of the strip specimens under the LCF, the fracture surface should be thoroughly examined. The SEM (scanning electron microscope) was employed to examine their fracture surface in microscopic level.

3.3.1 MACROSCOPIC EXAMINATION

The fracture surfaces of all specimens are shown in Appendix A. Only three typical fracture surfaces (T6R15A60S30, T8R15A60S30, and T12R15A60S30) are chosen here for general discussion, as shown in Figure 3.20.

3.3.1.1 GENERAL OBSERVATION

There are usually two crack propagation regions, which are the outside region and the inside region, on the fracture surface. It is known that the tensile stress causes the crack to propagate and the compressive stress closes the crack. Therefore, the inside cracks propagate when the specimen is opened, and the outside cracks develop when the specimen is closed. As shown in Figure 3.20, the inside portion is much larger than the outside portion. It can be explained by the residual stress

and the amplitude of leg rotation. After the monotonic bending stage, a tensile residual stress remained on the inside surface and on the contrary, a compressive residual stress remained on the outside surface. It is known that the tensile residual stress accelerates the initiation and propagation of cracks, and on the contrary the compressive residual stress retards the initiation and propagation of cracks. During the cyclic loading stage, the inside portion was elongated and the outside portion was contracted when the specimen was opened, and vice verse. Also to attain the same stroke amplitude, the specimen legs will rotate more when the specimen is being opened than being closed. Therefore, during a typical cycle, more elongation was made on the inside surface than on the outside surface, and consequently, more crack propagation occurred on the inside surface.

3.3.1.2 CRACK INITIATION

The crack origins all are on the surfaces. For 6 mm and 8.3 mm thick specimens, the cracks were generally initiated from the punch marks (for residual strain measurements), tack weld point (for attaching the cable transducer) and scratch lines (for positioning the punch marks). After realizing some cracks initiated from the scratch lines, those scratch lines were not used in 11.9 mm thick specimens. There were also other sources of origin, such as surface irregularities and surface inclusions.

In addition to the above sources of crack initiations, there were two other possible origins: one was the micro voids that formed during the monotonic bending stage because the residual strain exceeded the ultimate strain, so the 'necking' occurred on and near the outside surface; the other was the micro 'wrinkles' that formed during the monotonic bending stage because of the significant compressive strain induced by the heavy bending deformation on the inside surface. Enami (2005) observed that compressive strain could produce microwrinkles on the surface because of microbuckling. The same observation can be found from the full-scale pipe tests as shown in Figure 3.21 by Aydin (2006).

3.3.1.3 CRACK PROPAGATION

From the observations of the test results, the cracks first occurred on the inside surface followed by the outside surface. As test progressed, more and more small cracks occurred and some of them grew and coalesced. Further, the crack propagation was then localized in these coalesced cracks and the growth of other cracks was depressed. There were some differences between the behaviour of inside surface and outside surface, and between the thin (6 mm and 8.3 mm) and thick (11.9 mm) specimens. For the inside surface, small cracks firstly were found around the punch marks and the sizes of them became larger as they were closer to the strip crest. This phenomenon could be found both in thin and thick specimens. But for the thin specimens, those small cracks were along the scratch lines and so they were straight. And for the thick specimens, the small cracks not only formed around the punch marks but also at other locations, although the cracks at other locations were much smaller than those around the punch marks. In addition, all those cracks were irregular and sparsely distributed on the surface because of the absence of scratch lines. As for the outside surface, small cracks firstly occurred around the punch marks and then at other locations and the former were much bigger than the latter. But for the thin specimens, the cracks near or at the crest coalesced firstly and then this crack dominated the crack propagation. For the thick specimens, the coalesced cracks were not guaranteed to be along the punch marks. After the coalescing of some cracks, the other cracks were suppressed because of the decrease of loading.

Several specific characteristics on the fracture surface can be found by examining the fracture surfaces. The first is the appearance. The fracture surface shows distinct appearances from the surface to the interior: bright and smooth near the surface, and dull and rough in the interior. This feature was directly related to the speed of crack propagation. When the cracks propagated slowly, the cracks were repeatedly closed and opened many times and this cyclic action ‘polished’ the fracture surfaces and made them smooth and bright. On the contrary, when the cracks propagated fast, because the weakened ‘polishing’ effect, the fracture surface exhibited dull and rough. In addition, the specimens were subjected to

bending action and so the deformation was bigger near the surface than in the interior. This unevenly distributed deformation had the effect of 'polishing' the surface area more than the interior area. The second characteristic is the striations. Striations were distinct on the fracture surfaces of specimens with short fatigue lives, and they became blurry in the specimens with long lives; and they disappeared totally in the specimens with very long lives. Three reasons were related to those striations: the first was the loading change from cycle to cycle because the test was stroke-controlled, and the second was the large stroke that induced large deformation during each cycle, and the last was the very slow loading rate that allowed sufficient oxidation during each cycle. The third characteristic is that the fracture surfaces exhibited widely diversified cross section shape, as shown schematically in Figure 3.22. The cross section was flat only when the coalesced and dominated cracks were coincident with the crest plane and this seldom occurred. The cracks generally initiated from different origins, so as they propagated, they tried to be coincident with the crest plane because the bending moment was the biggest on the crest. When those cracks propagated to the crest, then they propagated in the plane of crest. This explained the shapes shown in Figures 3.22a to 3.22e. The shape shown in Figure 3.22f occurred when three conditions were satisfied: the crack propagation area on the outside surface was not too small compared with that on the inside surface, and the existence of a small offset between the plane that the crack on the outside surface dwelled and that the crack on the inside surface abided, and those two planes located on different sides of the crest. When those conditions occurred simultaneously, the bending action would tear apart the outside portion and the inside portion from the interior of cross section.

3.3.1.4 FRACTURE

Because the stroke-controlled method was used in this test program, the fracture occurred progressively instead of suddenly. Based on this, the unstable fracture area did not show up obviously in those specimens.

As a summary, how the cracks initiated, propagated and fractured is schematically illustrated in Figure 3.23.

3.3.2 MICROSCOPIC EXAMINATION

More details of the failure can be revealed by the microscopic examination, which allows the conclusions drawn from macroscopic examination to be verified. The SEM analysis results of two specimens, T6R15A45S80 and T6R20A60S20, are used here to provide the microscopic investigation.

3.3.2.1 SPECIMEN T6R15A45S80

Figures 3.24 and 3.25 show a series of low- to high-magnification micrographs of the top and bottom half portions of the fracture surface of specimen T6R15A45S80.

Figure 3.24 contains five pictures. In picture 3.24a, it can be seen that three zones on this surface and the middle wedge-like one is exactly the final fracture zone. In the outside zone, the fracture surface was damaged, but poorly-defined dimples can be identified in picture 3.24c. In the middle zone, which is picture 3.24e, reveals nearly equiaxed dimples on this surface, so it can be concluded that the final fracture region was in a totally ductile failure mode.

Figure 3.25 consists of six pictures: the left half is the inside portion and the right half is the middle portion. It can be seen that the inside portion was more heavily damaged than the outside portion and moreover, the dark points in pictures 3.25b and 3.25c clearly show that the fracture surface became rusty. In the middle portion besides the crack tip, which exactly falls in the final fracture zone, elongated dimples can be clearly found from picture 3.25f and this indicates the failure mode is ductile.

From the above analysis, no striation was found and only dimples were identified, so it can be concluded that the failure of the investigated specimen failed was dominated by the ductile mode rather than the fatigue (brittle) failure.

3.3.2.2 SPECIMEN T6R20A60S20

Figures 3.26 and 3.27 give a series of low- to high-magnification micrographs of the top and bottom half portions of the fracture surface of specimen T6R20A60S20.

Figure 3.26 includes five pictures and they give the fracture surface of outside portion. Picture 3.26a clearly reveals that this portion of fracture surface consists of three zones: two crack propagation zone and one final fracture zone. In the crack propagation zones, clamshell marks can be clearly identified, and higher magnification SEM resolves poorly-defined fatigue striations because the fracture surface was heavily damaged and became rusty; in the final fracture zone, equiaxed dimples concludes that this zone was in a totally ductile failure mode.

Figure 3.27 consists of seven pictures: the left half is about the middle portion and the right half is about the inside portion. In the middle portion, although the surface was damaged, some dimples can be identified (see picture 3.27c). In the inside portion, as magnification is increased, progressively finer striations are resolved and moreover, picture 3.27g shows some “tire tracks”, which were caused by surface rubbing together as fatigue crack opened and closed.

3.4 SUMMARY AND CONCLUSIONS

In the strip test program, a total of 39 strip specimens were tested by a totally reversed stroke-controlled method to investigate the influences of thickness, bend angle, bend radius, and stroke range on the LCF behaviour.

By studying the spectra and hysteresis loops of MTS load and MTS stroke, bending moment and rotation, stress and clip strain, the LCF behaviour was thoroughly investigated and some observations, such as the phenomenon of ‘stroke softening’ and ‘rotation softening’, were made. Moreover, the residual strain after monotonic bending was evaluated both by measurement and by theoretic analysis. It was found that the result of theoretic analysis has a good agreement with that of measurement.

By examining the fracture surface in macroscopic scale, it was found that crack initiated from multi-locations, such as punch marks, tack weld points and scratch lines, on both inside and outside surfaces. The cracks propagated to rupture from surfaces to interior and from middle to edge. Furthermore, it was found that the crack propagation area from inside surface is much larger than that from outside surface, and this indicates that opening contributes more than closing to the failure of a strip specimen.

By investigating the fracture surface in microscopic scale, it was found that the failure was dominated by the ductile fracture in specimen T6R15A45S80 and by the fatigue, the crack propagation, in specimen T6R20A60S20.

Table 3.1: Mechanical properties of materials

Thickness, t (mm)	6.0	8.3	11.9
Young's modulus, E (GPa)	206.3	207.4	193.5
Proportional limit, σ_p (MPa)	287.5	222.0	226.0
Static yield stress, σ_y (MPa)	497.0	469.0	489.0
Dynamic yield stress, σ_{yd} (MPa)	519.0	490.0	507.0
Static ultimate stress, σ_u (MPa)	552.0	556.0	543.0
Dynamic ultimate stress, σ_{ud} (MPa)	584.0	590.0	572.0
Reduction in area (%)	55.8	54.6	63.0
Elongation (%)	29.9	30.5	33.5
Ultimate strain (%)	12.1	10.8	9.3

Note:

1. The ultimate strain is the strain at the point of the onset of necking.
2. Static values were obtained at zero strain rate, and dynamic values were obtained at the tested strain rate (Galambos 1998).

Table 3.2: Complete matrix and designations of strip specimens

Designation	t mm	R mm	θ_{al} degree	ΔS mm	S_a mm
T6R15A45S30	6	15	45	30	15
T6R15A45S50	6	15	45	50	25
T6R15A45S80	6	15	45	80	40
T6R15A60S30	6	15	60	30	15
T6R15A60S50	6	15	60	50	25
T6R15A60S80	6	15	60	80	40
T6R20A45S30	6	20	45	30	15
T6R20A45S50	6	20	45	50	25
T6R20A45S80	6	20	45	80	40
T6R20A60S20	6	20	60	20	10
T6R20A60S30	6	20	60	30	15
T6R20A60S50	6	20	60	50	25
T8R15A45S30	8.3	15	45	30	15
T8R15A45S50	8.3	15	45	50	25
T8R15A45S80	8.3	15	45	80	40
T8R15A60S20	8.3	15	60	20	10
T8R15A60S30	8.3	15	60	30	15
T8R15A60S50	8.3	15	60	50	25
T8R20A45S30	8.3	20	45	30	15
T8R20A45S50	8.3	20	45	50	25
T8R20A45S80	8.3	20	45	80	40
T8R20A60S30	8.3	20	60	30	15
T8R20A60S50	8.3	20	60	50	25
T8R20A60S80	8.3	20	60	80	40
T12R15A45S20	11.9	15	45	20	10
T12R15A45S30	11.9	15	45	30	15
T12R15A45S50	11.9	15	45	50	25
T12R15A45S70	11.9	15	45	70	35
T12R15A60S12	11.9	15	60	12	6
T12R15A60S20	11.9	15	60	20	10
T12R15A60S30	11.9	15	60	30	15
T12R15A60S50	11.9	15	60	50	25
T12R20A45S20	11.9	20	45	20	10
T12R20A45S30	11.9	20	45	30	15
T12R20A45S50	11.9	20	45	50	25
T12R20A45S70	11.9	20	45	70	35
T12R20A60S12	11.9	20	60	12	6
T12R20A60S20	11.9	20	60	20	10
T12R20A60S30	11.9	20	60	30	15
T12R20A60S50	11.9	20	60	50	25

Table 3.3: Details of loading rate

Program 1: Stroke range = 12 mm, mean loading rate =8.57 mm/min

$$0 \underset{0.1}{\overset{0.1}{\rightleftharpoons}} 4 \underset{0.067}{\overset{0.067}{\rightleftharpoons}} 5 \underset{0.133}{\overset{0.133}{\rightleftharpoons}} 6 \underset{0.1}{\overset{0.1}{\rightleftharpoons}} 6 \underset{0.133}{\overset{0.133}{\rightleftharpoons}} 5 \underset{0.067}{\overset{0.067}{\rightleftharpoons}} 4 \underset{0.1}{\overset{0.1}{\rightleftharpoons}} 0$$

Program 2: Stroke range = 20 mm, mean loading rate =11.45 mm/min

$$0 \underset{0.104}{\overset{0.104}{\rightleftharpoons}} 7 \underset{0.133}{\overset{0.133}{\rightleftharpoons}} 9 \underset{0.133}{\overset{0.133}{\rightleftharpoons}} 10 \underset{0.133}{\overset{0.133}{\rightleftharpoons}} 10 \underset{0.133}{\overset{0.133}{\rightleftharpoons}} 9 \underset{0.133}{\overset{0.133}{\rightleftharpoons}} 7 \underset{0.104}{\overset{0.104}{\rightleftharpoons}} 0$$

Program 3.1: Stroke range = 30 mm, mean loading rate = 11.19 mm/min

$$0 \underset{0.286}{\overset{0.286}{\rightleftharpoons}} 10 \underset{0.333}{\overset{0.333}{\rightleftharpoons}} 13 \underset{0.571}{\overset{0.571}{\rightleftharpoons}} 15 \underset{0.3}{\overset{0.3}{\rightleftharpoons}} 15 \underset{0.571}{\overset{0.571}{\rightleftharpoons}} 13 \underset{0.333}{\overset{0.333}{\rightleftharpoons}} 10 \underset{0.286}{\overset{0.286}{\rightleftharpoons}} 0$$

Program 3.2: Stroke range = 30 mm, mean loading rate = 8.11 mm/min.
This program just employed by specimen T6R20A45S30.

$$0 \underset{0.5}{\overset{0.5}{\rightleftharpoons}} 10 \underset{0.45}{\overset{0.45}{\rightleftharpoons}} 13 \underset{0.749}{\overset{0.749}{\rightleftharpoons}} 15 \underset{0.3}{\overset{0.3}{\rightleftharpoons}} 15 \underset{0.749}{\overset{0.749}{\rightleftharpoons}} 13 \underset{0.45}{\overset{0.45}{\rightleftharpoons}} 10 \underset{0.5}{\overset{0.5}{\rightleftharpoons}} 0$$

Program 4: Stroke range = 50 mm, mean loading rate = 10.64 mm/min

$$0 \underset{1}{\overset{1}{\rightleftharpoons}} 20 \underset{0.45}{\overset{0.45}{\rightleftharpoons}} 23 \underset{0.749}{\overset{0.749}{\rightleftharpoons}} 25 \underset{0.3}{\overset{0.3}{\rightleftharpoons}} 25 \underset{0.749}{\overset{0.749}{\rightleftharpoons}} 23 \underset{0.45}{\overset{0.45}{\rightleftharpoons}} 20 \underset{1}{\overset{1}{\rightleftharpoons}} 0$$

Program 5: Stroke range = 70 mm, mean loading rate = 8.33 mm/min

$$0 \underset{1.2}{\overset{1.2}{\rightleftharpoons}} 30 \underset{0.4}{\overset{0.4}{\rightleftharpoons}} 33 \underset{0.4}{\overset{0.4}{\rightleftharpoons}} 35 \underset{0.2}{\overset{0.2}{\rightleftharpoons}} 35 \underset{0.4}{\overset{0.4}{\rightleftharpoons}} 33 \underset{0.4}{\overset{0.4}{\rightleftharpoons}} 30 \underset{1.2}{\overset{1.2}{\rightleftharpoons}} 0$$

Program 6: Stroke range = 80 mm, mean loading rate = 8.07 mm/min

$$0 \underset{1.5}{\overset{1.5}{\rightleftharpoons}} 35 \underset{0.45}{\overset{0.45}{\rightleftharpoons}} 38 \underset{0.749}{\overset{0.749}{\rightleftharpoons}} 40 \underset{0.3}{\overset{0.3}{\rightleftharpoons}} 40 \underset{0.749}{\overset{0.749}{\rightleftharpoons}} 38 \underset{0.45}{\overset{0.45}{\rightleftharpoons}} 35 \underset{1.5}{\overset{1.5}{\rightleftharpoons}} 0$$

Note:

The numbers which the arrows point to are the strokes (in mm), and the numbers above and below the arrows are the consumed time (in min).

Table 3.4: Characteristic parameters of stroke spectra

Stroke range, ΔS (mm)	12	20	30	50	70	80
Maximum stroke, S_{max} (mm)	6	10	15	25	35	40
Minimum stroke, S_{min} (mm)	-6	-10	-15	-25	-35	-40
Stroke amplitude, S_a (mm)	6	10	15	25	35	40
Mean stroke, S_m (mm)	0	0	0	0	0	0

Table 3.5: Characteristic parameters of rotation spectra

Designation	$\delta\theta_{slmax}$	$\delta\theta_{slmin}$	$\Delta\theta_{sl}$	$\delta\theta_{sla}$	$\delta\theta_{slm}$
T6R15A45S50	0.3975	-0.2647	0.6622	0.3311	0.0664
	0.3609	-0.2124	0.5733	0.2866	0.0742
T6R15A45S80	0.6556	-0.1468	0.8024	0.4012	0.2544
T6R15A60S30	0.2978	-0.2299	0.5277	0.2638	0.0339
T6R15A60S50	0.5406	-0.3550	0.8956	0.4478	0.0928
	0.4841	-0.2916	0.7757	0.3878	0.0962
T6R20A45S30	0.2152	-0.1852	0.4004	0.2002	0.0150
T6R20A45S50	0.3933	-0.2980	0.6913	0.3456	0.0476
	0.3537	-0.2442	0.5978	0.2989	0.0548
T6R20A45S80	0.7929	-0.4545	1.2475	0.6237	0.1692
T6R20A60S30	0.3367	-0.2487	0.5854	0.2927	0.0440
T6R20A60S50	0.5152	-0.3914	0.9066	0.4533	0.0619
	0.4747	-0.3262	0.8010	0.4005	0.0743
T8R15A45S30	0.1944	-0.1704	0.3648	0.1824	0.0120
T8R15A45S50	0.3907	-0.2909	0.6816	0.3408	0.0499
T8R15A45S80	0.6872	-0.4280	1.1152	0.5576	0.1296
T8R15A60S30	0.2804	-0.2131	0.4935	0.2468	0.0336
T8R15A60S50	0.5121	-0.3559	0.8680	0.4340	0.0781
	0.4895	-0.2897	0.7792	0.3896	0.0999
T8R20A45S30	0.2001	-0.1695	0.3696	0.1848	0.0153
T8R20A45S50	0.3936	-0.2953	0.6890	0.3445	0.0491
	0.3536	-0.2390	0.5926	0.2963	0.0573
T8R20A45S80	0.7394	-0.4170	1.1564	0.5782	0.1612
T8R20A60S30	0.2628	-0.2025	0.4652	0.2326	0.0301
T8R20A60S50	0.5070	-0.3374	0.8445	0.4222	0.0848
	0.4538	-0.2736	0.7274	0.3637	0.0901
T12R15A45S20	0.1382	-0.1303	0.2686	0.1343	0.0039
T12R15A45S30	0.2149	-0.1929	0.4078	0.2039	0.0110
T12R15A45S50	0.3804	-0.2941	0.6745	0.3373	0.0431
T12R15A60S12	0.0987	-0.1021	0.2007	0.1004	-0.0017
T12R15A60S20	0.1879	-0.1467	0.3346	0.1673	0.0206
T12R15A60S30	0.2281	-0.2128	0.4410	0.2205	0.0076
T12R20A45S20	0.1287	-0.1189	0.2476	0.1238	0.0049
T12R20A45S30	0.1930	-0.1609	0.3540	0.1770	0.0161
T12R20A45S50	0.3206	-0.2545	0.5751	0.2876	0.0330
T12R20A45S70	0.5583	-0.3767	0.9350	0.4675	0.0908
T12R20A60S12	0.0816	-0.0830	0.1647	0.0823	-0.0007
T12R20A60S20	0.2211	-0.1798	0.4009	0.2004	0.0206
T12R20A60S30	0.3173	-0.2320	0.5493	0.2747	0.0426
T12R20A60S50	0.5813	-0.3776	0.9589	0.4797	0.1019

Note: For some specimens tested by 50 mm stroke range, they have two rows of rotation data.

Table 3.6: Residual strains after monotonic bending

Specimen	Outside surface			Inside surface		
	Theoretical[1] (mm/mm)	Measured[2] (mm/mm)	Difference[3] (%)	Theoretical[1] (mm/mm)	Measured[2] (mm/mm)	Difference[3] (%)
T6R15A45S30	0.167	0.174	4.4	-0.167	-0.150	-9.8
T6R15A45S50	0.167	0.167	0.1	-0.167	-0.124	-25.9
T6R15A45S80	0.167	0.174	4.4	-0.167	-0.150	-9.8
T6R15A60S30	0.167	0.186	11.5	-0.167	-0.144	-13.8
T6R15A60S50	0.167	0.182	9.4	-0.167	-0.139	-16.7
T6R15A60S60	0.167	0.167	0.1	-0.167	-0.124	-25.9
T6R20A45S30	0.130	0.152	16.6	-0.130	-0.122	-6.3
T6R20A45S50	0.130	0.146	12.1	-0.130	-0.130	-0.2
T6R20A45S80	0.130	0.140	7.4	-0.130	-0.135	3.1
T6R20A60S30	0.130	0.152	16.6	-0.130	-0.117	-10.3
T6R20A60S50	0.130	0.166	27.2	-0.130	-0.123	-5.4
T6R20A60S80	0.130	0.147	12.3	-0.130	-0.121	-6.9
T8R15A45S30	0.217	0.242	11.7	-0.217	-0.187	-13.8
T8R15A45S50	0.217	0.244	12.8	-0.217	-0.194	-10.3
T8R15A45S80	0.217	0.270	24.6	-0.217	-0.184	-15.3
T8R15A60S30	0.217	0.243	12.3	-0.217	-0.204	-6.1
T8R15A60S50	0.217	0.232	7.1	-0.217	-0.181	-16.4
T8R15A60S80	0.217	0.263	21.3	-0.217	-0.195	-9.9
T8R20A45S30	0.172	0.194	12.6	-0.172	-0.158	-7.9
T8R20A45S50	0.172	0.212	23.3	-0.172	-0.163	-4.9
T8R20A45S80	0.172	0.206	19.6	-0.172	-0.156	-9.0
T8R20A60S30	0.172	0.197	14.4	-0.172	-0.156	-9.1
T8R20A60S50	0.172	0.212	23.3	-0.172	-0.133	-22.5
T8R20A60S80	0.172	0.239	38.9	-0.172	-0.179	4.2
T12R15A45S20	0.296	0.352	18.8	-0.296	-0.280	-5.6
T12R15A45S30	0.296	0.348	17.5	-0.296	-0.277	-6.6
T12R15A45S50	0.296	0.344	16.1	-0.296	-0.272	-8.3
T12R15A45S70	0.296	0.356	20.1	-0.296	-0.266	-10.3
T12R15A60S12	0.296	0.331	11.6	-0.296	-0.265	-10.4
T12R15A60S20	0.296	0.330	11.5	-0.296	-0.258	-13.1
T12R15A60S30	0.296	0.351	18.2	-0.296	-0.278	-6.2
T12R15A60S50	0.296	0.343	15.7	-0.296	-0.269	-9.3
T12R20A45S20	0.240	0.292	21.6	-0.240	-0.240	-0.2
T12R20A45S30	0.240	0.282	17.6	-0.240	-0.219	-8.8
T12R20A45S50	0.240	0.298	24.0	-0.240	-0.210	-12.4
T12R20A45S70	0.240	0.306	27.5	-0.240	-0.241	0.4
T12R20A60S12	0.240	0.291	21.2	-0.240	-0.231	-3.9
T12R20A60S20	0.240	0.283	17.8	-0.240	-0.211	-12.2
T12R20A60S30	0.240	0.296	23.3	-0.240	-0.224	-6.9
T12R20A60S50	0.240	0.304	26.5	-0.240	-0.221	-7.9

Note:

[1] Theoretical strain was obtained from Equation 3.7.

[2] Measured strains were obtained by using the method descibed in Section 3.1.3.1.

[3] Difference = (Measured Strain - Theoretical Strain)/Theoretical Strain×100.

Table 3.7: Cycles to failure (this test)

Designation	N_{fd} (cycles)	Designation	N_{fd} (cycles)
T6R15A45S30[1]	68 1/2	T12R15A45S20	114
T6R15A45S50	22 3/4	T12R15A45S30	38 3/4
T6R15A45S80	5 1/4	T12R15A45S50	12 3/4
T6R15A60S30	33 1/4	T12R15A45S70	4
T6R15A60S50	8 3/4	T12R15A60S12	226
T6R15A60S80[2]	6 3/4	T12R15A60S20	57
T6R20A45S30	109 1/4	T12R15A60S30	44 3/4
T6R20A45S50	26 3/4	T12R15A60S50[3]	11 1/2
T6R20A45S80	3 1/4	T12R20A45S20[4]	280
T6R20A60S20	77	T12R20A45S30	78 3/4
T6R20A60S30	29	T12R20A45S50	22 1/4
T6R20A60S50	8 3/4	T12R20A45S70	7
T8R15A45S30	62 3/4	T12R20A60S20	77
T8R15A45S50	11	T12R20A60S30	15
T8R15A45S80	3 1/4	T12R20A60S50	5
T8R15A60S20	55	T12R20A60S12	616
T8R15A60S30	19 3/4		
T8R15A60S50	7 1/4		
T8R20A45S30	129 1/4		
T8R20A45S50	14 3/4		
T8R20A45S80	3 1/4		
T8R20A60S30	29 3/4		
T8R20A60S50	8 3/4		
T8R20A60S80	Can not be tested		

Note:

[1] For T6R15A45S30, it was overloaded during the 2nd cycle.

[2] For T6R15A60S80, because the welds between loading strips and strip legs were partially broken, its actual stroke range was decreased to 60 mm.

[3] For T12R15A60S50, because the loading strips were yielded during the 1st cycle, the stroke range was decreased to 40 mm.

[4] For T12R20A45S20, the cycles to failure of 280 is obtained by extrapolation based on the recorded loading spectra, because the program was out of work after 250 cycles and no data were recorded after that.

Table 3.8: Cycles to failure (previous test results)

S. Das (2002)		B. W. Myrholm (2001)	
Designation	N_{fd} (cycles)	Designation	N_{fd} (cycles)
T6R15A45S50	11	T7R15A45S50	17
T6R15A45S60	7	T7R15A45S60	8
T6R15A45S70	4	T7R15A45S70	6
T6R15A45S80	3 1/2	T7R15A45S80	4
T6R20A45S50	32	T7R20A45S60	13
T6R20A45S60	11	T7R20A45S70	9
T6R20A45S70	7 1/2	T7R20A45S80	5
T6R20A45S80	6	T7R20A45S90	3
T8R15A45S50	7		
T8R15A45S60	4 1/2		
T8R15A45S70	3		
T8R15A45S80	2 1/2		
T8R20A45S50	12		
T8R20A45S60	6		
T8R20A45S70	4		
T8R20A45S80	3		

Note:
In this table, T6, T7 and T8 represent that the thickness of strip specimen are 6 mm, 6.74 mm and 8 mm respectively.

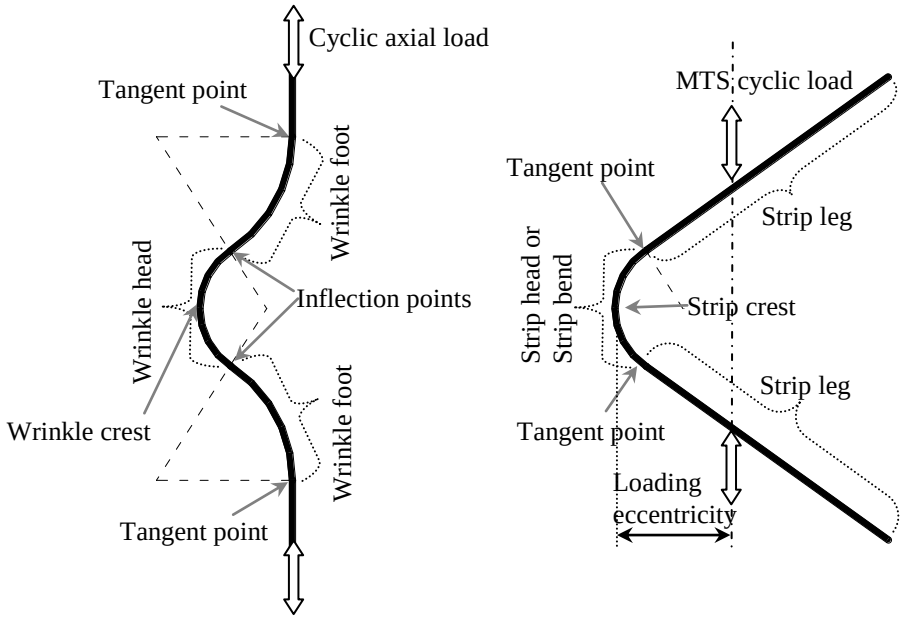

Figure 3.1: Schematic illustration of a pipe wrinkle and a strip specimen

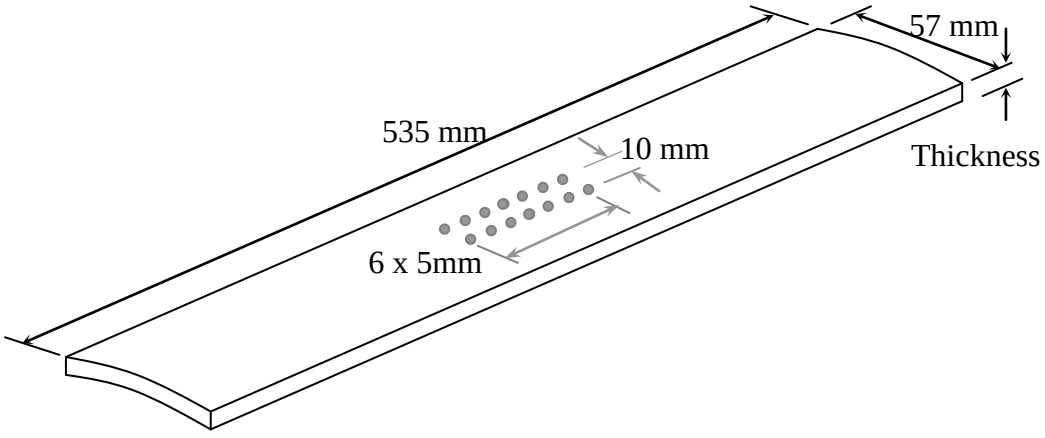

Figure 3.2: Schematic illustration of a straight strip and punch marks

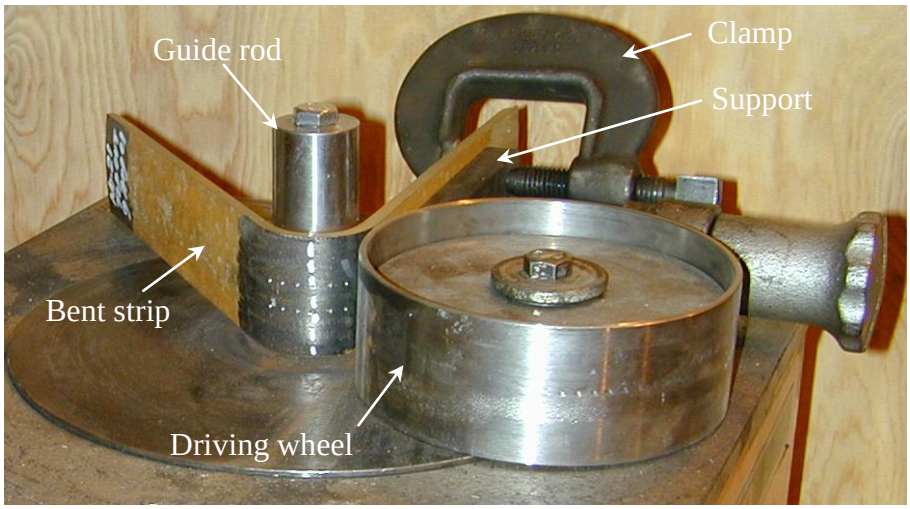

Figure 3.3: A rebar bending machine and a bent strip

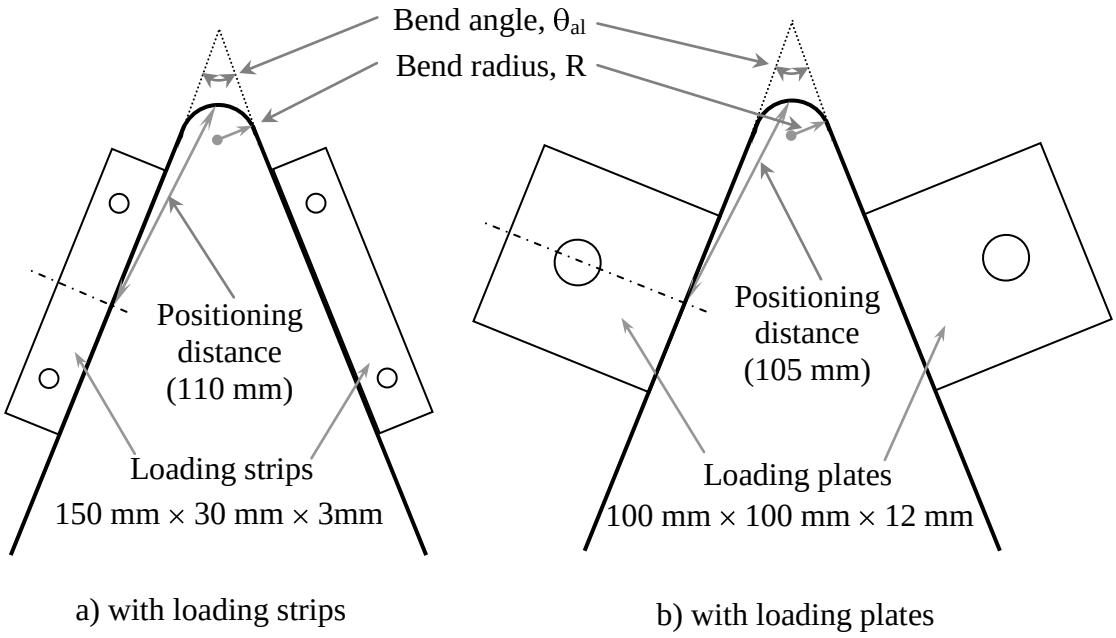

Figure 3.4: Schematic illustration of strip specimens

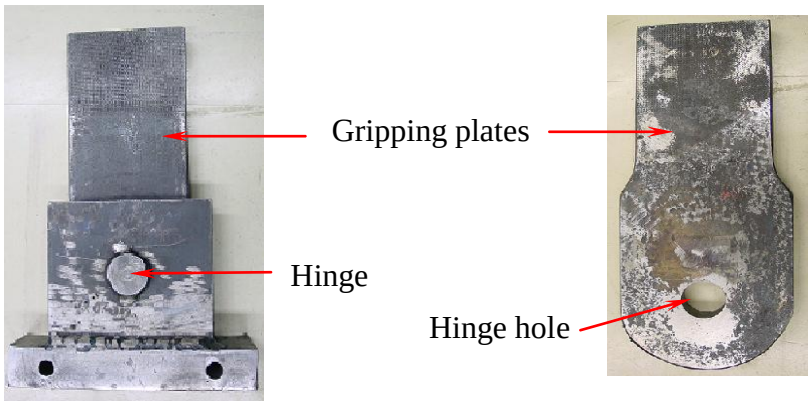

a) Used for specimens with loading strips

b) Used for specimens with loading plates

Figure 3.5: Loading mounts

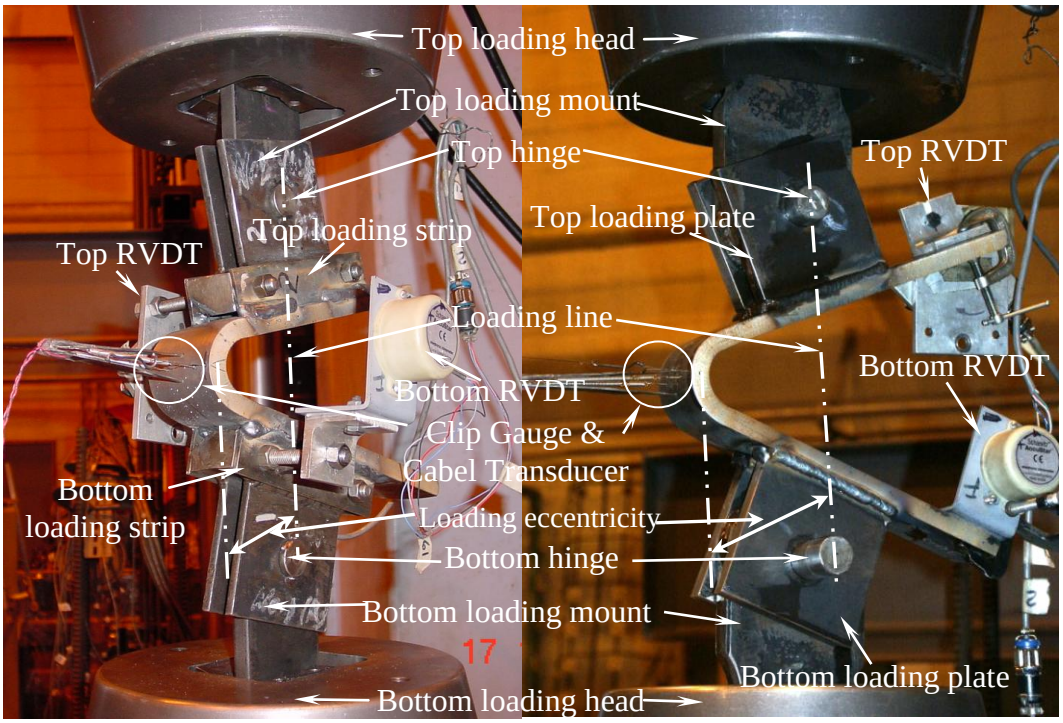

a) Type one

b) Type two

Figure 3.6: Test set-up

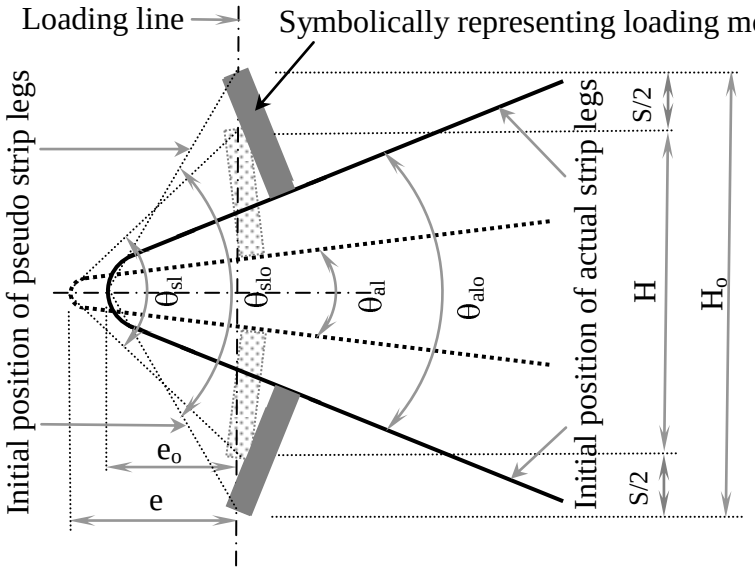

Figure 3.7: Schematic illustration of deformation and rotation parameters

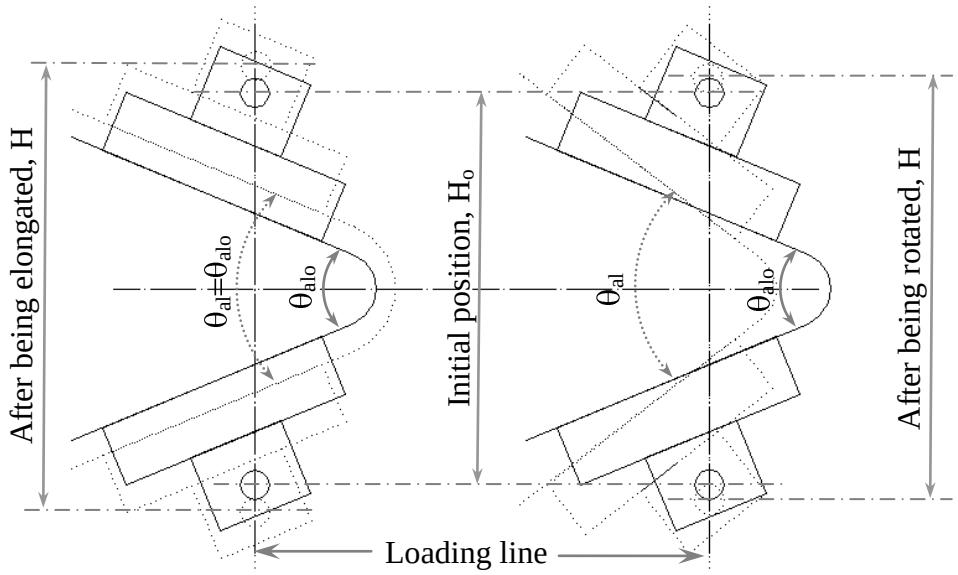

a) due to elongation b) due to rotation

Figure 3.8: Schematic illustration of strip deformation

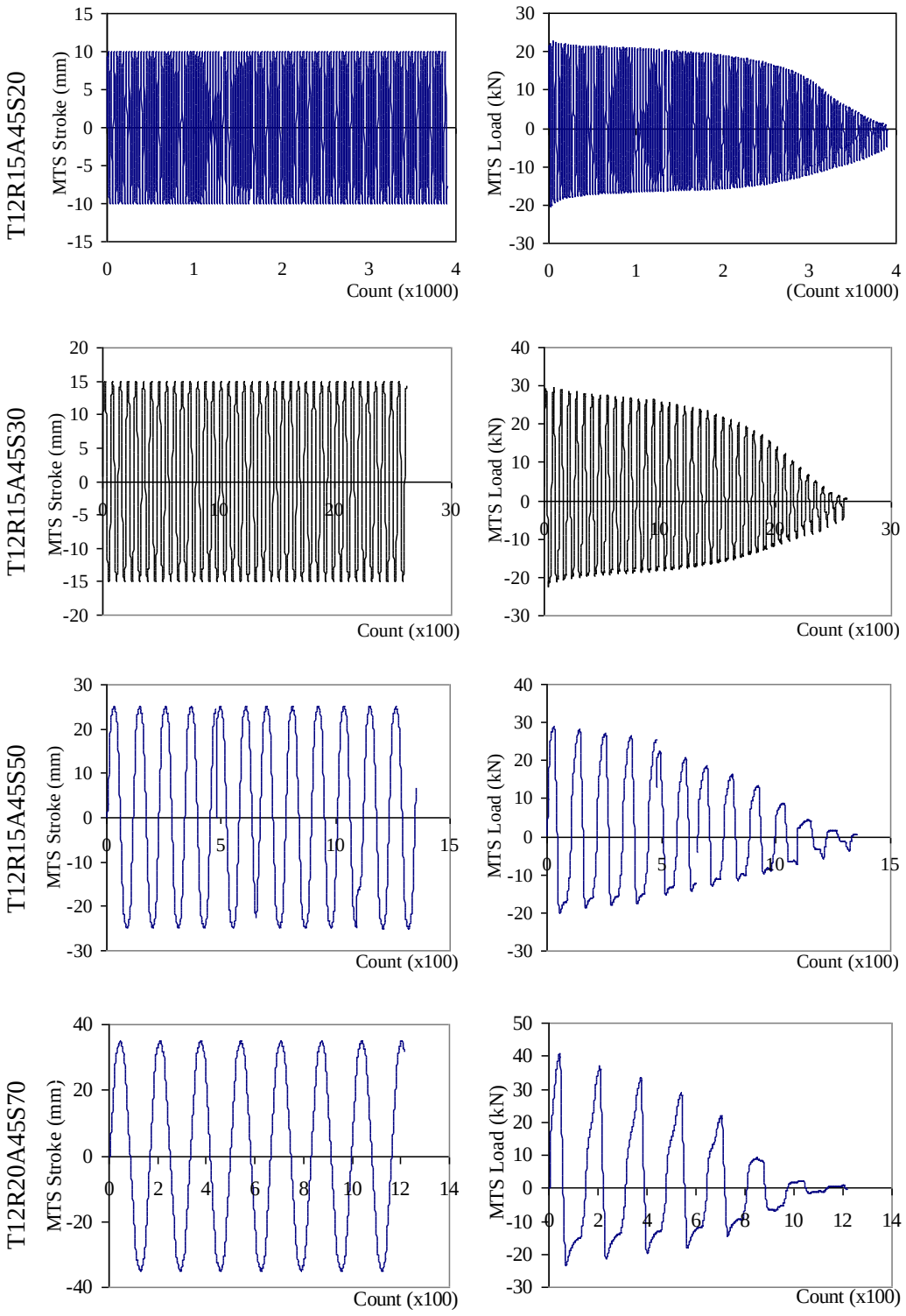

a) MTS stroke b) MTS load

Figure 3.9: Typical MTS stroke and MTS load spectra

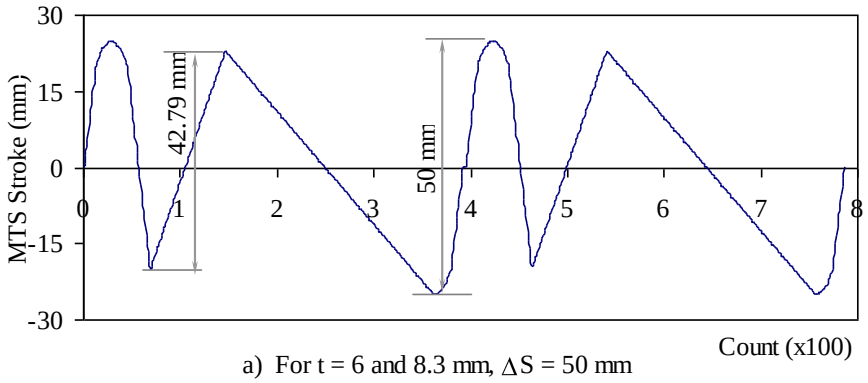

a) For t = 6 and 8.3 mm, ΔS = 50 mm

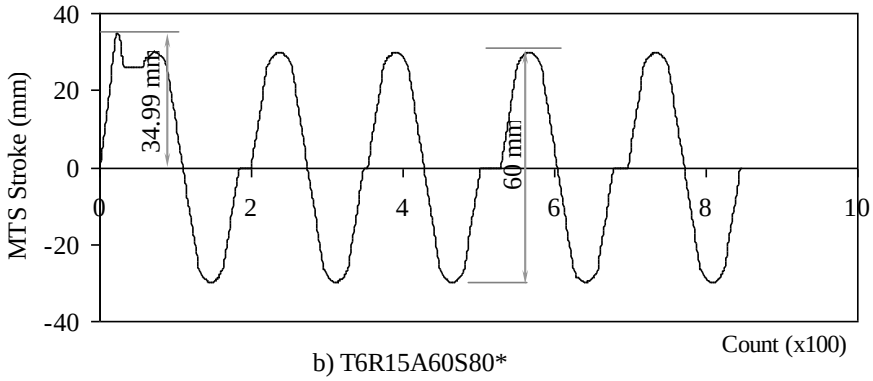

b) T6R15A60S80*

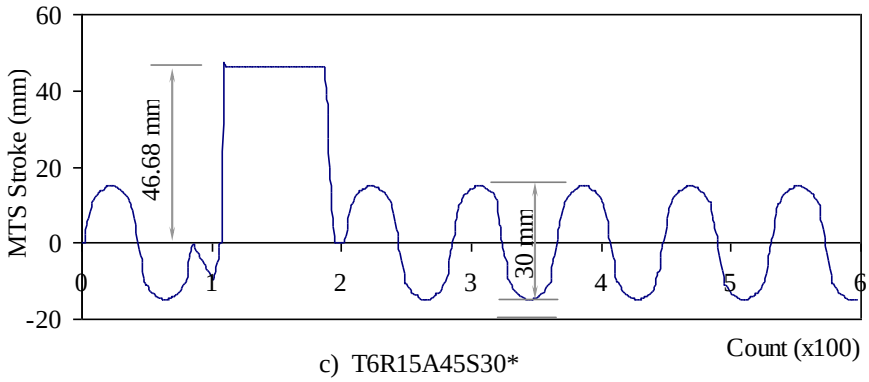

c) T6R15A45S30*

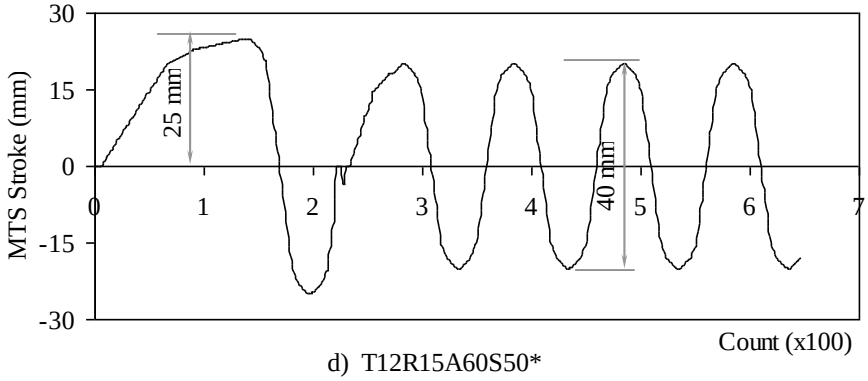

d) T12R15A60S50*

Figure 3.10: Irregular stroke spectra (partial)

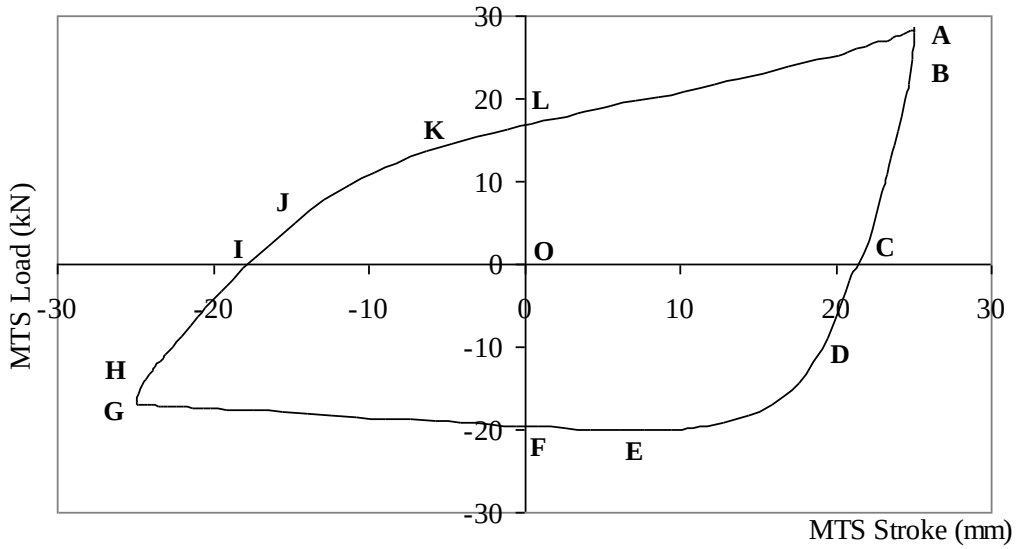

Figure 3.11: A typical load vs. stroke hysteresis loop of specimen T12R15A45S50

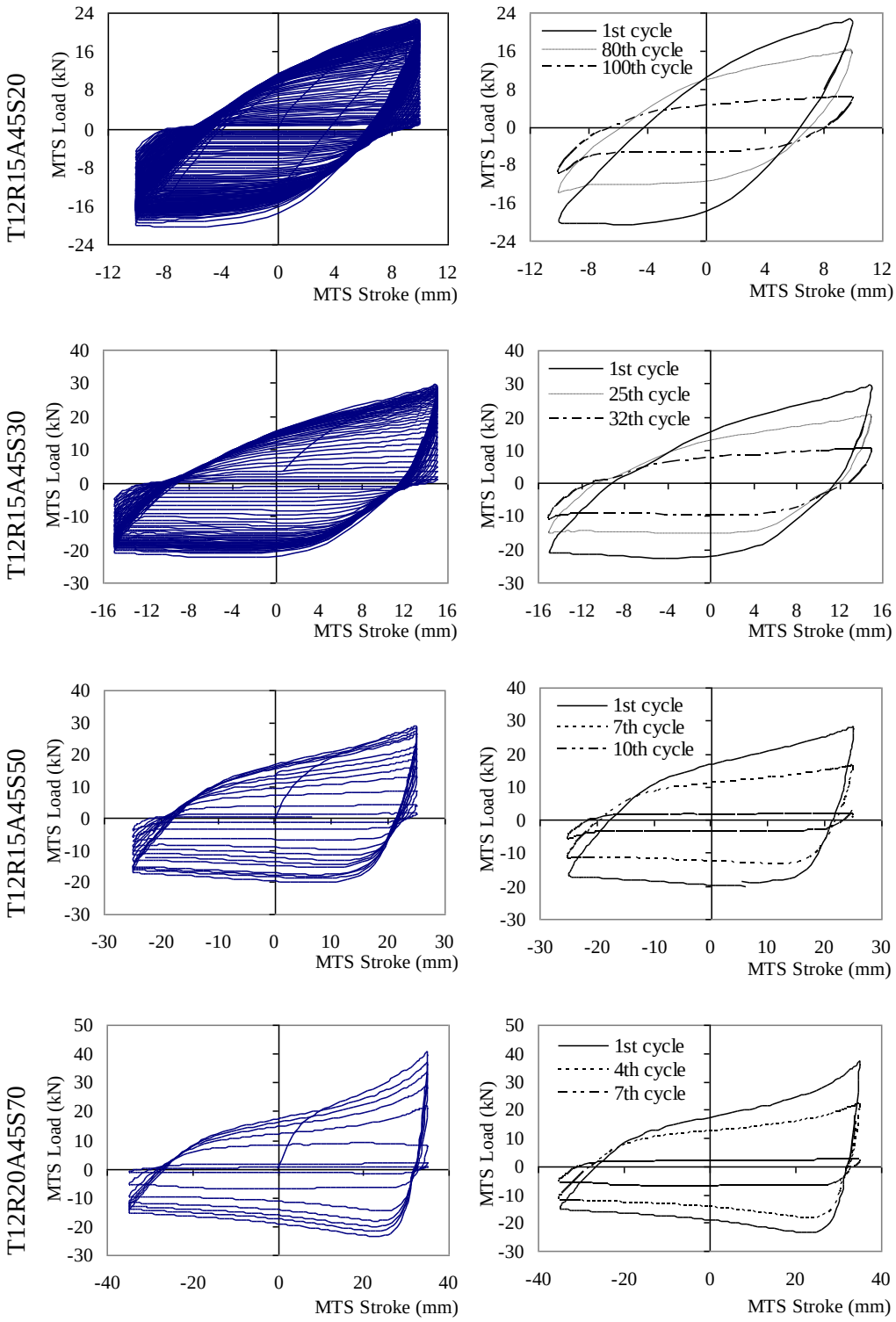

a) All Loops b) Typical Loops

Figure 3.12: Typical MTS load and stroke hysteresis loops

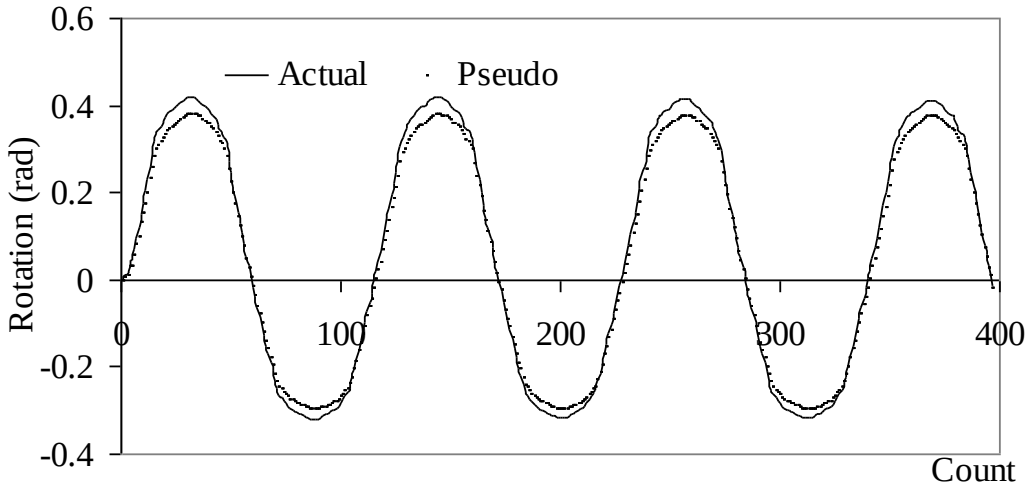

Figure 3.13: Comparison of actual leg rotation and pseudo leg rotation of specimen T12R15A45S50

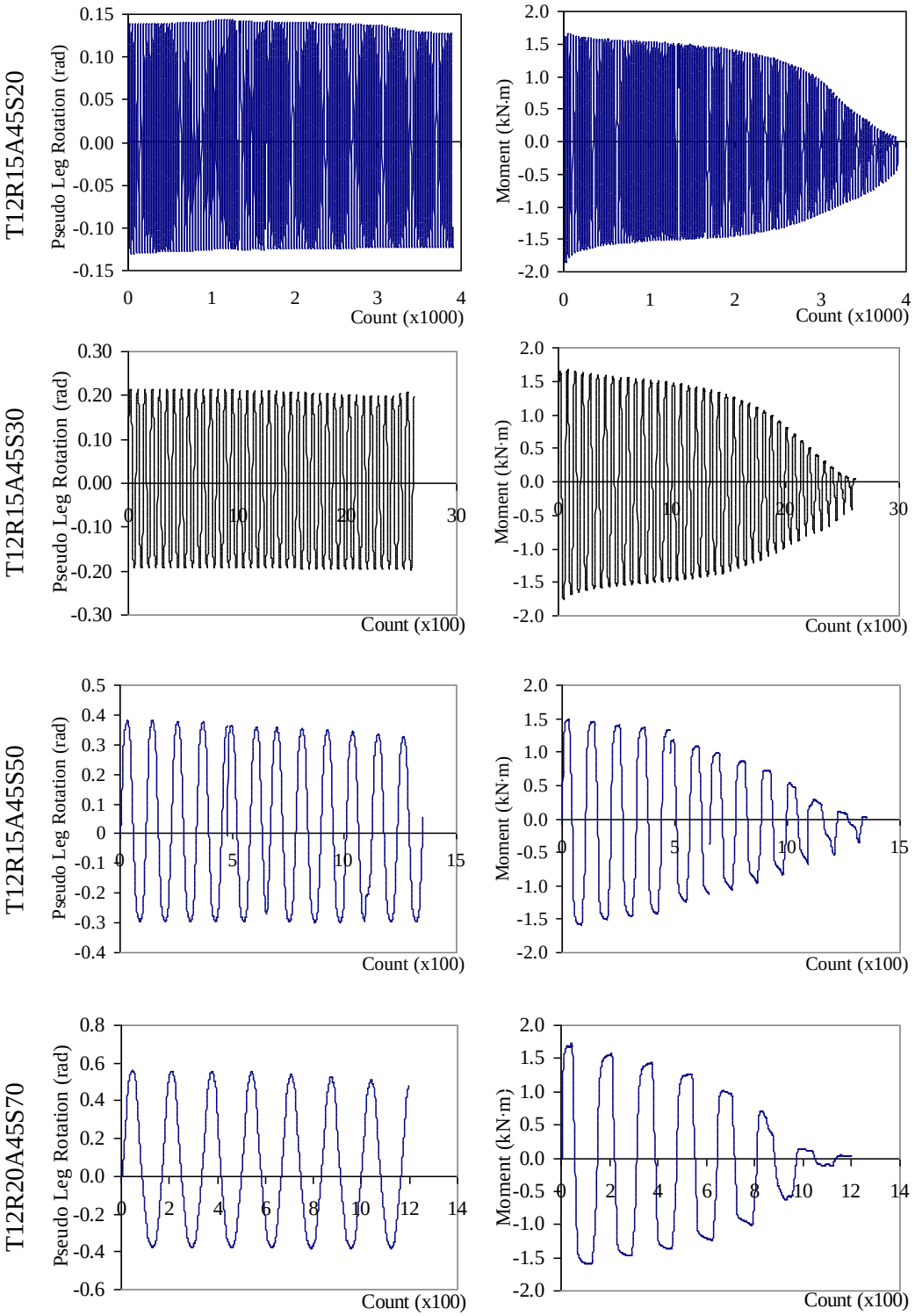

a) Pseudo leg rotation b) Bending moment

Figure 3.14: Typical bending moment and rotation spectra

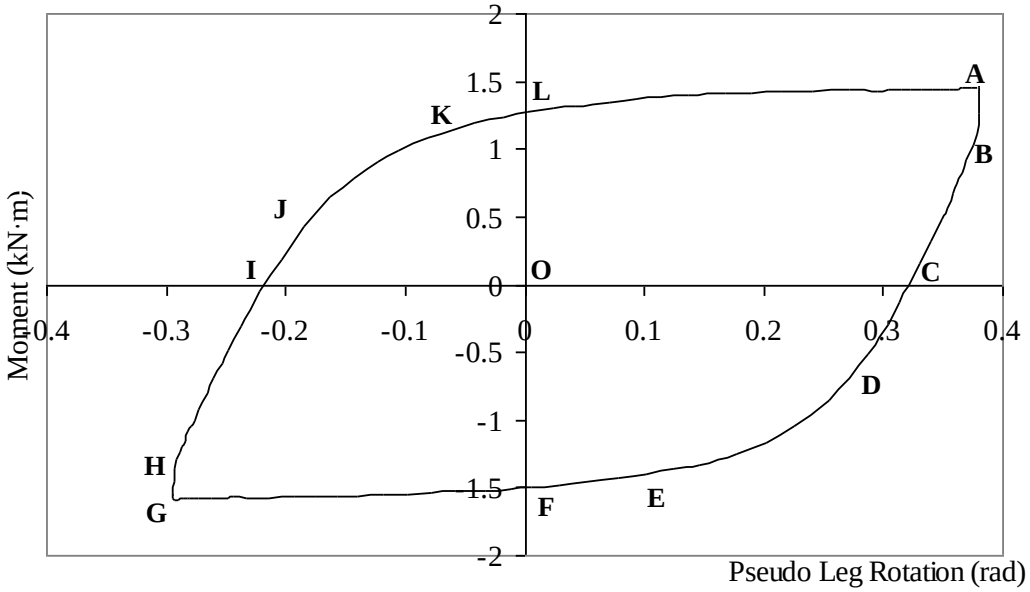

Figure 3.15: A typical bending moment vs. rotation hysteresis loop of specimen T12R15A45S50

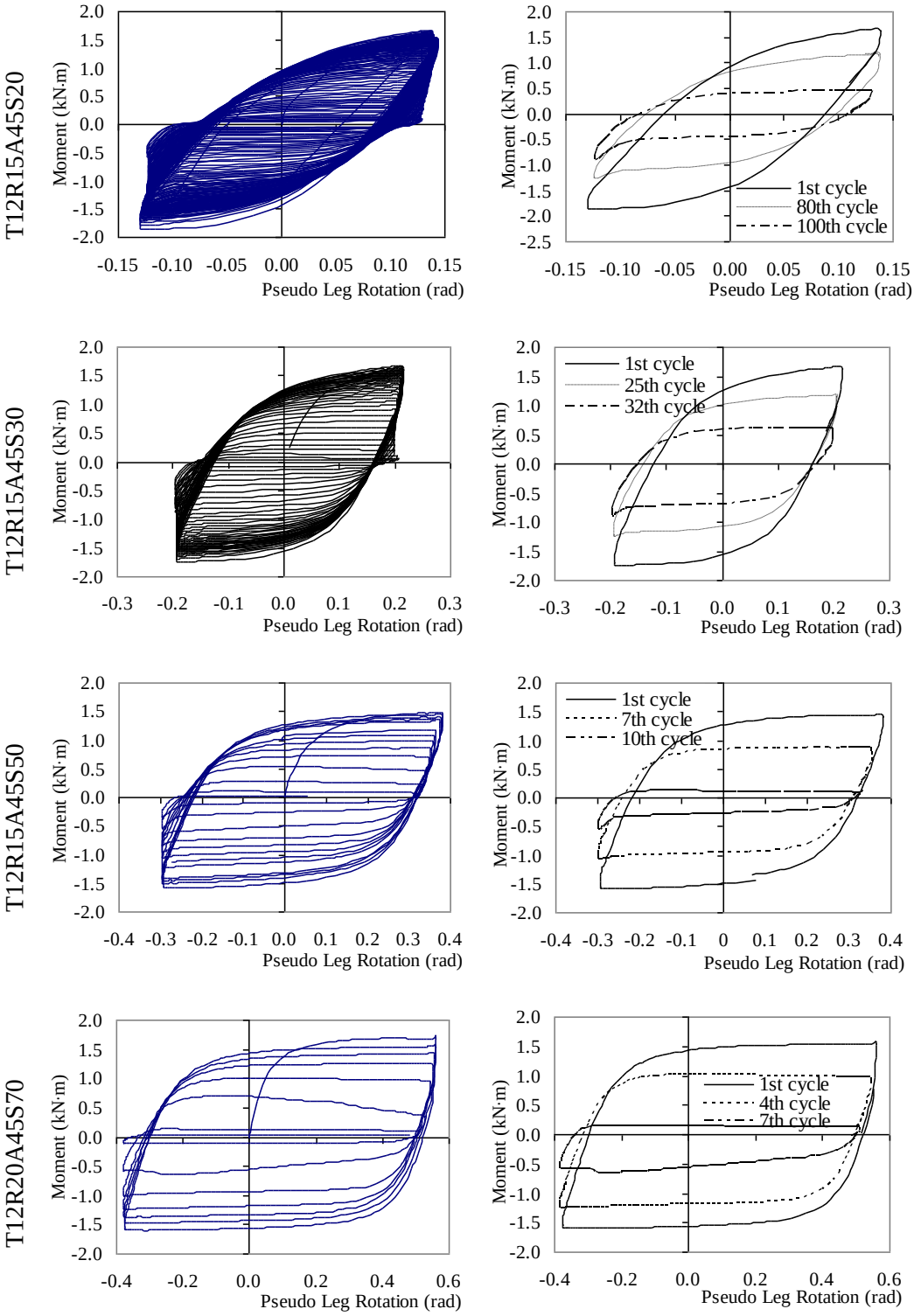

a) All Loops b) Typical Loops

Figure 3.16: Typical moment rotation hysteresis loops

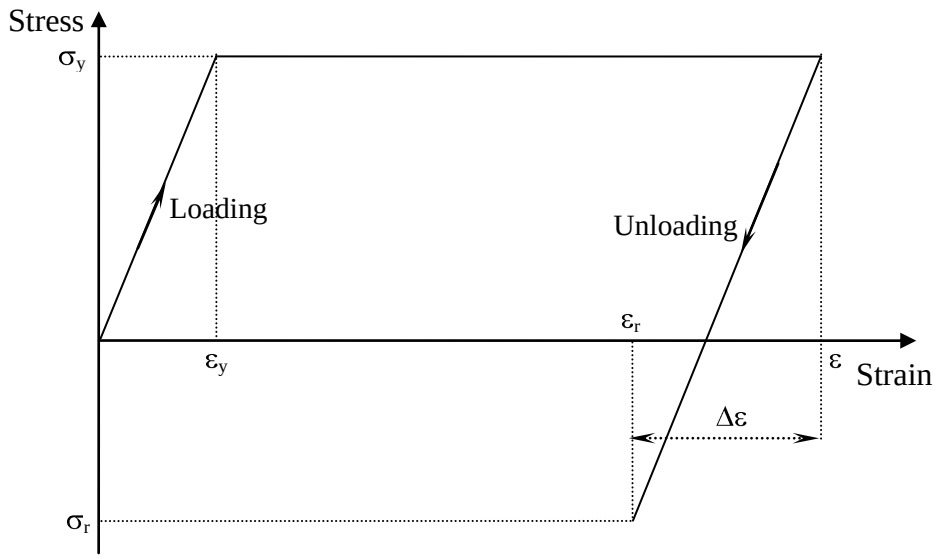

Figure 3.17: An elastic, perfectly plastic material mode

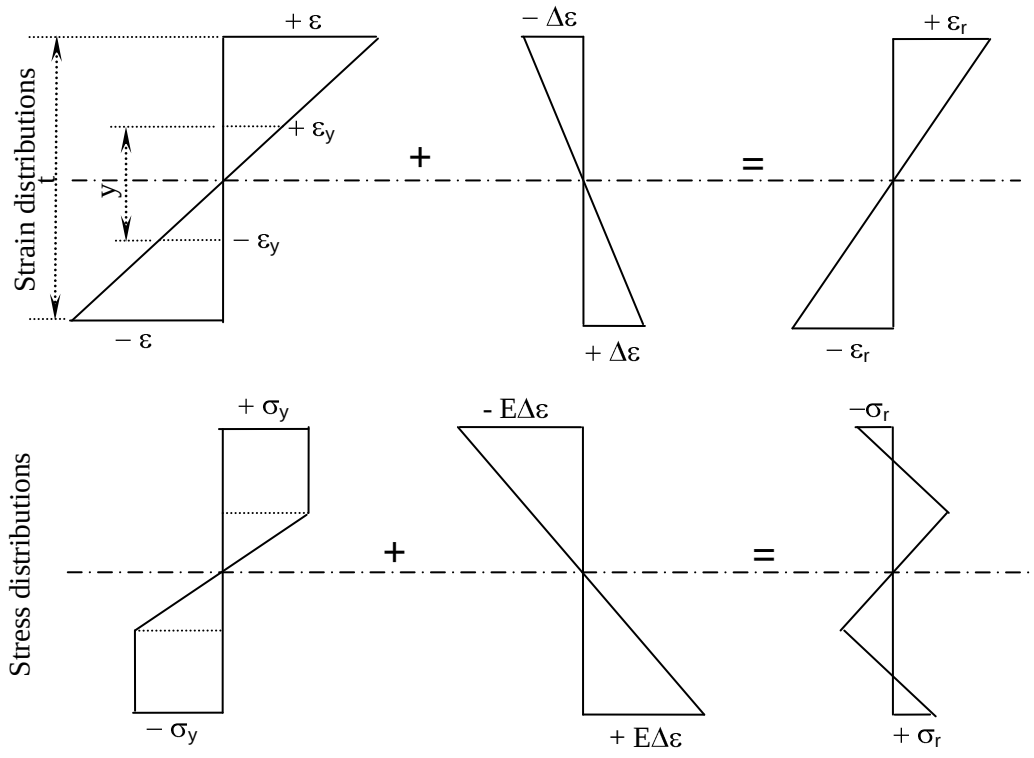

a) Loading state b) Unloading state c) Final state

Note: t is the specimen thickness and y is the height of elastic core.

Figure 3.18: Illustration of determination of residual strain and residual stress

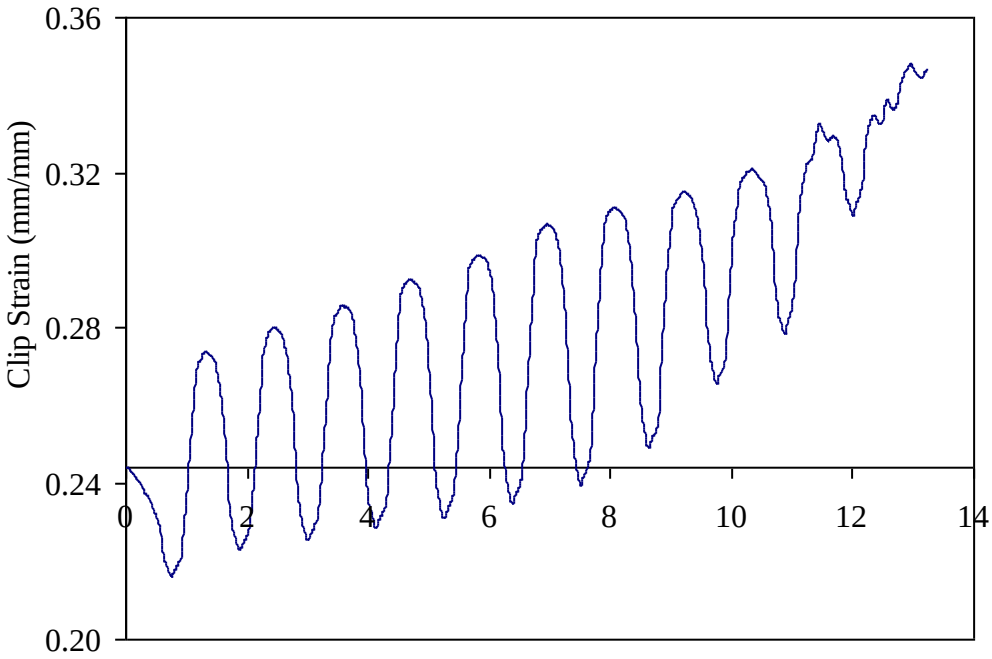

Figure 3.19: Clip strain spectrum (T8R15A45S50)

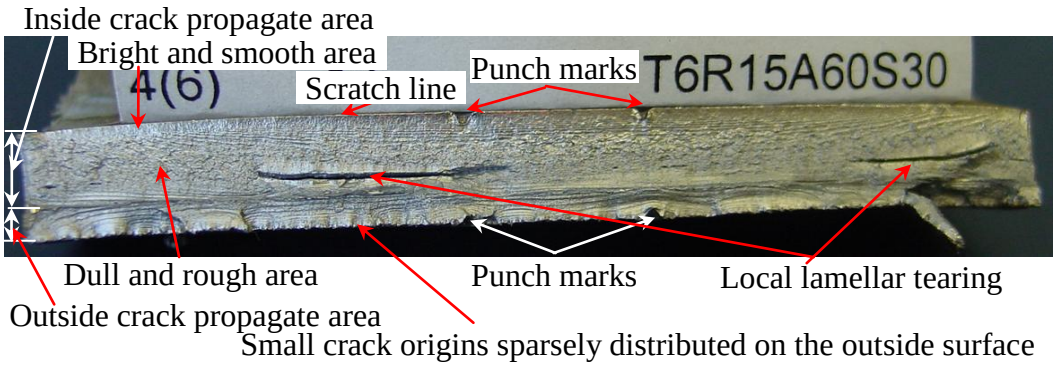

a) T6R15A60S30

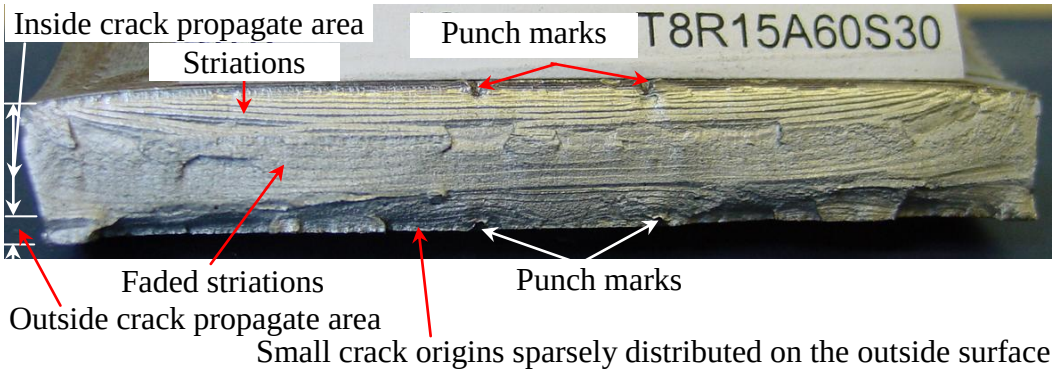

b) T8R15A60S30

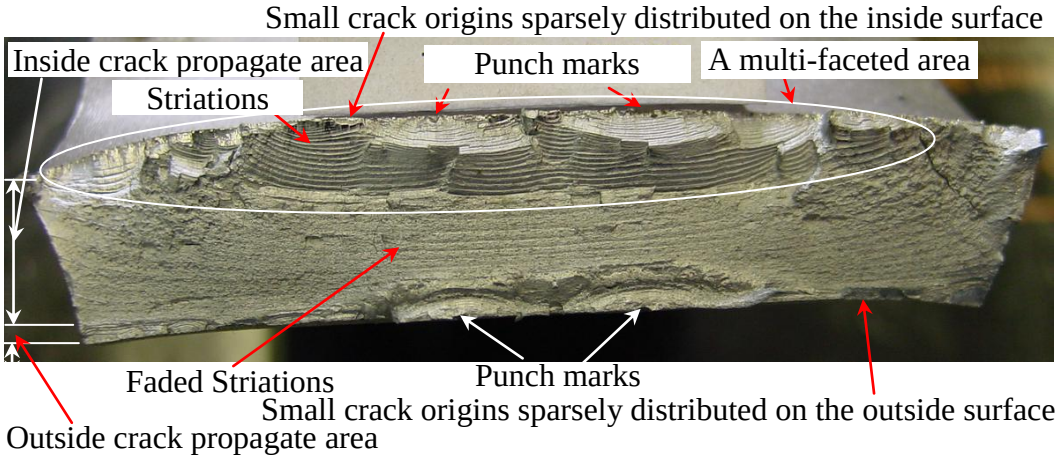

c) T12R15A60S30

Figure 3.20: Typical fracture surfaces

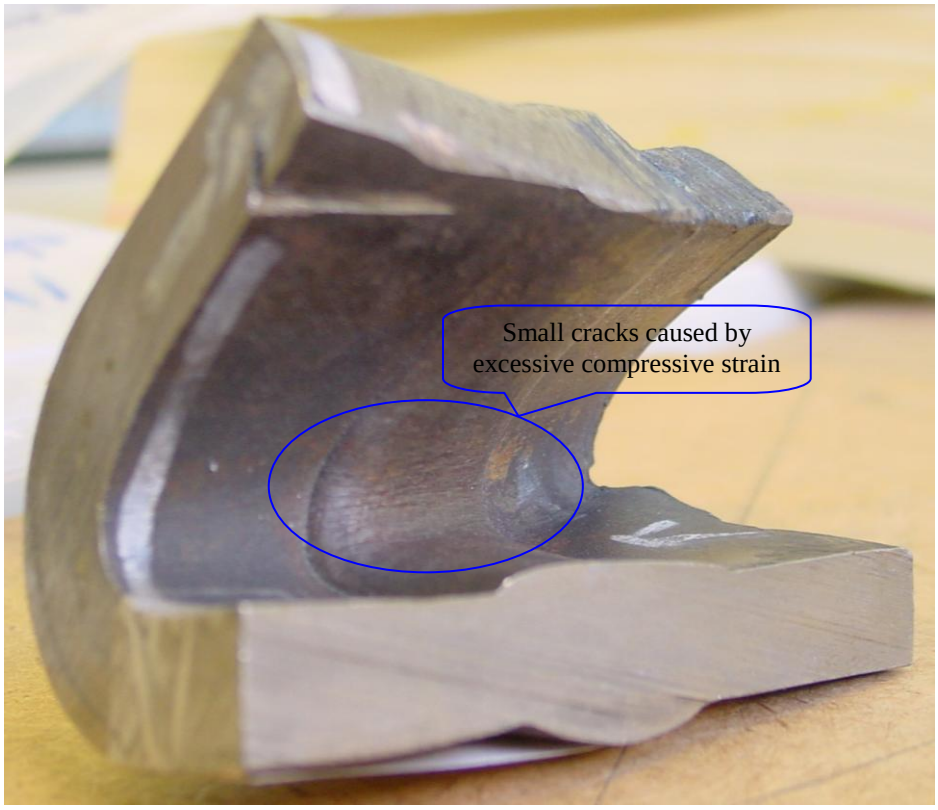

Figure 3.21: Cracks due to too large compressive strain

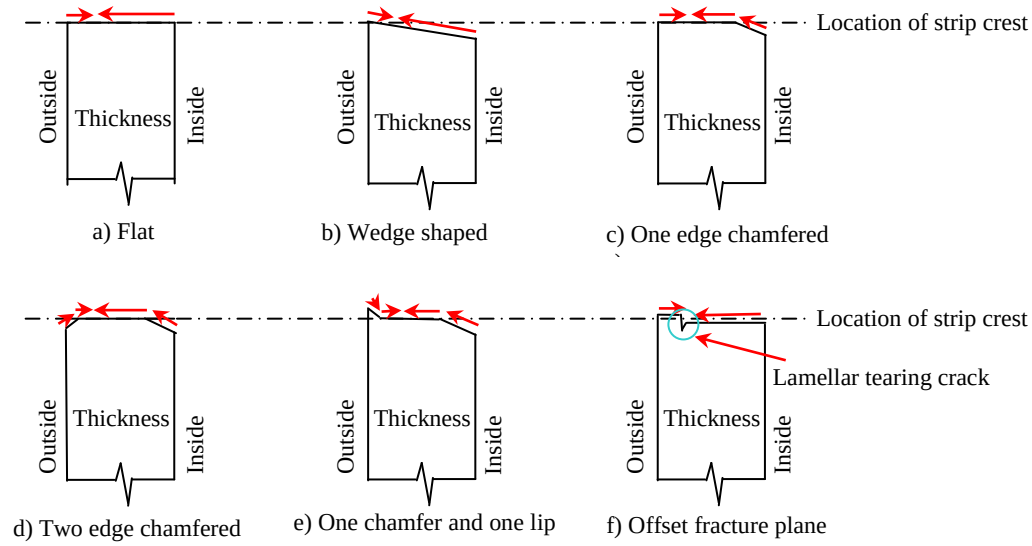

Note:

The arrows show the directions of crack propagation.

Figure 3.22: Schematic illustration of cross section shapes of fracture surface

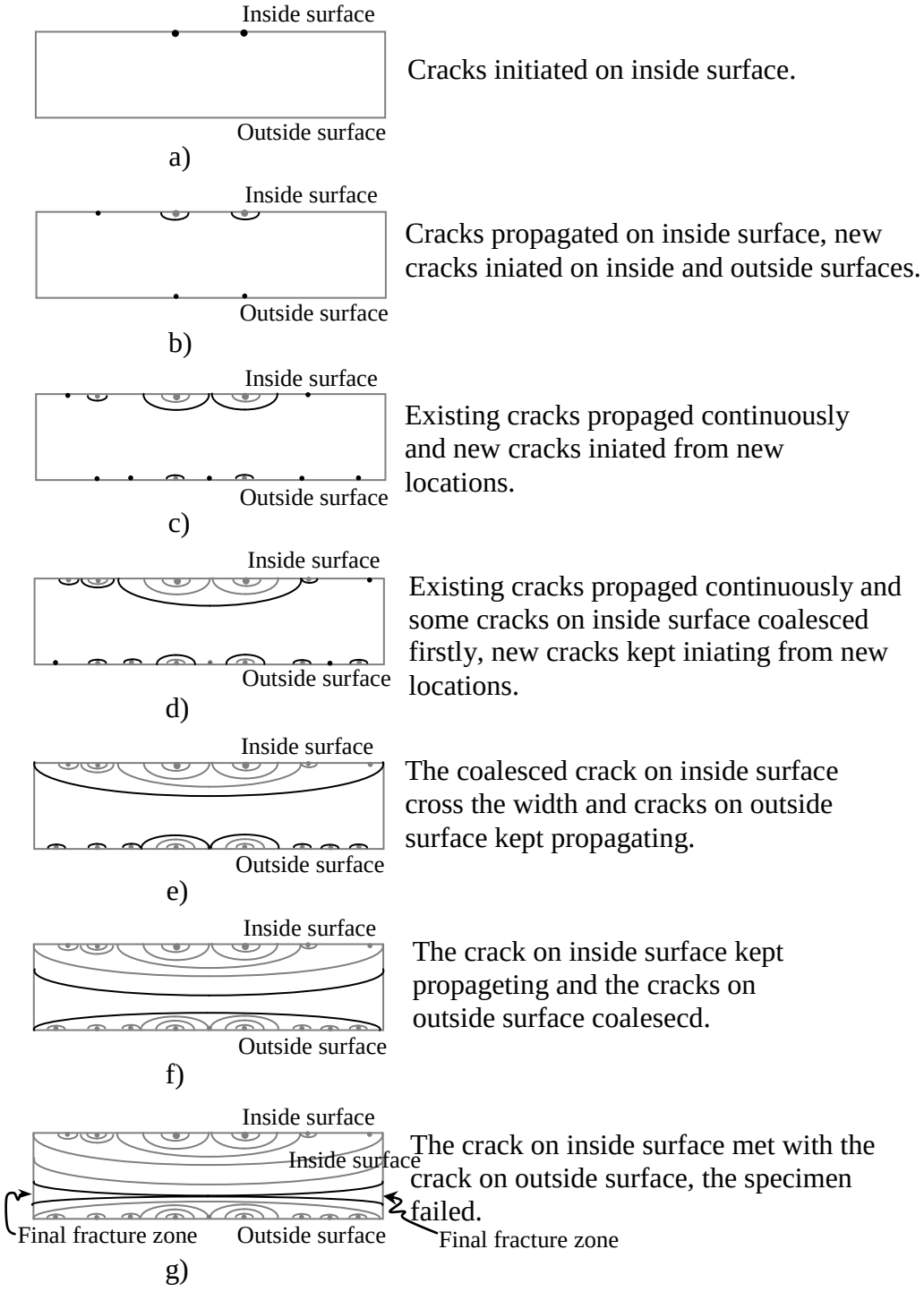

Figure 3.23: Schematic illustration of crack propagation

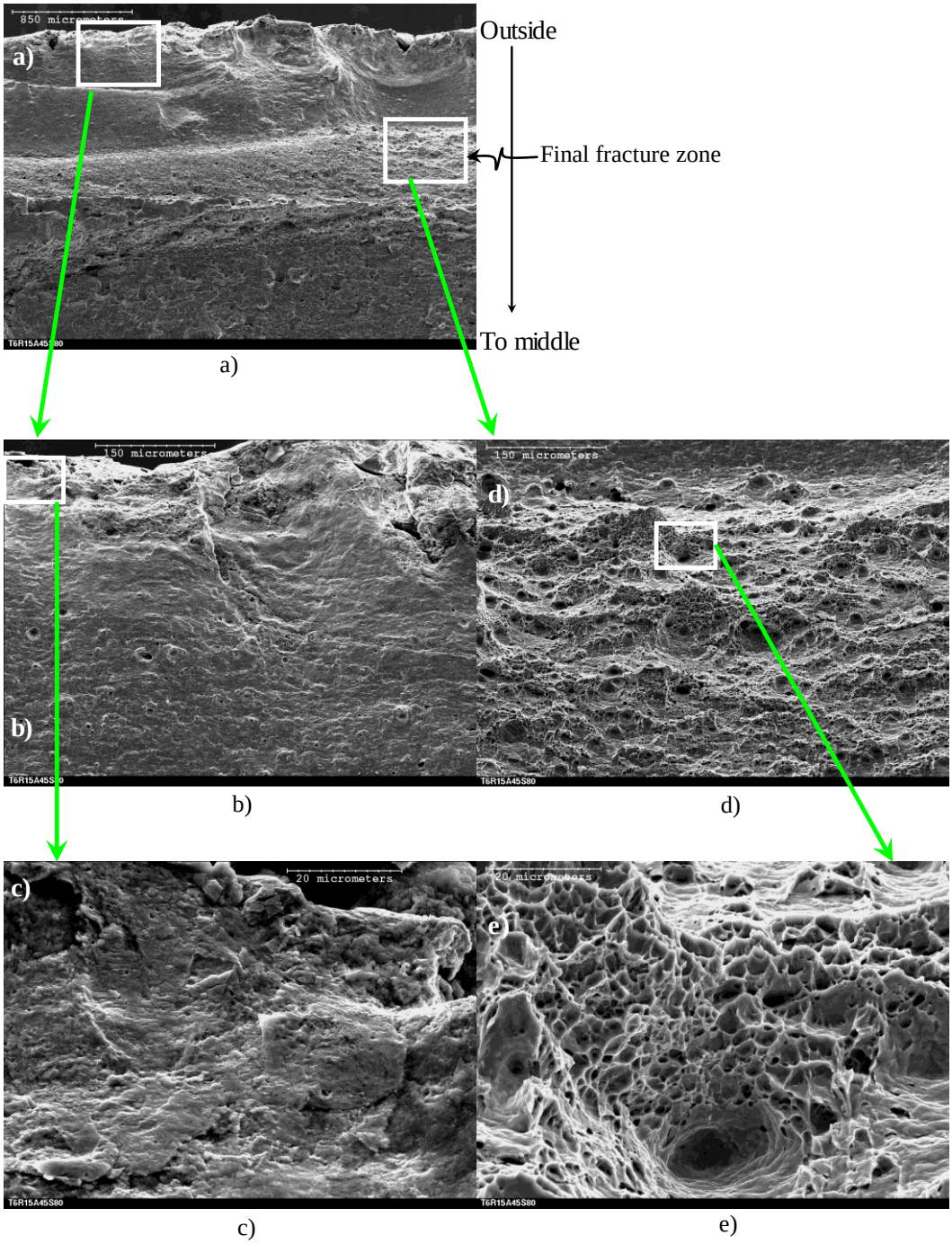

Figure 3.24: Top half of the fracture surface of specimen T6R15A45S80 (SEM)

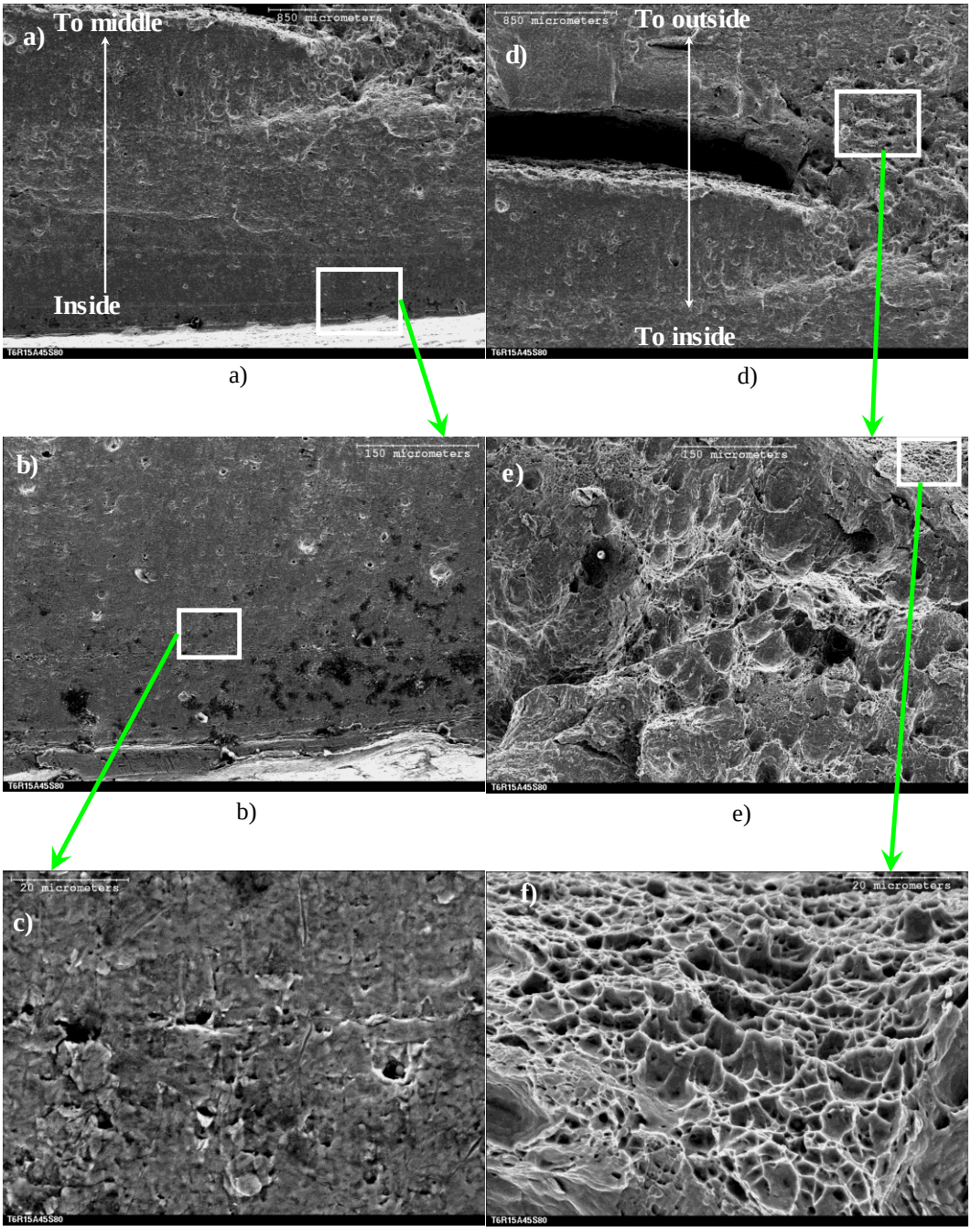

Figure 3.25: Bottom half of the fracture surface of specimen T6R15A45S80 (SEM)

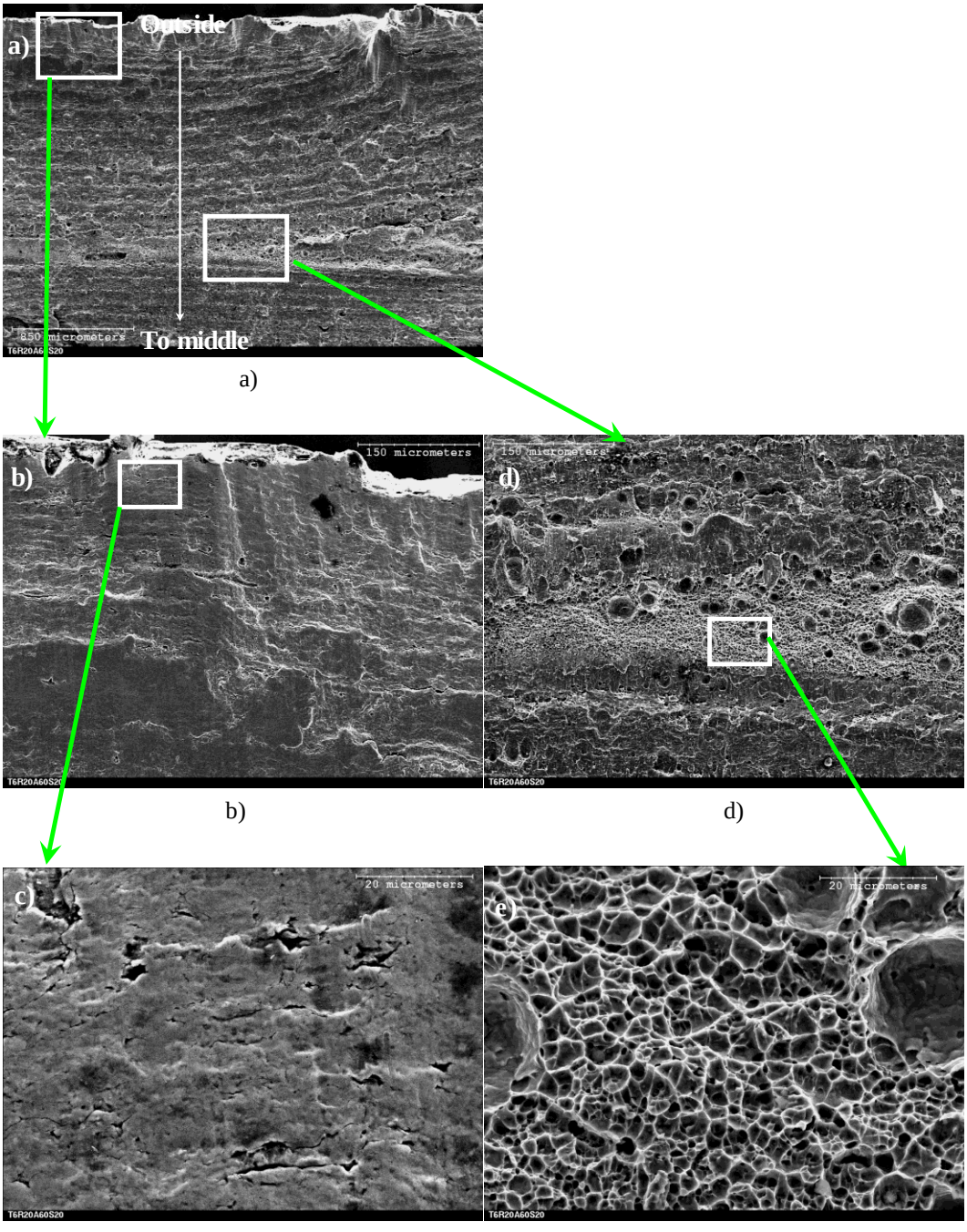

Figure 3.26: Top half of the fracture surface of specimen T6R20A60S20 (SEM)

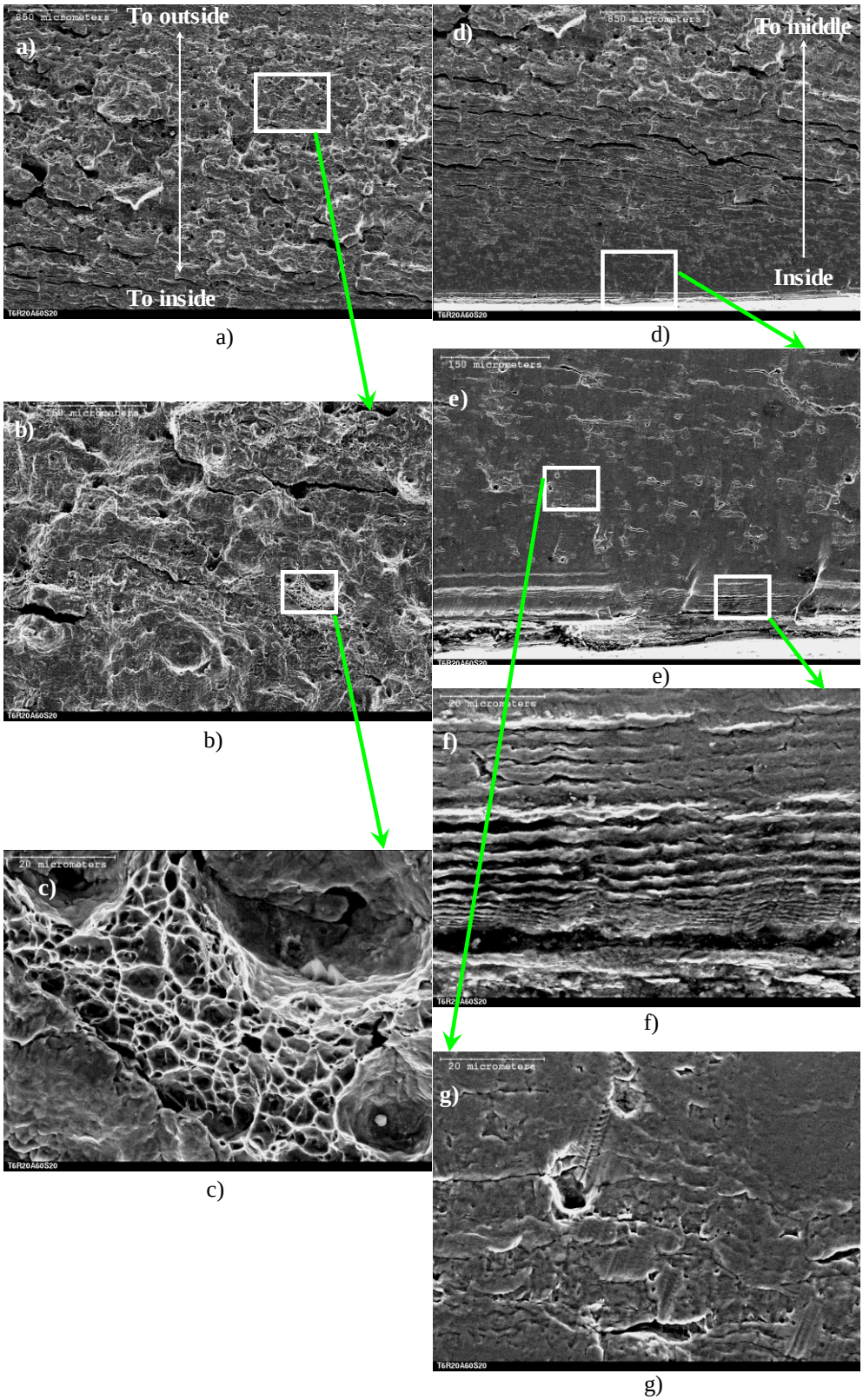

Figure 3.27: Bottom half of the fracture surface of specimen T6R20A60S20 (SEM)

4 FULL-SCAL PIPE TESTS

The full-scale pipe tests were designed to investigate the LCF behaviour, so the gap between strip specimens and full-scale pipe specimens could be found and bridged. In Chapter 6, the LCF life prediction models will be developed from the strip test results. The full-scale pipe tests will be used to provide the experimental verification for the developed LCF life prediction models.

4.1 TEST PROGRAM

The full-scale pipe test program was specially designed so that the specimens were wrinkled by a combination of axial load, bending moment, and internal pressure, and were fractured by a well-controlled cyclic loading procedure.

4.1.1 SPECIMEN DESIGN

Two specimens were designed based on four considerations. First, full-scale pipe specimens used the same materials as strip specimens, so their results could be compared directly. Second, D/t ratios were so chosen that the specimens could represent actual pipes used in the field. Third, L/D ratios were strictly designed to prevent the occurrence of global buckling since the wrinkling is the interest of this research. Finally, the pipe specimens had to be long enough to make rooms for installing the jack and the load cell between the two moment arms. These two specimens were made from two different types of material, one was the NPS16 Tokyo Gas Co. (TG) pipe, which had a nominal grade of X60, a nominal outside diameter of 406 mm, a nominal length of 1550 mm (L/D = 3.8), and a nominal thickness of 11.9 mm; the other was the NPS20 TransCanada Pipelines Ltd. (TCPL) pipe, which had a nominal grade of X65, a nominal outside diameter of 508 mm, a nominal length of 1800 mm (L/D = 3.5) and a nominal thickness of 6.4 mm. These geometries are summarized in Table 4.1.

4.1.1.1 MATERIAL MECHANICAL PROPERTIES

The mechanical properties of the pipe specimens are the same as the strip specimens and are summarized in Table 3.1.

4.1.1.2 GEOMETRY AND DESIGNATION

The actual geometries of pipe length, outside diameter, and wall thickness were measured by tape measure, caliper, and ultrasonic thickness gauge, respectively; and the results are given in Table 4.1.

In addition, the designation shown in this table indicates the test type, the pipe diameter and series number, for instance LCF16N1 represents the LCF test of number one, 16 inch diameter pipe.

4.1.2 TEST SET-UP

The test set-up was adopted and modified from the existing test set-up, as shown in Figure 4.1 (Dorey, 2001). The original test set-up was designed to apply combined axial load, bending moment, and internal pressure to the pipe specimens. The axial load is directly applied by the MTS6000 machine, the bending moment is produced by the jack pushing/pulling the two moment arms, and the internal pressure is generated by pumping water into the test specimens. Since large deformation is required for the LCF tests, the test set-up was modified to accommodate the large deformation by inserting a spacer at the jack location. In addition, tie rods were installed at pivots to provide in-plane stability, and lateral bracings were designed and installed to prevent out-of-plane instability.

To minimize the potential eccentricity and welding defect, and for the ease of test set-up, the following assembly procedure was used in this test program.

1) Assembled the top and bottom assemblies: firstly, placed the curved roller on the moment arm and bolted them together; followed by flipping them over so the roller was sitting on the strong floor; then, bolted the 76 mm thick end plate to the top flange of the moment arm.
2) Moved the bottom assembly under the MTS6000 machine and aligned it with the loading head.

3) Welded the pipe specimen on the end plate of top assembly.
4) Inspected the weld quality by X-ray. Before moving to the next step, all weld defects had to be fixed.
5) Flipped over the top assembly and the welded pipe and placed the un-welded pipe end on the top of end plate of bottom assembly.
6) Aligned the pipe specimen with the loading head and the bottom assembly, and welded them together.
7) Repeated step 4.
8) Installed the jack at the far end of the moment arms.

It can be seen that in both steps 3) and 6), the end plate faced up, thus overhead welding was avoided and the weld quality was assured.

4.1.3 MEASUREMENTS AND INSTRUMENTATION

Before assembling the test set-up, the geometric imperfections of pipe were measured. Before the test, the corresponding instrumentation was installed to capture the global and local behaviours under the monotonic and cyclic loadings. The following will describe the instrumentation according to the measured parameters.

4.1.3.1 IMPERFECTIONS

Generally, the geometric imperfection is one of the major factors affecting pipe buckling. It impacts the wrinkle location and the load-carrying capacity of the pipe. Previous full-scale pipe tests conducted at the U of A concluded that the imperfection did not significantly change the load-carrying capacity of pipe, especially for the pressurized pipes. However, the imperfection could affect the wrinkle location.

To measure the geometric imperfections of straight pipes, the measuring apparatus was specially designed and manufactured at the U of A, and it is shown in Figure 4.2. This apparatus has four key parts: the base pedestal, the central rail, the tailor fitted carriage and the top end fixture. The pipe to be measured sat on the base pedestal, the tailor fitted carriage could move along the central rail to

measure imperfections, and the top end fixture fixed the central rail on the top end of pipe. A typical installation procedure can be described as follows: first, the central rail was connected to the base pedestal that only the revolution about its own axis is allowed; second, the pipe was put on the base pedestal, and then it was aligned and fixed by roughly making its axis coincident with the axis of central rail; third, the tailor fitted carriage was so installed that only sliding along the central rail was permitted; at last, the top fixture was fixed on the top of pipe. In this apparatus, the only sensor was the linear variable differential transducer (LVDT), which was mounted on the carriage to scan imperfections.

Since the central rail can rotate freely about its own axis and the tailor fitted carriage is able to slide along the central rail, the measuring apparatus can scan any point on any cross section along the axis of pipe. However, it is impossible, also unnecessary, to measure the imperfection at every point. A practical way is to measure the imperfections according to a prior determined mesh, i.e. the measurement is only conducted at the intersections of mesh grids. In this test, along the circumferential direction, the cross section of the pipe was equally divided into 16 pieces; along the axis of pipe, the imperfection was measured at 11 equally–spaced elevations. Therefore, a total of 16 × 11 points was measured. For the 16 inch pipe, the mesh size was approximately 80 mm × 100 mm; and for the 20 inch pipe, the mesh size was about 100 mm × 110 mm.

The so-obtained measured data are not imperfections. In effect, the measured data are the changes of the distance from the intersection of central rail and tailor fitted carriage to the tip of LVDT, which always touches the inside wall of pipe by being pushed by a small spring inside of LVDT. According to its definition, the geometric imperfection is the deviation from the perfect shape of the measured object, so the geometric imperfection greatly depends on how the perfect shape is defined. For the measured pipe, its perfect shape is no doubt a cylinder, so the target becomes to determine the radius of this cylinder. In addition, the measured data contain the systematic errors which are caused by the measuring apparatus itself, and they have to be removed. Therefore, the measured data have to be processed.

Dorey (2001) employed the same apparatus to measure the imperfections of his pipes, and developed a method to calculate the imperfections from the measured data. In his method, the central rail was assumed crooked and not coincident with the axis of pipe. However, his method indistinctively assumed the tailor fitted carriage perpendicular to the axis of pipe, and this is not true if the axis of pipe is not parallel to the central rail. So it can be expected that his method only works well when the errors caused by the inclination of pipe are not significant compared with the imperfections themselves.

It is also obvious that the easiest way to find this perfect cylinder is by the mean-value method, as Coppa (1966) did. However, it will lead to much greater errors because this method takes the average value of measured data as the perfect shape and does not minimize the errors. Up to date, the most accepted method is the least-squares method, which makes the sum of the square of the differences of the investigated variable minimum, so it will give the smallest errors. Moreover, this method can count all systematic errors and does not need to make additional measurements. Therefore, this research program employed the least-squares method to handle the imperfection of pipe.

After finding this perfect cylinder, the imperfection can be obtained by subtracting the radius of this perfect cylinder from the measured data. The details can be found in Appendix B.

4.1.3.2 ROTATIONS

The measurement of rotation was important because it was the basis to evaluate and control the curvatures of pipe specimens. A total of seven RVDTs were installed, the layout is schematically shown in Fig. 4.3.

Five RVDTs were installed on the outside surface and along the neutral axis of pipe to measure its rotation: one was right on the middle cross section; one was half pipe diameter below the middle cross section; one was half pipe diameter above the middle cross section; and the other two, which also measured the rotations of moment arms, were on the bottom end plate and top end plate,

respectively. Another RVDT was attached to the jack to measure its in-plane inclination. The last one was fixed on the end of top moment to monitor the out-of-plane tilt of entire loading system.

4.1.3.3 HORIZONTAL DISPLACEMENTS

In this test, horizontal displacement was also called lateral deflection. To monitor the lateral deflection of the pipe, a total of eight LVDTs were installed (refer to Fig. 4.3): two on end plates and six on three selected cross sections. These three cross sections were selected as follows: one at the middle cross section which was right at the middle of pipe, one at the upper cross section which was D/2 above the middle cross section, and the last one at the lower cross section which was D/2 below the middle cross section. On each cross section, two LVDTs were installed: one on the concave side and the other on the convex side. In addition, these LVDTs together could provide an alternative way to evaluate the curvature of pipe specimen during test.

4.1.3.4 VERTICAL DISPLACEMENTS

A total of seven cable transducers were installed in this test set-up, and they are schematically shown in Fig. 4.3. Among of them, three were installed between the bottom end plate and the floor to measure the relative vertical displacement between them (the rotation of bottom end plate could be also obtained); three were installed between the top and bottom end plates to measure their relative vertical displacements or the pipe shortening on one hand and to estimate the relative rotation of those two end plates on the other hand. The last one was installed as follows: from the loading head of MTS6000 machine vertically down to the top moment arm, along this moment arm to its end on the jack side, and then directly down to the bottom moment arm and fixed there. The last cable transducer was so installed to get the total stroke of the test set-up or the sum of jack stroke and MTS stroke.

4.1.3.5 STRAINS

Fig. 4.3 schematically shows the layout of strain gauges and demec points.

The strain gauges were put on the outside surface of pipe to measure the strains in both the axial and circumferential directions. They were used to investigate how the strains were distributed on the pipe, and to determine when the wrinkle formed and to evaluate the ovalization of pipe if possible.

In addition, demec points were also prepared to take another set of strain readings over a gauge length of about D/2. Punch marks were made just beside the demec points as a spare means whenever the demec points stopped to work. These demec points and punch marks were used to evaluate the deformation of wrinkle during post-buckling stage.

4.1.3.6 LOCAL BEHAVIOUR

Two types of local behaviour were concerned. The first one was the wrinkle shape, which was requisite in investigating the post-buckling behaviour and the LCF behaviour of pipe, and it was measured by a custom-made device. The other one was the relative axial displacement over a gauge length of the entire wrinkle, which was indispensable in exploring the LCF behaviour and evaluating the LCF life of pipe, and it was measured both automatically by two small LVDTs during cyclic loading stage and manually by caliper during the whole loading stage. The two small LVDTs were installed after the wrinkle was fully developed and just before the cyclic loading being applied.

The main measurements and instrumentation are summarized in Table 4.2 and the layout of instrumentation is shown in Figures 4.3.

4.1.4 TEST PROCEDURE

4.1.4.1 GENERAL

The complete loading of pipes consisted of two stages: the monotonic loading stage and the cyclic loading stage. During the monotonic loading stage, a wrinkle was formed by a specific combination of global curvature and axial deformation; during the cyclic loading stage, the wrinkled pipe was fractured by LCF. Theoretically, LCF loadings related to axial deformation and in-plane rotation can

be categorized into three cases: cyclic in-plane rotation, cyclic axial deformation, and combination of the two. The cyclic in-plane rotation can come from the seasonal frost heave and thaw settlements in a local area of soil. The cyclic axial deformation can be caused by seismic activity, thermal effect and repeatedly opening and shutting the service, etc. The last case is that the pipe is subjected a combination of cyclic in-plane rotation and cyclic axial deformation. In field, which one is prevalent depends on many factors, e.g. the location and the buried depth of the line, the conveyed medium and the operation regulation, etc. However, this test program focused only on the second case, where the cyclically varied axial deformation is dominant.

4.1.4.2 LOADING PROCUDURE

In this test, the design of a monotonic loading procedure was guided by the preliminary FEA results and the design of cyclic loading was directed by the strip specimen test results.

Because the actual loading procedure was not the same for the two pipe specimens, the detailed loading procedure will be introduced respectively in the later sections.

4.2 GENERAL ANALYSIS

In this section, the internal forces at pivot points and at an arbitrary cross section will be analyzed, and the deformation parameters will be determined from the related measured variables, and finally some theoretical analysis of prebuckling behaviour of pipe will be conducted.

4.2.1 INTERNAL FORCES

In this test set-up, the MTS load, jack load, and water pressure were the three main external loads; the axial loads in tie rods were also external loads but they were much smaller compared with the three main external loads.

From the free body diagrams shown in Figure 4.4 and the corresponding equilibrium conditions at the interested locations, the following equations can be obtained:

AT TOP PIVOT

$$V_{tp} = P_{tt} + P_j \sin\theta_j \tag{4.1.1}$$

$$N_{tp} = P_{MTS} - P_j \cos\theta_j \tag{4.1.2}$$

$$M_{tp} = P_j \sin\theta_j \left(-h_{ts}\cos\theta_t + l_{ma}\sin\theta_t\right) + P_j \cos\theta_j \left(h_{ts}\sin\theta_t + l_{ma}\cos\theta_t\right) \tag{4.1.3}$$

where

V_{tp} = the shear force at top pivot,

N_{tp} = the axial load at top pivot,

M_{tp} = the bending moment at top pivot,

P_{tt} = the resulting axial force in the top four tie rods,

P_j, P_{MTS} = the jack load and MTS load respectively,

h_{ts} = the distance from the top hinge to the central line of moment arm,

l_{ma} = the length of bending moment arm, it was 1.1 m in this test,

θ_j = the inclination angle of jack, and

θ_t = the slope angle of top moment arm.

AT BOTTOM PIVOT

$$V_{bp} = P_{bt} - P_j \sin\theta_j \tag{4.2.1}$$

$$N_{bp} = P_{MTS} - P_j \cos\theta_j \tag{4.2.2}$$

$$M_{bp} = P_j \sin\theta_j \left(h_{bs}\cos\theta_b - l_{ma}\sin\theta_b\right) + P_j \cos\theta_j \left(h_{bs}\sin\theta_b + l_{ma}\cos\theta_b\right) \tag{4.2.3}$$

where the parameters are similar to those defined above except that the subscript ‘b’ represents the bottom pivot or the bottom moment arm.

AT AN ARBITRARY CROSS SECTION

$$V = N_{tp}\sin\theta + V_{tp}\cos\theta \tag{4.3.1}$$

$$N = N_{tp}\cos\theta - V_{tp}\sin\theta - P_w + P_p \tag{4.3.2}$$

$$M = M_{tp} + N_{tp}\Delta + V_{tp}h \tag{4.3.3}$$

where

V, N and M = the shear force, normal force and bending moment on an arbitrary cross section respectively,

$P_w = \pi D_i^2 p / 4$ = the load caused by water pushing the end plate, where D_i is the inside diameter of pipe and p is the water pressure,

$P_p = -A\mu\sigma_h$ = the load caused by the Poisson's effect in the presence of hoop stress, where A is the cross sectional area of pipe wall, μ is the Poisson's ratio and σ_h is the hoop stress,

θ = the slope angle of the cross section,

Δ = the lateral deflection of the center of the cross section,

h = the distance from the top pivot to the center of the cross section, and

the other parameters are the same as before.

In the above equations, the following relation holds between water pressure and hoop stress:

$$\sigma_h = \frac{pD}{2t} \tag{4.4}$$

where, t is the pipe wall thickness, and the other parameters are the same as before.

4.2.2 DEFORMATION PARAMETERS

To investigate the global and local behaviours, their corresponding deformation parameters have to be determined. For this research program, these parameters included the global curvature, local curvature, global relative axial displacement, and local relative axial displacement.

4.2.2.1 CURVATURE

The curvature is a measure of curving and it is defined as the rate of slope angle change. For a perfect circle, the curvature is same everywhere; but for an arbitrary

arc, the curvature varies from point to point. Hence, the curvature can be viewed as a point behaviour and this makes its application difficult. To bypass this obstacle, a loose definition can be employed to define the curvature as the change of slope angle over a specific gauge length. According to this loose definition, the curvature depends on both the change of slope angle and the gauge length. If the gauge length is the length of the whole curve, the so-obtained curvature is called global curvature, and if the gauge length is the length of a segment of this curve, the so-obtained curvature is called local curvature. Therefore, based on this loose definition, the curvature is segment behaviour. Because of its simplicity, this research program abided by this loose definition.

In full-scale pipe tests, the layout of RVDTs is shown in Figure 4.3. Because the end plates could be treated as 'rigid', two RVDTs installed on them measured the slope angles at both pipe ends. In addition, three RVDTs were put on the pipe wall and they recorded the slope angles at those three locations. So the global curvature can be obtained as follows:

$$\Phi_g = \frac{\theta_{R5} - \theta_{R1}}{L_o} \tag{4.5.1}$$

where Φ_g is the global curvature, L_o is the length of undeformed pipe, θ_{R1} and θ_{R5} are the readings of RVDT 'R1' and 'R5', as shown in Fig.4.3, respectively.

And the local curvature can be given by

$$\Phi_{lij} = \frac{\theta_{Ri} - \theta_{Rj}}{L_{oij}} \tag{4.5.2}$$

where Φ_{lij} is the local curvature of pipe segment 'ij', L_{oij} is the length of undeformed pipe segment 'ij', θ_{Ri} and θ_{Rj} are the readings of RVDT 'Ri' and 'Rj' respectively. Also, Ri ≠ Rj and Ri and Rj can not be R1 and R5 respectively at the same time.

4.2.2.2 RELATIVE AXIAL DISPLACEMENT (RAD)

Three types of RAD will be involved in the succeeding sub-sections, so they will be introduced one by one in the following. For clarity, these parameters are schematically illustrated in Figure 4.5.

RELATIVE AXIAL DISPLACEMENT BETWEEN PIVOTS

It can be obtained by

$$S = H_o - H \tag{4.6.1}$$

where S is the RAD between pivots, H_o and H is the distances between the two pivots before the pipe being deformed and after the pipe being deformed respectively.

RELATIVE AXIAL DISPLACEMENT OF CONCAVE SIDE

It is defined as

$$\delta L_{cg} = L_o - L_c = S + h_p\left(2 - \cos\theta_{R1} - \cos\theta_{R5}\right) + \frac{D}{2}\left(\sin|\theta_{R1}| + \sin|\theta_{R5}|\right) \tag{4.6.2}$$

where

δL_{cg} = RAD of concave side,

L_c = the chord length of deformed pipe on concave side,

h_p = the distance from a pivot to its nearest end cross section of pipe (0.33 m for this test), and

the other parameters are the same as before.

RELATIVE AXIAL DISPLACEMENT OF WRINKLE

In this research program, the RAD of wrinkle was defined by

$$\delta L_w = L_{wo} - L_w \tag{4.7}$$

where δL_w is the RAD over a gauge length of a whole wrinkle on the concave side, L_{wo} and L_w is the length of undeformed and deformed gauge length of a whole wrinkle respectively.

4.2.3 THEORETICAL ANALYSIS

For the tested pipes, the water pressure produced hoop stress and at the same time, the axial load and bending moment generated axial stress, so it was in a biaxial stress state. Neglecting the effects of local buckling, Mohareb (1995) drew a relation between the hoop stress and axial stress based on the von Mises yield criterion and it can be expressed as follows according to the symbols used in this thesis:

$$\frac{\sigma_{ay}}{\sigma_y} = 0.5\frac{\sigma_h}{\sigma_y} \pm \sqrt{1 - \frac{3}{4}\left(\frac{\sigma_h}{\sigma_y}\right)^2} \tag{4.8}$$

where σ_y is the yield stress of material, σ_{ay} is the axial stress that makes the material yield with the presence of hoop stress of σ_h.

In addition, because the pipe was subjected to bending moment and axial load, their interaction had to be investigated to understand its actual behaviour. For discussion convenience, the following normalized quantities were defined:

$$n = \frac{N}{N_y} \tag{4.9.1}$$

where n is the normalized normal force on a cross section, $N_y = A\sigma_{ay}$ is the yield normal force of a cross section and N is the same as before.

$$m = \frac{M}{M_y} \tag{4.9.2}$$

where m is the normalized bending moment on a cross section, $M_y = S\sigma_{ay}$ is the initial yield bending moment of a cross section and M is the same as before.

$$\phi = \frac{\Phi_g}{\Phi_y} \tag{4.9.3}$$

where ϕ is the normalized global curvature, Φ_y is the global curvature at initial yielding of pipe and Φ_g is the same as before.

Based on the plastic theory, the moment-curvature relation can be obtained theoretically. Chen and Han (1985) analyzed the unpressured pipe and derived

some approximate relations. If the above defined normalized parameters are used, these relations can be rewritten as follows:

$$m = \begin{cases} a\phi & \phi \le \phi_1 \quad \text{elastic} \\ b - \dfrac{c}{\sqrt{\phi}} & \phi_1 < \phi \le \phi_2 \quad \text{primary plastic} \\ m_{pc} - \dfrac{f}{\phi^2} & \phi > \phi_2 \quad \text{secondary plastic} \end{cases} \tag{4.10}$$

where,

$$a = m_1/\phi_1 \tag{4.10.1}$$

$$b = \frac{m_2\sqrt{\phi_2} - m_1\sqrt{\phi_1}}{\sqrt{\phi_2} - \sqrt{\phi_1}} \tag{4.10.2}$$

$$c = \frac{m_2 - m_1}{1/\sqrt{\phi_1} - 1/\sqrt{\phi_2}} \tag{4.10.3}$$

$$f = \left(m_{pc} - m_2\right)\phi_2^2 \tag{4.10.4}$$

In the above equations, m_1 and ϕ_1 are the corresponding values of m and ϕ respectively when the primary yielding occurs, m_2 and ϕ_2 are the corresponding values of m and ϕ respectively when the secondary yielding occurs, and m_{pc} is the value of m when the state of full plasticity is reached. These parameters can be obtained by the following approximate expressions:

for all n,

$$\begin{cases} m_1 = 1 - n \\ \phi_1 = 1 - n \end{cases} \tag{4.10.5}$$

for $0 \le n \le 0.4$

$$\begin{cases} m_2 = 1 + 0.21n - 1.05n^2 \\ \phi_2 = 1/\left(1 - 1.395n + 1.206n^2\right) \end{cases} \tag{4.10.6}$$

for $0.4 < n \le 1$

$$\begin{cases} m_2 = 1.528(1 - n) \\ \phi_2 = 2.625(1 - n) \end{cases} \tag{4.10.7}$$

for $0 \le n \le 0.65$

$$m_{pc} = 1.273(1 - 1.18n^2) \quad (4.10.8)$$

for $0.65 < n \le 1$

$$m_{pc} = 1.82(1 - n) \quad (4.10.9)$$

Under a specific level of water pressure, the hoop stress can be obtained by Equation (4.4), and then σ_{ay} can be given by Equation (4.8). Because the shear force was very small in the tests, it can be neglected. Then using Equations (4.3.2) and (4.3.3), the axial load and bending moment can be computed. Furthermore, the normalized parameters can be calculated from Equations (4.9.1) to (4.9.3). Finally, the approximate moment – curvature curve and the approximate interaction diagram can be obtained from Equation (4.10) to (4.10.9). The results will presented and discussed in the following sections.

4.3 TEST RESULTS AND DISSCUSSION

In this section, the test results will be presented and discussed for each specimen separately. For each specimen, the loading procedure will be introduced and discussed with the spectra of some key variables; then the pipe behaviour under monotonic loading and cyclic loading will be discussed.

4.3.1 SPECIMEN LCF16N1

4.3.1.1 SPECTRA OF SOME KEY VARIABLES

The MTS load, jack load and water pressure were all external loads and they were applied to the pipe specimen either directly or indirectly via moment arms, and their joint action caused the pipe to wrinkle and fracture. In the meantime, the MTS machine experienced a significant stroke and the moment arms underwent significant rotations. By reviewing the spectra of these five variables (three external loads, one stroke, and one rotation) and how the pipe was loaded and controlled, the responses of the specimen such as the deformation and the rotation could be easily understood.

Because the loading procedure and loading history were complicated, the following presentation and discussion will follow the so-divided two loading stages, monotonic and cyclic loading stages, and the spectra of the aforementioned variables are shown in Figure 4.6 and Figure 4.7, respectively.

MONOTONIC LOADING STAGE

For convenience, a so-called nominal net axial load (NNAL), N_{NN}, will be introduced firstly and it can be defined as follows:

$$N_{NN} = P_{MTS} - P_j + P_p - P_w \tag{4.11}$$

where all parameters are the same as before.

It can be seen that N_{NN} is exactly the net axial load on the pipe wall if the pipe is straight. During the monotonic loading stage, the NNAL was controlled, and it was also given in Figure 4.6. As shown in Figure 4.6, when the counter number reached to 5, the water was pressurized to 11.44 MPa (40% of SMYS), and the MTS load was increased to 1320 kN. This gave a zero NNAL in the pipe wall, so the recorded strain was exactly the hoop strain caused by the internal water pressure. Also because of this water pressure, the pipe specimen expanded outward. All collars were loosened at this moment to prevent forming inward imperfections. From this moment to the end of monotonic loading, the water pressure was kept constant, so its spectrum was a straight line.

When the count number went up to 10, the MTS load was increased to 2019 kN; the corresponding NNAL was 1570 kN and the MTS stroke was 5 mm. Up to this moment, there were still no jack load and rotation of the moment arms. From this point on, the NNAL was kept constant at this level and the jack load or jack stroke was increased to acquire the desired average rotation of the moment arms. The constant NNAL of 1570 kN chosen for the monotonic bending stage corresponded to the axial load in the pipe wall caused by a temperature change of 45°C.

When the count number was accumulated to 109, the jack load climbed to its maximum pushing level of 818 kN, and the corresponding MTS load was 2857

kN, the average rotation was 2.68 degree and the MTS stroke was 11 mm. After this, the jack load could not be increased because of the yielding of the pipe and the increase of second order effect from axial load, so the rotation-controlled method took action.

When the count number was increased to 226, the average rotation of moment arms reached to the desired level of 7 degree. After this moment, the moment arms were locked to keep this average rotation constant and the MTS load/stroke was increased to develop the wrinkle around the whole circumference. Also because the NNAL was not controlled after this moment, it will not be discussed further. At this moment, the corresponding jack load was 376 kN in push, MTS load was 2434 kN and MTS stroke was 40 mm.

As the MTS load was increased, the pipe was shortened, so the jack cylinder had to retreat to lock the rotations of moment arms and as a result, the jack load changed direction from pushing to pulling. When the count number rose to 391, the MTS load arrived at its summit of 5224 kN, and the corresponding jack load was 728 kN in pulling and the MTS stroke was 65 mm. After this moment, the MTS load could not be increased anymore, so the stroke-controlled method was employed.

When the count number was added up to 427, the jack load reached its nadir of 764 kN in pulling, and the corresponding MTS load was 5189 kN and the MTS stroke was 70 mm.

When the count number was expanded to 503, the wrinkle was considered as being fully developed and the monotonic loading stage was over. The corresponding MTS stroke was 100 mm, MTS load was 4038 kN, and jack load was -562 kN.

CYCLIC LOADING STAGE

For this test, the cyclic loading stage could be sub-divided into two periods: in the 1st cyclic loading period, the pipe seam weld was fractured by cyclical axial deformation; and in the 2nd cyclic loading period, the wrinkle on concave side was

fractured by cyclic bending action. It had to be mentioned that the 2nd cyclic loading period was not planned and it was employed in order to fracture the wrinkle on concave side.

A typical cycle of loading in the 1st period was conducted as follows: firstly, the MTS load was unloaded to the minimum level of 200 kN under the condition of constant water pressure; secondly, the water was pressured to 22.89 MPa (80% of SMYS), and then was depressurized to 11.44 MPa (40% of SMYS) again; finally the MTS stroke was increased to 100 mm. This loading period was over after about 16 cycles because the water was observed shooting out from the pipe seam weld, which was located near the neutral axis.

In the 2nd cyclic loading period, the average rotation of moment arms was controlled to generate a constant rotation range, and the procedure was as follows: firstly, the jack pulled the moment arms to reach a specific rotation level, and then released the jack load to zero. In the test, an attempt was firstly made to obtain a big rotation change, but it was found that cracks occurred on the lower foot when the average rotation change reached to about 4.69^{o}. Because the objective of this test was to obtain a long LCF life, it was decided to decrease the average rotation change to about 1^{o} after this cycle. After this type cyclic loading were completed about 34 cycles, the loading was increased to facilitate the fracture of pipe. The wrinkle on concave side was fractured by only 2 cycles of this increased loading. In addition, two more loading cycles were tried to fracture the wrinkle on convex side, but it was stopped because it was found too risky. Figure 4.7 follows the loading descriptions from the beginning to the ending of the 2nd cyclic loading period, but the following discussion will ignore those abnormal cycles and only focus on the first 34 cycles.

Figure 4.7a shows the spectrum of MTS stroke. It shows that the maximum MTS stroke was kept constant at the level of 100 mm during the 1st cyclic loading period, but the minimum stroke decreased as the test progressed. The reason can be explained as follows: the maximum MTS stroke was produced by the MTS machine and could be exactly controlled, but the minimum MTS stroke was

generated by increasing the water pressure to the maximum level of 80% SMYS in each cycle. As the pipe wall was progressively damaged, the pipe would stretch more that caused the minimum MTS stroke decreased. During the 2nd cyclic loading period, the MTS stroke was not controlled, so the maximum stroke, the minimum stroke and the stroke range all floated as the test proceeded. It can be observed that the stroke range decreased as the test progressed and this was a result of the accumulation of plastic deformation in the wrinkle area.

Figure 4.7b shows the spectrum of water pressure. This spectrum exhibits that both the minimum water pressure and the maximum water pressure were kept constant during the 1st cyclic loading period. From the aforementioned loading procedure, it is known that a water pressure-controlled method was employed, so it is not surprising that the water pressure was well controlled. During the 2nd cyclic loading period, because the pipe was empty, the spectrum shows a zero water pressure.

Figure 4.7c shows the spectrum of MTS load. During the 1st cyclic loading period, the MTS load decreased gradually as the test progressed. This indicated the cyclic loading damaged the pipe progressively. During the 2nd cyclic loading period, the MTS load was controlled in the minimum level of 200 kN all the way to keep the loading system stable, so its spectrum becomes to a straight line.

Figure 4.7d gives the spectrum of jack load. During the 1st cyclic loading stage, the spectrum reflects the efforts made by the jack to lock the rotation of moment arms. As the pipe was gradually damaged, the pipe capacity to keep its shape was weakened, so the jack had to do more to hold the pipe in position. The spectrum shows that the jack load, especially the maximum load which pulled the moment arms, increased as the test progressed. During the 2nd cyclic loading period, the jack load was totally released at the end of each cycle after obtaining the desired rotation range, so the spectrum exhibits that the maximum jack load was well controlled to zero. Also to acquire the desired rotation range by only pulling the moment arms, the minimum jack load increased (or the pulling load decreased) as

the test proceeded. And this is because the pipe wall at the wrinkle crest was progressively damaged and made its net cross section decreased.

Figure 4.7e presents the spectrum of average rotation of moment arms. During the 1st cyclic loading period, the average rotation of moment arms was kept constant, so the spectrum shows a straight line. During the 2nd cyclic loading stage, the progressive decrease of maximum average rotation indicated that the pipe failed to restore its original shape when the jack load was totally removed. Because the plastic deformation was accumulated in the wrinkle region, a dimple was formed around the wrinkle crest and it was this dimple that caused the drop of maximum average rotation. In addition, because the rotation range was kept constant, it is not surprising that the minimum average stroke decreased correspondingly.

4.3.1.2 MOMENT VS. CURVATURE

Because the RVDTs installed on the pipe wall did not work well after the wrinkle formed, the following discussion will only focus on the global curvature.

The formation of wrinkle changed the geometries of the cross sections at or near the wrinkle and moved the neutral axes toward the unwrinkled (tension) side. This made the determination of the moment at those cross sections during the post-buckling stage difficult. However, the bending moment at pivots was not influenced by the formation of wrinkle, so the investigation of moment – curvature relation can be conducted at this location. Figure 4.8 gives the results at the top pivot.

At first, the pipe was in the elastic region, so the relation between bending moment and global curvature was linear. As the pipe entered the elastic-plastic region, the slope of curve gradually decreased and this indicated that the pipe became ‘soft’. When the pipe was fully plasticized, the slope of the curve became almost zero, and the pipe could not bear any additional bending moment. The long plateau shown in Figure 4.8 indicated that this type of pipe had great ductility and it can endure large curvature without losing significant moment capacity. In addition, the presence of the plateau is a reliable signal of the critical

cross section of pipe being fully plasticized. After passing this plateau, the slope of the loading path gradually decreased. It can also be seen that the descending path was much smoother than the ascending path. When the global curvature reached about 0.1576 1/m, the rotations of moment arms were locked and the MTS load was increased to form an encircled wrinkle around the pipe. From this moment to the end of 1st cyclic loading period, the global curvature was kept constant, so the loading path is a vertical straight line. The details during this loading period will be shown and discussed in next section.

During the 2nd cyclic loading period, a cyclic pulling jack load was applied to the moment arms to fracture the pipe wrinkle on concave side and several observations can be obtained from Figure 4.8. First, the hysteresis loop was floating toward the origin side as the test progressed. This is because the plastic deformation was accumulated in the wrinkle area. Second, the first loop floated away about a distance of 0.04 1/m. This is because a large end rotation was applied. Third, the last five loops were much bigger than the previous loops because they were made by positive and negative bending moments; moreover, the last three loops were recorded after the wrinkle on concave side was totally fractured, they should not be added to the fatigue life. At last, the peak pulling jack load dropped as the test progressed and this was a result of the progressive damage on pipe wall by the cyclic bending.

4.3.1.3 PIVOT AXIAL LOAD VS. RELATIVE AXIAL DISPLACEMENT BETWEEN PIVOTS

The relation between the pivot axial load and RAD between pivots during the whole loading stage is shown in Figure 4.9, and this type of curve can indicate the shortening of pipe to some extent.

Path ‘OA’ combines two loading steps of pressuring the pipe and increasing the MTS load to 2019 kN, which is also the pivot axial load. During this period, the pipe was in the elastic region, so the path is linear. Path ‘AB’ represents the loading step of bending the pipe under the condition of constant water pressure. During this period, the pivot axial load was unchanged, so the path is a horizontal

straight line. Then the rotations of moment arms were locked and the MTS load was increased. As a result, the pivot axial load was also increased. At point ‘C’, the pivot axial load reached its maximum value of about 5950 kN. Although the peak is relative flat and wide, there is no obvious plateau there. This indicates that the wrinkle on the convex side formed at almost the same moment as the section became fully plasticized, and this feature is different from the wrinkle formation on the concave side. At point ‘D’, the RAD between pivots went as far as about 96 mm, which is slightly less than the MTS stroke (100 mm). Then the 1st cyclic loading was applied by cyclically changing water pressure and MTS stroke under the condition of the rotations of moment arms being locked. And this cyclic loading produced a cyclic change of RAD between pivots about 15 mm. In addition, the pivot axial load dropped as the pipe experienced more cycles and this indicated the pipe was softened by this cyclic loading. After this, the second type cyclic loading was applied and it is shown in the figure is a very thick and short ‘line’. Because this type cyclic loading was only produced by bending, the change of relative pivot displacement was very small.

4.3.1.4 INTERNAL PRESSURE VS. RELATIVE AXIAL DISPLACEMENT BETWEEN PIVOTS

Because all tensile deformation during the first 16 cycles was produced by the cyclic internal water pressure, it is worthwhile to investigate the relation between the water pressure and the RAD between pivots. This relation is shown in Figure 4.10.

Along path ‘OA’, the pipe was pressured to 11.44 MPa and there were almost no RAD between pivots. Along path ‘AB’, the internal pressure was kept constant and the pivots experienced about 97 mm RAD along with an encircled wrinkle was formed around the pipe. Along path ‘BC’, the internal pressure was also kept constant, but the MTS load was decreased to 200 kN, so about 6 mm RAD was released between pivots. Along path ‘CD’, the pipe was pressurized to 22.89 MPa, and corresponding about 7 mm of RAD was released between pivots. Along path ‘DE’, the internal pressure was decreased to 11.44 MPa again, but the

corresponding RAD between pivots was so small that could be ignored. After about 16 cycles, a through crack formed right on the seam weld and made the pipe lose its containment ability. So the internal pressure was dropped to zero, the path 'EF'. After that, the unpressured pipe was cyclically loaded by jack only.

4.3.1.5 INTERACTION DIAGRAM

According to Equation (4.10), the theoretical interaction diagrams can be approximately obtained. During the test, some of RVDTs installed on the pipe conflicted with the wrinkle in the late monotonic loading stage, so the axial load and bending moment on these three cross sections could not be obtained during the whole monotonic loading stage. But both end cross sections were not affected by the wrinkle, so the following discussion will focus on top end cross section and the results are shown in Figure 4.11.

In this figure, along path 'OA', the pipe was axially loaded to 0.2 P_y, but no bending moment was applied. Along path 'ABCDEFG', the axial load was held constant, but the bending moment was increased to allow the pipe deflects. At point 'B', primary plasticity occurred; specifically the extreme fiber on the concave side was plasticized by compressive stress. At point 'C', secondary plasticity appeared; specifically the extreme fiber on convex side was plasticized by tensile stress. At point 'D', the maximum bending moment was obtained; local buckling took place on the critical cross section of the pipe. It can be seen that even for the top end of pipe, where the smallest moment resided, most of its cross section was plasticized. At point 'E', the convex side became elastic; and at point 'F', concave side fell into the elastic region too. At point 'G', the moment arms were locked to keep their average rotation constant. Along path 'GHIJKLMNP', the pipe was compressed by the MTS machine to propagate the wrinkle along the whole circumference of pipe. At point 'H', the moment changed direction because the jack load changed direction from pushing to pulling. At point Í', the extreme fiber on convex side became plasticized; and at point 'J', the extreme fiber on concave side got plasticized too. At point 'K', the entire cross section was plasticized. At point 'L', the MTS load could not increase anymore and the axial

load reached its maximum value. At point ‘M’, some portion of cross section started to behave elastically; and at point ‘N’, the concave side totally went back to the elastic region. At point ‘P’, the whole cross section retreated to the elastic region. At point ‘Q’, the desired wrinkle shape was developed and so the monotonic loading stage was over. It has to be emphasized that the theoretical interaction diagrams could not represent the actual stress state in the pipe because the stress was reversed from tension to compression when the loading was changed from bending to compression. This stress reversal generated residual stresses in the pipe, which will affect the timing of the primary and secondary plasticity.

4.3.1.6 STRAIN BEHAVIOUR

The strain gauge has a strain range limit of about 2.5%. In addition, the strains are localized at the wrinkle region when the wrinkle is developed. Based on these two considerations, the following discussion of axial strains is limited to the period of forming a wrinkle on concave side during the monotonic bending stage. However, because the hoop strain is relatively small, the discussion will extend to the cyclic loading stage.

For discussion convenience, some count numbers and their corresponding action and response are specified as follows: at count number 40, the concave side was plasticized, and the corresponding jack load was 617 kN, and the average rotation of moment arms was 0.81^{o}; at count number 80, the convex side was plasticized and the corresponding jack load increased to 797 kN, and the average rotation went up to 1.71^{o}; at count number 109, the jack load climbed to its maximum value of 818 kN, and the corresponding average rotation was 2.68^{o}; at count number 150, the jack load decreased slightly to 808 kN, but the average rotation of moment arms accumulated to 3.51^{o}; at count number 180, jack load dropped to 727 kN and average rotation went as high as 4.43^{o}; and at count number 225, the jack load went down to 429 kN, and the corresponding average rotation reached to 6.94^{o} and the bending was stopped.

ALONG AXIAL DIRECTION

Figure 4.12 shows the strain distributions along the axial direction at different radial locations. It shows that strain was evenly distributed when the count number was less than 40. At count number 80, the strains exhibited a slight change and showed a little bit uneven distribution, this could be attributed to the increased second order effect of axial load. When the count number reached 109, strain showed a peak-valley pattern distribution along the -30^{o} line and this indicated that the local buckling occurred near this line instead of the zero degree line. The peak was generated by the bulging of wrinkle head, where the compressive strain was decreased, and the valley was produced by sinking of wrinkle foot, where the compressive strain was increased. When the count number accumulated to 150, the wrinkle extended to as far as the 45^{o} line because all of them shown the peak-valley pattern distribution. When the count number was greater than 150, only the strain within the wrinkle region varied, and this indicated that the strain was totally localized.

ON CROSS SECTION

By analyzing the strain distribution on a cross section, whether the wrinkle spread to this cross section can be identified. In addition, the plane section remains plane assumption can be verified if there is no local buckling. In this test, the strain distributions on three cross sections were measured and typical results are presented in Figure 4.13. For the two cross sections above and below the middle of pipe, this figure clearly shows that the plane section remains plane. For the middle cross section, the linear distribution was disrupted on the concave side when the count number reached 100. This indicated local buckling appeared. However, for the other locations, the linear distribution still worked. Therefore, it can be concluded that the wrinkled section and unwrinkled sections work independently, and the plane section assumption is valid only for the unwrinkled section.

HOOP STRAINS

When the pipe is pressured, it is in a bi-axial stress state. Nine hoop strain gauges were evenly placed on three cross sections to catch the monotonic and cyclic

behaviours of pipe in the hoop direction. The results are shown in Figure 4.14 and presented in a spectrum form. Because the hoop strain was mainly caused by water pressure, the spectra did not cover the 2nd cyclic period during which the pipe was empty. The concave side had the maximum tensile hoop strain because of the superimposed effect of internal pressure and bending moment, the convex side held the minimum hoop strain because of the counterbalance effect of internal pressure on that of bending moment, and the neutral axis had the medium hoop strain.

4.3.1.7 GLOBAL BEHAVIOUR VS. LOCAL BEHAVIOUR

When the wrinkle is fully developed, the deformation will be localized at the wrinkled region, but no literature shows to what extent this localization can go. In the following, two types of deformation will be investigated to show the relation between global behaviour and local behaviour.

RELATIVE AXIAL DISPLACEMENT

Figure 4.15a shows the local RAD between punch marks ‘4’ and ‘7’ measured by a caliper, and for discussion convenience, the area between punch marks ‘4’ and ‘7’ is called the wrinkle area. The measurement was taken only after the occurrence of wrinkle (count number = 189), and both of global RAD and local RAD are based on this initial state. They are the increments of RAD from this defined initial state. It can be seen that the measurement data can be best-fitted by two straight lines for each cyclic loading period respectively. The slope of the best-fit line indicates the degree of the global RAD localization. The smaller the slope is, the less the localization will be. On the contrary, the larger the slope is, the more the localization will be; specifically, the global RAD is totally localized when the slope reaches the unit. During the first cyclic loading period, the slope is 0.940 and this indicates 94.0% of global RAD was localized. During the second cyclic loading period, the slope dropped to 0.792 and this means 79.2% of global RAD was localized.

Figure 4.15b shows the relation between the global RAD and the local RAD measured by LVDTs during the cyclic loading stage. During the first cyclic loading stage, the measurement results are squeezed into a narrow band, and they can be regressed approximately by a straight line. The slope of this line is around unity, and this indicates the global RAD is totally localized. During the second cyclic loading stage, the measurement results can also be regressed by a straight line, and the slope of this line is about 0.800. Similarly, this indicates about 80.0% of global RAD is localized in the wrinkle area.

Comparing Figure 4.15a with Figure 4.15b, it can be found that both measurement methods give the very close results.

GLOBAL CURVATURE VS. LOCAL CURVATURE

The curvature is a measure of curving: the bigger the curvature is, the shaper the curving will be. According to the loose definition that was made in Section 4.2.2.1, the curvature is related to both slope angle change and gauge length. If the gauge length is the length of the entire curve, the so-obtained curvature is called global curvature; and if the gauge length is the length of a segment of this curve, the so-obtained curvature is called local curvature. The following discussion will abide by this broad definition.

For a straight beam under the condition of pure bending, if there is no local buckling and global buckling, the local curvature at everywhere is the same as the global curvature. In this case, it can be said that the curvature is independent of gauge length. If a wrinkle occurs in the beam, the local curvature away from the wrinkle will decrease, and the local curvature over the wrinkle will increase. This phenomenon can be termed as ‘curvature localization’.

For this test, the above concepts can be used to approximately find when and locate where the wrinkle formed. Figure 4.16 shows the relations between global curvature and different local curvatures, where the global curvature was obtained from Equation (4.6) and the local curvatures were calculated according to the readings of RVDTs and their corresponding gauge lengths.

Figure 4.16a shows the curvatures of pipe segment ‘1−3’ and ‘3−5’, which are halves of the pipe. Their curvatures are almost coincident with the global curvature at first, but deviate from the global curvature after a specific point. Specifically, the curvature of segment ‘1−3’ is less than the global curvature and that of segment ‘3−5’ is greater than the global curvature. Therefore, it can be concluded that the wrinkle formed in pipe segment ‘3−5’. Figure 4.16b shows the curvatures over smaller pipe segments of ‘3−4’ and ‘4−5’, it can be easily identified that the wrinkle was on pipe segment ‘3−4’ based on the above discussion. Generally, the onset of wrinkle can be determined from the deviation point of global curvature and a local curvature over a proper gauge length. But the RVDT ‘R3’ did not work well at first, so the curvature of segment ‘3−4’ deviated from the origin. Based on this, the onset of the wrinkle will be taken as the deviation point of the global curvature and local curvature curve of segment ‘4−5’. It can be read from this figure that wrinkle formed when the global curvature was about 0.04 1/m.

4.3.2 SPECIMEN LCF20N1

For this pipe, it was similar to the 16 inch pipe in many aspects, so the following introduction and discussion will focus only on the differences.

4.3.2.1 SPECTRA OF SOME KEY VARIABLES

The spectra of some key variables during the two loading stages are shown in Figures 4.17 and 4.18, respectively.

MONOTONIC LOADING STAGE

The loading procedure was the same as the 16 inch pipe, and the only difference was the controlled variables. For the 20 inch pipe, the controlled water pressure was 5.00 MPa, the desired average rotation of moment arms was 2.5°, the designed maximum MTS stroke was 45 mm, and the governed NNAL was 1163 kN during the monotonic bending stage, which corresponded to the axial load in the pipe wall caused by a temperature change of 45°C.

CYCLIC LOADING STAGE

Same as the 16 inch pipe, the cyclic loading stage consisted of the 1st and the 2nd cyclic loading periods, but there were three major differences.

During the 1st cyclic loading period, besides the maximum stroke, which was controlled by the MTS machine, the minimum stroke was also controlled to make the MTS stroke range constant. The minimum stroke was acquired by the water pressure, so the peak water pressure was not constant anymore. The water pressure decreased as the pipe wall was gradually damaged. During the 2nd cyclic loading period, the loading was controlled to make both the maximum RAD of wrinkle and its minimum counterpart constant. The jack force decreased in this cyclic loading period as the test progressed, and this was also attributed to the progressive damage of pipe wall.

4.3.2.2 MOMENT VS. CURVATURE

The relation between the bending moment at top pivot and the global curvature is shown in Figure 4.19. Compared with the 16 inch pipe, there are some differences. First, there was no plateau and this indicated the pipe was not fully plasticized. Second, the hysteresis loops overlapped to form a single very dark and thick loop. This can be attributed to two reasons: one is that the decreased of loading capacity of pipe as a whole was not so significant as the strip specimens, because the cracked wrinkle was a small part of the whole cross section; the other is that the cyclic loading was well controlled during the 2nd cyclic loading period. Third, the vertical line was much thinner than that of 16 inch pipe that indicated the 1st cyclic loading period was better controlled.

4.3.2.3 PIVOT AXIAL LOAD VS. RELATIVE AXIAL DISPLACEMENT BETWEEN PIVOTS

The relation between the pivot axial load and RAD between pivots during the whole loading stage is shown in Figure 4.20. Compared with Figure 4.9, it can be seen that the behaviour was similar during the 1st cyclic loading period except that the drop of load after point ‘C’ was quicker in Figure 4.20. But during the 2nd

cyclic loading period, this figure does not exhibit the drifting of small hysteresis loops as Figure 4.9 does.

4.3.2.4 WATER PRESSURE VS. RELATIVE AXIAL DISPLACEMENT BETWEEN PIVOTS

This relation is shown in Figure 4.21. The characteristics are very similar to those of Figure 4.10.

4.3.2.5 INTERACTION DIAGRAM

The interaction diagram is shown in Figure 4.22. According to this diagram, only the concave side of top end cross section of pipe was yielded and the convex side was still elastic during the monotonic bending stage. And the entire top end cross section was elastic during the monotonic compression stage. This can be confirmed by the strain distribution along the pipe axial direction, which will be discussed in the next section.

4.3.2.6 STRAIN BEHAVIOUR

ALONG AXIAL DIRECTION

Figure 4.23 shows the strain distributions on the concave side, the convex side and the north and south sides. Three main observations can be made from the figure: first, the sharp variation of strain at the location of 646 mm above the bottom indicates that the wrinkle formed around this location; second, the much more significant variation of strain in the wrinkle region than that in other regions indicates the strain was localized; third, the faster increase of strain on the north side than that on the south side indicates that the wrinkle developed asymmetrically from the concave side and much quicker on the north side. In addition, the strain distribution on convex side exhibits that the secondary plasticity, i.e. tensile yielding on convex side, did not occur on the top end cross section, this confirms the observation drawn from interaction diagram.

HOOP STRAIN

Hoop strains at 12 points on three cross sections were recorded and the results are shown in Figures 4.24. Because the gauge ‘SHN2S’ did not work, Figure 4.24a only shows the results of three gauges. It can be seen that the three gauges on the lower cross section went out of range after a specific moment, and this indicated that the wrinkle was near these gauges. In addition, higher hoop strain on the north side can draw the conclusion that wrinkle grew more fast toward the north side than toward the south side.

4.3.2.7 GLOBAL BEHAVIOUR VS. LOCAL BEHAVIOUR

GLOBAL RELATIVE AXIAL DISPLACEMENT VS. LOCAL RELATIVE AXIAL DISPLACEMENT

The relation between the global RAD and the local RAD of wrinkle is shown in Figure 4.25. By best fitting the measurement data from LVDT and from caliper respectively, it can be seen that the slopes are very close to unit. This demonstrates again that the RAD was totally localized during the cyclic loading stage.

GLOBAL CURVATURE VS. LOCALCURVATURE

Figure 4.26 presents the relation between global curvature and local curvature. Figure 4.26a shows that the local curvature of pipe segment ‘1−3’ is above the global curvature, and the local curvature of pipe segment ‘3−5’ is below the global curvature. Therefore, it can be concluded that the wrinkle formed on pipe segment ‘1−3’. In addition, the local curvatures deviate from the global curvature when the global curvature is about 0.0205 1/m, which indicates the onset of wrinkling. Figure 4.26b shows that the local curvature of pipe segment ‘1−2’ is a little bigger than that of segment ‘2−3’ at first, but later it turns to the contrary. This phenomenon indicates that section ‘2’ was on wrinkle head and more wrinkle was on the segment ‘1−2’ than segment ‘2−3’. This conclusion is confirmed by the test observation, and actually the wrinkle crest was right under the cross section ‘2’. In addition, it can also be concluded that the wrinkle formed

around a global curvature of 0.0205 1/m. Therefore, by monitoring the variation of curvature can identify when and where the wrinkle occurs.

4.4 FAILURE MECHANISM

4.4.1 EXPERIMENTAL OBSERVATION

4.4.1.1 SPECIMEN LCF16N1

During the first cyclic loading period, i.e. cyclic axial deformation, the seam weld was firstly fractured (see Figure 4.27). By closer inspection, it was found that there were three cracks (see Figure 4.28): one penetration crack along the circumference direction and two surface cracks just besides the seam weld along the axial direction. Although the wrinkle at the seam weld was much smoother than that on the concave side, two detrimental factors led to this failure. Firstly, the weld height was much bigger than the wall thickness of pipe (see Figure 4.29), and this greatly counterbalanced the benign effect of smooth wrinkle. Secondly, the wrinkle at seam weld had a smaller loading eccentricity than that on the concave side, so it experienced more cyclic deformation under the loading of cyclic axial deformation, which applied the same loading to everywhere along the wrinkle.

During the second loading period, a dimple was observed on the wrinkle head of concave side and many cracks were found on the outside surfaces of wrinkle feet (see Figure 4.30). A dimple indicated that the wall was heavily cracked from the inside surface. In addition, the formation of multi-cracks on outside surface of wrinkle feet also verified the above conclusion.

Figure 4.31 shows that the wrinkle on concave side was totally fractured. After the test was completed, the whole wrinkle was cut into small pieces to check the extent of the damage. A montage of these pieces is shown in Figure 4.32. From this figure, it can be seen that multi-cracks formed everywhere on the inside surface of wrinkle.

4.4.1.2 SPECIMEN LCF20N1

The cracks are shown in Figures 4.33 to 4.35. The similar observations can be made for this specimen as those for specimen LCF16N1, so no more details will be given at here.

4.4.2 MACROSCOPIC EXAMINATION

4.4.2.1 SEAM WELD

For the seam weld of specimen LCF16N1, its fracture surface (see Figure 4.36) can be divided into four zones: two crack propagation zones and two rupture zones. The cracks were initiated from the surface and propagated from surface to interior, but the cracks on the inside surface were not on the same cross section with those on the outside surface. As for the crack propagation zone from outside surface, it was so small that it could be neglected, so the seam weld was penetrated mainly by the crack propagation from inside surface. Furthermore, some striations can be clearly found on the fracture surface. The space between two adjacent striations was much larger in the exterior portion than that in the interior portion. This indicates that more damage happened during the first few cycles. As the crack propagated to the outside surface, the thin uncracked wall was finally fractured by tearing, so the final rupture zone exhibited a shape of shear lip. As for the light rupture zone, it was produced by bending the uncracked portions of cross section of seam weld when making the samples for SEM.

As for the seam weld of specimen LCF20N1, again there are four zones on the fracture surface (see Figure 4.37). The zone generated during the 2^{nd} cyclic loading period was not of interest here because the seam weld was fractured by the 1^{st} cyclic loading. The cracks also initiated from different locations on surface and propagated from surface to interior. Compared with Figure 4.36, it can be seen that more propagation zone from outside surface although it was still small compared with its counterpart from inside surface. As cracks propagated, they met each other and then the wall was penetrated and water sprayed out of the pipe. No obvious final rupture zone was observed. Correspondingly, no shear lips

were formed in this specimen. The main reason was that the outside cracks were formed at the same cross section as the inside cracks.

4.4.4.2 WRINKLE ON CONCAVE SIDE

SPECIMEN LCF16N1

The picture of fracture surface is shown in Figure 4.38. The cracks were initiated from many origins on the surface and propagated from surface to interior. Because these cracks were not on the same cross section, tearing cracks formed nearly along the normal direction of pipe surface when they approached each other. In addition, the outside crack propagation zone was very small and the fracture of wrinkle was mainly attributed to the crack propagation from the inside surface. The heavily rusted portion of inside propagation zone was produced by the 1^{st} cyclic loading.

SPECIMEN LCF20N1

The picture of fracture surface is shown in Figure 4.39 and the similar discussion can be conducted as those made for specimen LCF16N1, so no further details will be given here.

4.4.3 MICROSCOPIC EXAMINATION

Only fracture surfaces of specimen LCF20N1 were examined here.

4.4.3.1 SEAM WELD

Figure 4.40.1 shows the inside portion of the seam weld and it contains four pictures. From them, it can be seen that the surface was damaged and no striations were resolved by increasing the magnification. However, those pictures show some secondary cracks on the surface, and moreover Figure 4.40.1d exhibits some corrosion products and pits on the surface. These corrosion products were caused by that the water corroded the cracked surface inside the pipe

Figure 4.40.2 gives the outside portion and it contains six pictures: the left half is the portion near the exterior and the right half is the middle portion. Figures

4.40.2a and 4.40.2b clearly show the magnified striations and some scattered corrosion pits (black spots) on the surface, and Figures 4.40.2c and 4.40.2d exhibit some secondary cracks around the corrosion pits. Figures 4.40.2e and 4.40.2f equiaxed dimples can be found; therefore, this portion failed in ductile mode. Figures 4.40.2g and 4.40.2h show the portion that caused by the 2^{nd} cyclic loading, because the surface was heavily damaged, no conclusion can be drawn from them.

4.4.3.2 WRINKLE ON CONCAVE SIDE

Figure 4.41.1 shows the outside portion of the fracture surface and it includes seven pictures. Figures 4.41.1a, 4.41.1b and 4.41.1e clearly exhibit striations, and Figures 4.41.1a to 4.41.1d show that finer striations are resolved as the magnification is increased. Also no dimples are found between striations. Figures 4.41.1e to 4.41.1g show what happened in final rupture zone, which could not be identified from macroscopic examination. The dimples show that this area was fractured in ductile mode.

Figure 4.41.2 gives the inside portion of fracture surface and it consists of five pictures. As the magnification is increased, no finer striations are resolved, but Figures 4.41.2d and 4.41.2e show secondary cracks around some scattered corrosion pits.

4.5 SUMMARY AND CONCLUSIONS

In the full-scale pipe test, two specimens were tested according to a complicated loading procedure that consisted of two loading stages, which were monotonic loading stage and cyclic loading stage, and three types of load, which were axial load, bending moment and water pressure.

Firstly, the loading procedure was presented by viewing the spectra of some key variables. Secondly, the relation between bending moment and global curvature, the relation between pivot axial load and RAD between pivots, and the global behaviours under monotonic loading and cyclic loading were investigated.

Moreover, by exploring the global behaviour and local behaviour, it was concluded that the global deformation was totally localized at the wrinkle region when the wrinkle was fully developed. In addition, the strain behaviour and interaction diagram were also discussed. Thirdly, by macroscopically examining the fracture surfaces, it was found that the cracks were initiated from multi-locations on the surfaces and then these cracks propagated from surfaces to interior. Further by microscopically examining the fracture surface, some corrosion products and pits were found on the fracture surface and some secondary cracks were observed forming around those corrosion products and pits. These corrosion products were caused by that the water corroded the cracked surface inside the pipe. Finally, the tests observed that the seam weld was firstly fractured. This observation indicated that the seam weld was more liable to failure under the condition of cyclic axial deformation.

Table 4.1: Geometries of pipe specimen

Specimen		Length mm	Outside diameter mm	Thickness mm
LCF16N1	Nominal	1550.0	406.4	11.9
	Actual	1546.5	406.3	12.4
LCF20N1	Nominal	1800.0	508.0	6.4
	Actual	1808.0	508.8	6.8

Table 4.2: Summary of instrumentation

Type	Quantity	Location	Purpose
Strain gauge	47/16" pipe 32/20" pipe	on pipe only	get axial strain distribution and hoop strain on selected cross sections
Demec point	14	on pipe only	as a back up of starin gauges
LVDT	8	on pipe only	measure the deflection or relative axial displacement over wrinkle
RVDT	7	on pipe, end plates and jack	measure the slope angle of pipe, inclination of jack and out-of-plane tilt of loading system
Cable transducer	7	between MTS head and floor	measure the relative axial displacement etc.

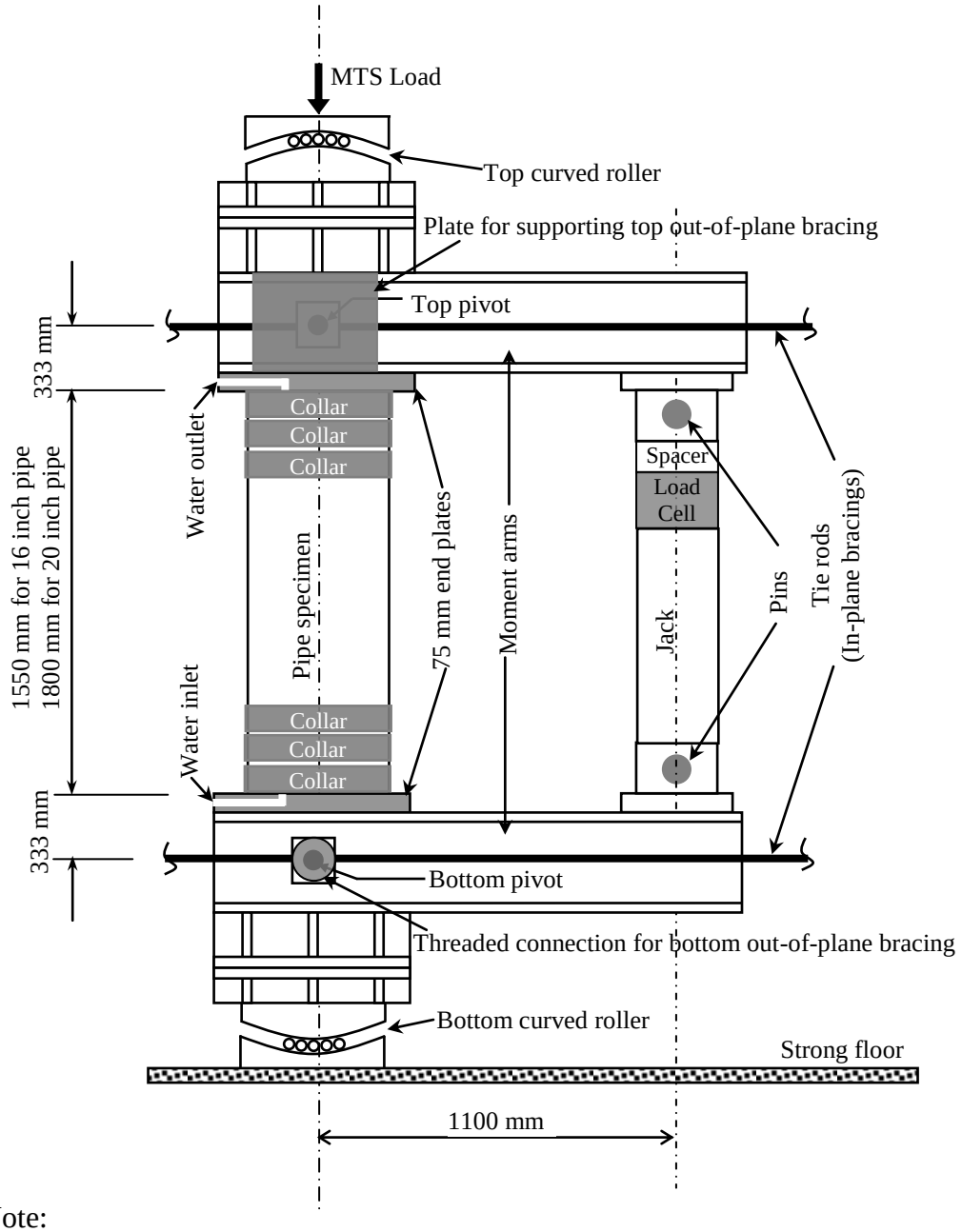

Note:

1. The loading capacity of the MTS machine is 6000 kN.
2. The loading capacity of jack is 1150 kN in push and 944 kN in pull, and its stroke capacity is 15" (381 mm).

Figure 4.1: Schematic illustration of test set-up

Front view

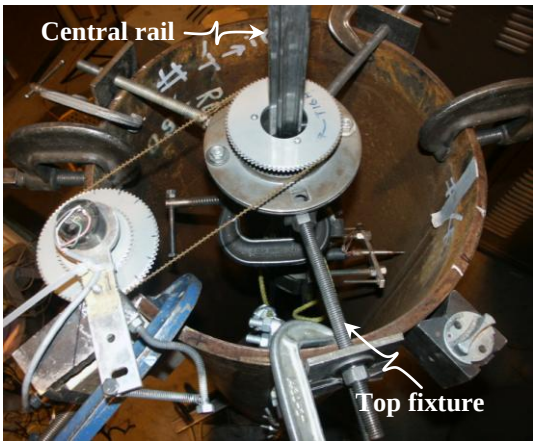

Top view

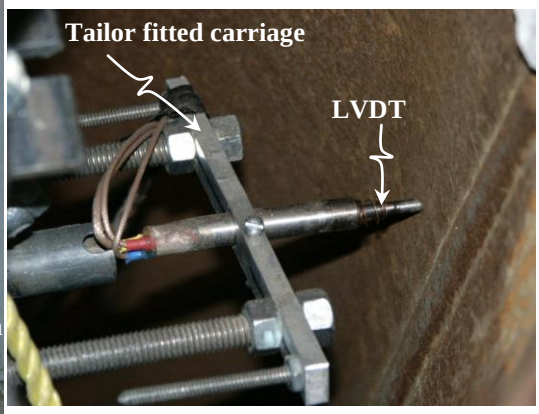

Closer view of LVDT

Figure 4.2: Imperfection measurement apparatus

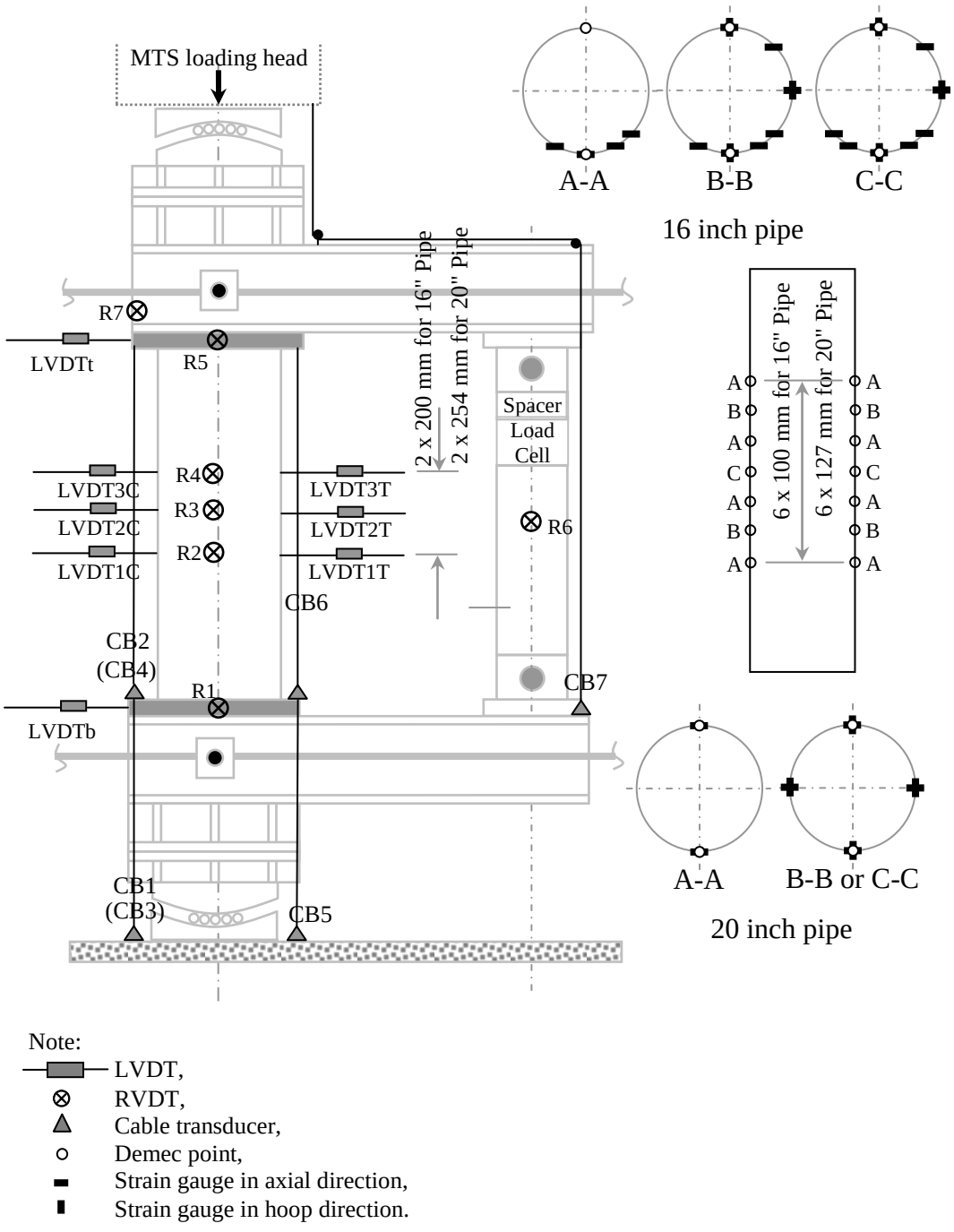

Figure 4.3: Layout of instrumentation

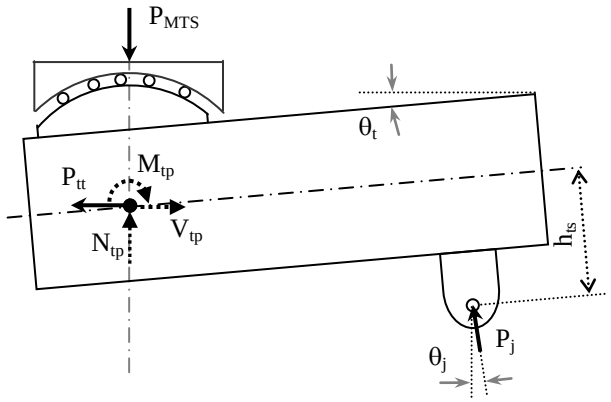

a) Free body diagram for top pivot

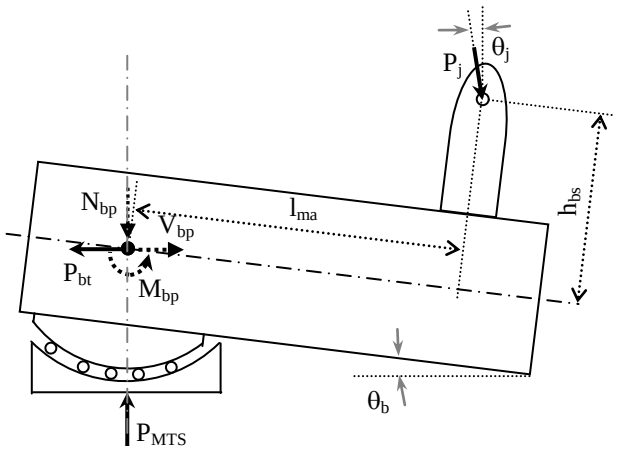

b) Free body diagram for bottom pivot

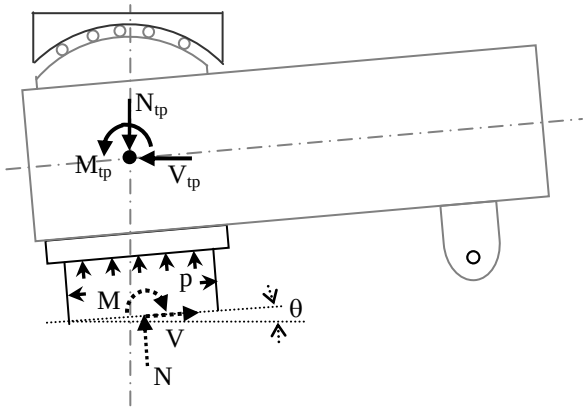

c) Free body diagram for an arbitrary cross section

Note:
Solid arrowed lines represent actual or equivalent external loads,
and dashed arrowed lines exhibit internal forces.

Figure 4.4: Free body diagrams for calculating internal forces

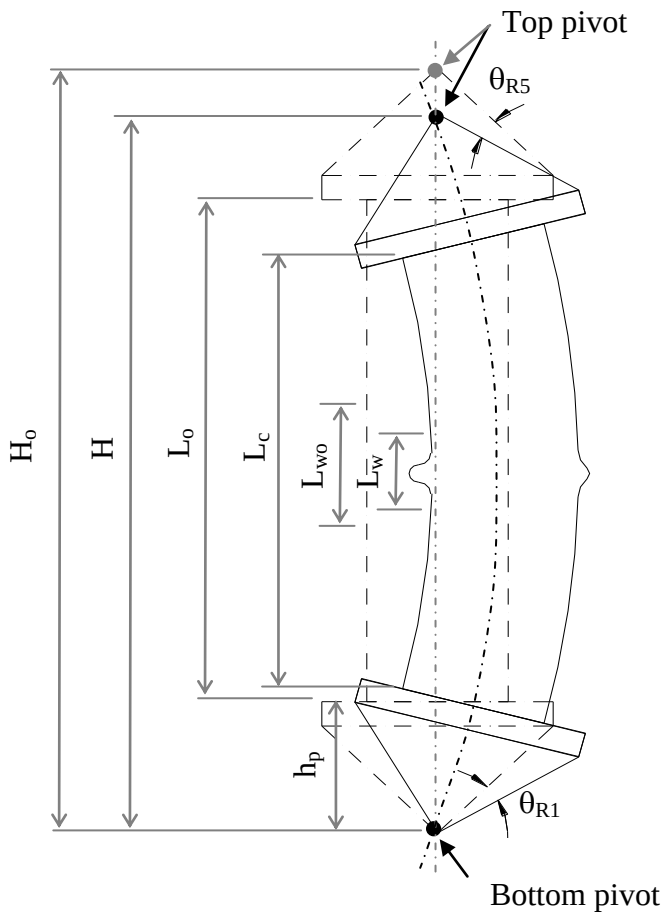

Note:
1 Dashed profile shows the undeformed shape and solid sketch indicates the deformed shape;
2 Moment arms and curved rollers are not shown in this figure;
3 h_p is the same for both ends and it keeps constant during loading.

Figure 4.5: Schematic illustration of deformation parameters

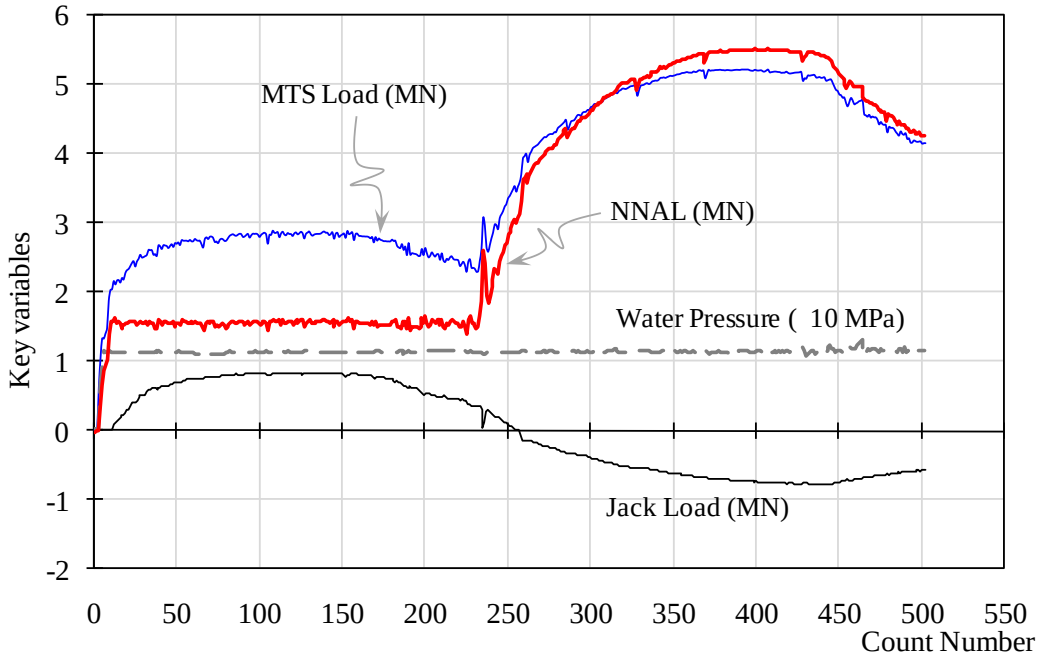

a) Spectra of loads

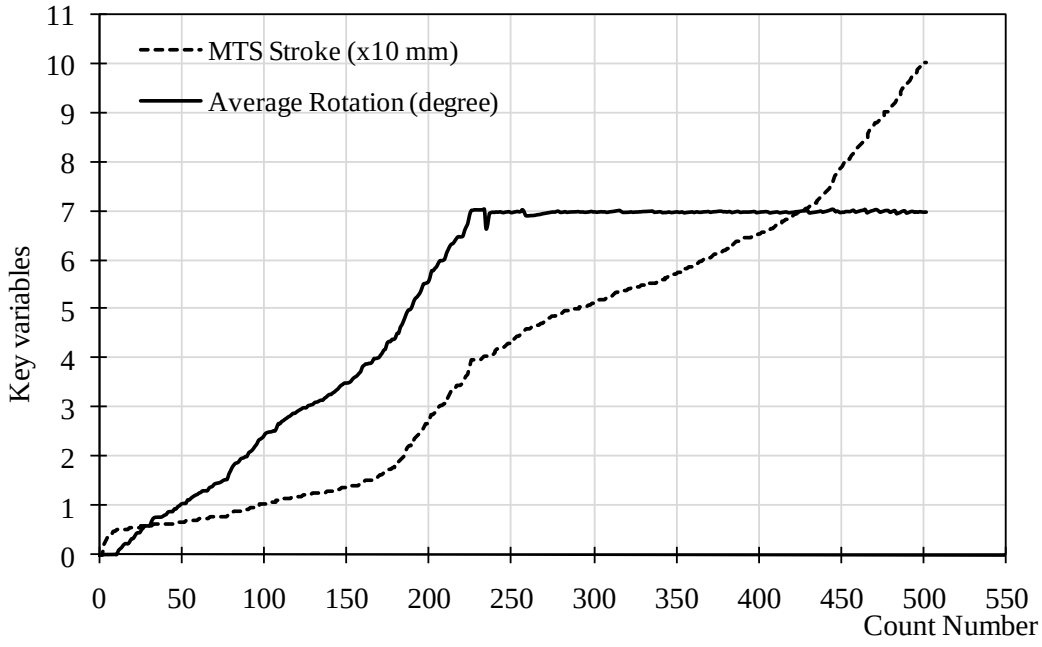

b) Spectra of MTS stroke and average rotaion

Figure 4.6: Spectra of some key variables in monotonic loading stage (LCF16N1)

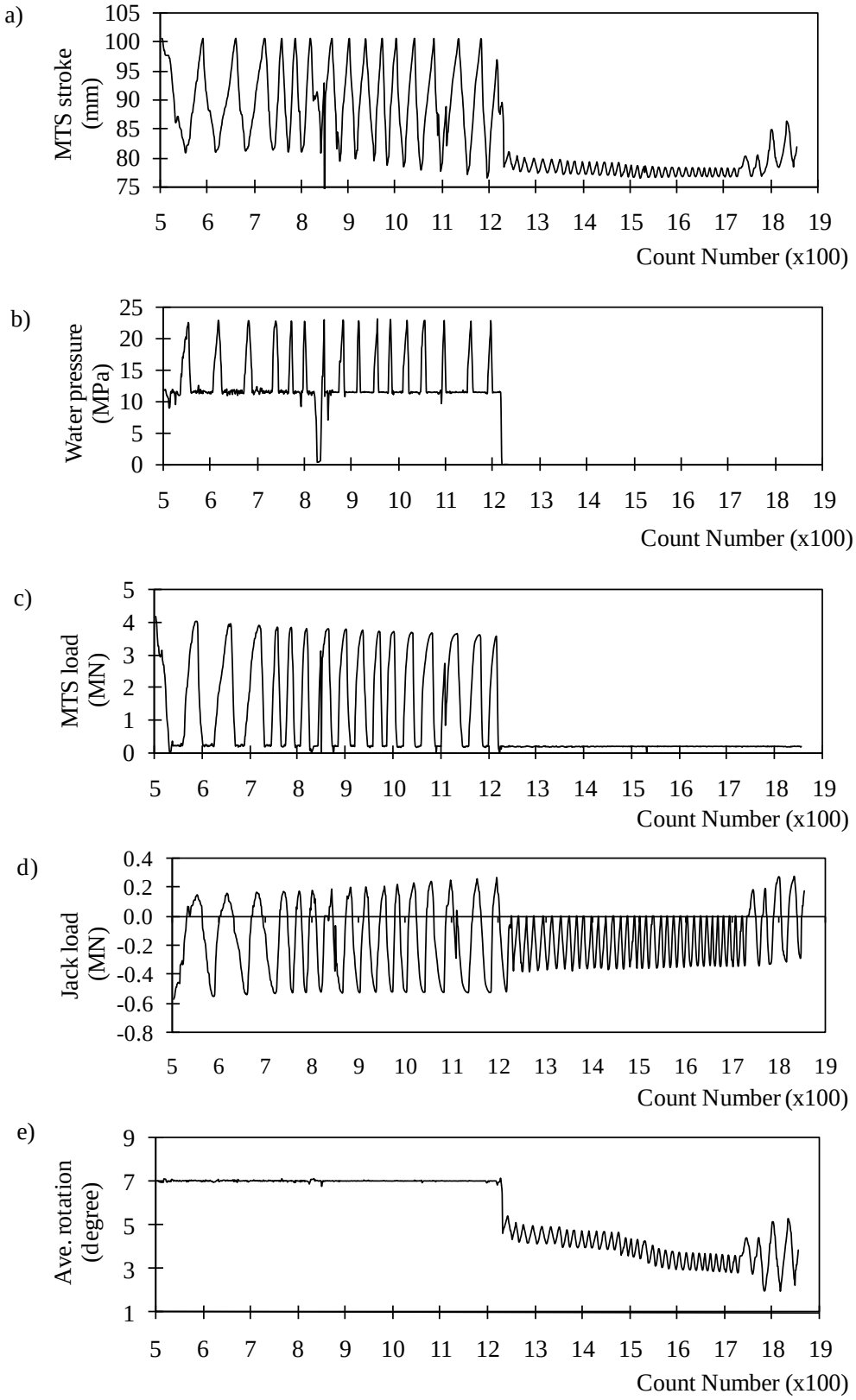

Figure 4.7: Spectra of some key variables in cyclic loading stage (LCF16N1)

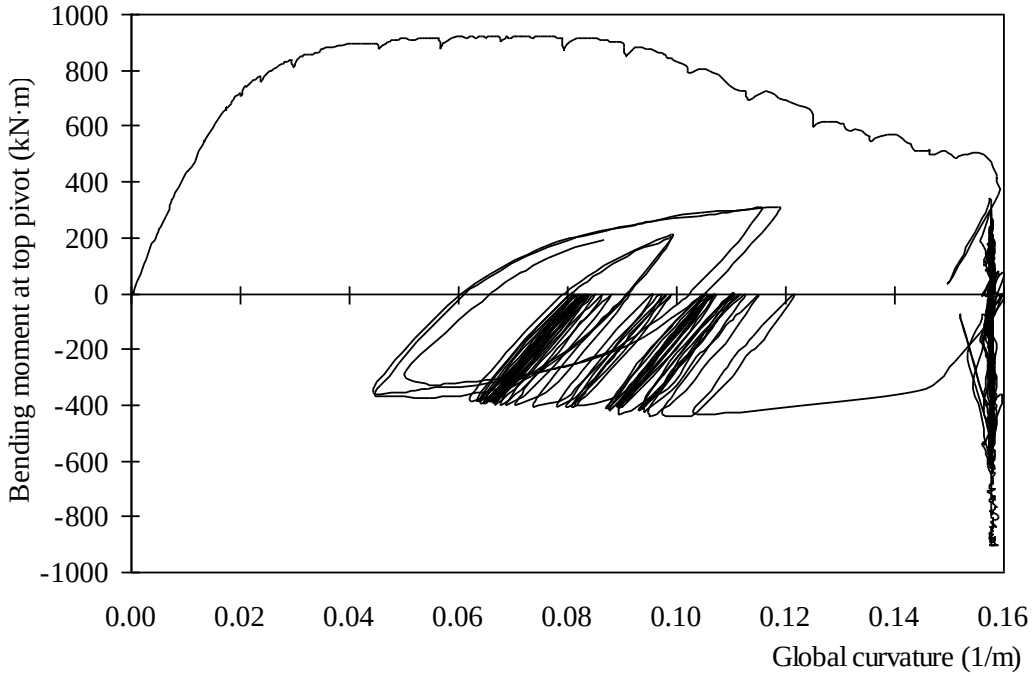

Figure 4.8: Moment – global curvature relations at top pivot (LCF16N1)

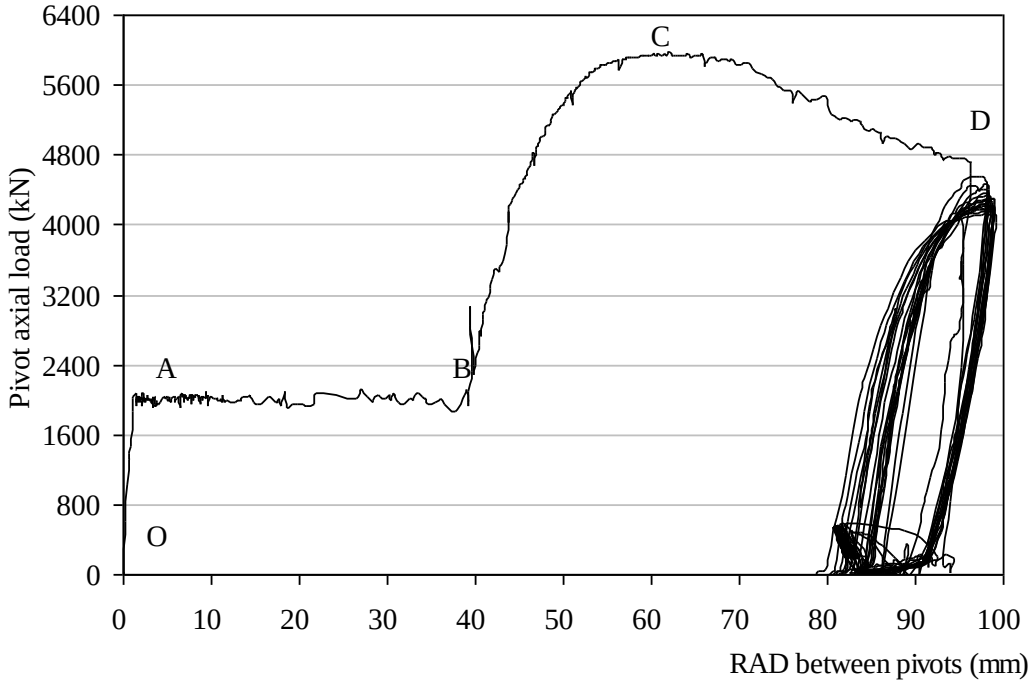

Figure 4.9: Pivot axial load vs. RAD between pivots (LCF16N1)

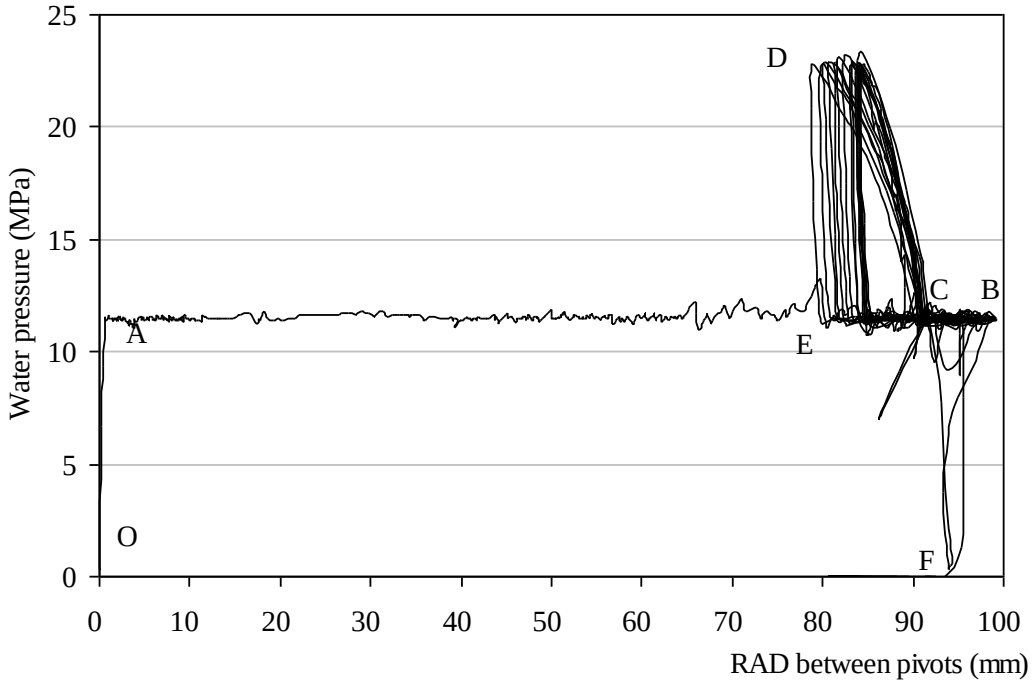

Figure 4.10: Water pressure vs. RAD between pivots (LCF16N1)

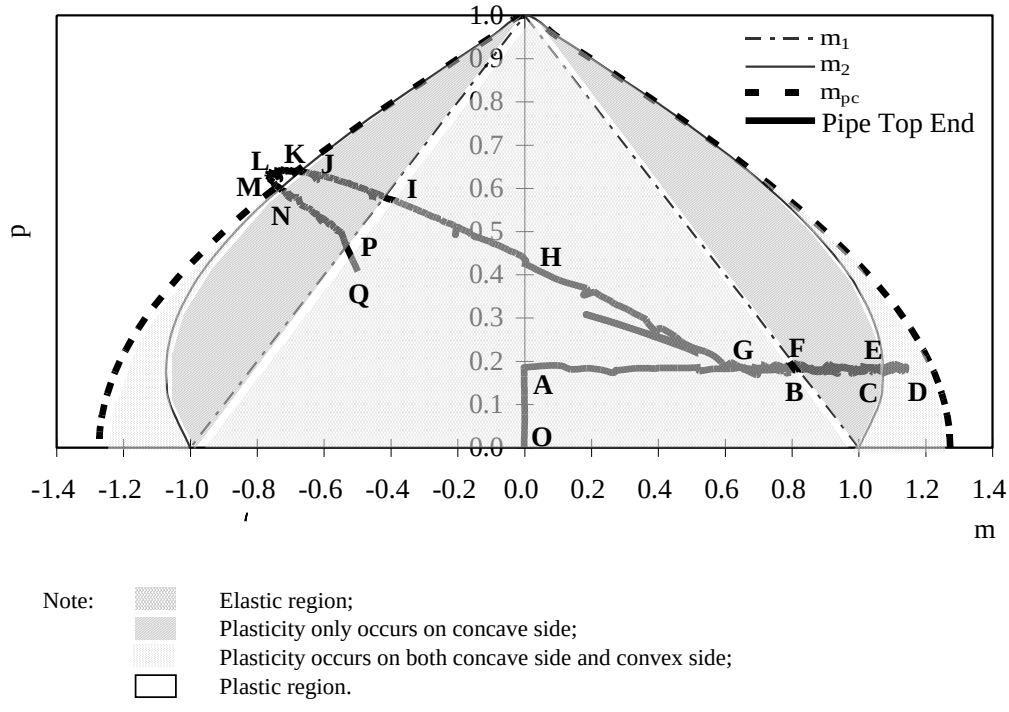

Note:
- Elastic region;
- Plasticity only occurs on concave side;
- Plasticity occurs on both concave side and convex side;
- Plastic region.

Figure 4.11: Interaction curves (LCF16N1)

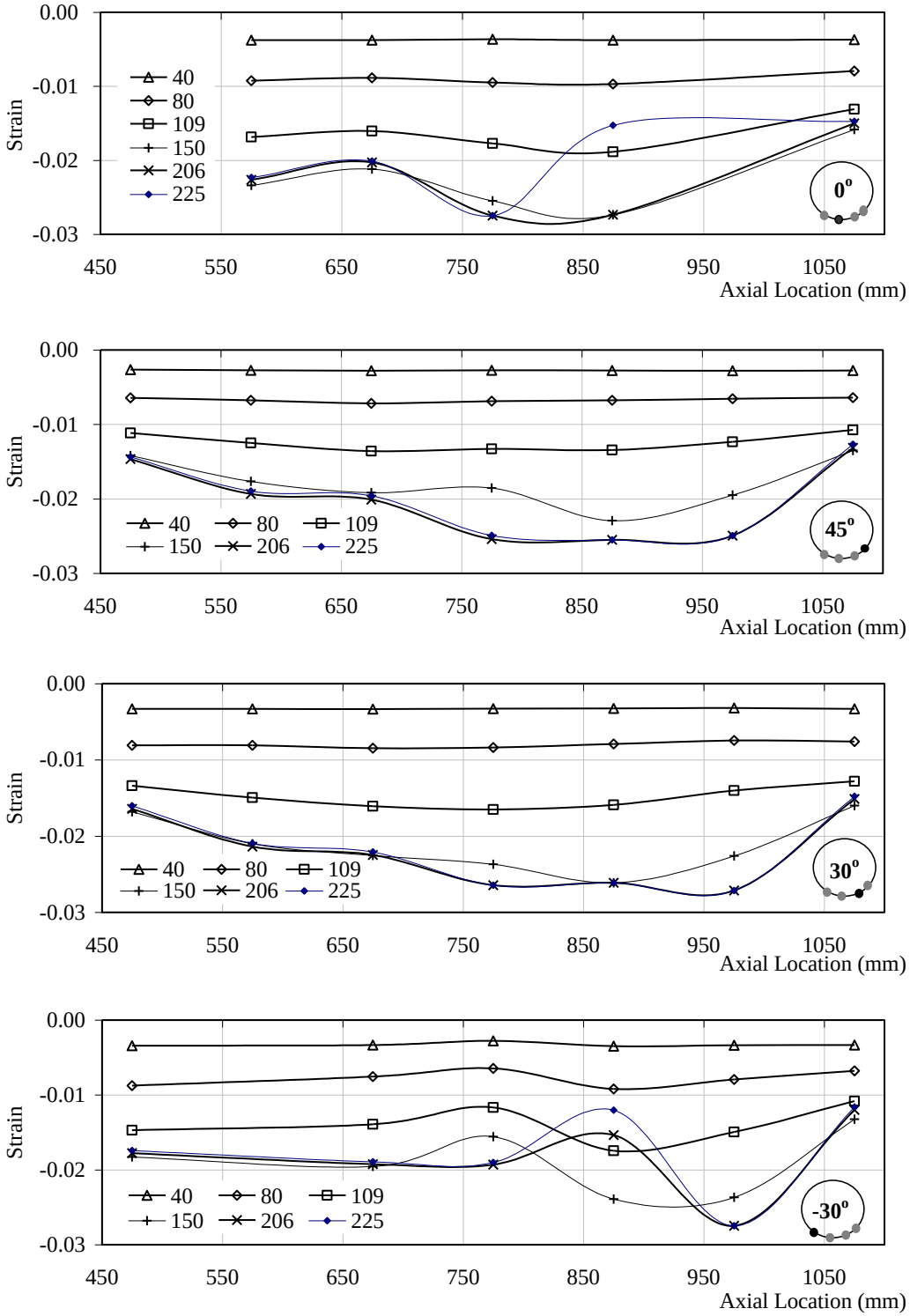

Note: The numbers in the legend are counter numbers.

Figure 4.12: Strain distribution along axial direction (LCF16N1)

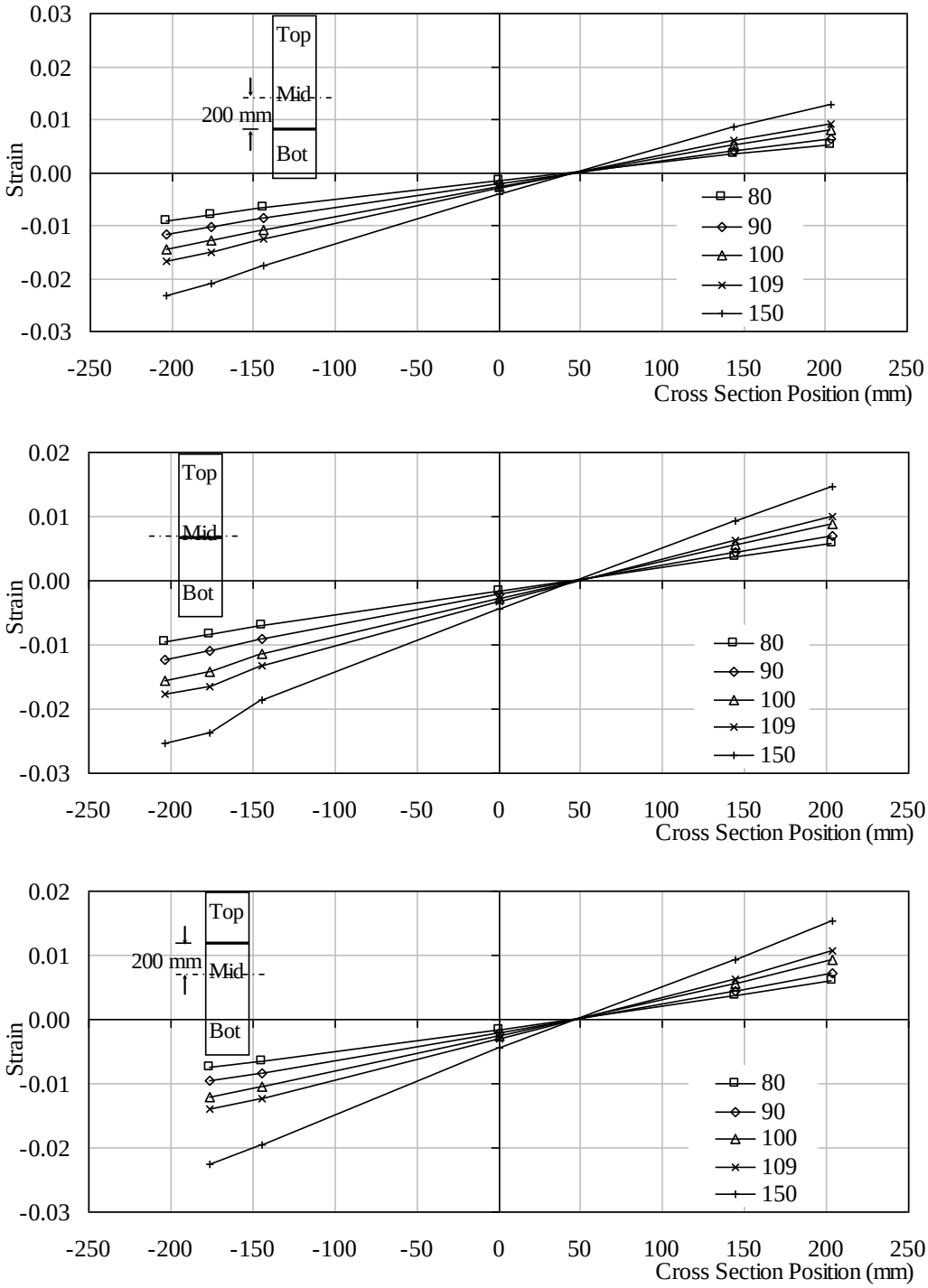

Note: The numbers in the legend are counter numbers.

Figure 4.13: Strain distributions on cross section (LCF16N1)

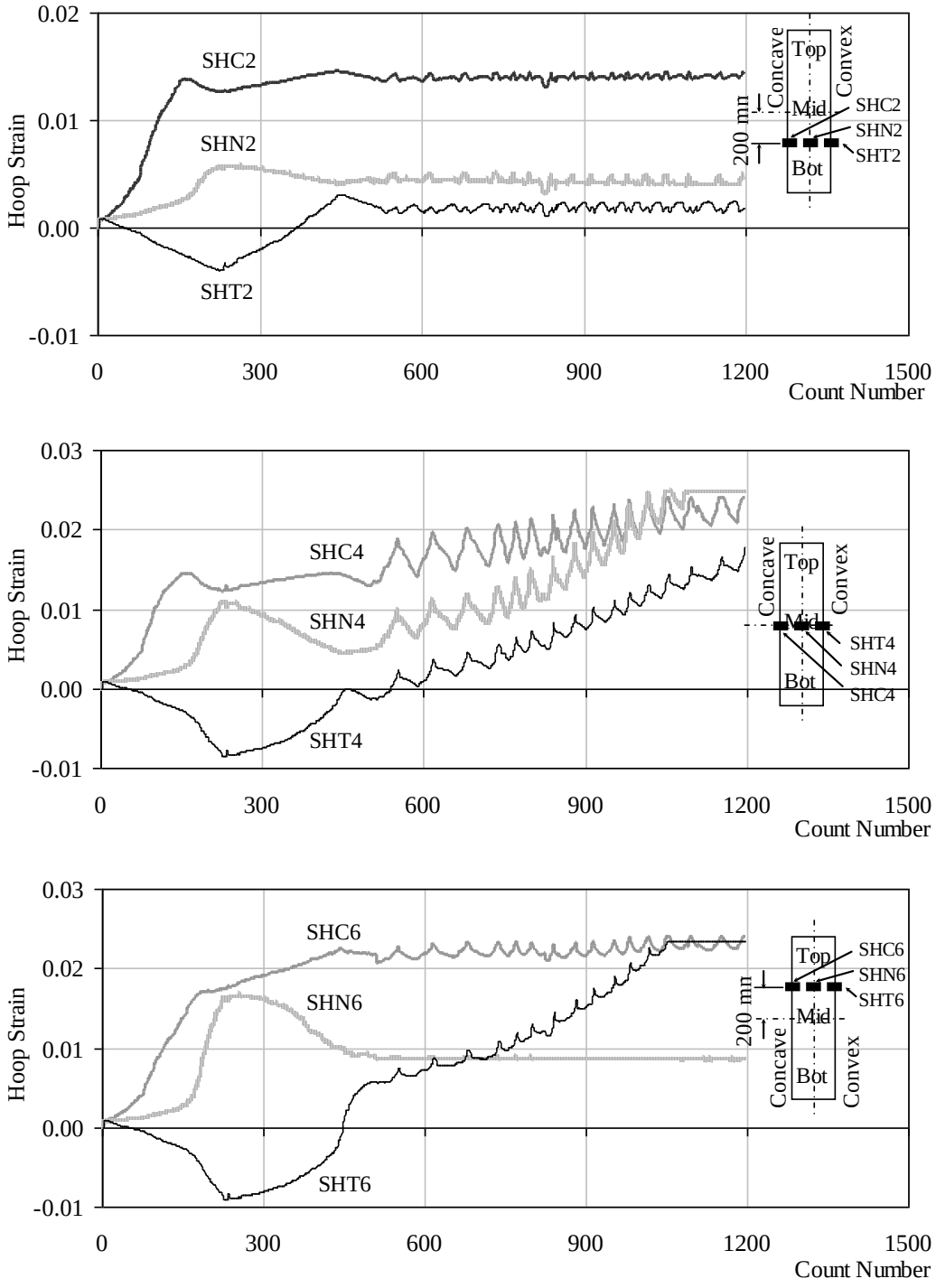

Figure 4.14: History of hoop strain (LCF16N1)

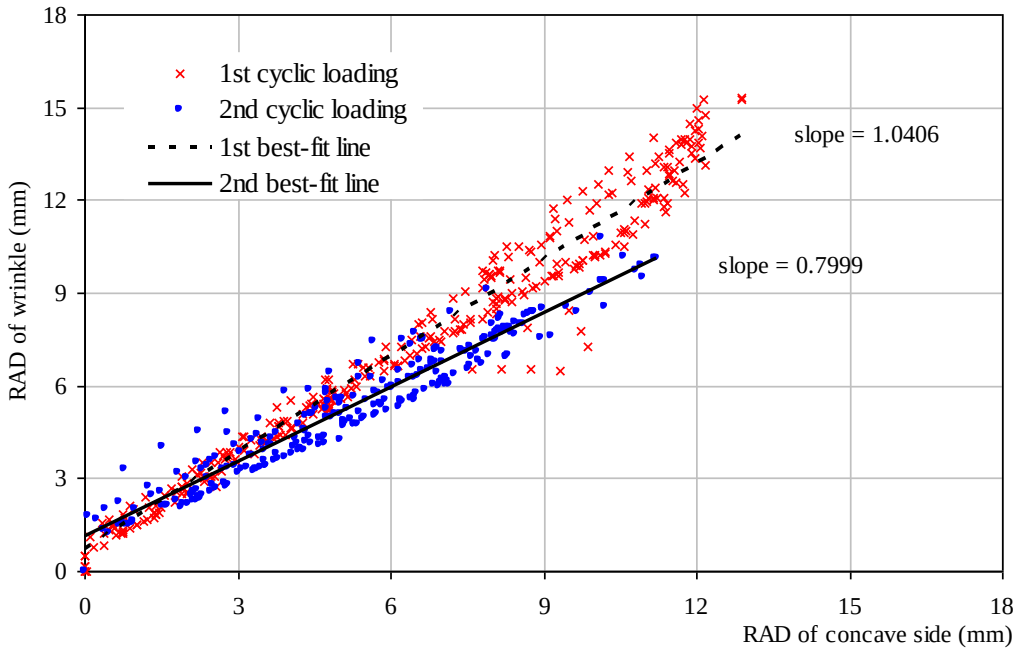

a) from caliper

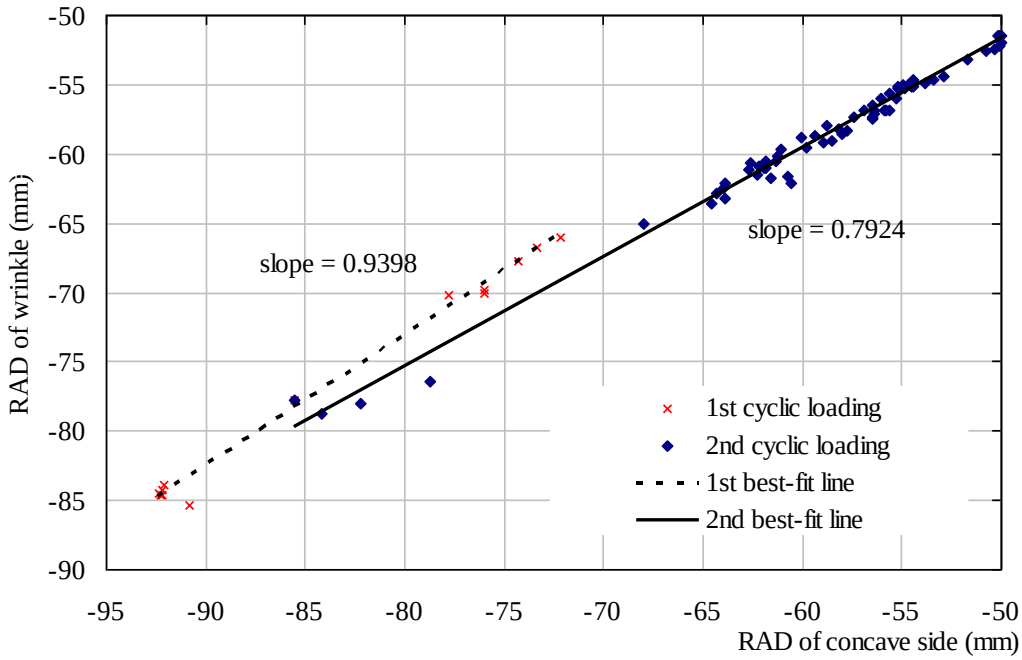

b) from LVDT

Figure 4.15: Local RAD vs. global RAD (LCF16N1)

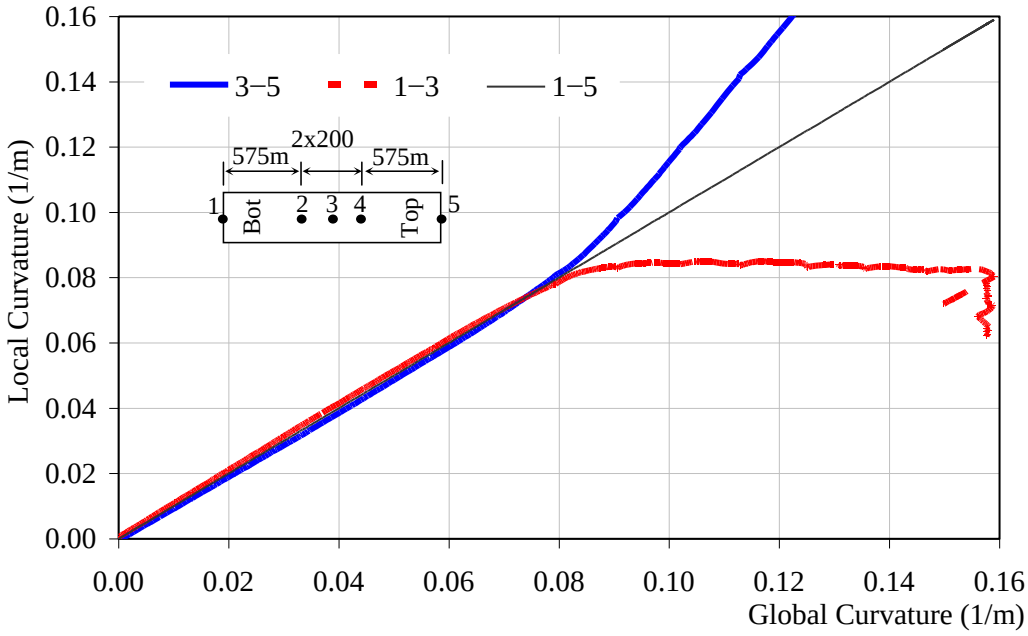

a) Curvature over segments ‘1–3’ and ‘3–5’

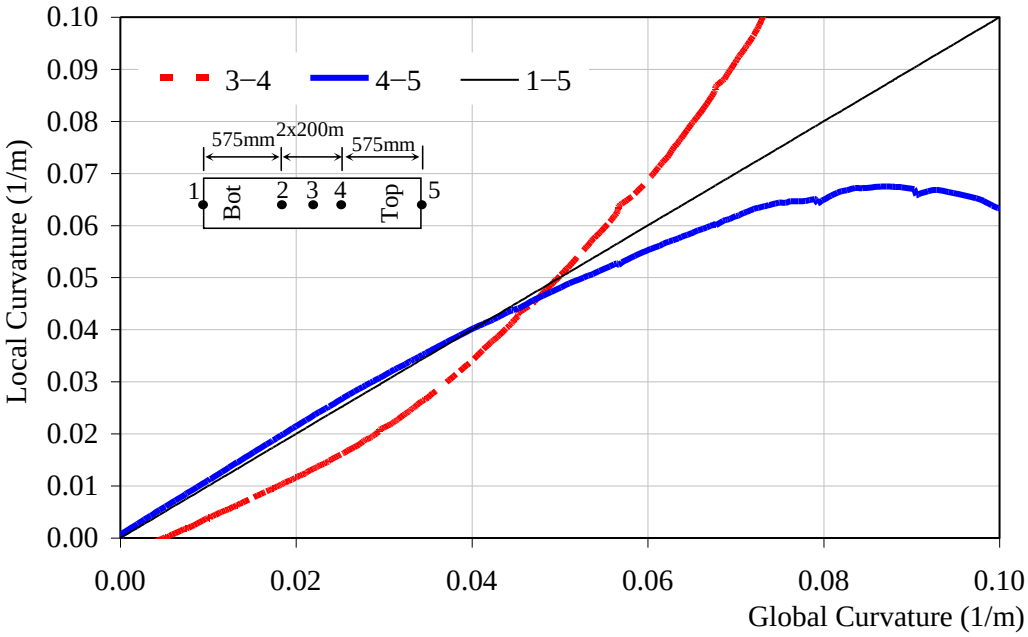

b) Curvature over segments ‘3–4’and ‘4–5’

Figure 4.16: Global curvature vs. local curvature (LCF16N1)

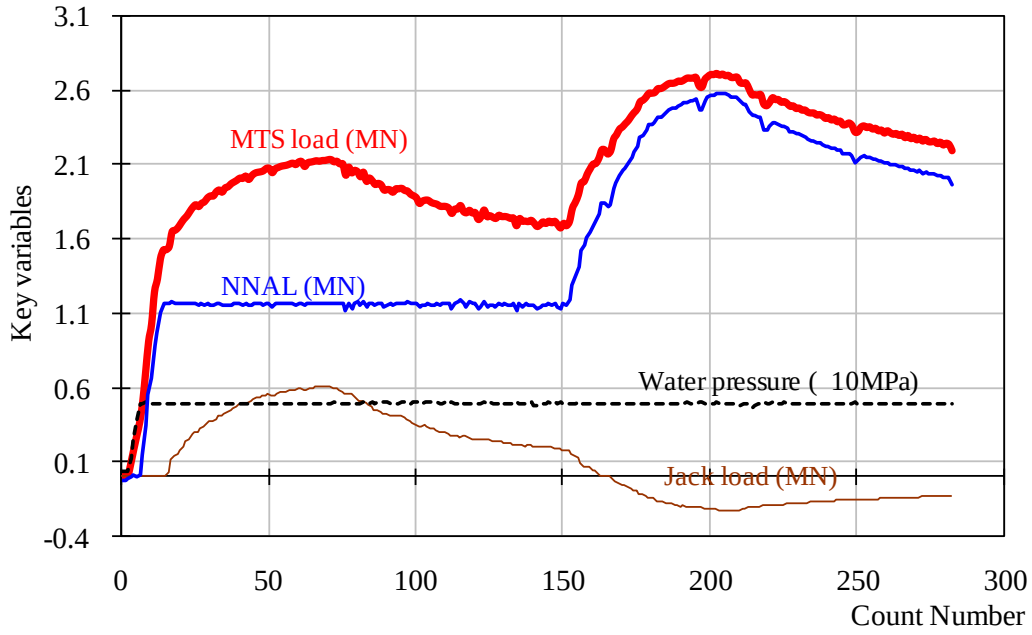

a) Spectra of load

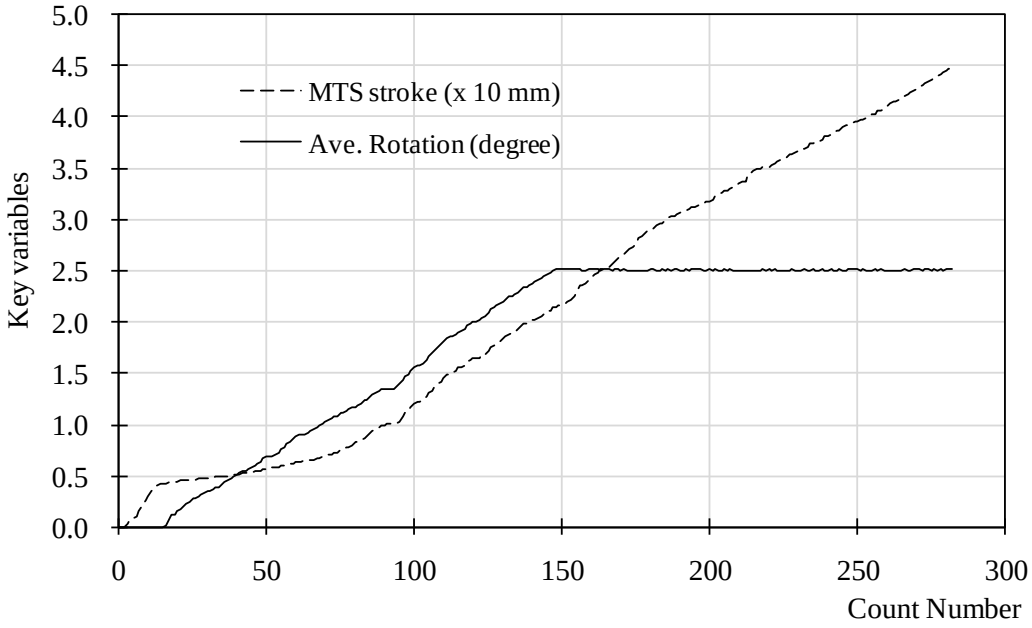

b) Spectra of stroke and rotation

Figure 4.17: Spectra of some key variables in monotonic loading stage (LCF20N1)

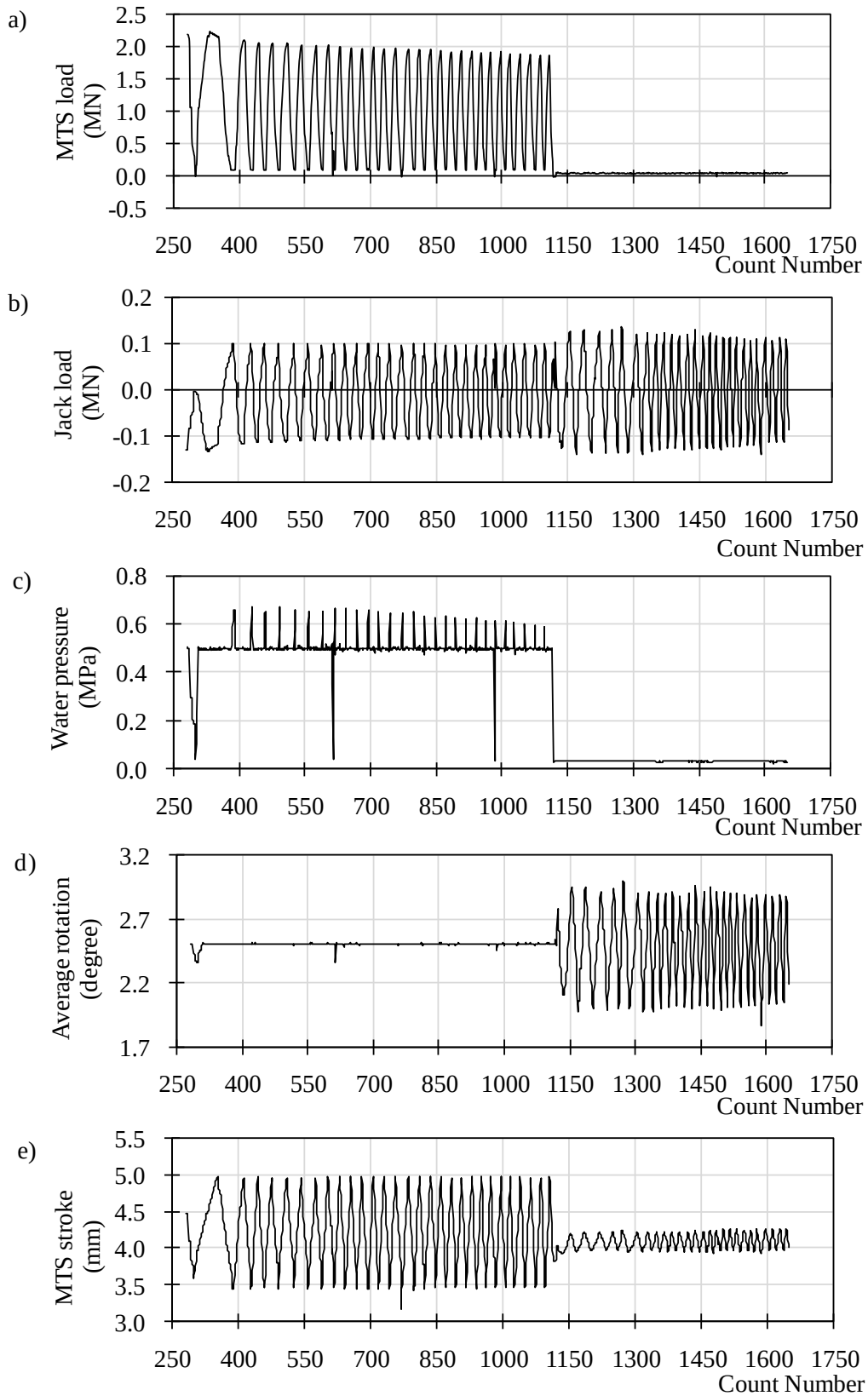

Figure 4.18: Spectra of some key variables in cyclic loading stage (LCF20N1)

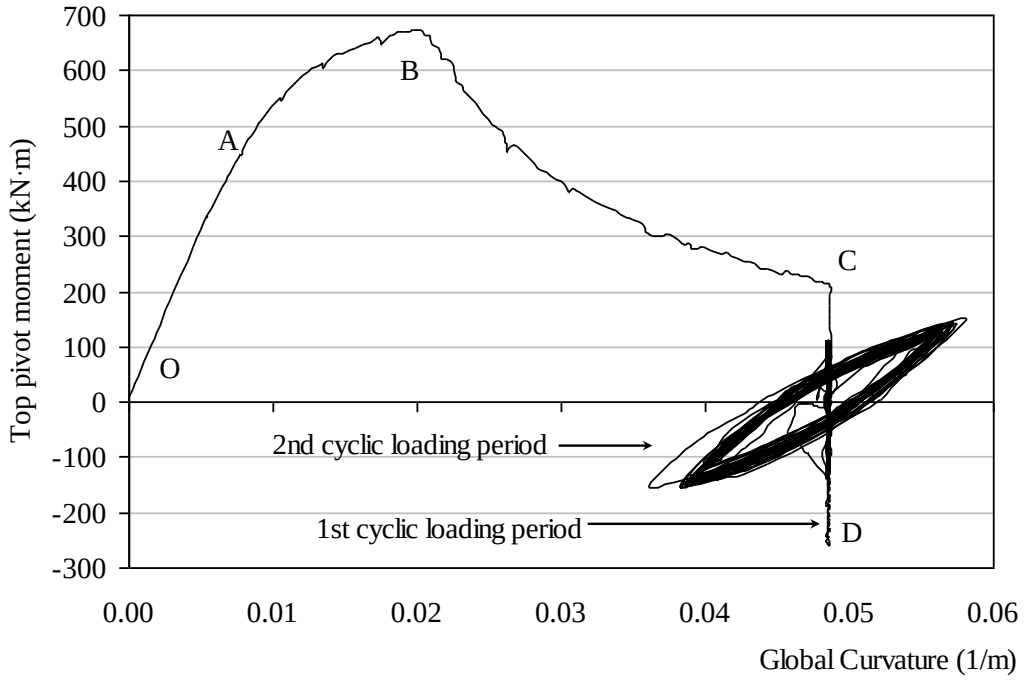

Figure 4.19: Top pivot moment vs. global curvature (LCF20N1)

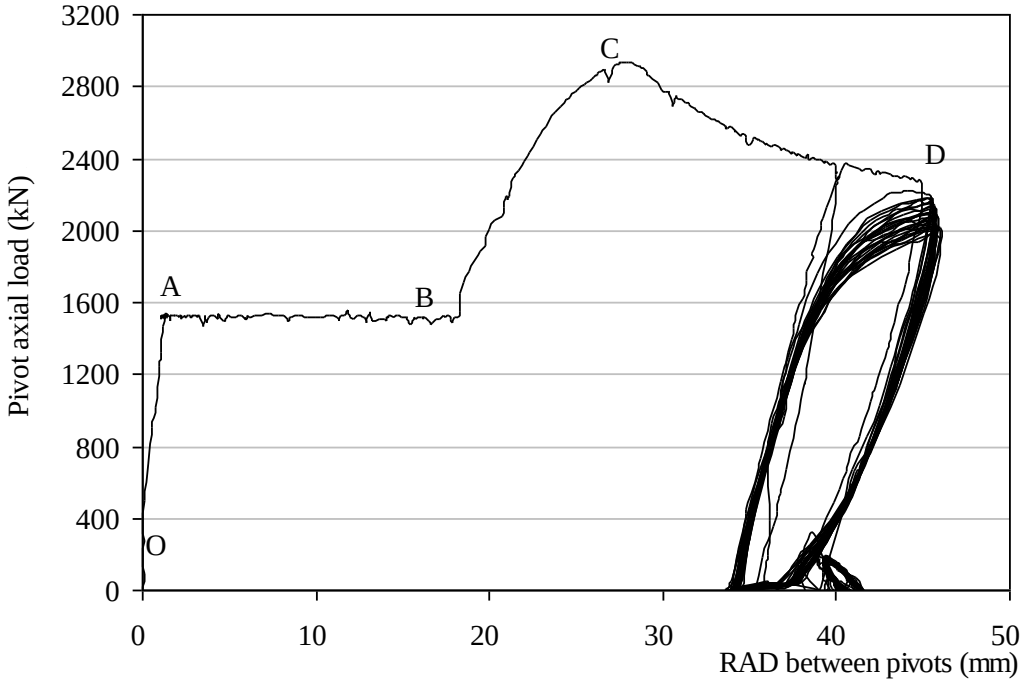

Figure 4.20: Pivot axial load vs. RAD between pivots (LCF20N1)

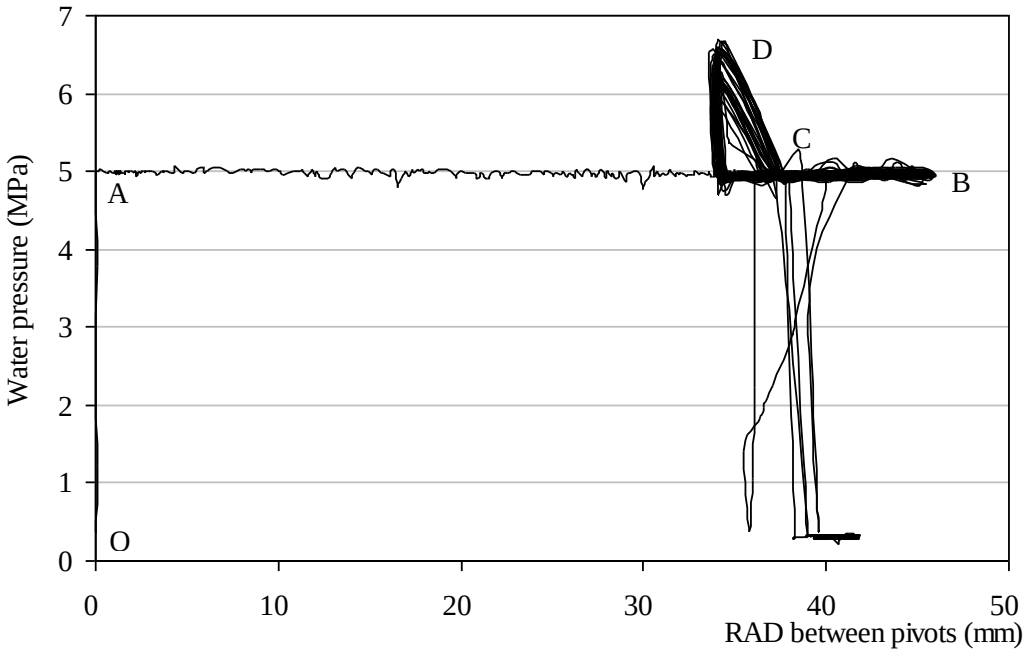

Figure 4.21: Water pressure vs. RAD between pivots (LCF20N1)

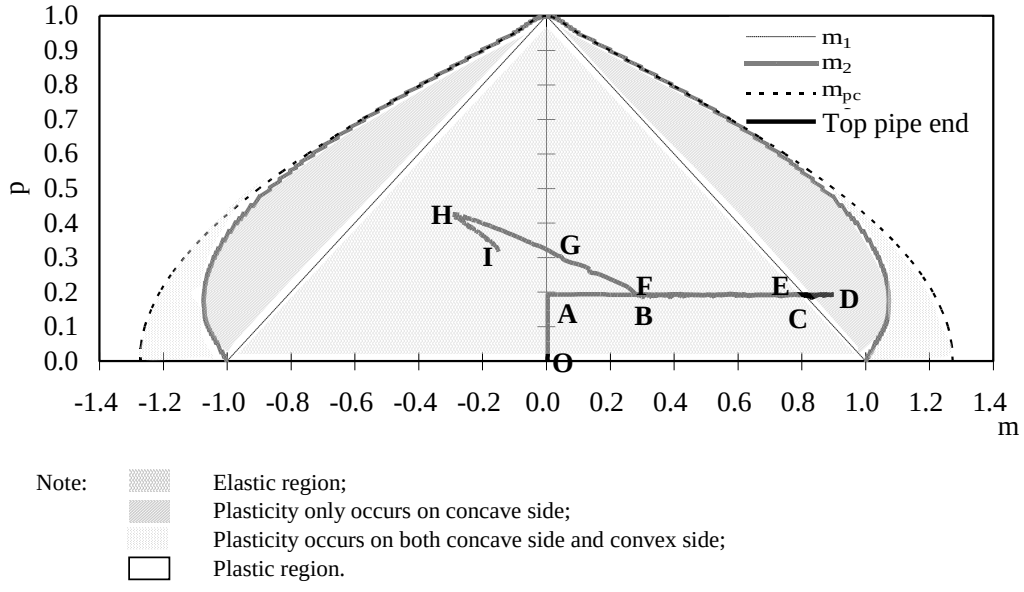

Note:
- Elastic region;
- Plasticity only occurs on concave side;
- Plasticity occurs on both concave side and convex side;
- Plastic region.

Figure 4.22: Interaction diagrams (LCF20N1)

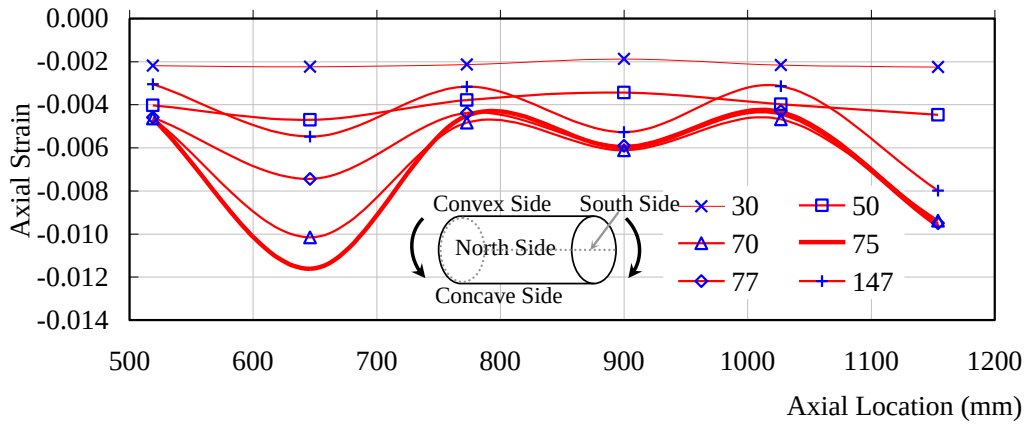

a) Concave side

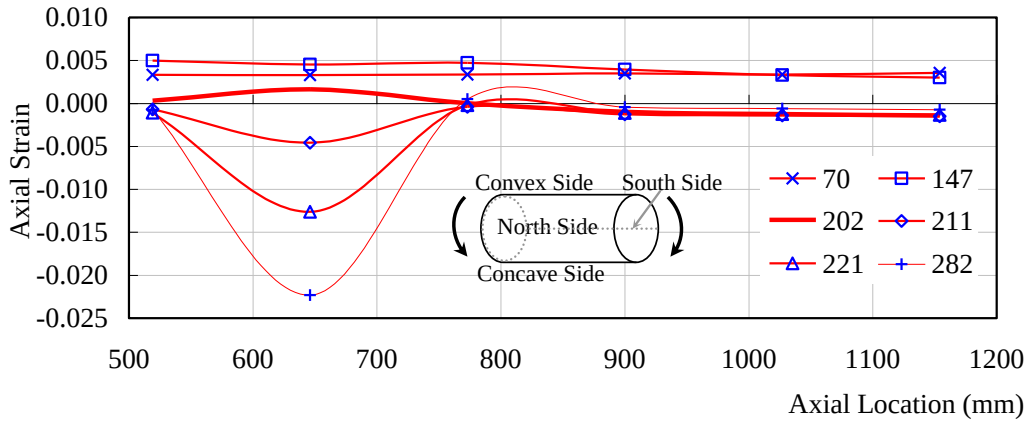

b) Convex side

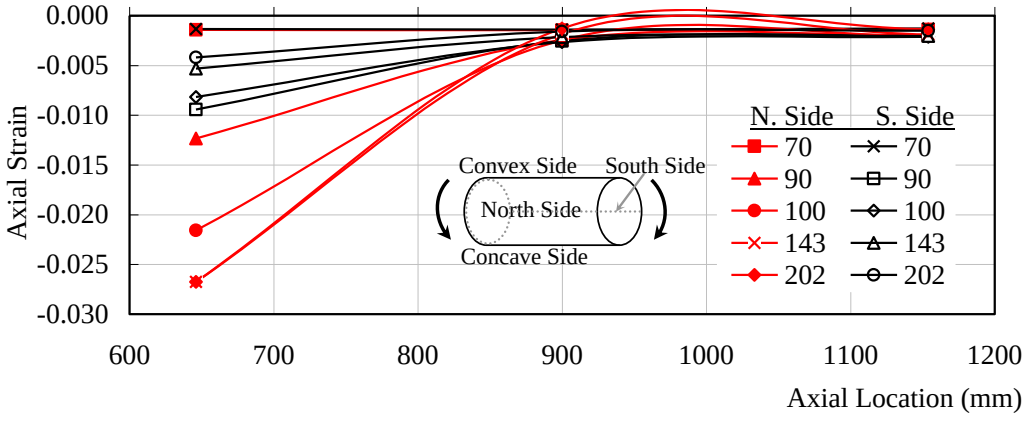

c) North & south sides

Note: The numbers in the legend are counter numbers.

Figure 4.23: Axial strain distribution (LCF20N1)

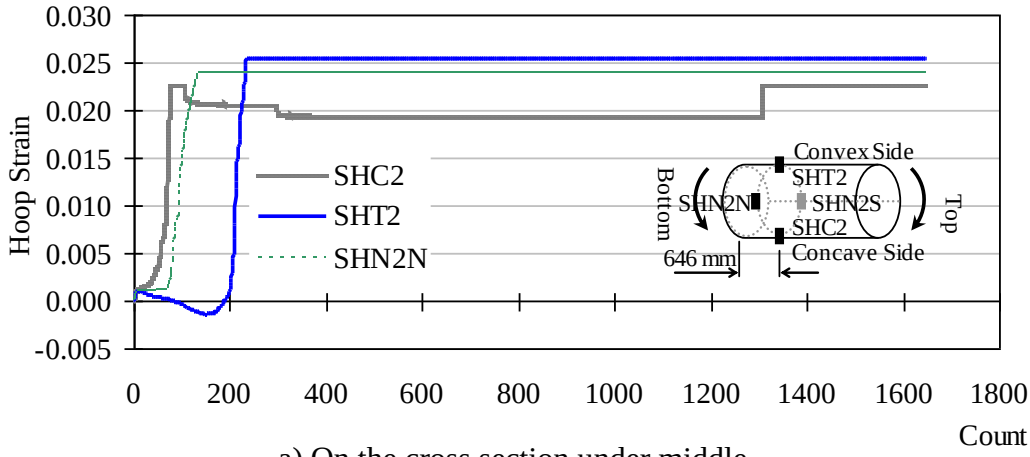

a) On the cross section under middle

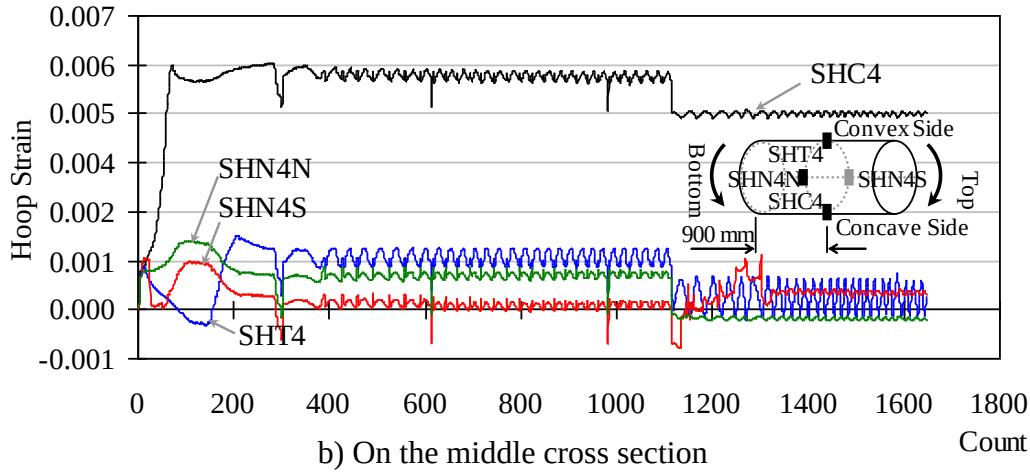

b) On the middle cross section

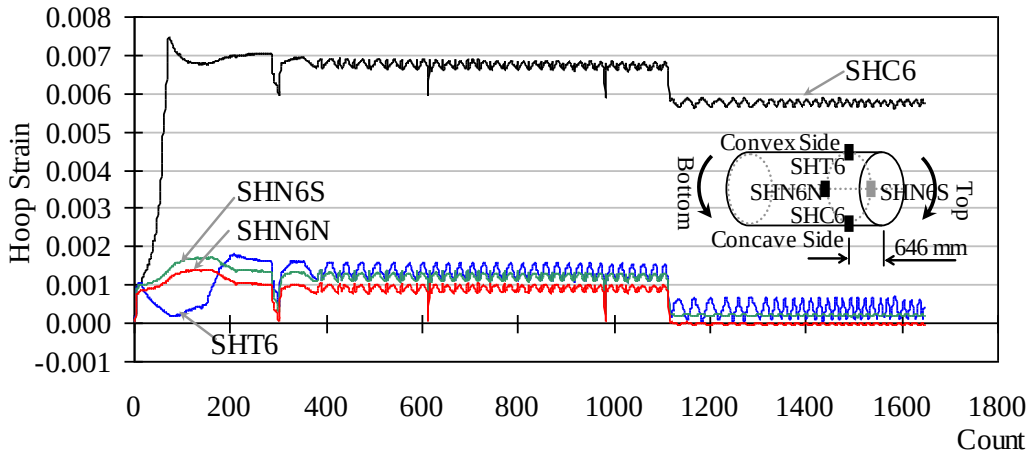

c) On the cross section over middle

Figure 4.24: History of hoop strain (LCF20N1)

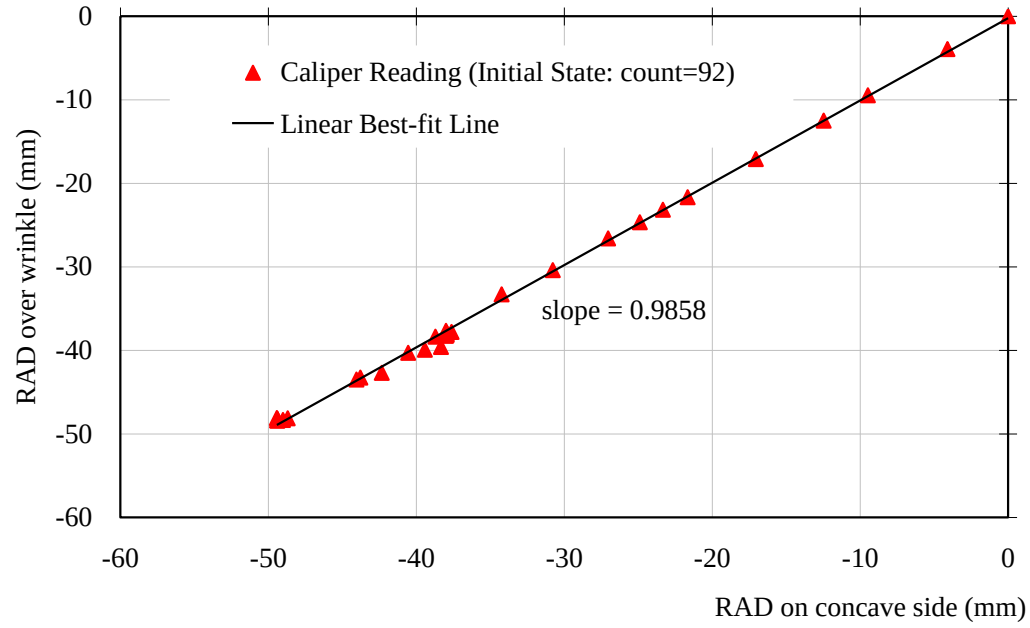

a) from caliper

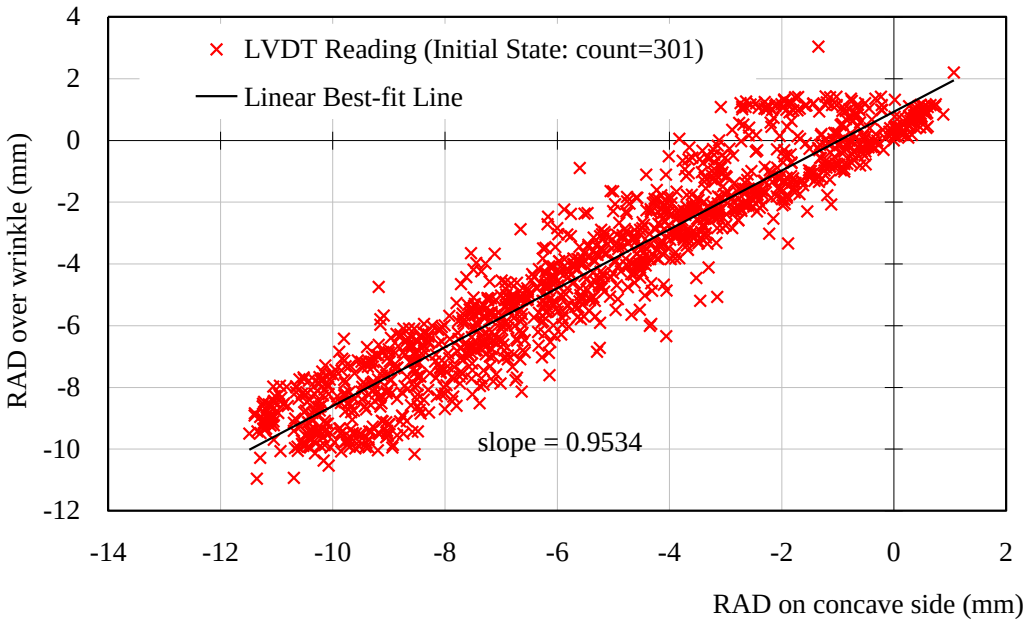

b) from LVDT

Figure 4.25: Local RAD vs. global RAD (LCF20N1)

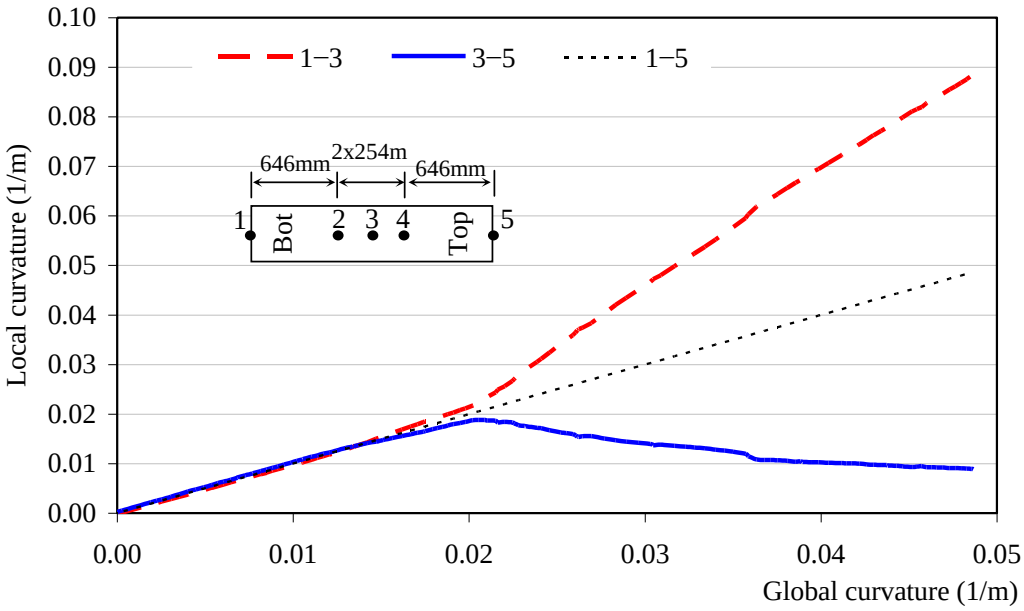

a) Over segments '1–3' and '3–5'

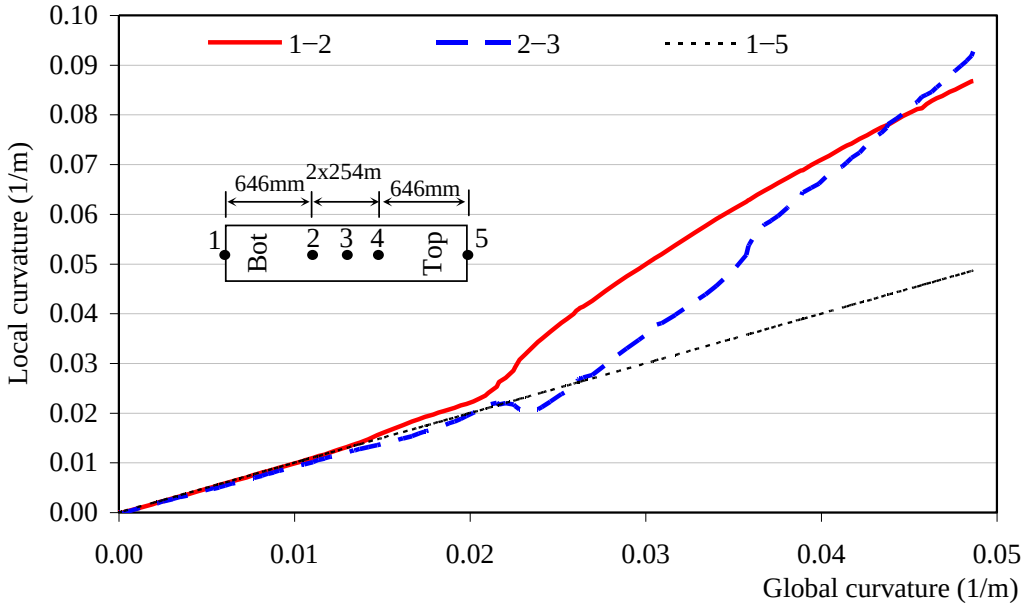

b) Over segments of '1–2' and '2–3'

Figure 4.26: Global curvature vs. local curvature (LCF20N1)

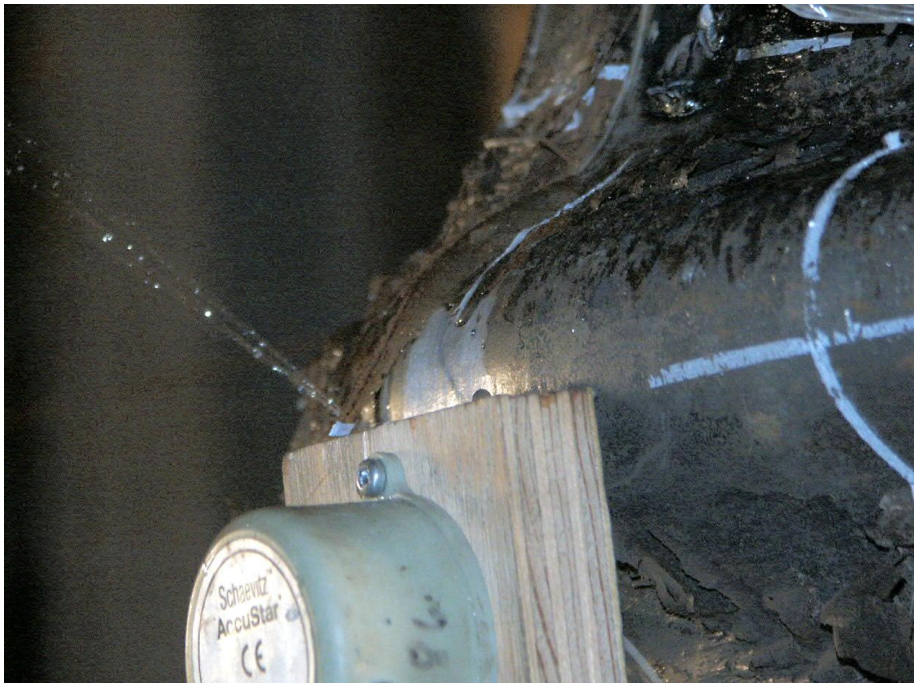

Figure 4.27: Pressurized water shooting out (LCF16N1)

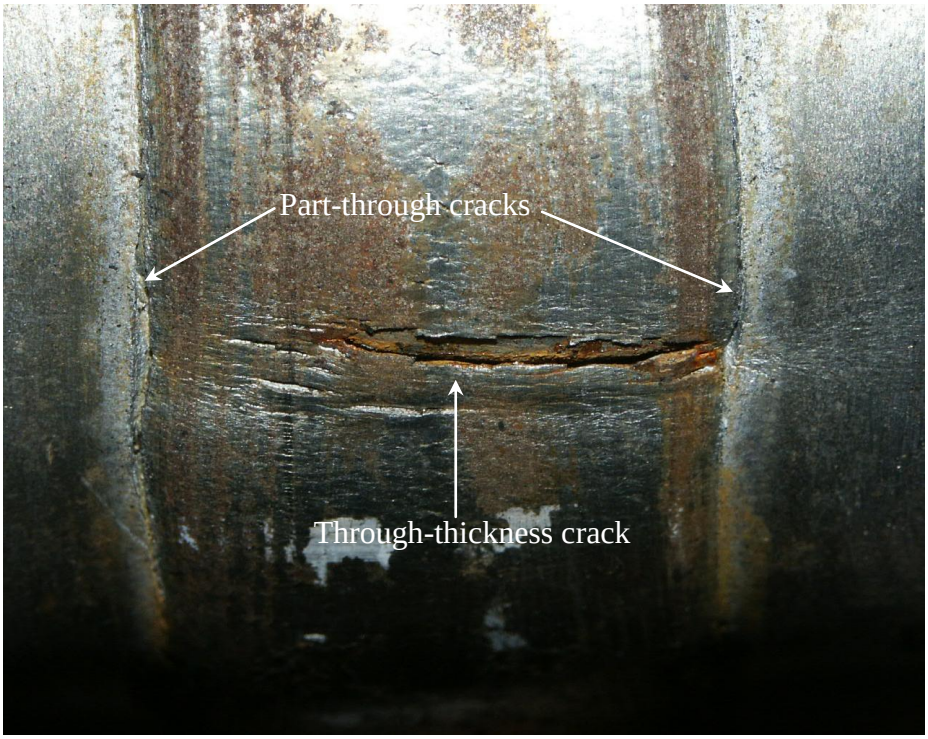

Figure 4.28: Close view of cracks on seam weld (LCF16N1)

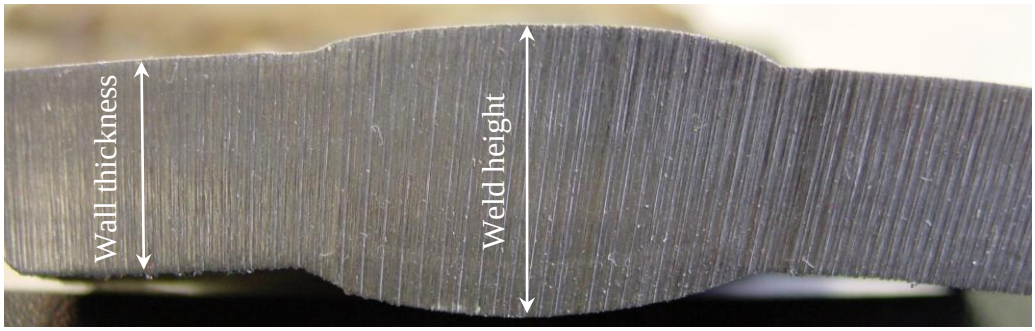

Figure 4.29: Cross section of pipe wall with seam weld (Specimen LCF16N1)

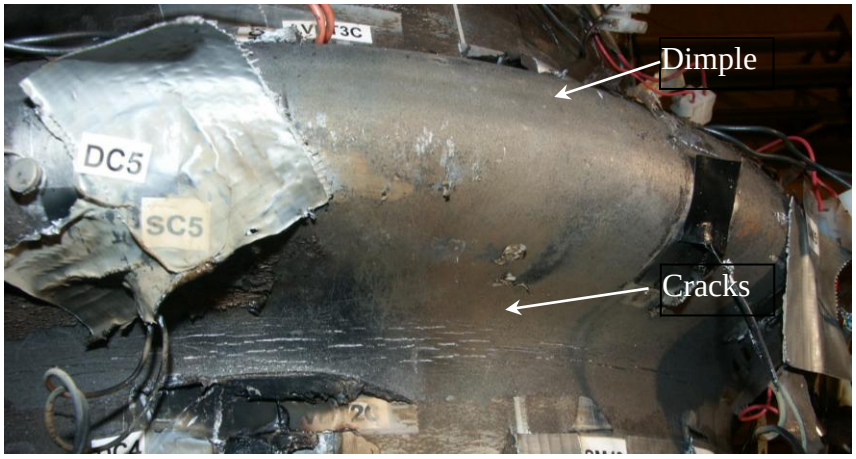

Figure 4.30: Cracks on the lower wrinkle foot and dimple formed on wrinkle crest (specimen LCF16N1)

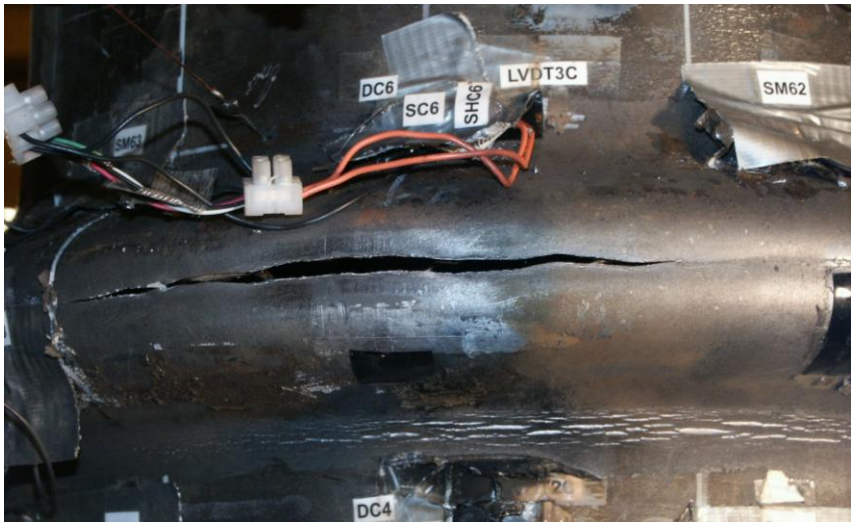

Figure 4.31: Wrinkle crest on concave side being totally fractured (LCF16N1)

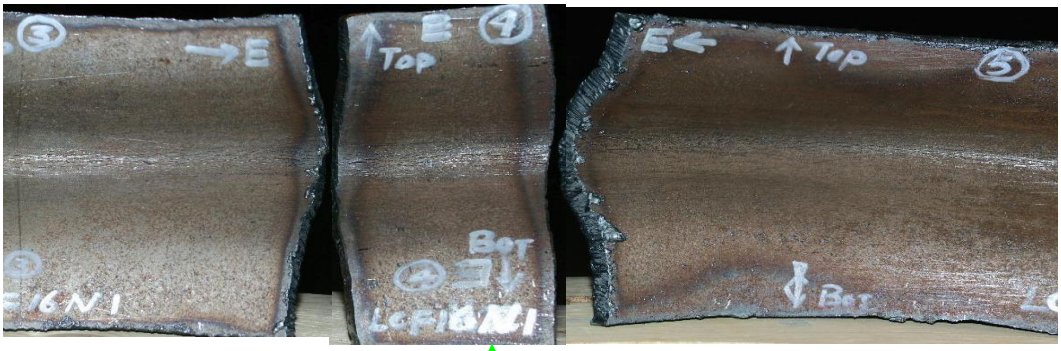

Figure 4.32: A montage of overlapping pictures
of the inside surface of wrinkle (LCF16N1)

Figure 4.33: Pressurized water spraying from specimen LCF20N1

Figure 4.34: Crack on concave side when specimen LCF20N1 was fractured

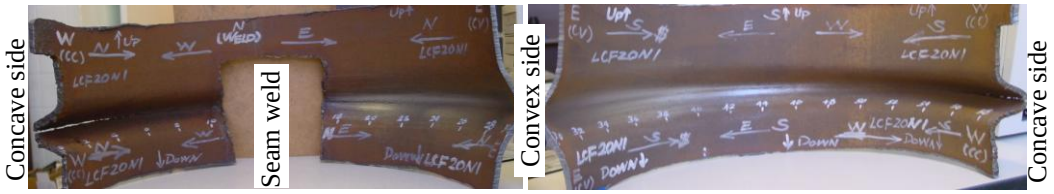

a) In pieces of half pipe

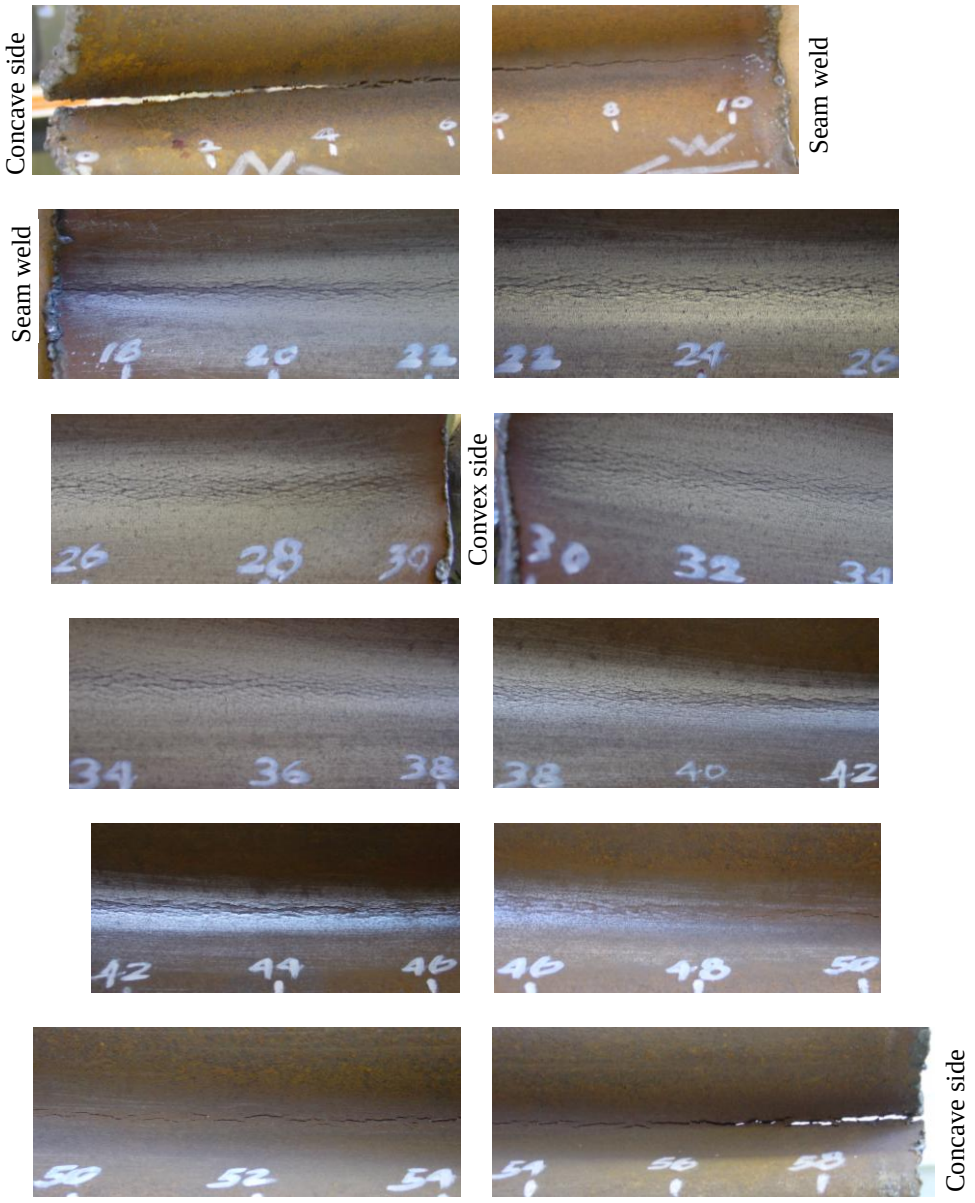

b) In smaller pieces

Figure 4.35: A montage of overlapping pictures
of the inside surface of wrinkle (LCF20N1)

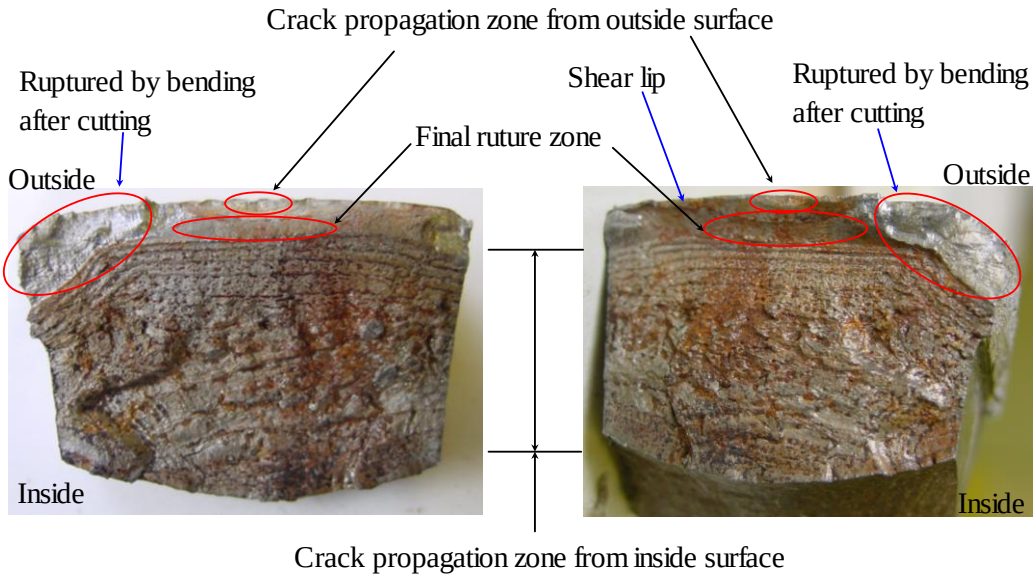

Figure 4.36: Fracture surface of seam weld (specimen LCF16N1)

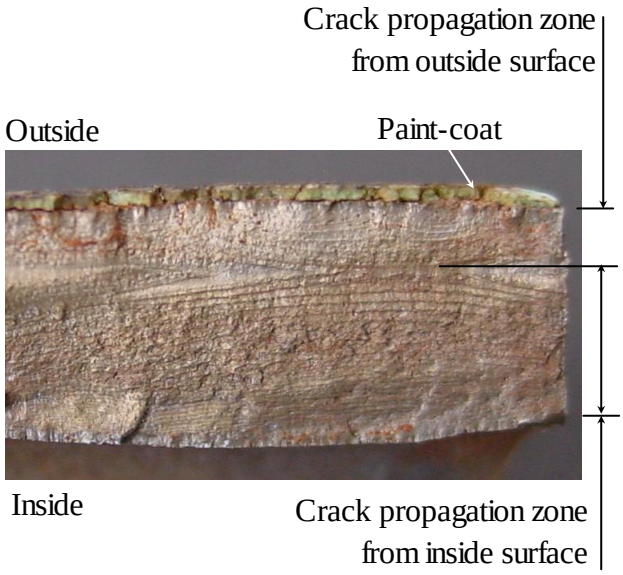

Figure 4.37: Fracture surface of seam weld (specimen LCF20N1)

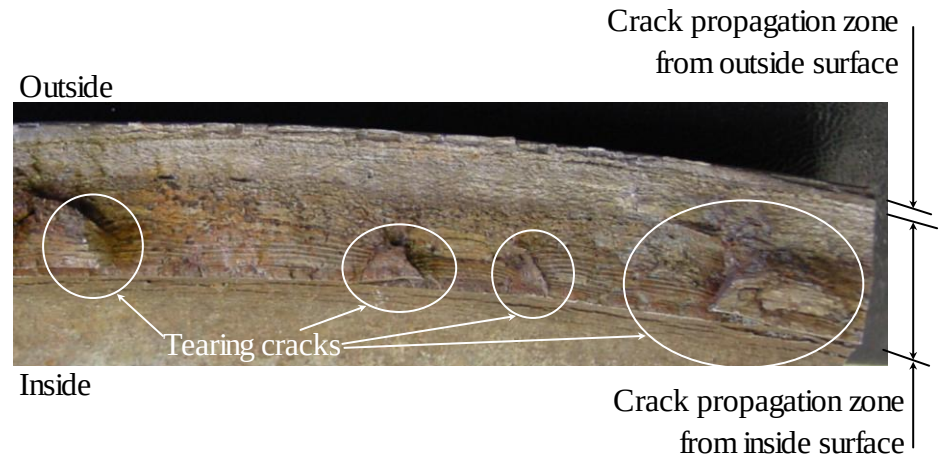

Figure 4.38: Fracture surface of wrinkle on concave side (specimen LCF16N1)

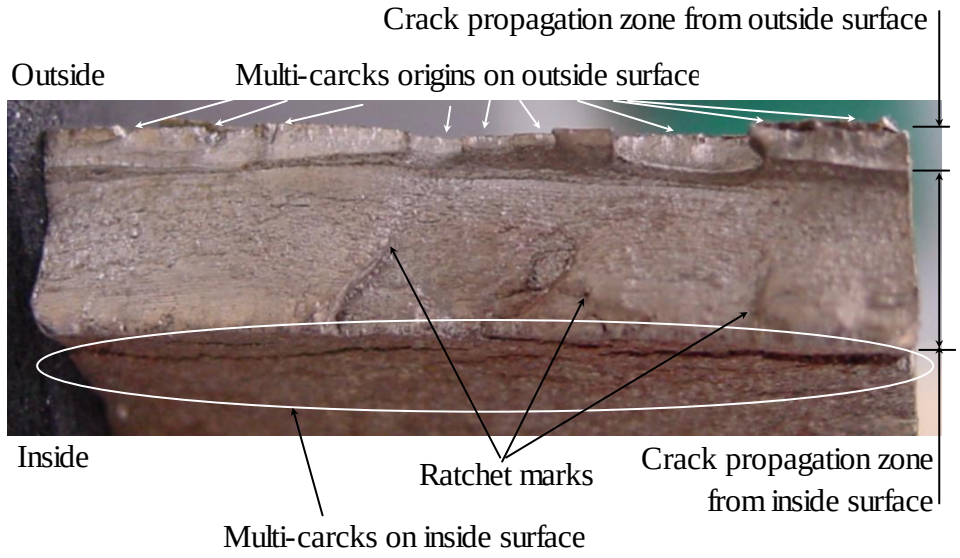

Figure 4.39: Fracture surface of wrinkle on concave side (specimen LCF20N1)

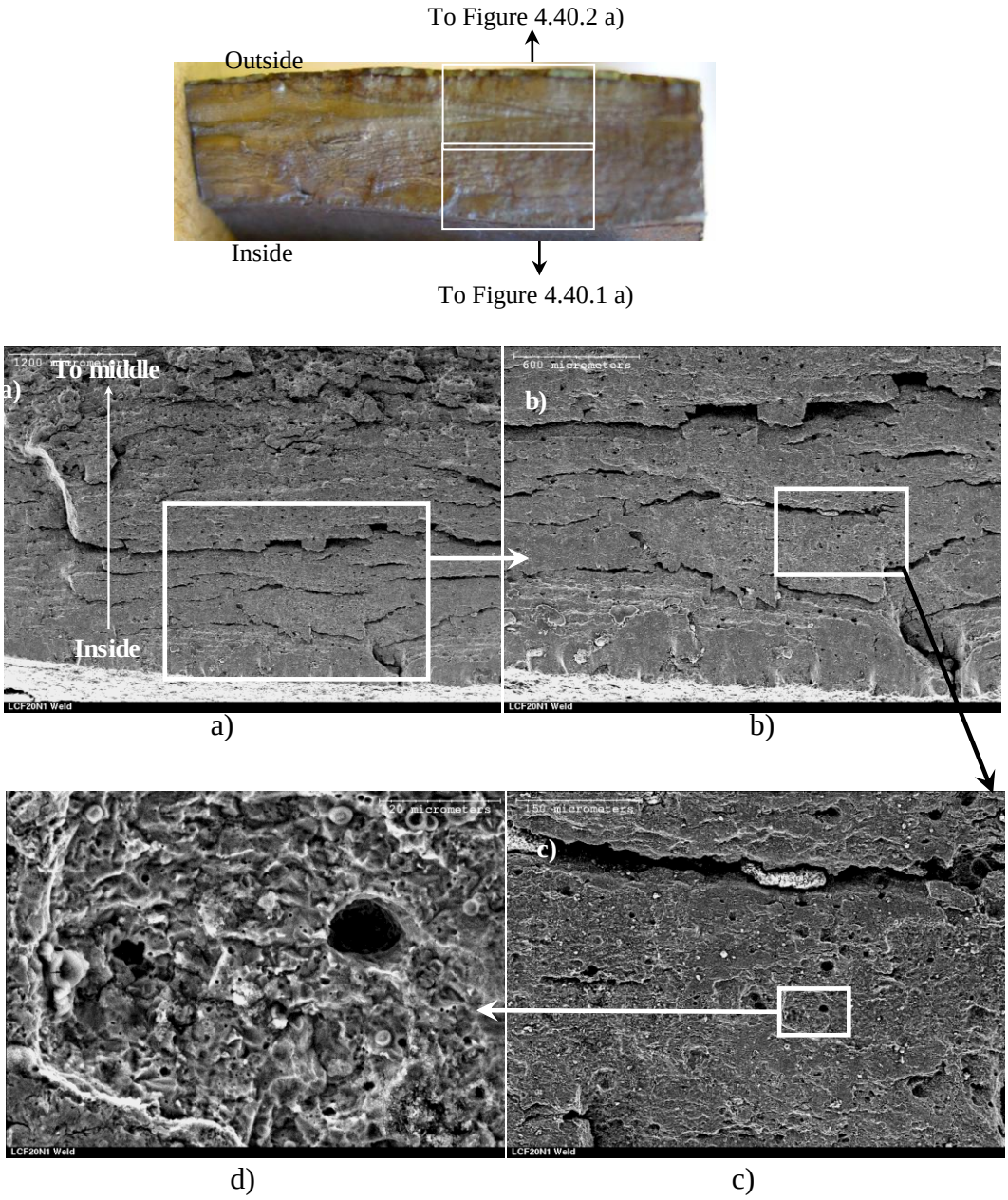

Figure 4.40.1: SEM of fracture surface of inside portion of seam weld (specimen LCF20N1)

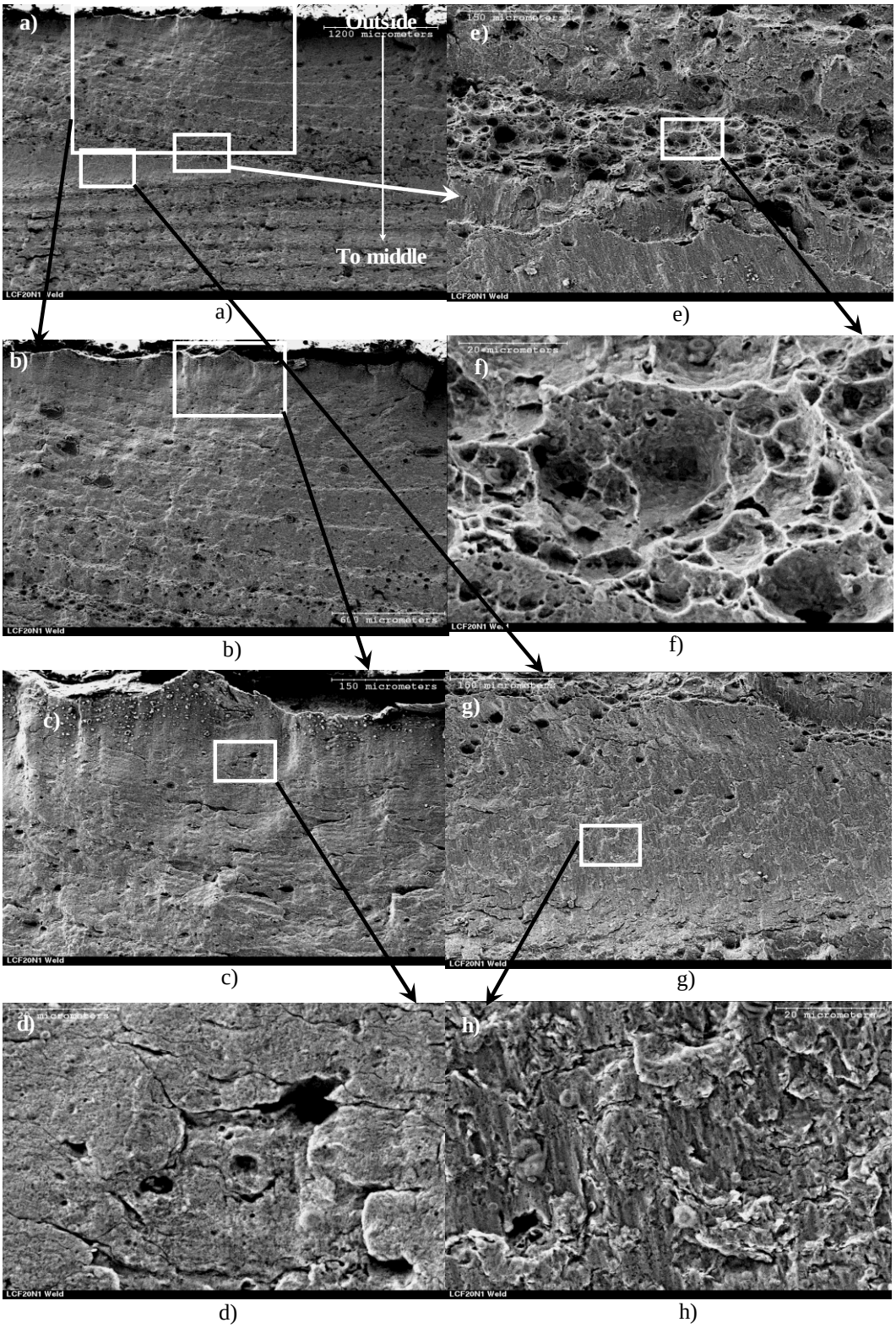

Figure 4.40.2: SEM of fracture surface of outside portion of seam weld (specimen LCF20N1)

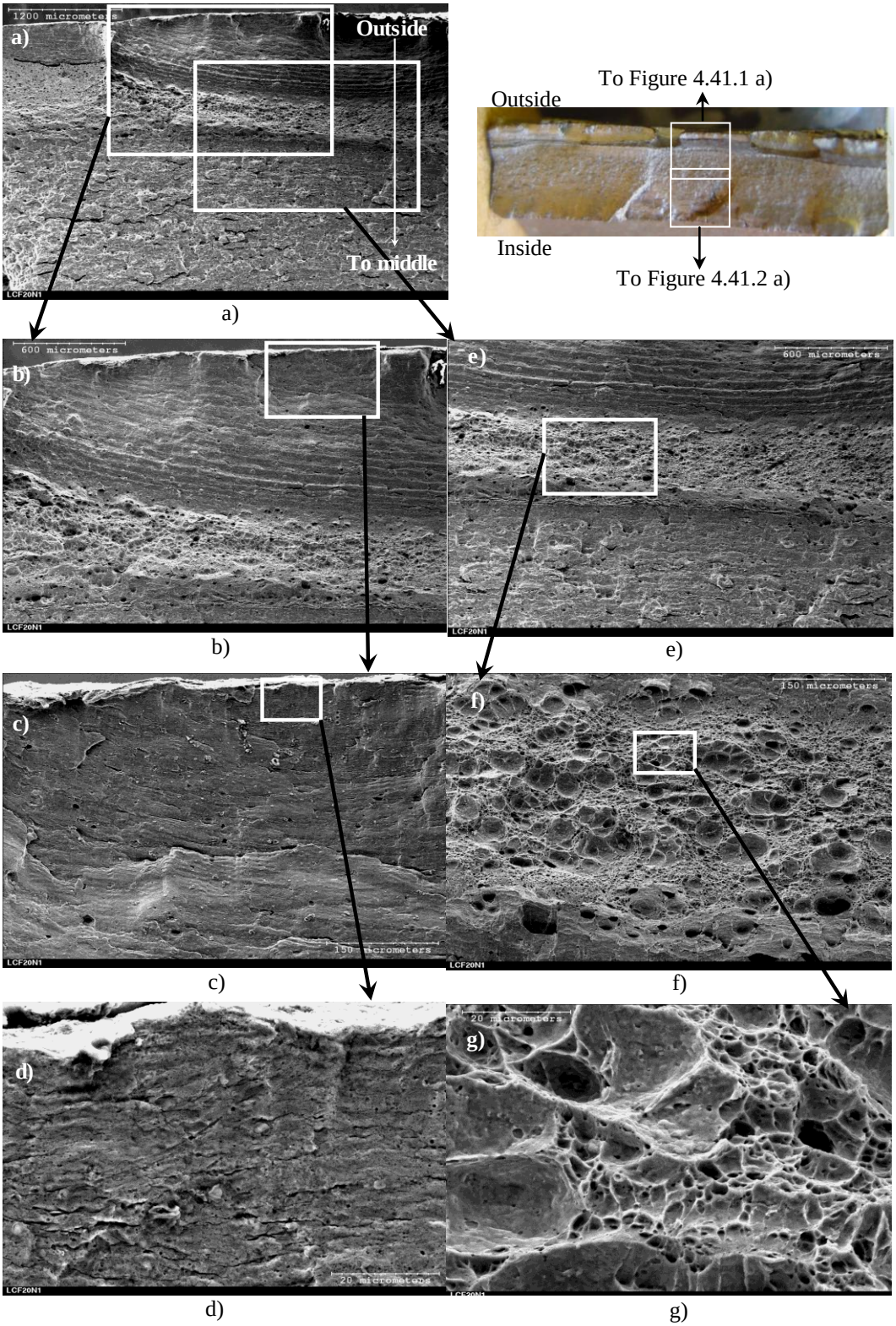

Figure 4.41.1: SEM of fracture surface of outside portion of wrinkle on concave side (specimen LCF20N1)

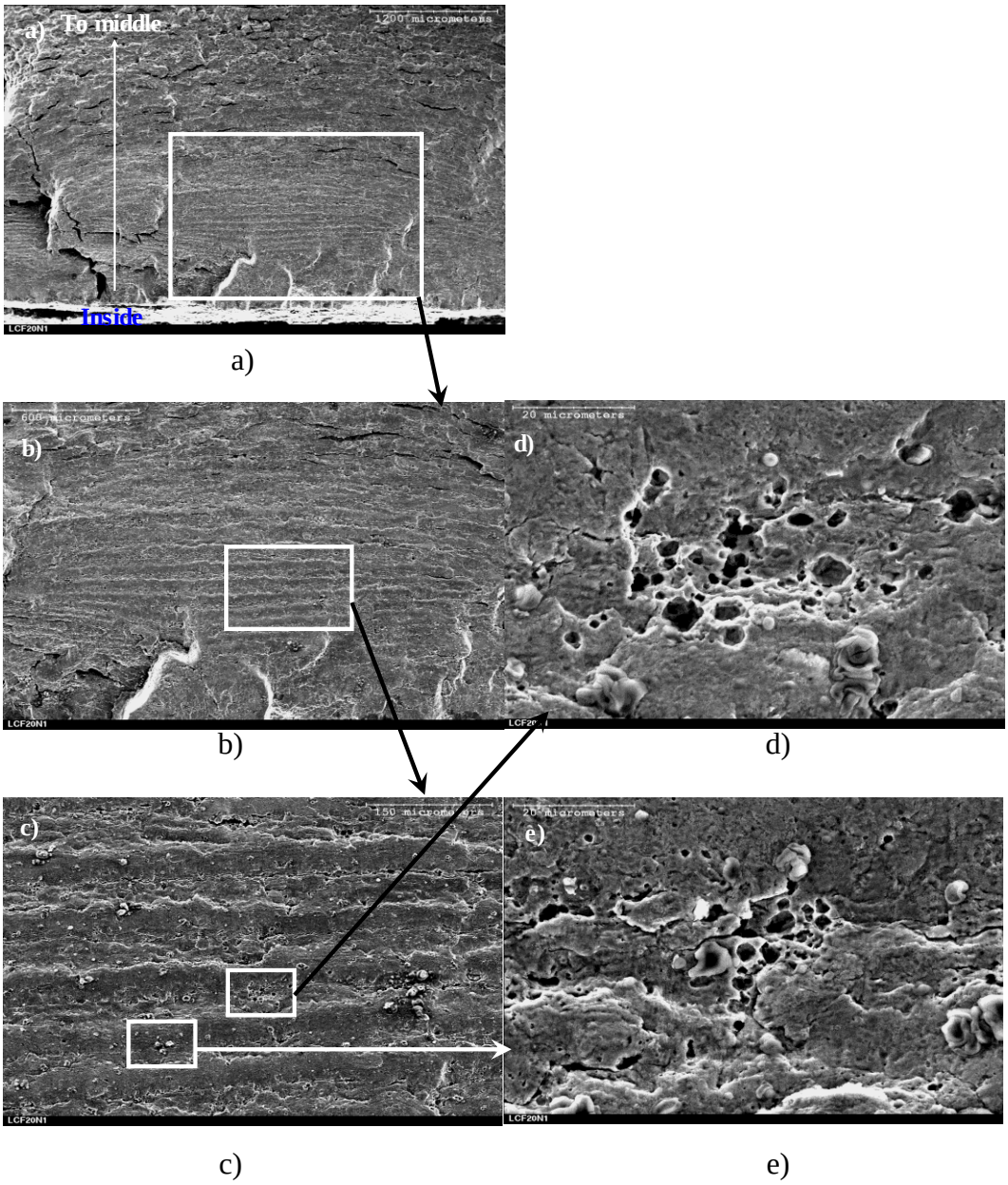

Figure 4.41.2: SEM of fracture surface of inside portion of wrinkle on concave side (specimen LCF20N1)

5 FINITE ELEMENT ANALYSIS

Three finite element models are developed in this chapter; they are: the strip model, the half pipe model, and the full-scale pipe model. The strip model mainly focuses on the residual strains, which are requisite for evaluating the ductile damage due to the monotonic loading, in the strip bend by simulating the process of monotonically bending a straight strip. The half pipe model is used to conduct the parametric study, and it concentrates on the impact of the internal pressure on the wrinkle profile by simulating a pipe being monotonically loaded by a combination of bending moment, axial load and internal pressure. The full-scale pipe model simulates the full-scale pipe test, and it is developed to provide the parameters that the LCF life prediction model requires but they are difficult to be measured in the field pipes, such as wrinkle geometries. Because all three models involve large strains, ABAQUS/Standard Version 6.2 (Hibbitt, Karlsson, Sorenson Inc. 2001) finite element package is employed to carry out the simulations and the analyses.

5.1 STRIP MODEL

During the process of monotonic bending, a straight strip was bent around the guide rod to the designated angle by the drive wheel (see Figure 3.1). After being bent, significant residual strains were left within the strip bend, and it was the residual strains that permanently changed its shape from straight to bent. Moreover, these residual strains are essential for developing the LCF life prediction model, which will be discussed in the next chapter.

The residual strains can be obtained by direct measurement, theoretical method, or FEA. The direct measurement and the theoretical method were given in Chapter 3, therefore only their reliability will be discussed here. In the direct measurement, there are many error sources, such as the contact condition between the transparent tape and the strip surface, the deformed shapes, and the replicated profiles of punch marks, etc. In the theoretical method, a few assumptions are

made in Equations (3.6) and (3.7) to calculate the residual strains, e.g. the actual cross section of strip specimens is a curved quadrilateral instead of a perfect square. In order to provide objective comparison, a third (FEA) method is needed to evaluate the reliability of the residual strains obtained from each method. Moreover, the strip specimens were so heavily deformed that their strip bends were necked, so it is more reasonable to present the residual strains on true scale instead of on engineering scale. Since the theoretical method and the direct measurement method can only provide the residual engineering strains, so the FEA method has to be employed for this purpose.

5.1.1 FINITE ELEMENT MODEL

To simulate the monotonic bending process, three components have to be modeled: the strip specimen, the guide rod, and the drive wheel. The boundary conditions and the contact conditions have to be simulated properly. In addition, because a very large rotation was applied to the strip by the drive wheel, the model has to possess the ability to handle this rotation. The following develops the finite element model based on these considerations.

5.1.1.1 ELEMENT

STRIP SPECIMEN

Strip specimens were directly cut from full-scale pipes along their longitudinal directions. Although the width of strip specimens was limited to a small size (57 mm) to minimize the influence of the curvature of the pipe wall, this influence could not be totally eliminated.

Based on the fact that the investigated strip is a shell, it is natural to consider the shell element because this will make the node input and the mesh generation much easier than other types of elements. For the shell element type, the first and also the most important consideration is that the finite element has to be able to handle large strain involving materials with a nonzero effective Poisson’s ratio, the second one is that it is a type of curved element so that the curved cross section can be modeled. Based on these considerations, the S4R element was

selected. S4R is a four-node, quadrilateral, stress/displacement shell element with reduced integration. For shell section, the model employed Simpson's rule for integration and the number of integration points was five. Because Simpson's rule has integration points on shell surface, the residual true strain on strip surface can be obtained directly.

In addition, strip specimens were gripped at a location that was about 120 mm away from its middle cross section, so the strip beyond the clamp was not be modeled. Also near the free end of the strip, the residual stress and the residual strain were almost zero, so there was no need to model this end either. Therefore, only a total strip length of 240 mm was modeled, as shown in Figure 5.1. By chopping these two portions from the model, the computer run time was greatly reduced.

GUIDE ROD

Compared with the strip, the guide rod was so rigid that its deformation could be ignored, so it was conveniently modeled by a rigid surface in the model.

DRIVE WHEEL

Same as the guide rod, the drive wheel was very rigid compared with the strip, so it was modeled by a rigid surface too.

5.1.1.2 BOUNDARY AND CONTACT CONDITIONS

In strip tests, strip specimens were bent around the guide rod by the drive wheel. During this process, the specimens were fixed at one end, the guide rod was totally fixed, and the drive wheel revolved about its own axis and rotated around the axis of the guide rod. In ABAQUS, the fixed condition can be modeled easily, but it is difficult to simulate the revolution of the drive wheel around its own axis. If focusing on the applied loads on the strip, it can be found that the drive wheel exerted a negligible load in the tangential direction of the strip surface because the drive wheel could freely revolve about its own axis. Based on this observation, the drive wheel was fixed about its own axis in the finite element model, i.e. it could not rotate around its own axis. But a zero friction coefficient was given to

the surface between the strip and the drive wheel. This induced a zero load on the strip along its tangential direction. As for the contact condition between the strip and the guide rod, a friction coefficient of 0.6 (Hecht 2003), was employed in the finite element model.

5.1.1.3 MESH

To design the mesh, the first issue is to determine the mesh layout. For strip specimens, the portion of most interest is the strip bend, where the material was plasticized and the residual strain and the residual stress developed. Therefore, a finer mesh was used in the strip bend and coarser mesh in other areas. In addition, because there is no limitation for the aspect ratio of S4R elements in ABAQUS, it is convenient to use a continuously varied mesh size along the longitudinal direction of strip. Also, the number of element along the transverse direction of the strip is kept constant. Specifically, the aspect ratio is unit on the middle of the strip, i.e. the element is square; and from the middle outward to its both ends, the aspect ratio is increased gradually by introducing a bias coefficient of 1.05.

A mesh study was conducted to determine the optimum mesh size. For strip specimens, the most important data is the residual strains, which are the basis to evaluate ductile damages. From the measurement and the theoretical analysis, it was found that the residual strains in the strip bend were almost evenly distributed. Hence, it can be concluded that the mesh is fine enough if an acceptable result is obtained on the middle of strip. In other words, the fineness of mesh can be adjudged based on the residual strains on the middle cross section only. Based on the results of mesh study, which will be discussed in the subsequent section, the model conservatively uses a 19 × 46 (a total of 874 elements) mesh size. A typical mesh is shown in Figure 5.2.

5.1.1.4 LOADING

To make a strip specimen with a bend angle of θ, the drive wheel has to rotate about the axis of the guide rod by an amount of $(180^{o} - \theta)$. During this process, the drive wheel not only rotates about the axis of guide rod, but also revolves

about its own axis. To simulate the rotation about the axis of guide rod, ABAQUS can define it in the boundary condition, but it is difficult to simulate the revolution about its own axis. To resolve this problem, as that discussed previously, a non-frictional contact condition is defined between the strip and the drive wheel.

5.1.1.5 MATERIAL MODEL

ELATISTIC MECHANICAL PROPERTIES

The employed Young's Modulus is given in Table 3.1, which was obtained from material coupon tests. The Poisson's ratio was taken as 0.3, which has been accepted for most ductile steels.

INELASTIC MECHANICAL PROPERTIES

Three series of coupon tests were conducted for three grades of materials that were used for the strip specimens, respectively. In ABAQUS, the material model requires the stress-strain curve provided on the true scale instead of on the engineering scale. But in coupon tests, because it was very difficult to measure the true stress and the true strain of strip specimens with rectangular cross-section, the results only gave the engineering stress and the engineering strain. Hence, the stress and strain have to be converted from the engineering scale to the true scale. Usually, conversion rules can be found in most 'Mechanics of Materials' books, but this research program requires a more detailed conversion to cover the whole loading range.

When the strain is small, it is same on the true scale as that on the engineering scale. But the selection of the boundary between the small strain and the large strain is usually arbitrary to some extent. This program used two times of the yield strain as the boundary, as suggested by Dowling (2007).

When the strain is between two times of the yield strain and the necking strain, at which the necking occurs, the constant volume assumption holds, so the following equations can be used:

$$\sigma_t = \sigma(1+\varepsilon) \tag{5.1.1}$$

$$\varepsilon_t^p = \varepsilon_t - \varepsilon_t^e \tag{5.1.2}$$

$$\varepsilon_t = \ln(1+\varepsilon) \tag{5.1.2.1}$$

$$\varepsilon_t^e = \frac{\sigma_t}{E} \tag{5.1.2.2}$$

where σ and ε are the engineering stress and the engineering strain, respectively; σ_t and ε_t are the true stress and the true strain, respectively; ε_t^p and ε_t^e are the true plastic strain and the true elastic strain, respectively; and E is the Young's modulus.

After the onset of necking, because the deformation is not uniform along the coupon specimen anymore, the engineering strain becomes dependent on the gauge length. In effect, it is the average strain over the gauge length. In this case, the true stress and true strain can only be obtained from their definitions as follows:

$$\sigma_t = \frac{P}{A} \tag{5.2.1}$$

$$\varepsilon_t^p = \ln\left(\frac{A_o}{A}\right) - \frac{\sigma_t}{E} \tag{5.2.2}$$

where P is the axial load; A_o and A are the initial cross-sectional area and the current cross-sectional area, respectively; and the other parameters are the same as before.

Moreover, when the coupon specimen is near to the final fracture state, its cross section is seriously necked. This will result in hoop tensile stresses in the necked region, so the true stress has to be corrected to account for this effect. Bridgman (Dowling 2007) developed an empirical correction relation for steel as follows:

$$\sigma_{tB} = B\sigma_t \tag{5.3.1}$$

$$B = 0.0684\chi^3 + 0.064\chi^2 - 0.205\chi + 0.825 \tag{5.3.2}$$

$$\chi = \log_{10}\varepsilon_t \qquad (0.12 \le \varepsilon_t \le 3.00) \tag{5.3.3}$$

where σ_{tB} are the corrected true stress, B is the correction factor, and the other parameters are the same as before.

It can be seen that to obtain the true stress and the true strain after the onset of necking, the current cross-sectional area has to be known. In this coupon test, the geometries of current cross-section could not be measured because of the limitation of the measurement techniques used. However, the final area of the fractured cross-section was measured approximately by putting the two fractured parts together. Between the necking and the fracture, the true stress–strain curve was assumed to be linear.

Thus, the true stress – true strain curves of the tested three sets of materials can be obtained over their entire loading histories, and the results are shown in Figure 5.3.

At last, there was no strain reversal in those strip specimens, thus the isotropic hardening rule was selected as the material hardening behaviours.

5.1.2 PARAMETERS

For the residual strains in strip specimens, the possible influencing factors include the material mechanical properties, the material thickness, the bend radius, and the bend angle. The effect of the material mechanical properties can be incorporated into the finite element model by the material model. From the theoretical analysis (see Equations (3.6.1) to (3.6.3)), it is deduced that the residual strains depend only on the yield strain and the R/t ratio and they are independent of the bend angle. To verify this conclusion, the FEA will investigate the impacts of the bend radius and the material thickness by focusing on the R/t ratio, and it will check if the bend angle impacts the residual strains.

5.1.2.1 MATERIAL

The materials used in this program came from two sources, and they had two material grades and three sets of thickness. The Tokyo Gas Ltd. provided the 11.59 mm thick material with a nominal grade of X60, and the TransCanada

Pipelines Ltd. supplied the 8.3 mm and the 6.0 mm thick materials with the nominal grade of X65. The influences of these three types of material will be investigated by employing their true stress–true strain relations in the finite element model.

5.1.2.2 BEND ANGLE

To investigate the influence of bend angle on the residual strains, the material thickness and the bend radius were kept constant and only the bend angle was changed. Specifically, this FEA focused on the 6 mm thick strips with a bend radius of 20 mm, and investigated nine sets of bend angles, i.e. 30^o, 45^o, 60^o, 75^o, 90^o, 105^o, 120^o, 135^o and 150^o.

5.1.2.3 R/t RATIO

This analysis was conducted on strips with 60^o bend angle. The investigation was limited to the aforementioned three types of material, which are 6.0 mm, 8.3 mm and 11.9 mm. The R/t ratio was altered by changing the bend radius for each specific thickness. Specifically, the analyzed bend radii were 15 mm, 20 mm, 25 mm, 30 mm, 35 mm, 40 mm and 45 mm, and this gave a very wide range of R/t ratios from 1.2 to 7.5.

5.1.3 RESULTS AND DISCUSSION

As discussed in Section 5.1.1.5, the engineering strain will become gauge length dependent after the necking occurs, so the engineering strain is only meaningful for a specific gauge length. In this research program, because the residual strains are far beyond the necking strain, the results will be presented on the true scale unless being specifically mentioned.

5.1.3.1 MESH STUDY

The mesh study was conducted on 6 mm strips with 20 mm bend radius and 60^o bend angle, and analyzed different mesh sizes. The minimum mesh size (at the middle of the strip) was altered from 19 mm^2 to 1 mm^2, and the corresponding total number of elements varied from 12 × 3 to 29 × 58. Because the residual

strains were the main concern, the residual true strains at the center of the middle cross section were employed in the mesh study to determine the optimum mesh size. The results are shown in Figure 5.4. From the figure, it can be seen that the residual true strains approach constant when a relatively fine mesh is reached. This study conservatively used a 19 × 46 mesh size for all the subsequent FEA.

5.1.3.2 EFFECT OF BEND ANGLE

The effects of the bend angle are shown in Figure 5.5. From this figure, it can be seen that the residual true strains are almost constant when the bend angle is less than 105^o, but they drop dramatically when the bend angle is greater than 105^o. The reason is that a big bend angle cannot form a large enough plastic zone to get rid of the influence of 'spring back'. As a result, decreased residual strains were obtained. However, the bend angles are all less than 105^o for the investigated strip specimens, so the residual strains can be considered to be independent of the bend angle in this research program.

5.1.3.3 EFFECTS OF MATERIAL AND R/t RATIO

Because the effect of material mechanical properties is incorporated into the finite element model, it will be discussed together with the R/t ratio. The results are shown in Figure 5.6. From this figure, the following two important observations can be obtained.

First, the residual true strain is larger on the inside surface than that on the outside surface. This difference decreases as the R/t ratio increases. The reason can be found from Equation (5.1.2.1) as follows: if the compressive engineering strain and the tensile engineering strain have the same amplitude, then the compressive true strain will be greater than the tensile true stain.

Second, all the data can be best-fitted by two curves for the outside surface and for the inside surface, respectively. These two curves show that for the investigated three sets of materials, the residual true strains are independent of the materials properties and they can be determined by the R/t ratio only. By reviewing Figure 5.3, it can be found that these three sets of materials are very

similar, and this may explain why the material does not impact the residual true strains.

By best curve fitting the results, the following equations can be obtained:

$$\varepsilon_{tr} = 0.6386(R/t)^{-1.1360} \quad \text{on inside surface} \tag{5.4.1}$$

$$\varepsilon_{tr} = 0.4303(R/t)^{-0.9536} \quad \text{on outside surface} \tag{5.4.2}$$

where ε_{tr} is the residual true strain, and the other parameters are the same as before.

5.1.3.4 STRESS AND STRAIN DISTRIBUTIONS

From the FEA, the distributions of true stress and true strain can be easily obtained for the investigated strip specimens. The following discussion takes a 6 mm thick strip specimen with 20 mm bend radius and 60^o bend angle as an example. It focuses on two specific cross sections (transverse middle and longitudinal central) and one specific point (center of middle section), which are illustrated in Figure 5.1.

ON TRANSVERSE MIDDLE CROSS SECTION

The distributions of residual true strain and residual true stress on the transverse middle cross section are shown in Figure 5.7. From it, some observations can be made as follows. First, the residual true strain is compressive on the inside surface and tensile on the outside surface. On the contrary, the residual true stress is tensile on the inside surface and compressive on the outside surface. Second, the residual true strain is evenly distributed on both the inside surface and the outside surface, but the residual true stress greatly varies. Specifically, the residual true stress shows a ‘W’ shaped distribution on the inside surface and an ‘M’ shaped distribution on the outside surface. For the ‘W’ shaped distribution, there are two small plateaus near the edges. From the plateau, the path goes down abruptly to the valley, and then slowly climbs up to the peak at the middle. In addition, the peak is just a little bit higher than the plateaus on both edges. As for the ‘M’ shaped distribution, there are two small feet on both edges. From the bottom of

the feet, the path ascends very quickly near the peak at first, and then it climbs up to the peak very slowly, finally it descends smoothly to the valley at the middle. But this valley is much shallower than the bottoms of the feet, i.e. the feet have the maximum compressive residual true stresses.

ON LONGITUDINAL CENTRAL CROSS SECTION

The distributions of residual true strain and residual true stress on the longitudinal central cross section are shown in Figure 5.8. From it, the following observations can be obtained. First, there is almost no residual true strain far away from the strip bend; near to the strip bend, the residual true strain goes up slowly at first, and then it climbs up quickly; within the strip bend, the residual true strain reaches its peak on the outside surface and its valley on the inside surface, and then keeps them constant. Second, the transition from zero residual true strain to the maximum or minimum residual true strain is much smoother on the fixed side of the strip than that on the free side of the strip. Third, on the inside surface, the residual true stress is very small from the fixed end at first, and then it rises up smoothly near the middle cross section, and finally it reaches its tensile maximum just passing the middle cross section; after this, it sharply goes down to the compressive minimum, then it undergoes a small ascending, and finally goes back to zero gradually. It is also shown that there is no such a plateau in the strip bend. Fourth, on the outside surface, at first the residual true stress is very small from the fixed end, then it goes down smoothly near the middle section, and finally it forms a near plateau around the middle section; after this, it sharply climbs up from its compressive valley to its tensile peak, then it undergoes a small and sharp descending, and finally it goes back to zero gradually.

AT THE CENTER OF MIDDLE SECTION

Figure 5.9 shows the variation histories of true strain and true stress at the center of middle section during the entire loading stage. On the inside surface, when the driving wheel is far away from this point, the true strain and true stress are zero. When the driving wheel is near this location, the true strain alters just a little bit while the true stress gradually reaches a considerable peak value, and this

indicates that the curved cross section is gradually flattened by the drive wheel. Then the true stress quickly drops to the compressive maximum, and the true strain goes down smoothly to the compressive valley; during the unloading stage, i.e. the time from '1' to '2', the true strain just drops a little bit in a linear manner, and this indicates the phenomenon of 'spring back'. But the true stress goes from the compressive side to the tensile side gradually, and finally a tensile residual true stress is left there. On the outside surface, the true strain and the true stress follow diametrically opposite ways compared with those on the inside surface. Another observation is that the magnitude of residual compressive true strain on the inside surface is about 1.17 times of that of residual tensile true strain on the outside surface. On the contrary, the amplitude of residual tensile true stress on the inside surface is about 1.66 times of that of residual compressive true stress on the outside surface.

Figure 5.10 shows the relations between the true stress and the true strain on both the inside surface and the outside surface. Because it can be obtained directly from Figure 5.9, no discussions will be given at here.

5.1.3.5 COMPARISON AND DISCUSSION

From the measurement and the theoretical analysis, only the residual engineering strain can be obtained. In Chapter 3, the residual engineering strains from measurement and theoretical analysis were presented and compared in Table 3.6. But from the FEA, only the residual true strain can be obtained in the case of large strain, so a conversion has to be made before comparison. Because it is difficult, and also impractical, to convert these true values to the engineering values, the comparison can only be conducted in the cases that the strains are less than the necking strain. Also, based on the fact that the residual strains in all strip specimens were all over the necking strain, which is the strain corresponding to the onset of necking, the following will only compare the results of FEA and that of theoretical analysis when the strain is less than the necking strain.

The theoretical residual engineering strain can be obtained approximately from Equation (3.7), and the conversion between the true strain and the engineering

strain was discussed in Section 5.1.1.5. The results are given in Table 5.1. From this table, it can be seen that the FEA results are just a little higher than the theoretical results. Moreover, the FEA results show that the difference between the amplitude of the compressive residual engineering strain on the inside surface and that of the tensile residual engineering strain on the outside surface is so small that it can be neglected. This observation coincides with the theoretical analysis.

5.2 HALF PIPE MODEL

During recent decades, the global behaviour of pipes, e.g. the relation between the bending moment and the global curvature, has been extensively investigated and well understood; but the local behaviour has been less researched. Moreover, the research results have not been widely accepted, e.g. the critical compressive strain. Therefore, it is necessary to further investigate the local behaviour and the relation between the local behaviour and the global behaviour.

It has been well documented that the wrinkle profile is related to the existence of the internal pressure. For un-pressurized pipes, the wrinkle has a so-called diamond pattern; for pressurized pipes, the wrinkle exhibits an outward bulging pattern (Das 2001, Mohareb et al. 2001, Souza and Murray 1999, Del Col et al. 1998, Yoosef-Ghodsi et al. 1995, Bouwkamp and Stephen 1974). Unfortunately, no effort has been given to investigate the relation between the wrinkle geometry and the internal pressure. Therefore, the postbuckling behaviour cannot be thoroughly understood. Furthermore, the evaluation of the wrinkled pipes (in postbuckling stage) cannot be conducted if the local behaviour cannot be quantified.

It is not easy to investigate the relation between the wrinkle geometry and the internal pressure by experiment. The main reason is the unpredictability of the wrinkle location, so the instrumentation cannot be installed at the right location. In addition, the wrinkle forms within a very small area, which limits the selection and the layout of instrumentation. However, with the development of inelastic and nonlinear analytical technologies, it has become possible that the FEA resolves these very large strain problems.

To conduct this type of FEA, the following considerations have to be included in the model. The first one is that the wrinkle location has to be controllable. If the wrinkle location can be predicted, then an element set and a node set can be defined in advance. This will simplify the post-data processing. The second one is that the wrinkle has to be far away from pipe ends so that the growth of the wrinkle is not significantly influenced by the constraints of pipe ends, which are welded to thick end plates. The third one is that the running time has to be as short as possible because the quantity of jobs needed to be run is huge. Moreover, to conduct an analysis that focuses on a local area, the mesh has to be fine enough and this will greatly magnify the job size. So based on these concerns, a half pipe model with prescribed imperfections was employed and the details will be discussed in the following sections.

5.2.1 ANALYSIS SCENARIO

In the field, buried pipes are generally subjected to a combination of axial load, internal pressure and bending moment, and they can be subjected to the soil movement in both their longitudinal and transverse directions. The longitudinal movement can be caused by an earthquake or by soil sliding down a slope, and the transverse movement can be the result of frost heave and thaw settlement. In this study, the analysis will focus on the wrinkles caused by bending. In this analysis, the axial load and the internal pressure are kept constant, and the bending moment is increased to form the wrinkle. Also, in order to compare with the full-scale pipe test results, the selected pipes are the same as the full-scale pipe specimens, and the loading procedures are also similar to the corresponding loading stages of the full-scale pipe tests. The only difference is that the axial load and the bending moment amplitudes in the FEA are half of the values used in the tests. An illustration of this type of loaded pipe is schematically shown in Figure 5.11, and the corresponding controlled loads in each case are given in Table 5.2.

5.2.2 FINITE ELEMENT MODEL

5.2.2.1 ELEMENT

PIPE

The S4R element was selected for the pipe based on two main reasons. Firstly, the thin pipe wall is a typical shell, and it can be easily modeled by the shell element. Secondly, the wrinkling of a pipe involves very large deformations and produces very large membrane strains, which can be greater than the necking strain within the wrinkle area.

In addition, the five-point Simpson rule was employed to calculate the cross-sectional behaviours of pipe because the true strains on pipe surfaces could be obtained directly by using this rule.

END PLATE (CAP)

The end plate (cap) is 75 mm thick, which is about 6 times thickness of the pipe wall, so it can be treated as a rigid body. In this analysis, it was modeled by the R3D3 element, which is a three-noded triangular rigid element. As a result, the running time was reduced.

5.2.2.2 MESH

To control the location of wrinkle, a prescribed imperfection layout was defined and mapped in the pipe that it was symmetric about the middle cross section and the axis of pipe. The modeled pipe was symmetric with respect to the bending plane, so only half of it was modeled.

To mesh this half pipe model, the mesh type and the mesh size have to be determined firstly. Mohareb et al. (2001) found that the non-uniform mesh layouts could trigger the wrinkle at the transition locations, where the four-node elements and the three-node elements are connected and/or the fine mesh and the coarse mesh meet. Therefore, this analysis used the uniform mesh layout. According to the results of the mesh study, which will be introduced in the subsequent sections,

this analysis employed a 95×121 mesh size, and a typical mesh is shown in Figure 5.12.

5.2.2.3 BOUNDARY CONDITIONS

In the half pipe model, both end plates are treated as rigid bodies and their movement and rotation are controlled by two pivot points (or reference nodes in ABAQUS). Specifically, the bottom pivot is constrained to allow only rotation in the bending plane; and the top pivot can only move along the axial direction and rotate in the bending plane.

The half pipe is obtained by cutting the full-scale pipe along its symmetric plane, so the pipe wall along the cutting plane has to be properly constrained. According to the symmetry, the cut wall is only allowed to move along the radial direction of the pipe and to rotate in the bending plane.

5.2.2.4 MATERIAL MODEL

The same material models were employed in the half pipe model as those used in strip model, and they were discussed in Section 5.1.1.5.

5.2.2.5 IMPERFECTION

To make the wrinkle form at the middle of the pipe, the imperfection is purposely introduced within a small area around the middle of the pipe. It is assumed to be evenly distributed along both the radial direction and the axial direction. In addition, to minimize the effect of imperfection size, the amplitude of imperfection was limited to be less than 6% of the pipe wall thickness. The imperfection was so selected based on three reasons: firstly, this analysis only focuses on the wrinkle geometry instead of the loading capacity; secondly, this analysis is a parametric study instead of an actual case study, so the imperfection can be deliberately applied to the area where the wrinkle is designed to occur; thirdly, a symmetrically distributed imperfection around the middle section can eliminate the asymmetric effect of wrinkle.

5.2.3 SOLUTION STRATEGY

For the investigated pipe, firstly it was locally buckled by bending. Then this local buckle became a wrinkle as more rotation was applied to the pipe. This is a typical unstable problem, and the ABAQUS can resolve it in three different ways.

The first approach is the dynamic approach, which treats the buckling response dynamically with inertia effects included as the structure snaps. But this approach needs to restart the terminated static procedure and switch it to a dynamic procedure when the static solution becomes unstable.

The second approach is the modified Riks method. This method can find the static equilibrium during the unstable phase of response if the loading can be considered proportional.

The last approach is the damping approach, which uses dashpots to stabilize the structure during the static analysis. This approach can handle the problems of local instabilities such as surface wrinkling, material instability, or local buckling, in which case the global load control methods such as the Riks method are not appropriate. In ABAQUS, the viscous forces are so introduced that they are big enough to prevent instantaneous buckling or collapse but not too big to affect the behaviour significantly while the problem is stable.

Because the dynamic approach needs to run two different procedures, it is inconvenient. The damping approach can be used, but it requires inputting appropriate viscous forces. Therefore, the modified Riks method was selected in this analysis.

5.2.4 PARAMETERS

The main objective of this analysis was to investigate the relation between the internal pressure and the wrinkle geometry, especially the wrinkle radius. Therefore, the internal pressure was the primary parameter. In this analysis, eight levels of internal pressures were selected, and they are 10%, 20%, 30%, 40%, 50%, 60%, 70% and 80% of SMYS. This selection is based on two reasons: the first one is that the maximum allowed internal pressure is 80% of SMYS

according to CAN/CSA Z245.1-02 (2002); the second one is to prevent forming the so-called diamond type wrinkle in pipe wall by selecting the minimum internal pressure of 10% of SMYS. The diamond type wrinkle usually occurs in unpressurized pipes as that discussed previously and it is not included this research.

In order to investigate the influence of D/t ratio on wrinkle geometry, two types of D/t ratios were used, and they are 35 and 85. The first one comes from the 11.9 mm thick Tokyo Gas pipes and the second one comes from the 6.0 mm thick TCPL pipes. These two types of pipes were also used in the full-scale pipe tests.

5.2.5 RESULTS AND DISCUSSION

5.2.5.1 TERMINOLOGIES AND SYMBOLS

For discussion convenience, the following will introduce some terminologies and their corresponding symbols.

CRITICAL STATE

The pipe is said to be in the critical state if the pipe reaches its maximum load-carrying capacity. On the load-deformation curve or the moment-curvature curve, it is the peak point. Correspondingly, this load is called the critical load, the curvature is named the critical curvature, and the strain is termed the critical strain, etc.

WRINKLE RADIUS, R_W

In this analysis, the wrinkle radius refers to the radius of wrinkle crest. The strain method is used to get the wrinkle radius from the FEA results. The expression is as follows:

$$R_w = \frac{t}{\varepsilon_e - \varepsilon_i} \tag{5.5.1}$$

where ε_e and ε_i are the engineering strain of the exterior fiber and that of the interior fiber, respectively; and t is the actual pipe wall thickness.

But for the finite membrane strain problems, ABAQUS can only give the true strain. From the FEA results of strip specimens, it found that the difference between the radius obtained from the true strains and the actual radius from the guide rod is so small that it can be neglected (see Table 5.3). Therefore, this analysis used the following formula:

$$R_w = \frac{t}{\varepsilon_{te} - \varepsilon_{ti}} \tag{5.5.2}$$

where ε_{te} and ε_{ti} are the true strain of the exterior fiber and that of the interior fiber, respectively; and t is the same as above.

WRINKLE CURVATURE, Φ_W

Similarly, the wrinkle curvature refers to the curvature at the wrinkle crest, and it is defined as follows:

$$\Phi_w = 1/R_w \tag{5.5.3}$$

GLOBAL CURVATURE, Φ_g

The global curvature is defined by the pipe length and the pivot rotations or the end rotations, and it is given by:

$$\Phi_g = \Delta\alpha/L_o \tag{5.5.4}$$

where $\Delta\alpha$ is the sum of both pivot rotations, and L_o is the length of the undeformed pipe.

GEOMETRIC PARAMETERS RELATED TO A WRINKLE

The bulging type wrinkle is the only concern of this analysis, and it can be divided into three parts: two wrinkle feet and one wrinkle head. The wrinkle feet are inward and their curvatures are defined as negative, and the wrinkle head is outward and its curvature is taken as positive. A typical bulging type wrinkle is illustrated in Figure 5.13.

In the subsequent discussions, the length of wrinkle head, l_{wh}, is the length of the undeformed wrinkle head, and similarly, the length of the wrinkle feet, l_{wf}, is the sum of the lengths of the two undeformed wrinkle feet, and the wrinkle length, l_w, is the length of the undeformed wrinkle. From these definitions, the following relation holds:

$$l_w = l_{wh} + l_{wf} \tag{5.5.5}$$

Also for discussion convenience, the following ratios are defined:

- Ratio of wrinkle length to pipe diameter, $r_w = l_w/D$
- Ratio of length of wrinkle feet to pipe diameter, $r_{wf} = l_{wf}/D$
- Ratio of length of wrinkle head to pipe diameter, $r_{wh} = l_{wh}/D$

5.2.5.2 MESH STUDY

The mesh study was conducted along both the circumferential direction and the longitudinal (or axial) direction. The mesh study focused on both global behaviour and local behaviour. Specifically, the bending moment–global curvature and the wrinkle radius were investigated. This is different from the traditional mesh study, which only concerns the prebuckling behaviour and the global behaviour.

CIRCUMFERENTIAL DIRECTION

When conducting the mesh study in this direction, the number of elements along the longitudinal direction was kept constant at 61, and the number of elements in the circumferential direction was changed. The mesh was considered fine enough if the increase of element quantities in the circumferential direction could not considerably change the result or when the solution was stable. Five types of mesh size were tried and the results are given in Figure 5.14.

Figure 5.14a shows the global behaviour, and it exhibits that even a mesh size as sparse as 11 × 61 can give satisfactory critical bending moment and stable prebuckling behaviour. But to get a steady postbuckling behaviour, the mesh size has to be at least as fine as 47 × 61, which is four times finer than that required by the prebuckling analysis. Figure 5.14b shows the results of wrinkle radius and it

again concludes that the wrinkle radius become stable when the mesh size is 47 × 61.

Based on the above mesh study, this analysis conservatively used 95 elements along the circumferential direction.

LONGITUDINAL DIRECTION

In this mesh study, the number of elements in the circumferential direction was kept constant as 95, and the number of elements along the longitudinal direction was changed from 31 to 185. The results are shown in Figure 5.15.

Figure 5.15a shows the global behaviour and Figure 5.15b exhibits the wrinkle radius. From these two figures, it can be concluded that a mesh size of 95 × 123 is fine enough to obtain stable postbuckling behaviour and satisfactory wrinkle radius.

Based on these two mesh studies, a mesh size of 95 × 121 was chosen to conduct the subsequent FEA.

5.2.5.3 WRINKLE DEVELOPMENT

When a local buckle occurs, the curvature of the buckled segment will change. Hence, by investigating the curvature variation, how a wrinkle develops can be understood.

Figures 5.16a and 5.16b show the wrinkle development in a 20 inch (508.0 mm) pipe and in a 16 inch (406.4 mm) pipe, respectively, where the water pressure is 40% of SMYS and the elements are on a piece of strip cut from the wrinkle. From these two figures, it can be seen that the wrinkle is very small at the critical state and it develops as the pipe is further deformed. It can also be seen that as soon as the wrinkle forms, the locations of inflections are nearly independent of the progress of global deformation. The locations of tangential points do not move outwards much and, specifically, the movement is only about the length of one element. Based on this observation, it can be concluded that the wrinkle length is independent of the loading stage.

5.2.5.4 WRINKLE LENGTH

Since the wrinkle length does not depend on the loading stage for a normal wrinkle, the wrinkle length can be compared among the wrinkles developed under different water pressures.

To determine the wrinkle length from the FEA, the following observations can be utilized. The local curvature is negative within the wrinkle foot and positive within the wrinkle head. The wrinkle head and the two wrinkle feet are connected by two inflection points, where the curvature is zero. The wrinkle foot and the normal pipe wall are connected by a tangential point, beyond which the curvature almost becomes constant. Therefore, the wrinkle length can be obtained by finding the locations where the local curvature starts to become near constant, and the length of wrinkle head can be determined by locating the points where the curvature changes from positive to negative.

The results of wrinkle lengths under different internal pressures are given in Table 5.4. From this table, it can be found that the wrinkle length is related to both D/t ratio and internal pressure. The higher the internal pressure and/or the smaller the D/t ratio, the longer the wrinkle length will be. Theoretically, the internal pressure tends to flatten the wrinkle, so a higher internal pressure will produce a longer wrinkle. As for the D/t ratio, its effect can be explained by focusing on a strip with a unit width which is cut from an actual pipe. If the pipe has the same diameter and the strip is constrained in the same way, then the thicker the strip the higher the critical load, will be, which will yield the longer wrinkle length. In addition, if two strips are cut from two pipes have the same thickness but different D/t ratios, the cross section of the strip cut from the larger diameter pipe will be flatter (closer to the rectangular section) than the one cut from a smaller diameter pipe. Because the flat strip has a weaker moment-resistance capacity than the curved strip, the former will give a shorter wrinkle length than the latter.

The other observation from this figure is that the wrinkle feet contribute more to the wrinkle length than the wrinkle head, and the internal pressure affects the length of wrinkle foot much more than that of wrinkle head. On the wrinkle head,

most of the internal pressure goes in the longitudinal direction of the pipe and this will be balanced by the axial load; but on the wrinkle feet, most of the internal pressure goes in the direction of perpendicular to the axial load and this will push the pipe wall outward, so the wrinkle feet will be prolonged.

Specifically, for the 16 inch (406.4 mm) pipe, the wrinkle length varies from about 0.54 to 0.93 times of the pipe diameter and the length of the wrinkle head fluctuates from 0.13 to 0.26 times of the pipe diameter when the internal pressure is changed from $0.1p_y$ to $0.8p_y$. For the 20 inch (508 mm) pipe, the wrinkle length increases from about 0.44 to 0.60 times of the pipe diameter and the length of the wrinkle head grows from 0.10 to 0.16 times of the pipe diameter when the internal pressure rises from $0.1p_y$ to $0.8p_y$.

Finally, it has to be mentioned that the location of the inflection points can be easily detected, but the tangential points are not so easy to be located. In the case of pure bending, the curvature is the same everywhere of normal pipe wall, so in this case the tangential points can be clearly identified by looking at where the curvature becomes constant. But in effect, the normal pipe wall does not have such a perfect uniform curvature distribution, so this makes the identification of tangential points very difficult. On the above analysis, an approximate definition was employed, and it defined the tangential point at which the change of local curvature was less than 0.1/m. It can be expected that the wrinkle length is definition-dependent. A strict definition will give a longer wrinkle length and a loose definition will yield a shorter wrinkle length.

5.2.5.5 WRINKLE RADIUS

Because an obvious wrinkle has not developed before the critical state is reached, only the stage after the critical state will be discussed in the following. Also because two types of D/t ratios were analyzed, they will be introduced separately.

16 INCH PIPE, D/t = 34

The FEA results show that the wrinkle radius, R_w, decreases as the global curvature increased, and the results are shown in Figure 5.17.

Figure 5.17a shows the overall profile of the wrinkle radius variation with the global curvature. It exhibits that the wrinkle radius drops very fast and follows a linear path at first, and this period can be called the wrinkle initiation zone, where a small wrinkle quickly forms. Then, the decrease of the wrinkle radius gradually slows down, and this period can be named as the wrinkle growth zone, where the wrinkle gradually develops. Finally, this decrease becomes very slow and follows a linear pattern, and this period can be termed as the wrinkle mature zone, where the wrinkle can be considered as fully developed.

To get a close observation of the variation of wrinkle radius from wrinkle growth zone to the wrinkle mature zone, portions of these curves can be presented on a magnified scale and the results are shown in Figure 5.17b. This figure shows that at the same global curvature level, the higher the internal pressure is, the larger the wrinkle radius becomes. And it also exhibits that the higher the internal pressure is, the later the wrinkle mature zone occurs.

From the above observations, it can be concluded that the wrinkle radius is greatly zone-dependent, and it matures only when the wrinkle is fully developed.

20 INCH PIPE, D/t = 85

The results are given in Figure 5.18. Compared with Figure 5.17, it can be found that the only difference between them is that the curves in Figure 5.18 are denser than those in Figure 5.17.

5.2.5.6 GLOBAL BEHAVIOUR

In the following, the bending moment−global curvature curves will be discussed to investigate the influence of internal pressure.

16 INCH PIPE, D/t = 34

The variation of bending moment with the global curvature is shown in Figure 5.19a. From this figure, a couple of observations can be made as follows.

Firstly, the internal pressure does not affect the prebuckling behaviour. It is obvious that all curves merge into a single curve although the internal pressure

varies greatly from $0.1p_y$ to $0.8p_y$. The reason is that for the investigated pipes, the prebuckling behaviour mainly depends on the material property and the cross sectional property.

Secondly, the critical bending moment is larger at the low internal pressure level than that at the high internal pressure level. Generally, the higher the internal pressure the lower the maximum bending moment will be. It is known that the high internal pressure will induce high hoop stresses. According to von Mises yield rule, see Equation (4.30), the high hoop stress will decrease the effective yield stress of the pipe, so the maximum bending moment will drop.

Thirdly, the peak is sharp when the internal pressure is low and it becomes flat when the internal pressure is high. The peak is almost a point when the internal pressure is $0.1p_y$, but the peak has a large plateau when the internal pressure is increased to $0.8p_y$.

Finally, the higher the internal pressure the longer the postbuckling path will be. The reason is that the high internal pressure tends to flatten the wrinkle, so the wrinkle development is retarded and the postbuckling path is prolonged.

20 INCH PIPE, D/t = 85

The variation of the bending moment with the global curvature is shown in Figure 5.19b. From this figure, the same observations can be made as those of the 16 inch pipe. The only difference is that the 20 inch pipe has sharper peaks and shorter postbuckling paths than that of the 16 inch pipe.

5.2.6 SUMMARY

Based on the analysis of the half pipe model, it can be seen that the wrinkle radius depends not only on the internal pressure but also on the global deformation and the D/t ratio. Generally, a lower internal pressure and/or a higher D/t ratio will produce a smaller wrinkle radius. During the postbuckling stage, the wrinkle radius decreases as the loading progresses, so it is impossible to get a relation between the wrinkle radius and the internal pressure.

However, for the purpose of engineering application, it is possible to get the wrinkle radius if the same standard, i.e. the same loading stage, is used for the wrinkled pipes with the same D/t ratio. So the problem turns into how to determine this standard. From the previous discussion, it is known that the wrinkle radius becomes more stable in the wrinkle mature zone than in the other two zones, so it will minimize the influence of loading stage on the wrinkle radius if the standard is made within this zone.

In the wrinkle mature zone, where the wrinkle is well developed, the wrinkle radius still decreases as the loading prolongs further, although this decrease is small. However, if the wrinkle is well developed, the pipes can fail in a very low LCF fracture or by tearing fracture if a large enough axial deformation is applied. Based on those considerations, it is recommended to select the intersection of the wrinkle development zone and the wrinkle mature zone as the standard loading stage, and then the wrinkle radius can be obtained according to the D/t ratio.

5.3 FULL-SCALE PIPE MODEL

5.3.1 INTRODUCTION

In the next chapter, a series of LCF life prediction models will be developed based on the results of strip tests for wrinkled pipes. However, to apply these models to full-scale pipes, the residual true strain at the wrinkle crest and the damage parameter have to be determined. The residual true strain is indispensable to evaluate the ductile damage, and the damage parameter is requisite to asses the fatigue damage. It is very difficult to obtain the residual true strain and the damage parameter directly from the experiment as discussed before. Therefore, the FEA method has to be employed to fulfill this task.

In Section 5.2, a half pipe model was developed for conducting the parameter study, but it can not be used to simulate full-scale pipes for two reasons. Firstly, the loading of full-scale pipes involves both the monotonic loading and the cyclic loading, but the half-pipe model is only monotonically loaded. Secondly, actual

imperfections are randomly distributed in pipe walls, so that full-scale pipes are asymmetric.

To develop the full-scale pipe model, the mesh has to be very fine because this analysis focuses on the local behaviour during the postbuckling stage. In addition, to acquire acceptable accuracy and confidence, the finite element model has to be validated by the parameters that were measured in full-scale pipe tests.

5.3.2 FINITE ELEMENT MODEL

Although the full-scale pipe model cannot copy the half pipe model, it can be developed based on the half pipe model.

5.3.2.1 ELEMENT

The same types of elements are employed in the full-scale pipe model as those in the half pipe model.

5.3.2.2 MESH

Because the imperfections are randomly distributed, the wrinkle can occur everywhere on the pipe wall. Also because a non-uniform mesh can trigger wrinkles in the transition zone, this analysis employs the uniform mesh layout. Moreover, according to the mesh study on the half pipe model, the full-scale pipe model uses a 126 x 122 mesh, which gives almost the same mesh size as the half pipe model. A typical mesh is shown in Figure 5.20.

5.3.2.3 BOUNDARY CONDITIONS

The boundary conditions adopted in the finite element model are as follows: out of the bending plane, all freedoms are constrained; in the bending plane, only the axial direction of the bottom pivot is constrained during the entire loading stage, the constraints of other freedoms are changed according to loading steps.

5.3.2.4 MATERIAL MODEL

Because the cyclic loading was employed in full-scale pipe tests, the full-scale pipe model tried the combined hardening for investigating cyclic behaviours by

specifying half-cycle test data. However, compared with test results, the combined hardening rule could not give better analysis results than the isotropic hardening rule, thus the same material model as used in both the strip model and half-pipe model was employed in this full-scale pipe model.

5.3.2.5 IMPERFECTION

In this analysis, the measured imperfections, as shown in Figures 5.21a) and 5.21b), were used for LCF16N1 and LCF20N1, respectively. These imperfections were mapped to the model automatically by a computer program, and the details are not included here.

5.3.2.6 LOADING STEPS

The loading steps in the FEA cannot be exactly simulated as the actual loading procedure because of the limitation of the adopted software package, but they are closely modeled to achieve the same objectives.

From the test, it is known that the rotation of top pivot was different from that of the bottom pivot, so the FEA has to account for this rotation difference. As a preliminary study, the total amount of pivot rotation was applied in one step, but it was found that the post-buckling path was much lower than the recorded path in the test. By further investigation, it was found that the rotation histories of pivots in the FEA were different from that in the test, although their starting and stopping positions were the same. So it is natural to split the rotation histories into many small steps and the FEA uses those small steps to simulate the bending of the pipe. For discussion convenience, this type of loading method can be called the step-wise loading method. Also, because the loading process is very complicated, the multi-steps were employed in this FEA and the details are as follows:

Step 1: Increase the internal pressure to 40% of SMYS, i.e. 11.45 MPa for the 16 inch (406.4 mm) pipe and 5.00 MPa for the 20 inch (508.0 mm) pipe;

Step 2: Increase the axial load to the designated value, which counteracts the axial loads caused by the thermal effect, the internal pressure, and the Poisson’s effect,

and it is 2019 kN for the 16 inch (406.4 mm) pipe and 1515 kN for the 20 inch (508 mm) pipe;

Step 3 to step 7: Rotate the pivots by the step-wise loading method, which includes five steps;

Step 8: Lock the rotation of pivots and push down the top pivot to the designated level, which is 96.5 mm for the 16 inch (406.4 mm) pipe and 45.6 mm for the 20 inch (508 mm) pipe;

Step 9: Release the axial displacement constraint at the top pivot;

Step 10: Decrease the axial load at the top pivot to the minimum level;

Step 11: Increase the water pressure to the actual maximum level, which is 24.19 MPa for the 16 inch (406.4 mm) pipe and 6.56 MPa for the 20 inch (508.0 mm) pipe;

Step 12: Release the internal pressure back to 40% of SMYS;

Step 13: Repeat step 8;

Step 14: Repeat step 9;

Step 15 to step 17: Repeat step 11 to step 13.

In the above, step 3 to step 7 simulate the process of monotonically bending the pipe by the desired rotations of moment arms; step 8 to step 13 generate the first cycle of loading and step 13 to 17 produce the second cycle, so two loading cycles are modeled. It can be seen that only 17 steps are analyzed because it is impossible and also unnecessary to simulate all the loading cycles of the test.

5.3.3 RESULTS, COMPARISON AND DISCUSSION

In the FEA, both the axial load and the bending moment were applied to the pivots, and the corresponding responses were the pivot rotation and the RAD between pivots. So the following will focus on two types of curves: one is the pivot moment vs. the pivot rotation, and the other is the pivot axial load vs. the

RAD between pivots. In addition, the deformed shape, the wrinkle geometry and the local behaviour will be discussed.

5.3.3.1 SPECIMEN LCF16N1

PIVOT MOMENT VS. PIVOT ROTATION

The results of both the test and the FEA are shown in Figures 5.22 and 5.23.

Figure 5.22 shows the results at both the top pivot and the bottom pivot. It can be seen that a considerable difference exists between the pivot moments of these two pivots in the FEA, but this difference is negligible in the test. The main reason is that the constraints of the pivots in the FEA are different from those in the test. In the actual test setup, although the pivots were pulled by four tie rods horizontally to restrict the horizontal movement in the bending plane, they were not totally restrained based on two reasons: on one hand, these tie rods were frequently adjusted to keep their internal forces below 6 kN for the safety concern during the test; on the other hand, they have finite stiffness to resist their axial deformations. But in the finite element model, the horizontal movement of the pivots is totally restricted. Therefore, their pivot moments are different.

Figure 5.23 shows the results of the average pivot moment vs. the average pivot rotation. The average pivot moment is the average of the top pivot moment and the bottom pivot moment; and similarly, the average pivot rotation is the average of the top pivot rotation and the bottom pivot rotation. From this figure, it can be found that the FEA curve is a little bit stiffer than the experimental curve during the pre-buckling stage, and this can be attributed to the difference of their pipe end constraints. In the actual test setup, the collars were used to constrain the pipe ends, but they were loosened as soon as the pipe was pressured to the designated level; but in the finite element model, the pipe wall at both ends were simply thickened to simulate the constraint effect of collars, and this gave more constraint on the pipe ends than the loosened collars. So the pipe in the finite element model is stiffer than that in the test. As for the maximum average pivot moment, the FEA result is only a little bit less than the test result; specifically, the

difference is only 3.28% of the test result. During the post-buckling stage, the FEA curve shows a shorter plateau and a smoother descending slope than the experimental curve. Because the wrinkle was near the collars in the test, this difference can also be attributed to the pipe end constraint. Specifically speaking, the stronger constraint of the pipe ends made the local buckling occur earlier and made the global deformation more localized in the wrinkle region in the FEA than in test.

PIVOT AXIAL LOAD VS. PIVOT RELATIVE AXIAL DISPLACEMENT

The results are shown in Figure 5.24. In the first ascending path, the FEA shows the almost the same results as the test. As for the plateau, the RAD between pivots in the FEA is only about 3 mm larger than that in the test, and the difference is only 8.18% of the test result. In the second ascending path, they show almost the same increasing rate. As for the maximum pivot axial load, the FEA gives a smaller value than the test, and the difference is about 6.62% of the test result. In the descending path, the test shows a slightly quicker decreasing rate than the FEA. For the first cycle of loading, the FEA gives a little bit fatter loop than the test, but the differences between the ascending and descending slopes of this loop are very small. In the second cycle, the loop of the FEA is very similar to that of the test.

GLOBAL RAD VS. LOCAL RAD

The phenomenon of ‘deformation localization’ can be easily understood by investigating the relation between the global deformation and the local deformation, and the results are shown in Figure 5.25. The global deformation is the RAD of the pipe on its concave side, and the local deformation is the RAD of the wrinkle on the concave side. From this figure, it can be seen that the whole curve can be roughly divided into three portions: along the segment ‘OA’, the local deformation increases proportionally to the global deformation, but the slope of this segment is very small; beyond the point ‘A’, the slope of the curve gradually increases, and this indicates that the local buckle gradually develops and the global deformation gradually localized into the wrinkle area; beyond the point

'B', the slope of the curve is near unity, and this indicates that the wrinkle is totally matured and the global deformation was totally localized into the wrinkle area. The same phenomenon was observed from the test (see Figure 4.20).

WRINKLE RADIUS

For this program, one of the major objectives of conducting the FEA is to obtain the wrinkle radius, which is essential to evaluate the ductile damage due to the monotonic loading. In the FEA, the wrinkle radius can be determined from the true strains on both the inside surface and the outside surface of the wrinkle crest according to Equation (5.5.2). Because the wrinkle radius depends on the loading stage, Figure 5.26 presents the results of the wrinkle radius on the scale of the RAD of the pipe on the concave side. During the test, some wrinkle shapes were replicated by a custom-made device, so their wrinkle radii can be measured. These measured results are also shown in Figure 5.26. It can be seen that the wrinkle radii given by the FEA agree well with the measured results, so the FEA can be used to evaluate the wrinkle radius.

DEFORMED PIPE SHAPE

Figure 5.27 shows the comparison of the deformed pipe shape between the FEA and the test, and it can be seen that both the wrinkle shape and the wrinkle location can be approximately predicted by the FEA.

5.3.3.2 SPECIMEN LCF20N1

PIVOT MOMENT VS. PIVOT ROTATION

The results of both the test and the FEA are shown in Figures 5.28 and 5.29. From these two figures, the same observations can be obtained for the specimen LCF20N1 as those for the specimen LCF16N1, so no further details will be presented.

PIVOT AXIAL LOAD VS. RAD BETWEEN PIVOTS

The test and FEA results are shown in Figure 5.30. It can be seen that they agree well with each other during the monotonic loading stage, but they show a big

difference during the cyclic loading stage. Specifically, the loops produced by the FEA are much thinner than the experimental results. The differences are caused by their different minimum values of the RAD between pivots. During the test, the minimum RAD between pivots was generated by increasing the water pressure and the maximum RAD between pivots was produced by controlling the MTS stroke. In the FEA, the pipe is exactly loaded according to the loads recorded in the test, so it is not surprising that the maximum RAD coincides well with the test results. But the minimum RAD between pivots is generated by the maximum internal pressure, which is also the same as that in the test, so the small minimum RAD between pivots indicates that the finite element model is much stiffer than the actual pipe. The similar cyclic behaviour can be obtained if the maximum internal pressure is increased to 70% of SMYS during the cyclic loading stage, and the results are given in Figure 5.31.

GLOBAL RAD VS. LOCAL RAD

The relation between the global RAD and the local RAD is shown in Figure 5.32. From this figure, the same conclusions as those in the 16 inch pipe can be drawn. But the wrinkle matures more quickly in the 20 inch pipe than in the 16 inch pipe.

WRINKLE RADIUS

Figure 5.33 shows the wrinkle radii predicted by the FEA and those measured during the test, and they agree very well.

DEFORMED PIPE SHAPE

Figure 5.34 shows the deformed pipe shape produced by the FEA and that generated by the test, and it can be seen that both the wrinkle shape and the wrinkle location can be approximately predicted by the FEA.

5.4 SUMMARY AND CONCLUSIONS

Three finite element models were developed in this chapter. The first one was the strip model. It simulated the process of monotonically bending a strip, and it was used to evaluate the residual true stress and the residual true strain in the strip

bend. The second one was the half pipe model, and it was created to investigate the wrinkle geometry. The last one was the full-scale pipe model, and it was used to provide a numerical solution to full-scale pipe tests and to obtain some requisite parameters for applying the developed LCF life prediction models to full-scale pipes.

From the strip model, it was found that the residual true strain depends on the R/t ratio only and this conclusion is coincident with that of the theoretical analysis. Further comparison found that the residual strain from the FEA agrees well with that from the theoretical analysis. It was also found that the residual strain is concentrated in the strip bend and evenly distributed in this area. Finally, the theoretical analysis is recommended for evaluating the residual engineering strain and the FEA is recommended for estimating the residual true strain.

From the half pipe model, it was found that the wrinkle geometry depends on the pipe geometry, the internal pressure and the global deformation. A large D/t ratio, and/or a low internal pressure, and/or a greater global deformation will generate a small and sharp wrinkle.

From the full-scale pipe model, it was found that the FEA can simulate both of the monotonic loading and the cyclic loading. By comparing with test results, it was found that the finite element model works well for the specimen LCF16N1, but shows some differences during the cyclic loading stage for the specimen LCF20N1. Moreover, the global deformation is found to localize into the wrinkle area as the wrinkle develops, and become totally localized when the wrinkle matures. The wrinkle radius is found to agree well with the measurement results; and the deformed pipe shape, the wrinkle location and the wrinkle shape are also found to be similar to those observed in the test.

Above all, these three models exhibit that the FEA is a powerful tool to conduct the post-buckling analysis and they can be used for future study.

Table 5.1: Comparison between the results of FEA and theoretical analysis

R/t	Inside surface			Outside surface		
	FEA[1]	Theoretical[2]	Difference[3]	FEA[1]	Theoretical[2]	Difference[3]
4.82	0.000	0.000	0.0%	0.100	0.094	6.1%
5.00	-0.098	-0.091	8.1%	0.098	0.091	7.6%
5.42	-0.088	-0.084	4.4%	0.087	0.084	3.5%
5.83	-0.083	-0.079	5.2%	0.083	0.079	4.6%
6.67	-0.073	-0.070	4.8%	0.073	0.070	3.9%
7.50	-0.065	-0.063	3.4%	0.064	0.063	2.1%

Note:

[1] FEA results are true strains.

[2] Theoretical results are obtained by converting the results of Equation (3.7) to true strains.

[3] Difference = (FEA - Theoretical)/Theoretical*100%.

Table 5.2: Applied loads in half pipe model

D (mm)	t (mm)	D/t	p (MPa)	P_p (kN)
407.26	12.42	32.8	2.86	836
			5.73	888
			8.59	939
			11.45	991
			14.32	1042
			17.18	1094
			20.05	1145
			22.91	1196
508.83	6.79	74.9	1.25	627
			2.50	672
			3.75	717
			5.00	762
			6.25	807
			7.50	853
			8.75	898
			10.00	943

Note: p is the water pressure and P_p is the axial load applied at pivot .

Table 5.3: Comparison of radius of rod and radius calculated from true strain

Thickness	True strain		Radius (mm)		
(mm)	Inside surface	Outside surface	Rod	FEA	Difference*
6.00	-0.2291	0.1857	15	14.47	-3.55%
	-0.1604	0.1374	20	20.15	0.75%
	-0.1274	0.1120	25	25.07	0.27%
	-0.1034	0.0934	30	30.49	1.64%
	-0.0867	0.0794	35	36.13	3.22%
	-0.0759	0.0700	40	41.12	2.80%
	-0.0668	0.0619	45	46.62	3.60%
8.30	-0.3244	0.2436	15	14.61	-2.58%
	-0.2339	0.1884	20	19.65	-1.73%
	-0.1791	0.1505	25	25.18	0.71%
	-0.1467	0.1276	30	30.26	0.87%
	-0.1252	0.1109	35	35.16	0.46%
	-0.1057	0.0950	40	41.35	3.37%
	-0.0923	0.0838	45	47.14	4.75%
12.56	-0.5349	0.3450	15	14.27	-4.84%
	-0.3940	0.2801	20	18.63	-6.83%
	-0.2934	0.2255	25	24.21	-3.17%
	-0.2285	0.1855	30	30.33	1.11%
	-0.1953	0.1629	35	35.06	0.17%
	-0.1661	0.1419	40	40.77	1.93%
	-0.1485	0.1285	45	45.34	0.77%

Note:

* Difference = (Radius of rod - Radius from FEA)/Radius of rod×100%.

Table 5.4: FEA results of wrinkle geometries

D/t	β	l_w mm	l_w/D	l_{wf} mm	l_{wf}/D	l_{wh} mm	l_{wh}/D
35	0.1	261.8	0.64	208.1	0.51	53.7	0.13
	0.2	263.7	0.65	207.3	0.51	56.3	0.14
	0.3	276.7	0.68	215.5	0.53	61.2	0.15
	0.4	284.6	0.70	214.0	0.53	70.6	0.17
	0.5	300.9	0.74	219.4	0.54	81.5	0.20
	0.6	317.9	0.78	230.2	0.57	87.7	0.22
	0.7	351.1	0.86	255.1	0.63	96.0	0.24
	0.8	378.9	0.93	272.6	0.67	106.3	0.26
85	0.1	224.3	0.44	174.8	0.34	49.5	0.10
	0.2	226.9	0.45	176.4	0.35	50.6	0.10
	0.3	230.8	0.45	178.3	0.35	52.5	0.10
	0.4	237.2	0.47	182.3	0.36	54.9	0.11
	0.5	245.5	0.48	187.0	0.37	58.5	0.11
	0.6	260.6	0.51	196.9	0.39	63.6	0.13
	0.7	278.4	0.55	207.3	0.41	71.0	0.14
	0.8	306.8	0.60	223.5	0.44	83.4	0.16

Note:

$\beta = p/p_y$

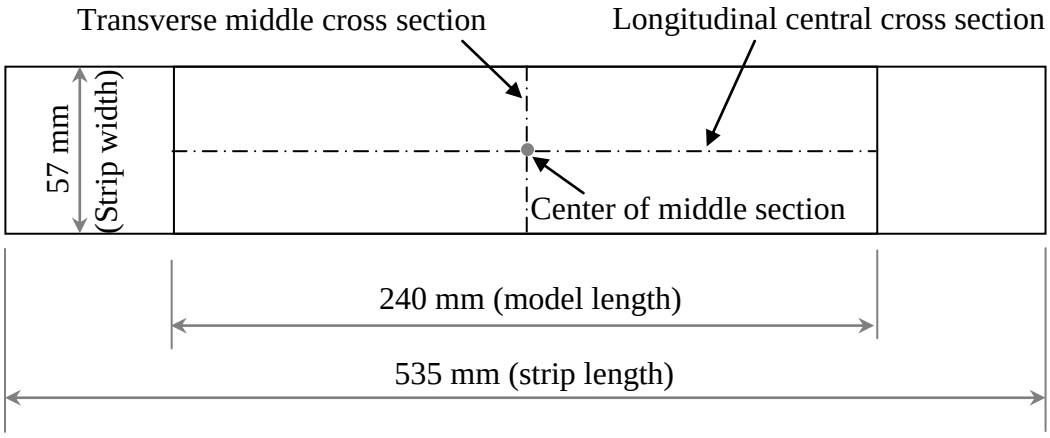

Figure 5.1: Illustration of specific locations

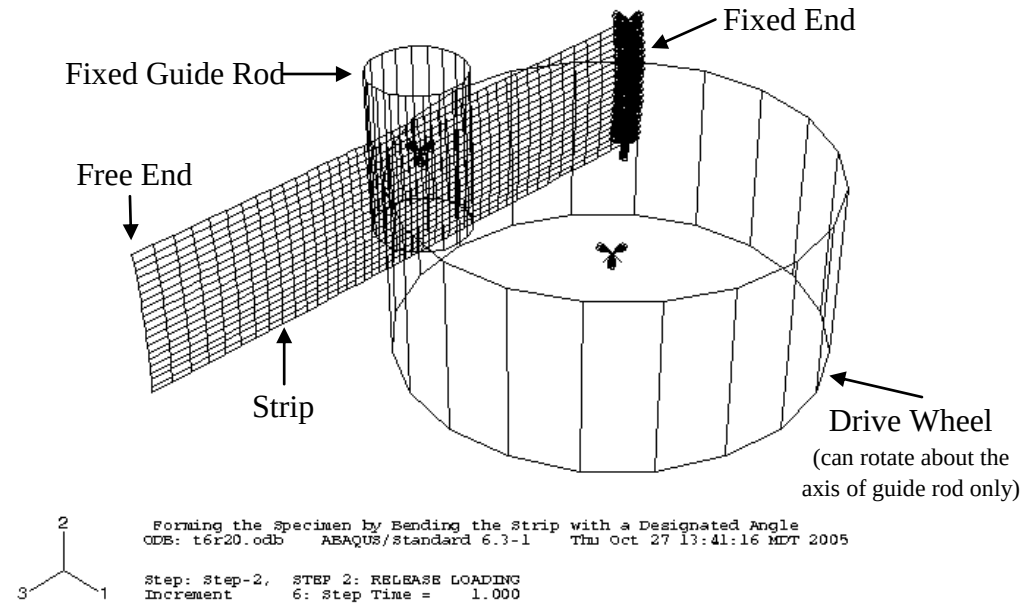

Figure 5.2: Finite element model of strip

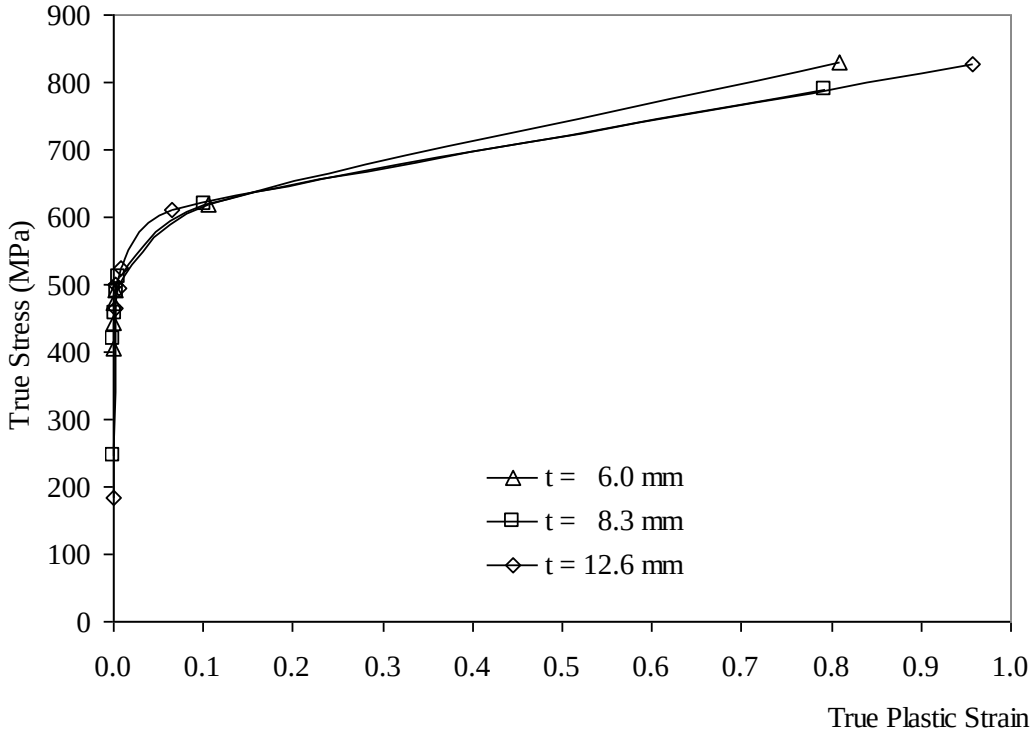

Figure 5.3: Plastic behaviours of material

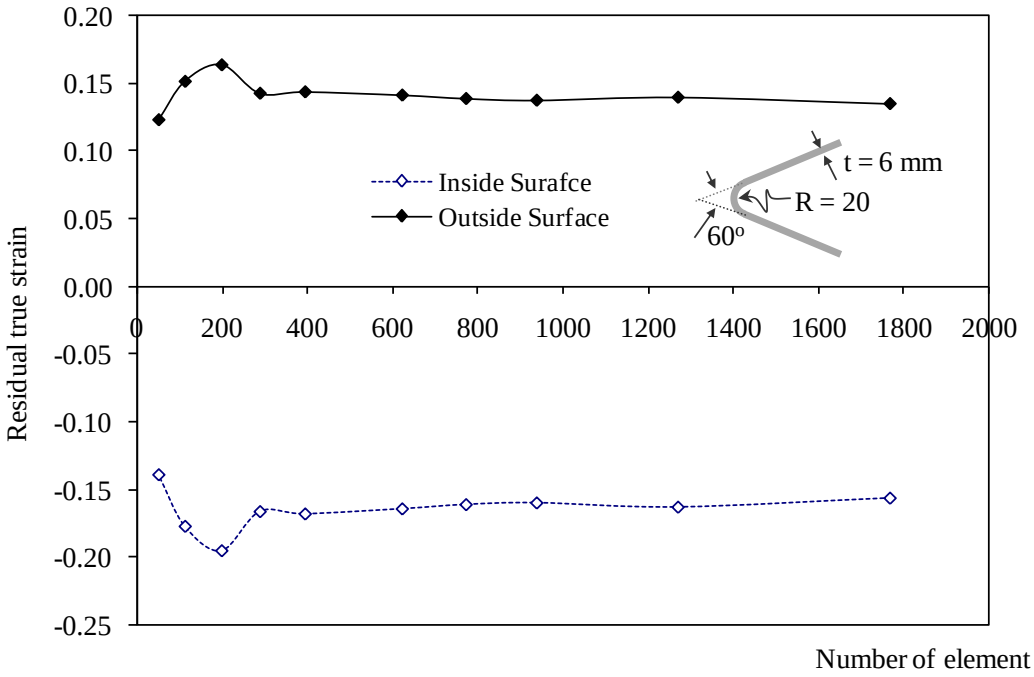

Figure 5.4: Variation of residual true strain with number of element

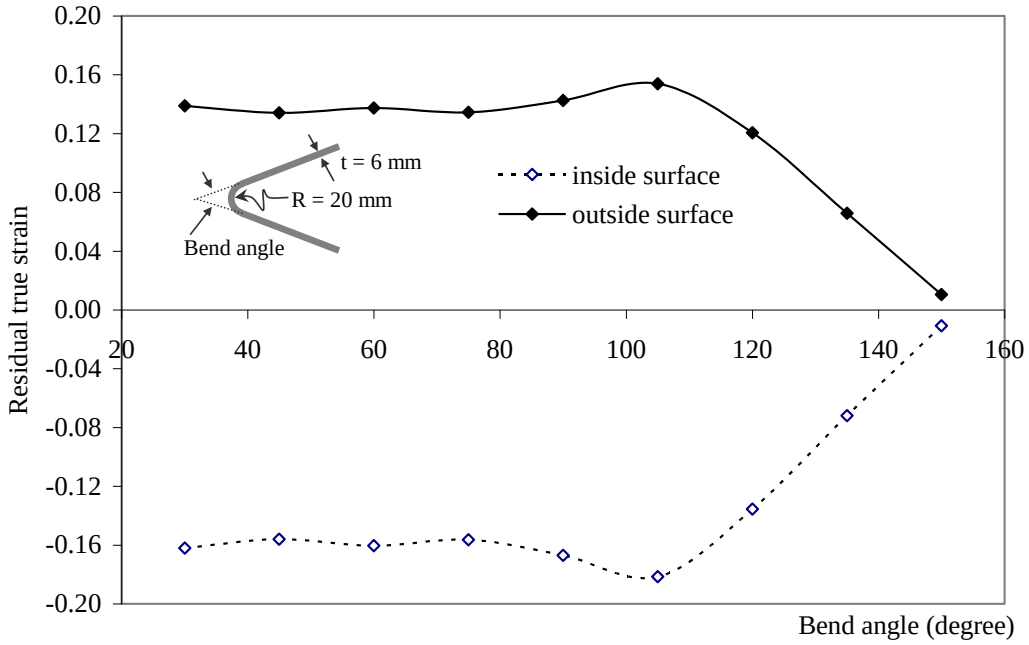

Figure 5.5: Variation of residual true strain with bend angle

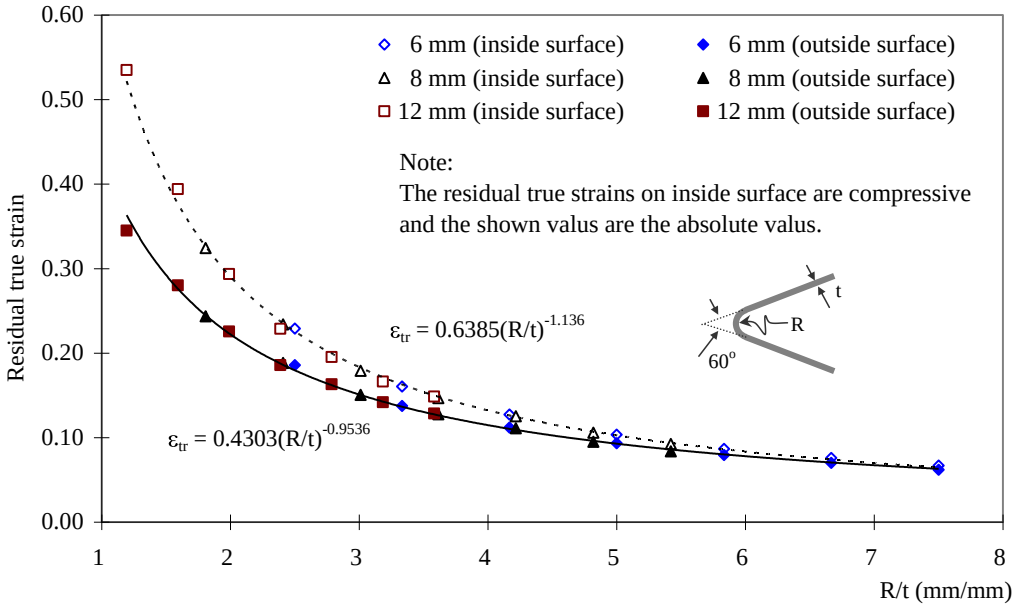

Figure 5.6: Variation of residual true strain with R/t ratio

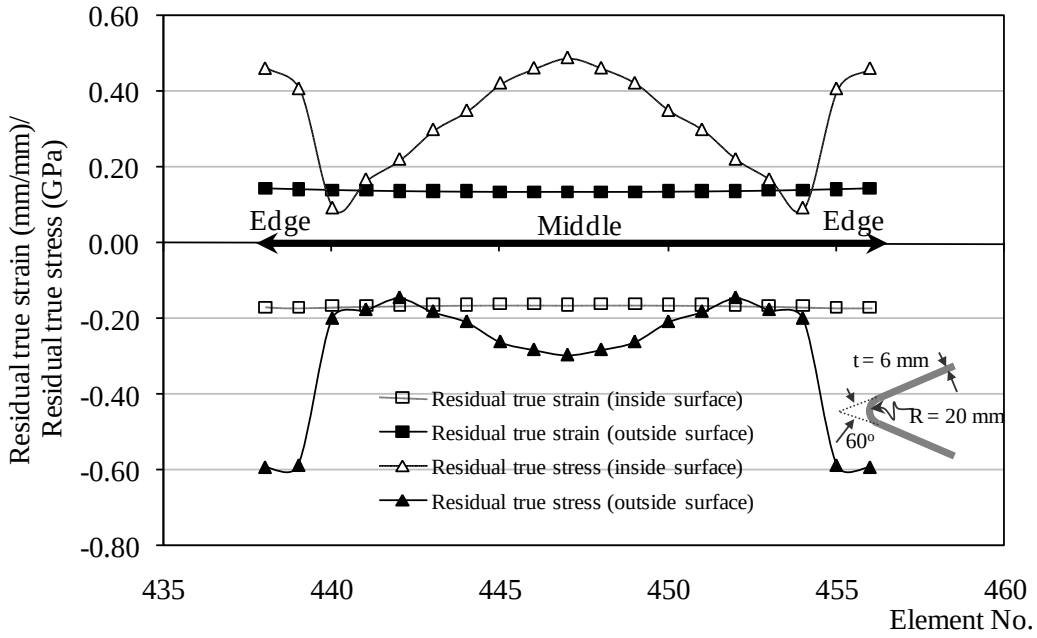

Figure 5.7: Distributions of residual true stress and residual true strain on the transverse middle cross section

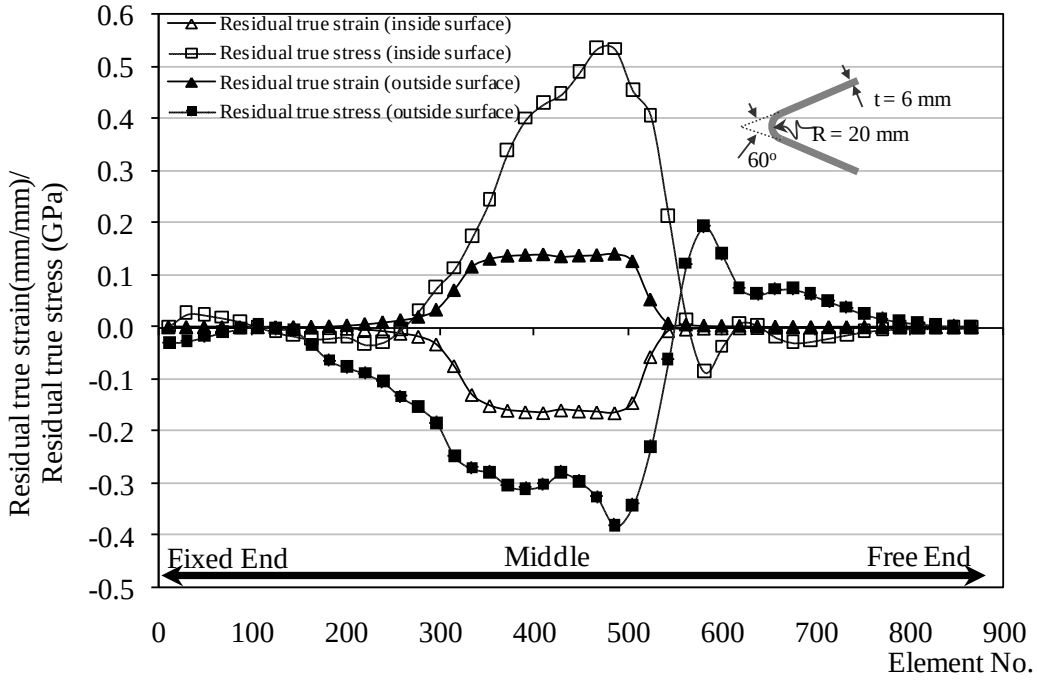

Figure 5.8: Distributions of residual true stress and residual true strain on the longitudinal middle cross section

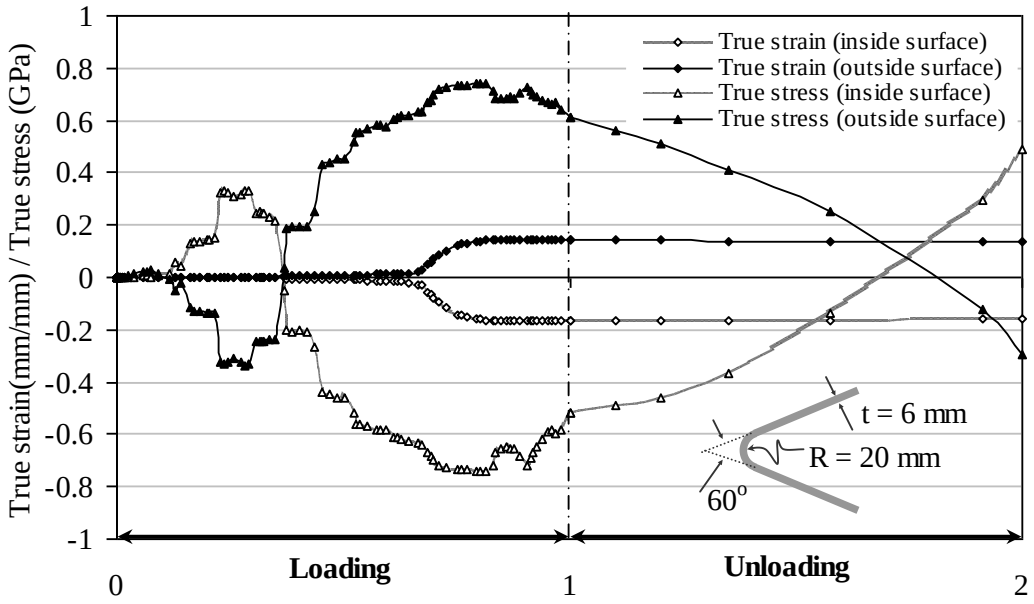

Figure 5.9: True stress and true strain histories at the center of middle cross section

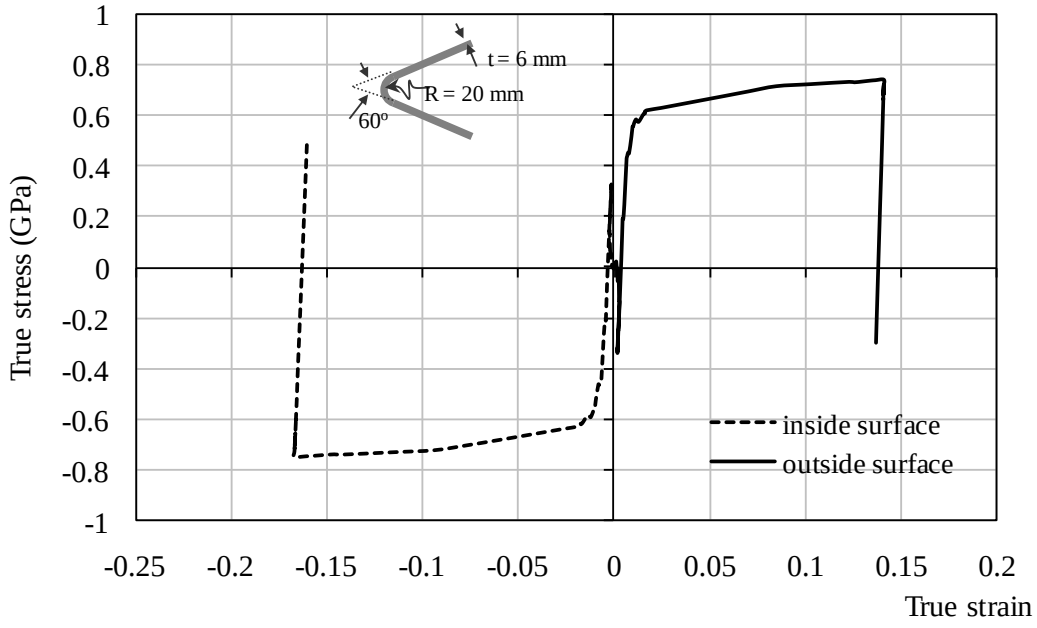

Figure 5.10: Relations of true stress and true strain at the center of middle cross section

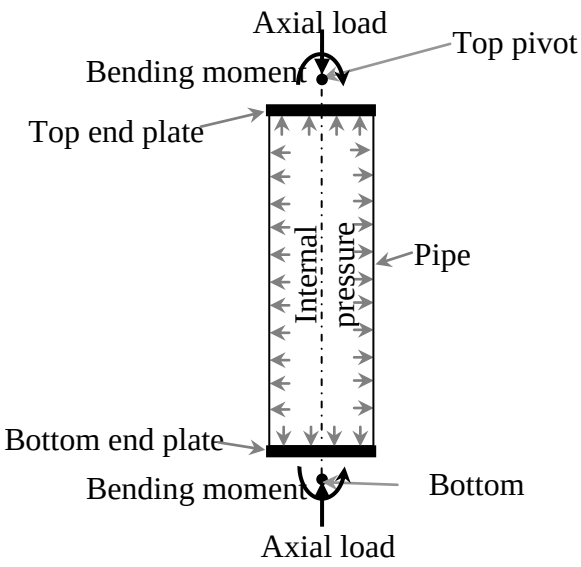

Figure 5.11: Illustration of loading of a pipe

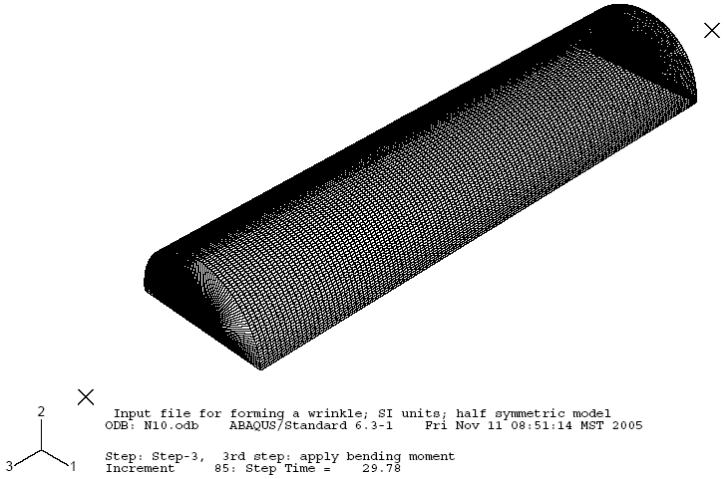

Figure 5.12: A typical mesh of half pipe model

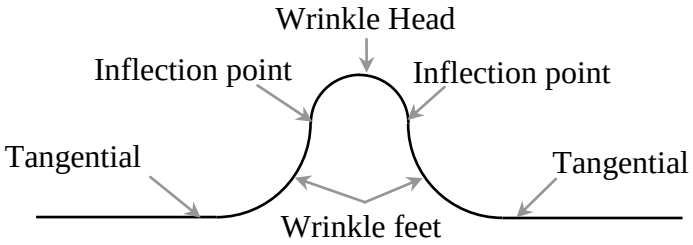

Figure 5.13: Illustration of a wrinkle and its geometry

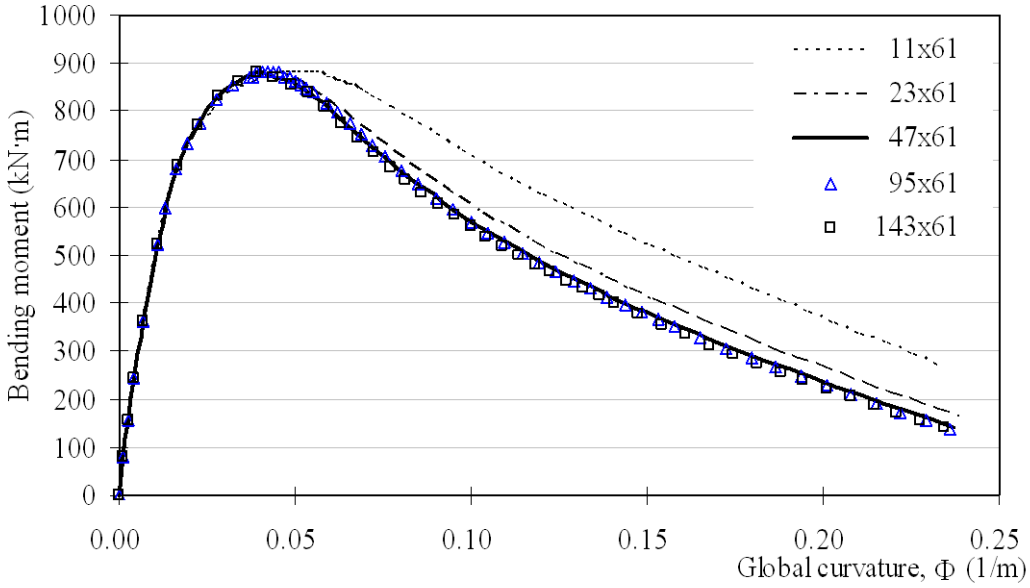

a) Global behaviour: bending moment vs. global curvature

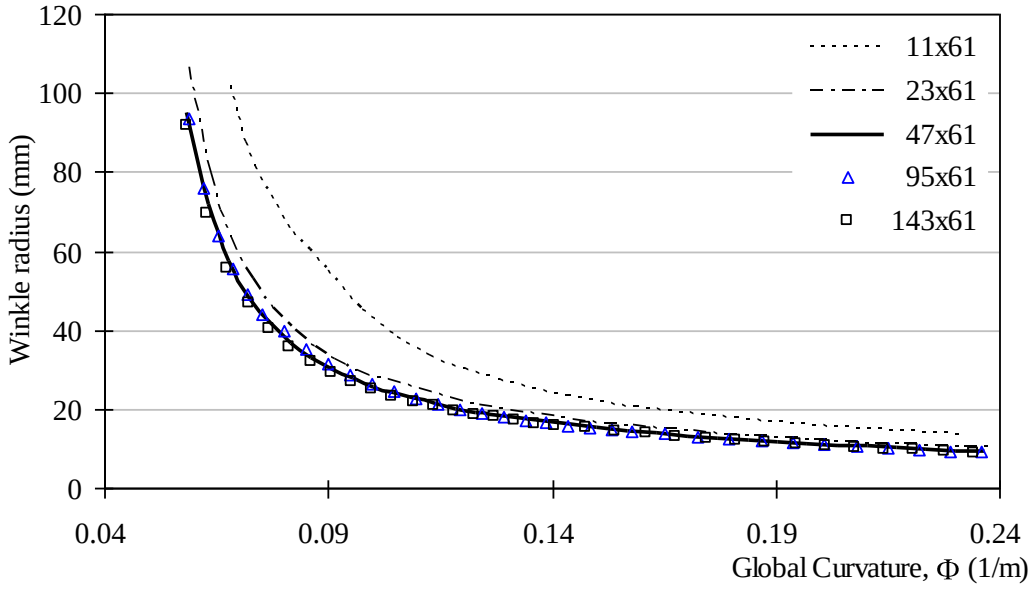

b) Local behaviour: wrinkle radius vs. global curvature

Figure 5.14: Mesh study: along circumferential direction

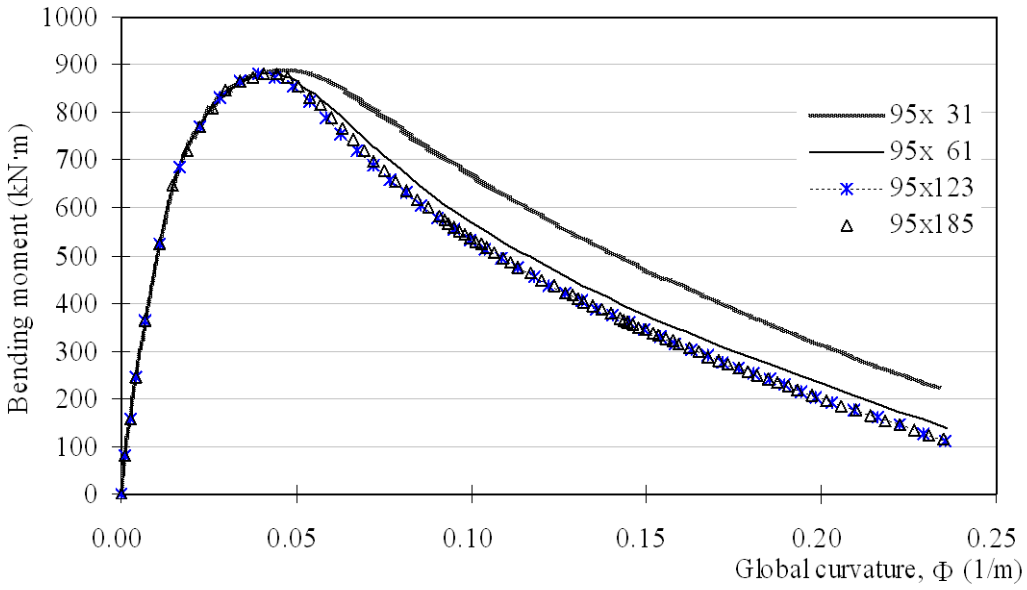

a) Global behaviour: bending moment vs. global curvature

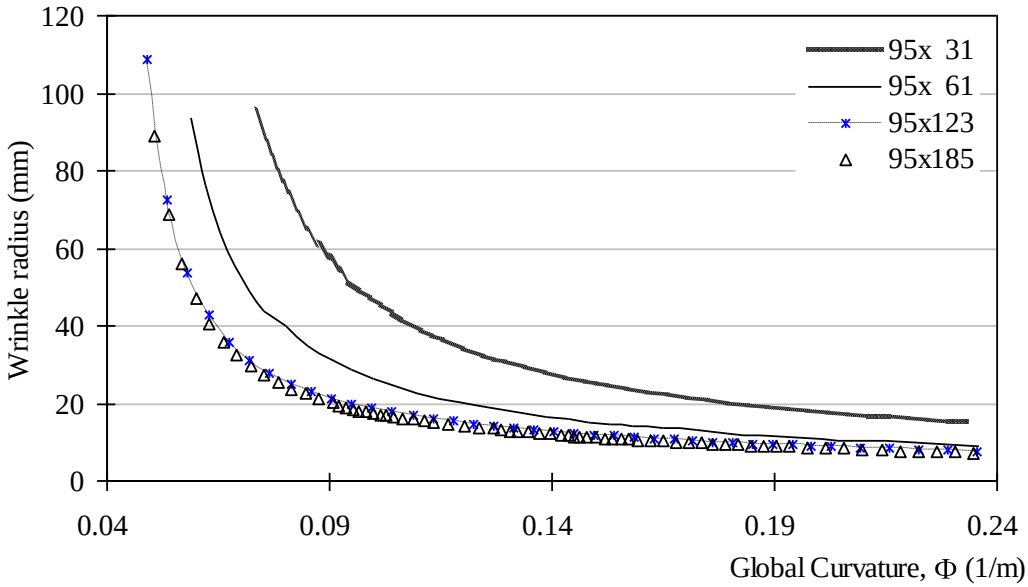

b) Local behaviour: wrinkle radius vs. global curvature

Figure 5.15: Mesh study: along longitudinal direction

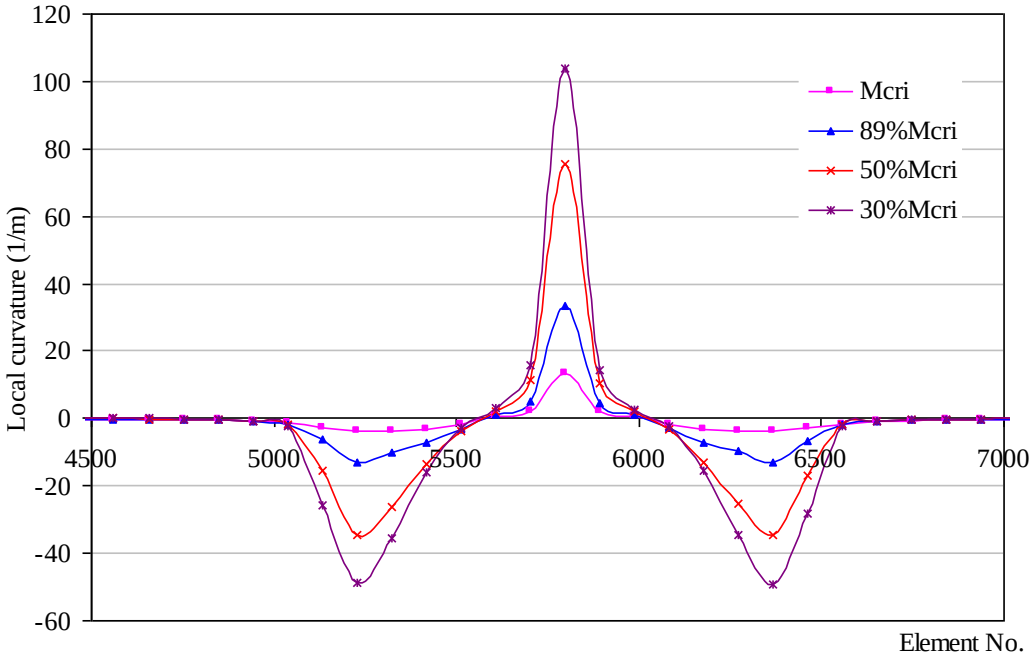

a) 16 inch pipe pressured to 40% SMYS

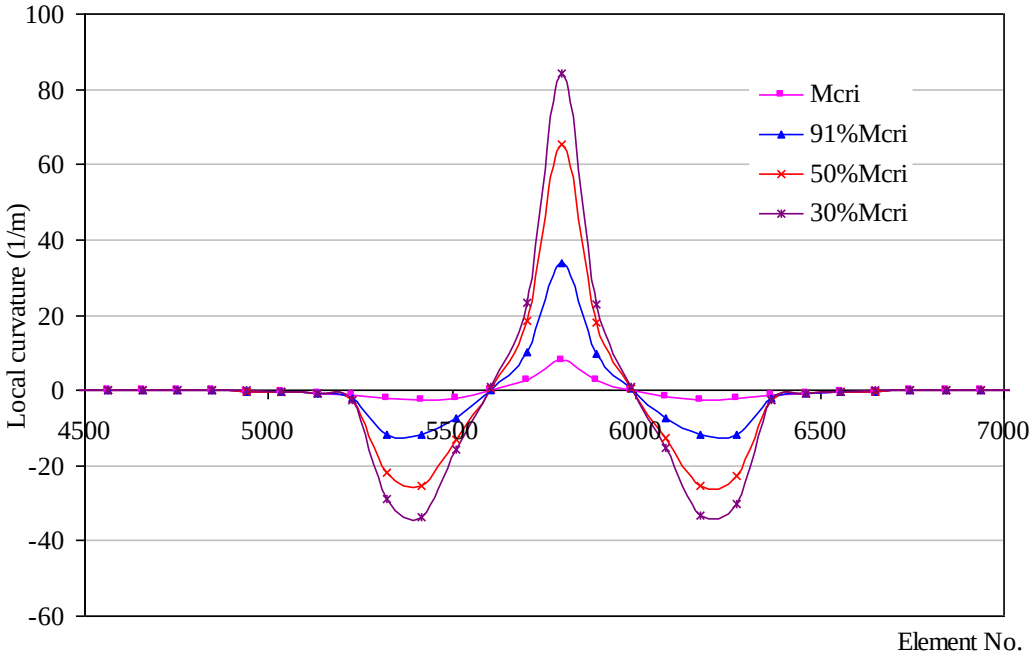

b) 20 inch pipe pressured to 40% SMYS

Figure 5.16: Illustration of wrinkle development

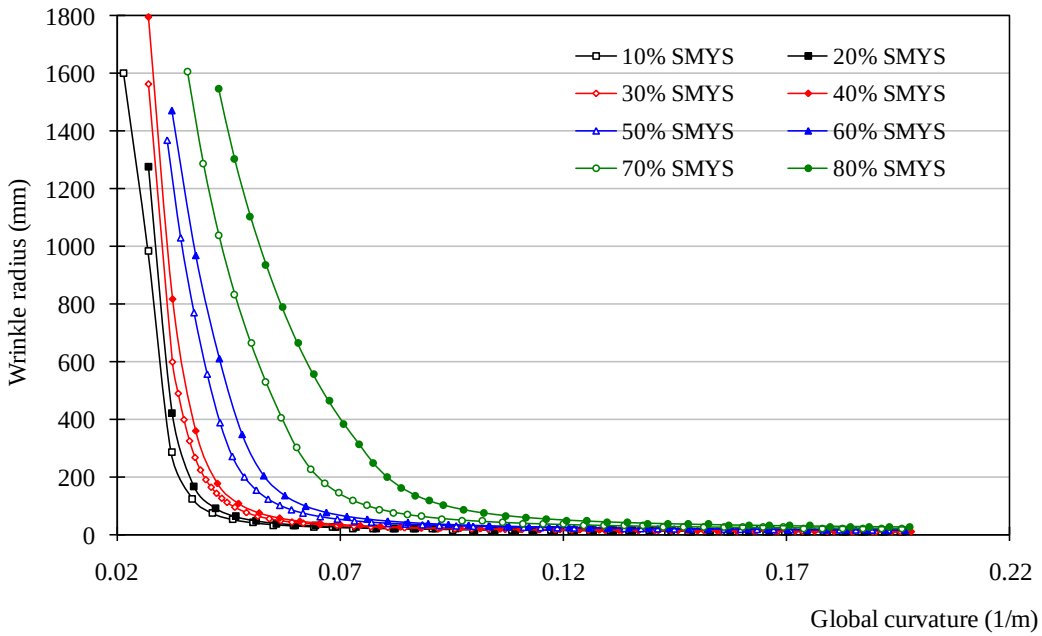

a) Overall view

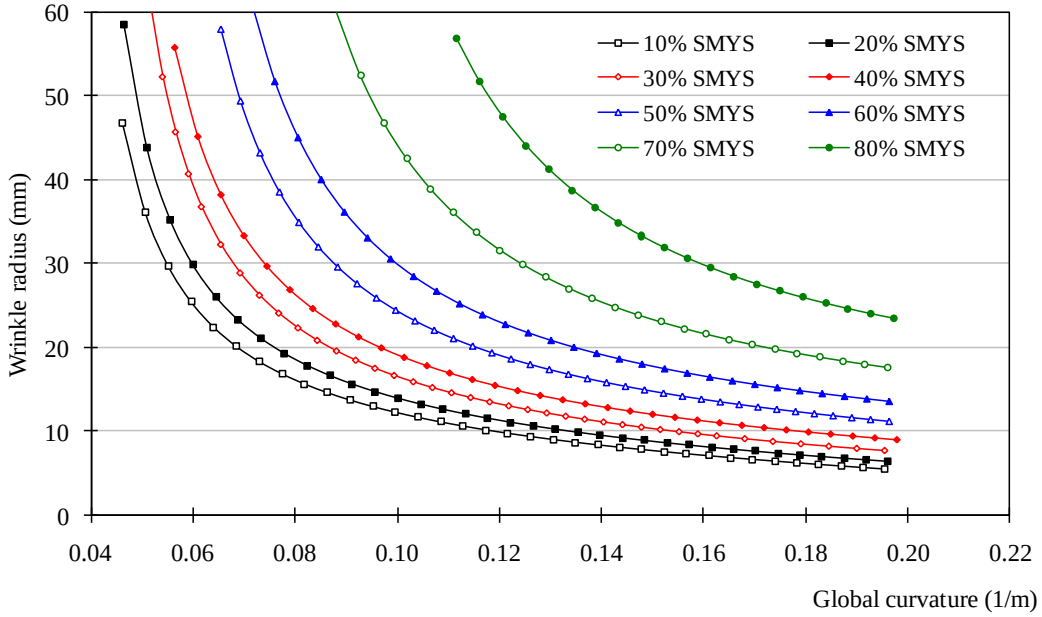

b) Closer view

Figure 5.17: 16 inch pipe: wrinkle radius vs. global curvature

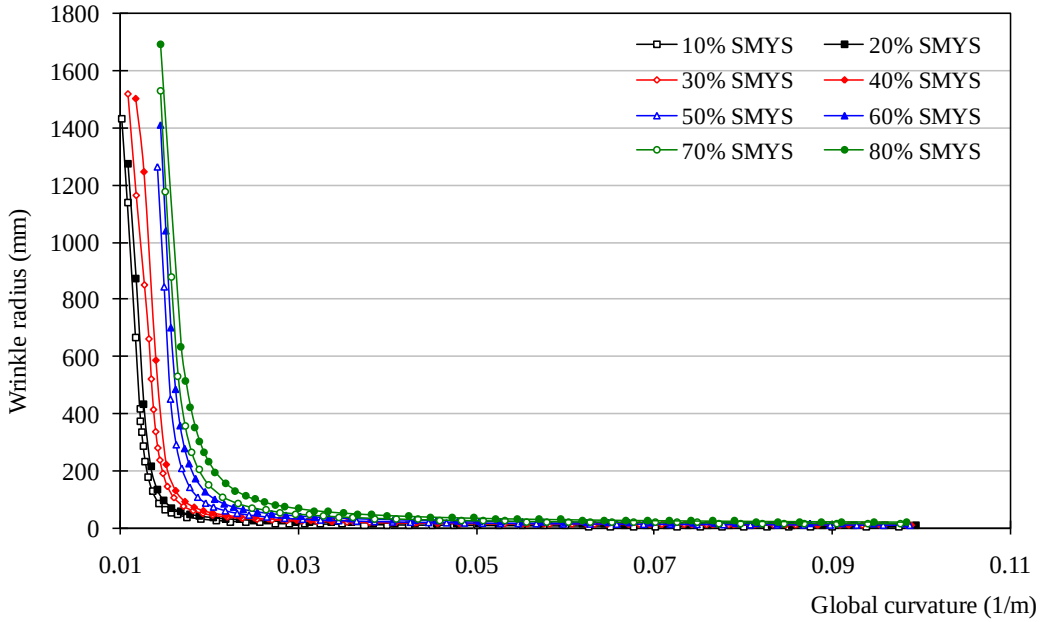

a) Overall view

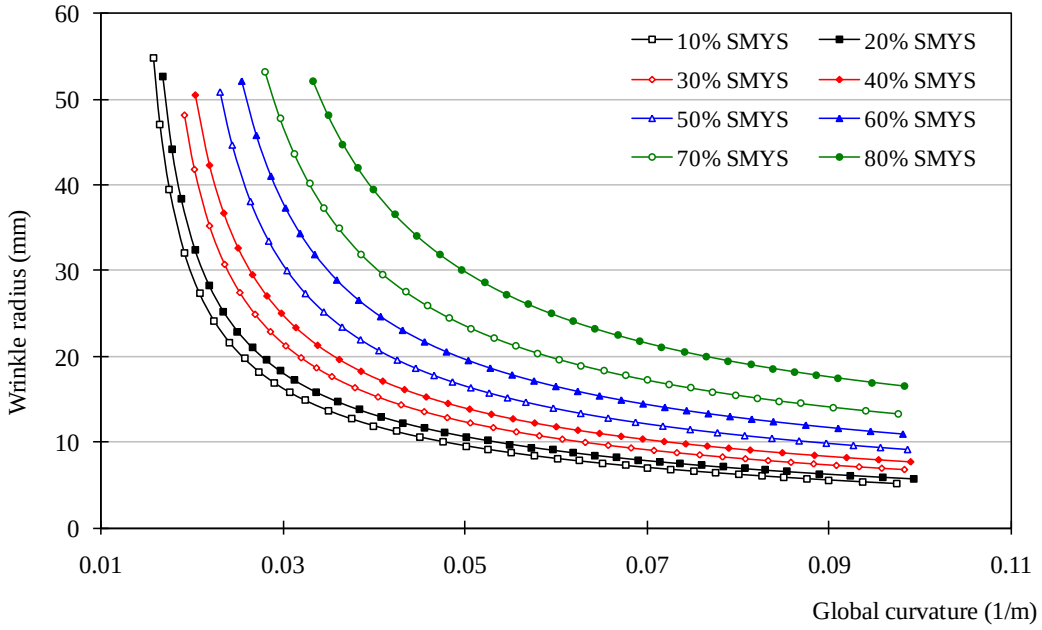

b) Closer view

Figure 5.18: 20 inch pipe: wrinkle radius vs. global curvature

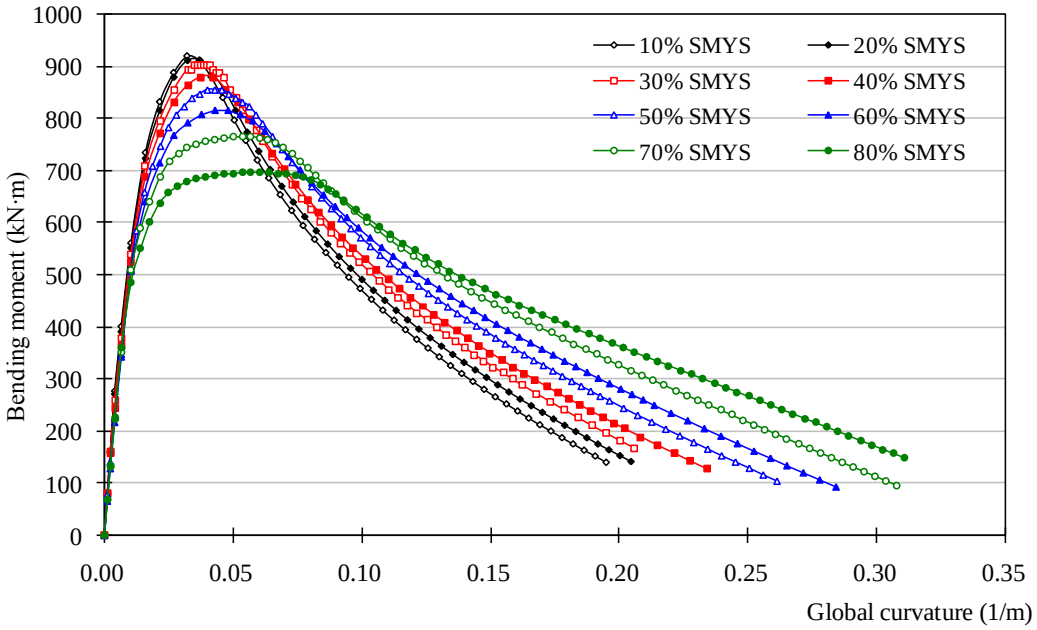

a) 16 inch pipe

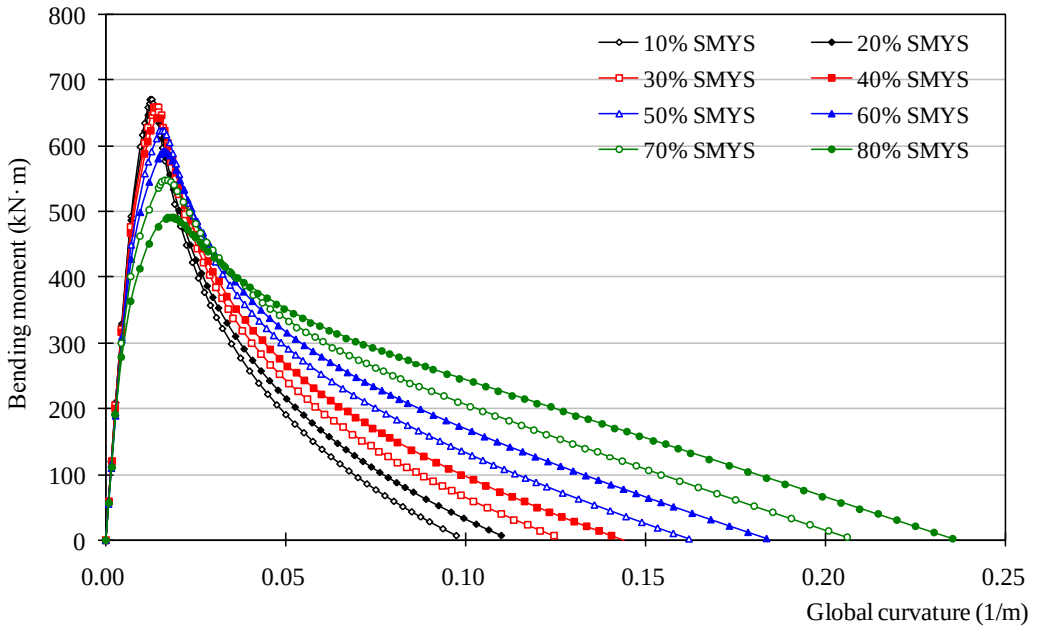

b) 20 inch pipe

Figure 5.19: Bending moment vs. global curvature

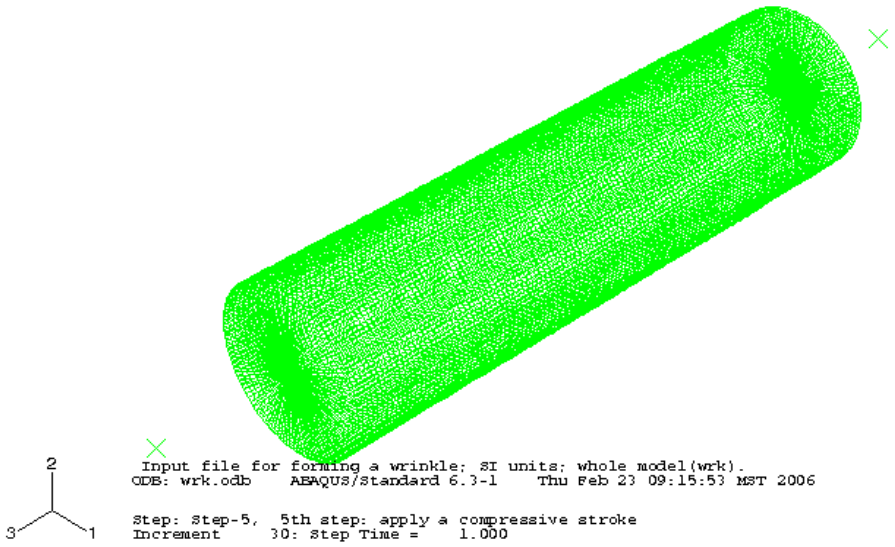

Figure 5.20: A typical mesh of specimen LCF16N1

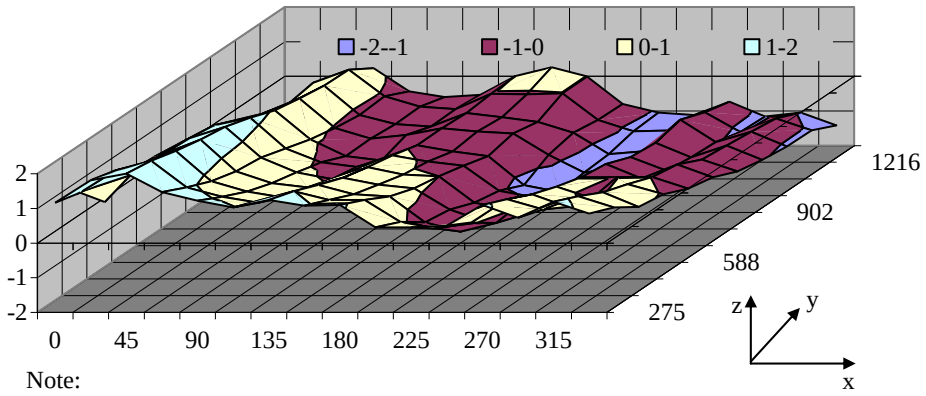

Note:
x = circuferential angle in degree, y = axial distance in m, and z = imperfection in mm.

a) LCF16N1

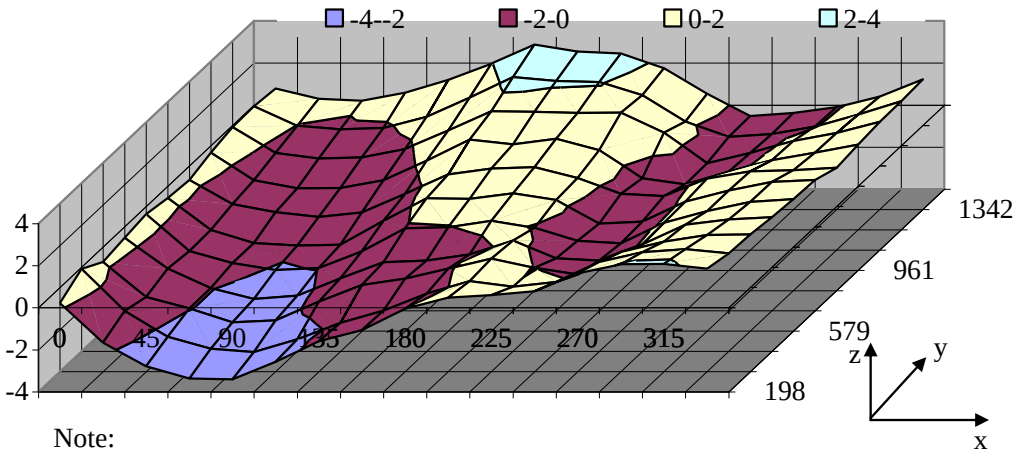

Note:
x = circuferential angle in degree, y = axial distance in m, and z = imperfection in mm.

b) LCF20N1

Figure 5.21: Imperfections of full-scale pipe specimens

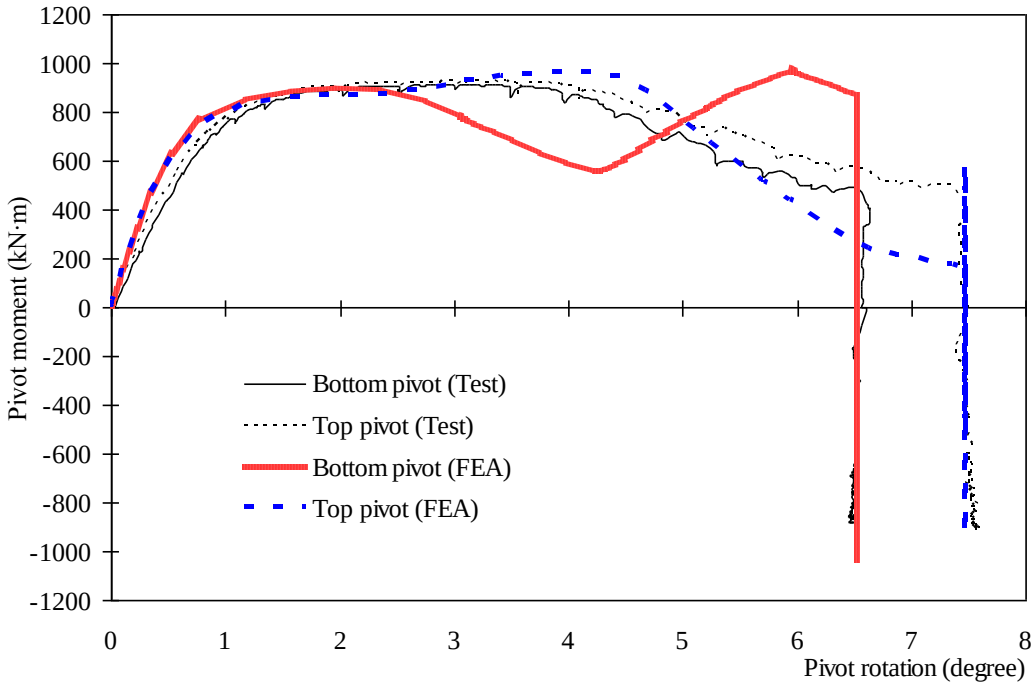

Figure 5.22: Pivot moment vs. pivot rotation (LCF16N1)

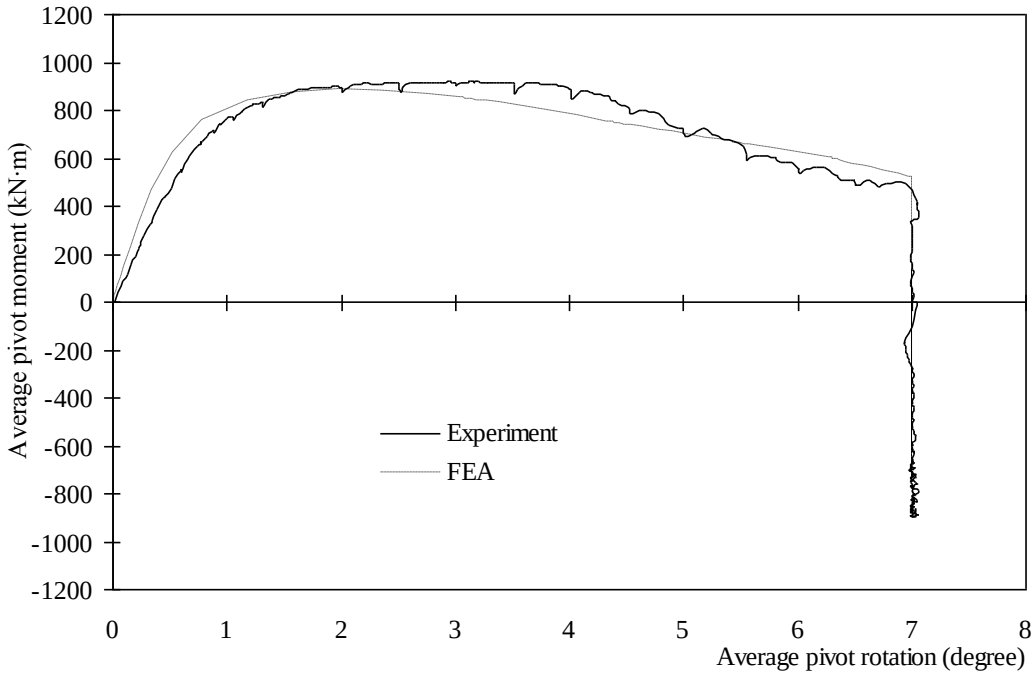

Figure 5.23: Average pivot moment vs. average pivot rotation (LCF16N1)

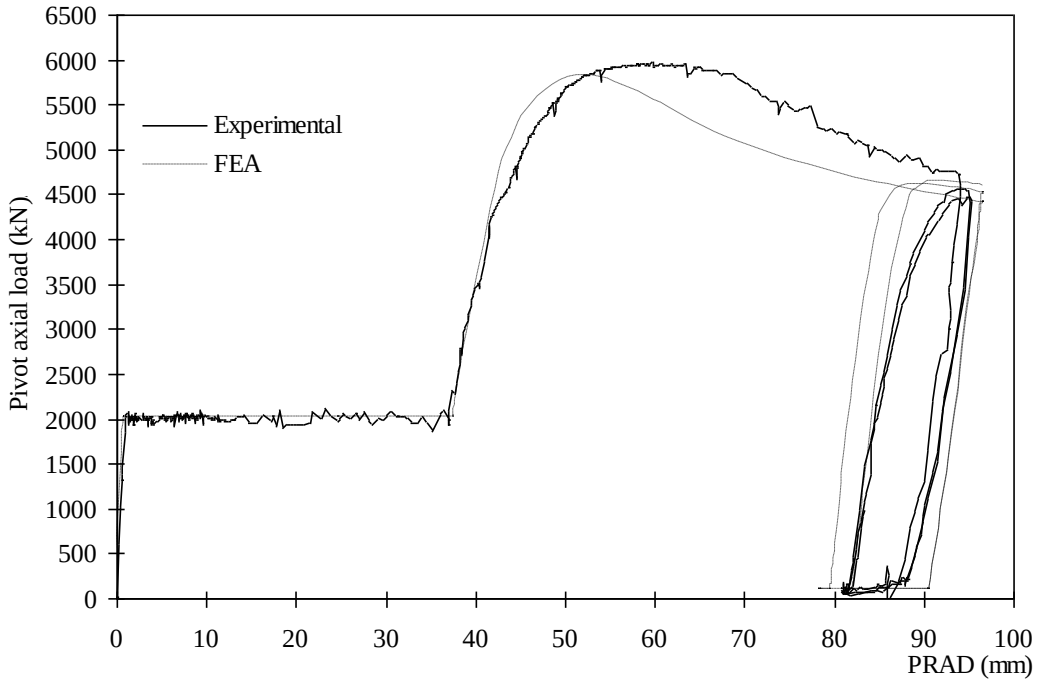

Figure 5.24: Pivot axial load vs. RAD between pivots (LCF16N1)

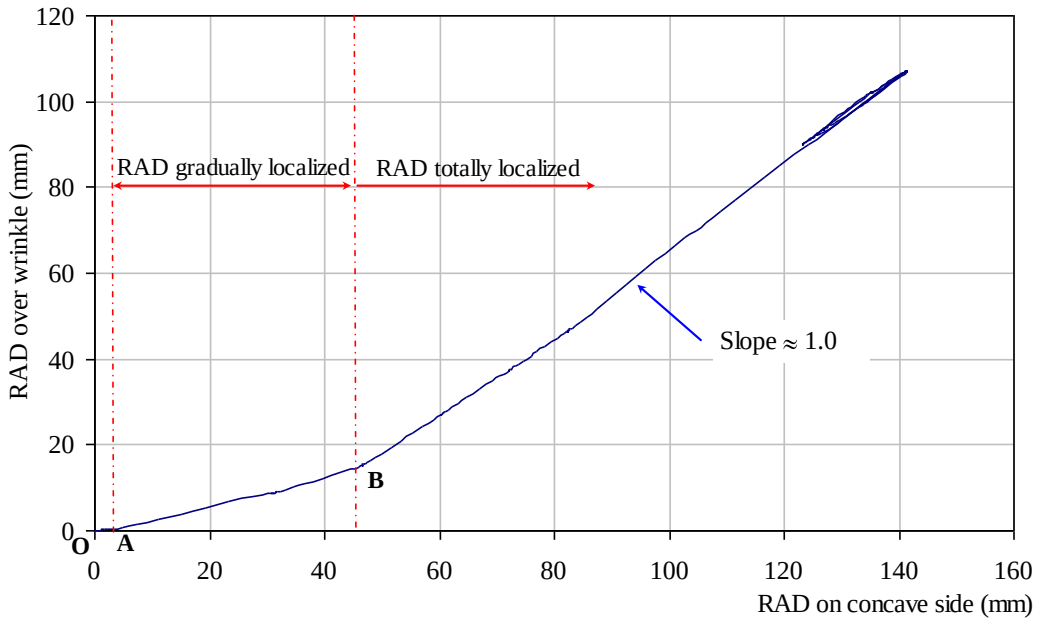

Figure 5.25: Local RAD vs. global RAD (LCF16N1)

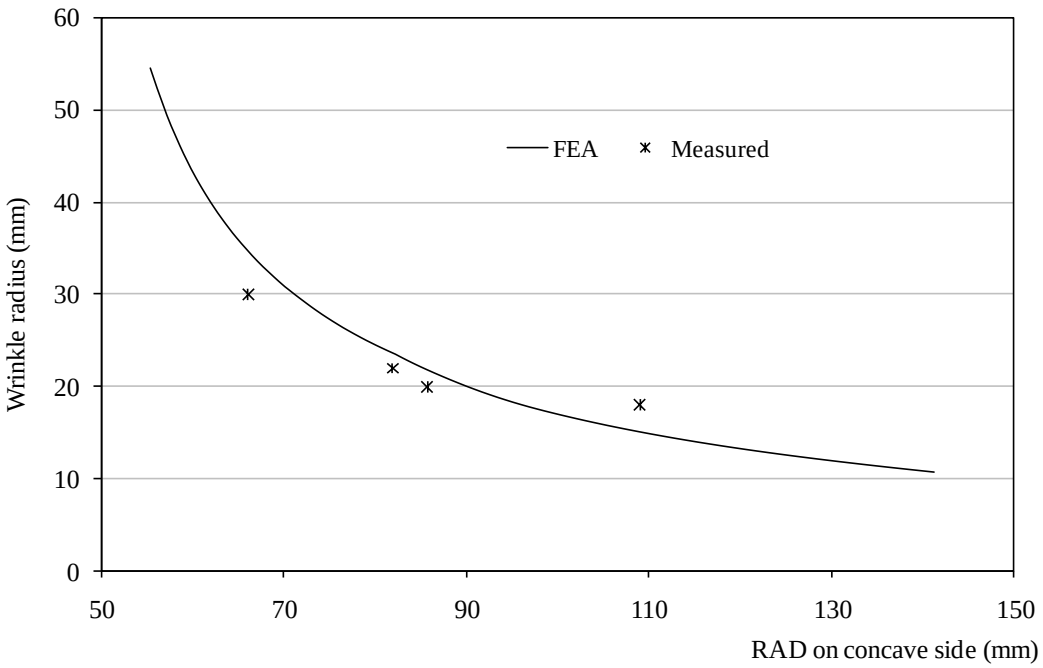

Figure 5.26: Wrinkle radius vs. RAD on concave side (LCF16N1)

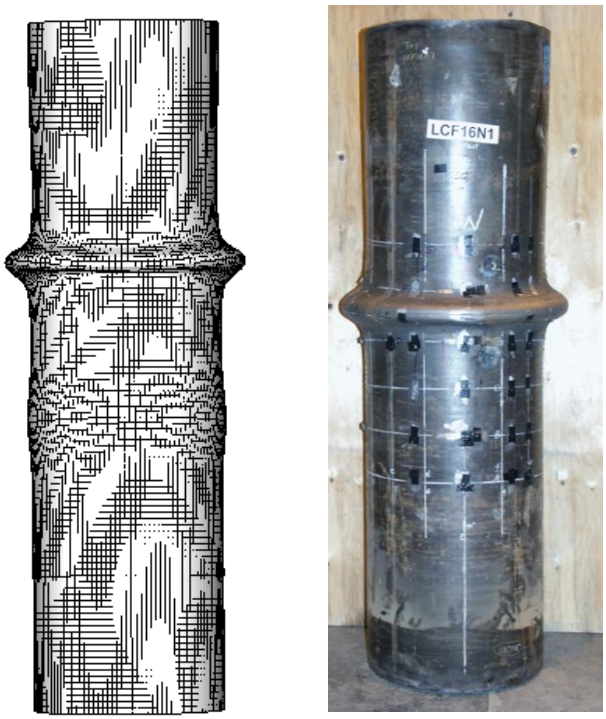

a) By FEA b) By test

Figure 5.27: Comparison of deformed pipe shape (LCF16N1)

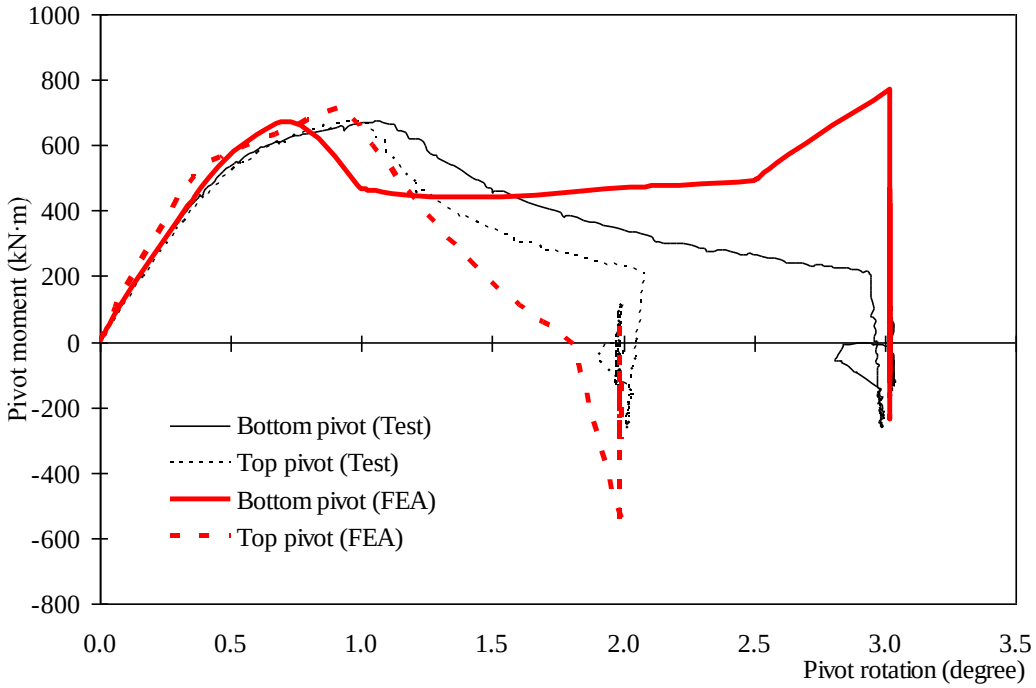

Figure 5.28: Pivot moment vs. pivot rotation (LCF20N1)

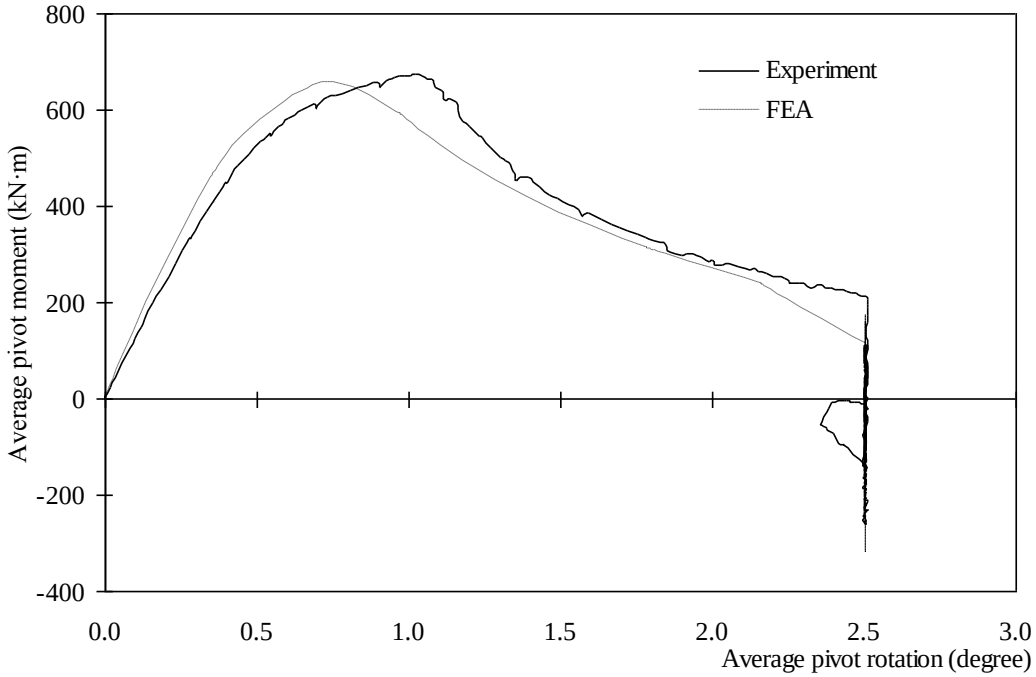

Figure 5.29: Average pivot moment vs. average pivot rotation (LCF20N1)

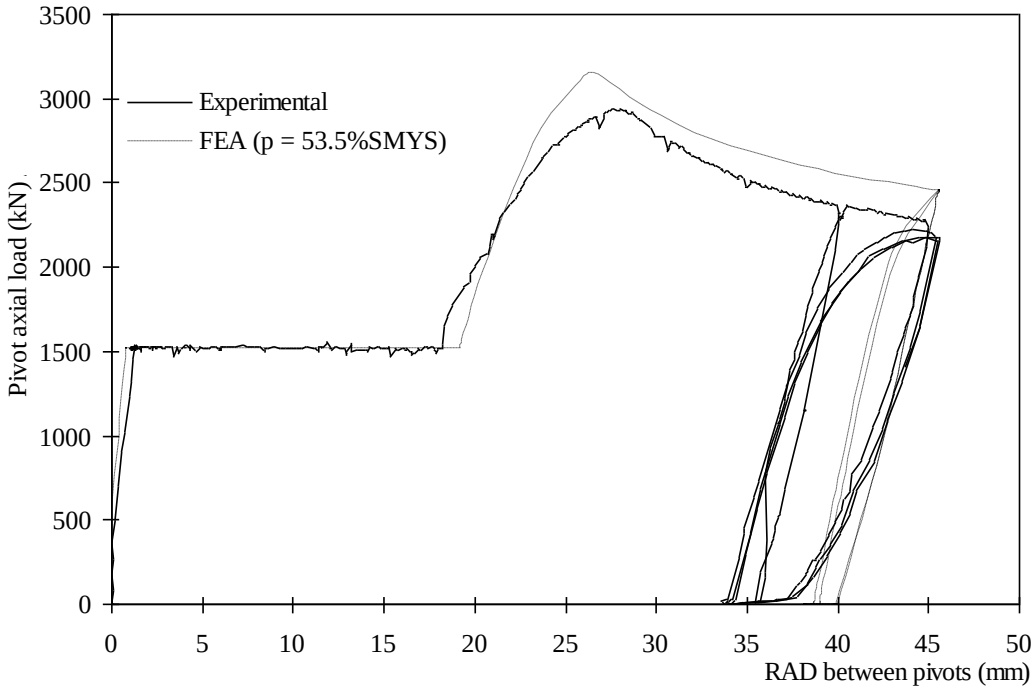

Figure 5.30: Pivot axial load vs. RAD between pivots
(p = 53.5%SMYS, LCF20N1)

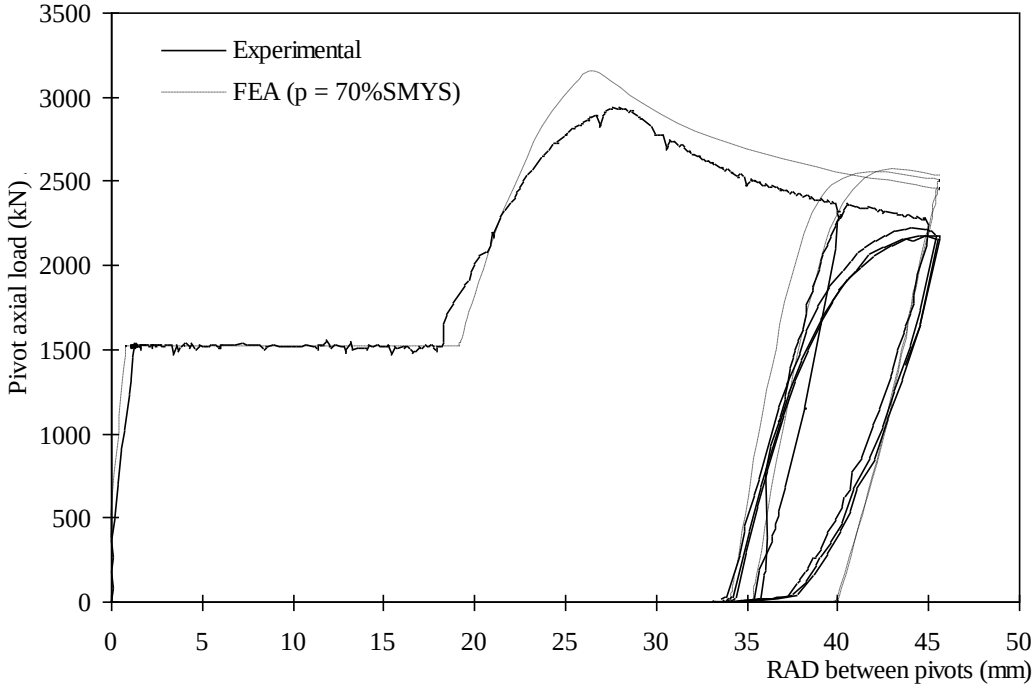

Figure 5.31: Pivot axial load vs. RAD between pivots
(p = 70.0%SMYS, LCF20N1)

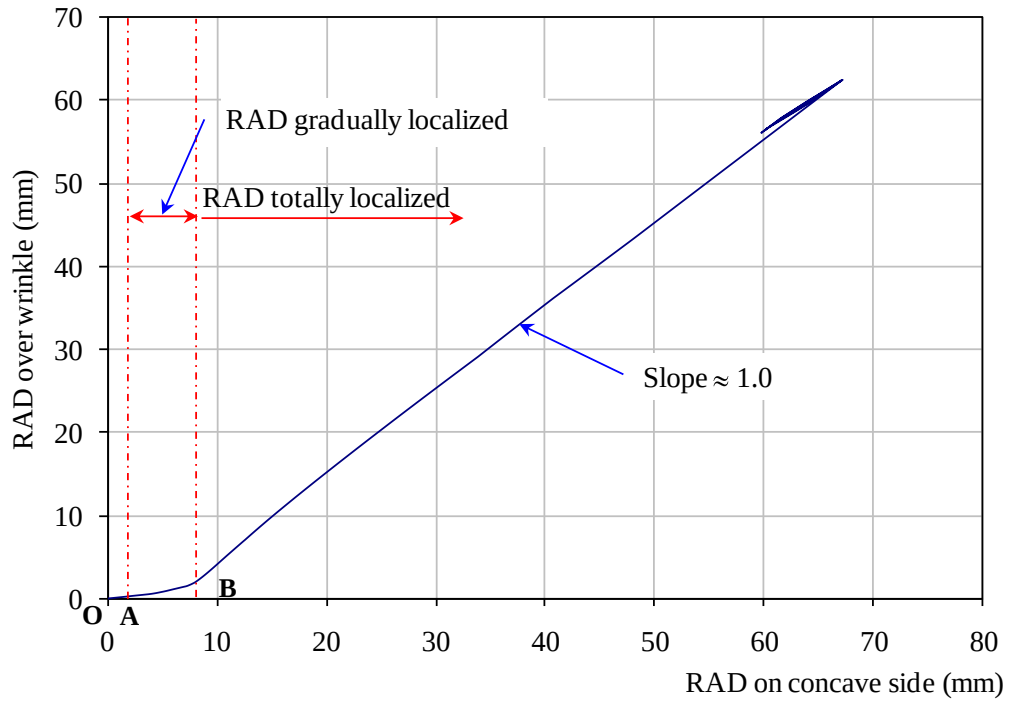

Figure 5.32: Local RAD vs. global RAD (LCF20N1)

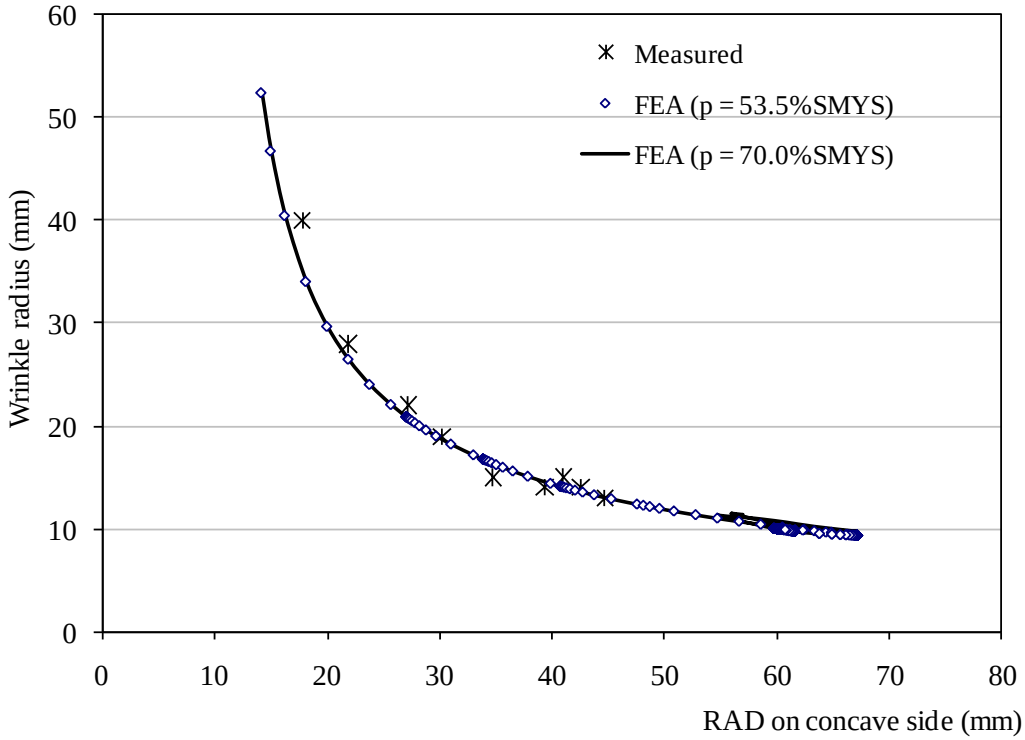

Figure 5.33: Wrinkle radius vs. RAD on concave side (LCF20N1)

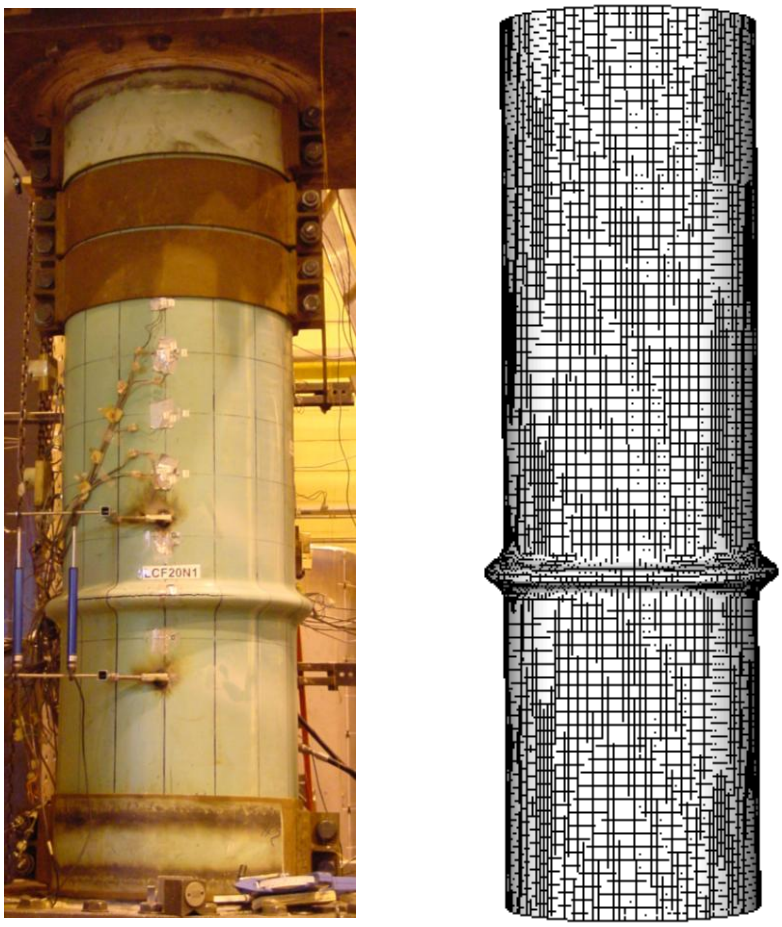

a) By test b) By FEA

Figure 5.34: Comparison of deformed pipe shape (LCF20N1)

6 LOW CYCLE FATIGUE LIFE PREDICTION MODELS

6.1 INTRODUCTION

To develop a LCF life prediction model, a set of specimens have to be tested by cyclic loading. Generally, these specimens have to have the same geometry and have to be made of the same material, and the cyclic loading has to be respectively designed for each specimen so that the test data are near evenly distributed on the fatigue curve that is plotted on a log-log scale. Based on these test data, a relation can then be formulated between the damage parameter, usually the strain range, and the fatigue life. The strip test results were used in this chapter to develop the LCF life prediction models. In the strip testing program, the strip specimens were made from three different grades of material and were formed to four different shapes, which include two bend radii and two bend angles. Therefore, the impacts of these parameters have to be counted in the models.

By reviewing the entire loading process of a typical strip test, it can be found that each specimen started with a straight strip, then it was monotonically bent to a specific shape, and finally was cyclically loaded by totally reversed strokes to fracture. Therefore, it is possible to develop a life prediction model respectively for each material grade, if the model can cover the entire loading period, i.e. the monotonic loading (bending) stage and the cyclic loading (cyclic stroke) stage. Specifically, the following three steps are followed: first, investigate the damage induced by monotonic loading and by cyclic loading, respectively; second, postulate an appropriate damage accumulation rule (DAR) to connect these two types of damage with the fracture of the specimen; finally, develop the models based on the postulated DAR.

Because the LCF life prediction models were based on the strip test results, the applicability of the developed models to the full-scale pipes will need to be verified. There are two main challenges when applying the developed models to full-scale pipes: one is determining the actually applied cyclic loading in full-

scale pipes which is analogous to what was used in the strip tests; and the other is identifying all the differences between an actual pipe wrinkle and a strip specimen and including them in model application if necessary.

6.2 DAMAGE AND DAMAGE ACCUMULATION RULE

The damage defined by the continuum damage mechanics (CDM), such as Lemaitre and Desmorat (2005), is difficult to measure and also impractical for this research program. Therefore, it will be defined and evaluated in a more conceptual way. As it was discussed before, the loading history of a strip specimen consisted of two stages: the monotonic loading stage and the cyclic loading stage. Therefore, correspondingly, there were two types of damage: ductile damage and LCF damage.

6.2.1 DUCTILE DAMAGE, D_m

For a strip specimen, the ductile damage is the damage caused by the monotonic bending. During the monotonic loading stage, a straight strip was bent around the guide rod by the drive wheel to a specific angle. As a result, there were significant residual strains and residual stresses resided within the strip bend. It was these residual strains that damaged the strip specimens and made them from being originally straight to being permanently bent. Therefore, this damage has to be properly evaluated, and its impact on LCF lives of strip specimens has to be investigated.

Iida (1987) investigated the effects of excessive prestrain in tension or in compression on the very low-cycle fatigue lives of two sets of mild steel and two groups of high strength steel. He evaluated the residual static fracture ductility by the following equations:

$$\left(2\varepsilon_{fR}\right)^k(1/4) = \left(2\varepsilon_f\right)^k(1/4) - \left(\varepsilon_{pre}\right)^k(1) \quad \text{for tensile prestrain} \tag{6.1.1}$$

$$\left(\varepsilon_{pre} + 2\varepsilon_{fR}\right)^k(1/4) = \left(2\varepsilon_f\right)^k(1/4) - \left(\varepsilon_{pre}\right)^k(3/4) \quad \text{for compression prestrain} \tag{6.1.2}$$

where, ε_{fR} is the residual static fracture ductility, ε_f is the static fracture ductility of a specimen not subjected to prestrain, ε_{pre} is the prestrain applied before the reversed strain cycling, and k is an empirical material constant.

Those two equations exhibit that the residual static fracture ductility decreases as the prestrain increases. In other words, the prestrain decreases the residual static fracture ductility. For the strip specimens tested in this research program, the role of monotonic bending played the same role as applying prestrain to strip specimens, but the so-generated prestrain was not evenly distributed in strip specimens. Hence, equations (6.1.1) and (6.1.2) cannot be applied to strip specimens directly. Instead, the ductile damage of a strip specimen will be evaluated conceptually.

In a typical tension coupon test, it is known that the specimen will fracture when it totally loses its energy-absorption capacity, so the energy-absorption capacity can be used to evaluate the ductile damage. Because the residual stress and the residual strain can be measured either on engineering scale or on true scale, the following will discuss how to evaluate the ductile damage on these two scales respectively.

6.2.1.1 ON ENGINEERING SCALE

On engineering scale, the damage parameter can be defined as:

$$D_m = \frac{U_c}{U} \tag{6.2.1}$$

where D_m is the ductile damage, U_c is the consumed energy-absorption capacity, and U is the total energy-absorption capacity. The definitions of U_c and U are also illustrated in Figure 6.1.

From Figure 6.1, it can be seen that D_m can be approximated by the following equation if line 'ABCE' is relatively flat.

$$D_m \approx \frac{\varepsilon_r}{\varepsilon_f} \tag{6.2.2}$$

where ε_r is the residual engineering strain, and it can be evaluated by Equation (3.7); ε_f is the static fracture ductility of material, and it can be obtained from the standard material tension coupon test.

6.2.1.2 ON TRUE SCALE

On true scale, the damage parameter can be similarly defined as follows:

$$D_m = \frac{U_{tc}}{U_t} \tag{6.3.1}$$

where all parameters are the same as those in Equation (6.2.1) except that they are defined on true scale. The definitions of U_{tc} and U_t are also illustrated in Figure 6.2.

Based on Figure 6.2, Equation (6.3.1) can be approximated by:

$$D_m \approx 2\frac{1-\varepsilon_{tr}/\varepsilon_{tf}}{1+\sigma_{tf}/\sigma_{ty}} + \left(\frac{\varepsilon_{tr}}{\varepsilon_{tf}}\right) \tag{6.3.2}$$

where ε_{tr} is the residual true strain, and it can be evaluated by FEA or by Equation (5.4.2) directly; ε_{tf} is the static true fracture ductility of material, and it can be obtained from the standard material tension coupon test.

6.2.1.3 DISCUSSION AND COMPARISON

Equation (3.7) exhibits that the residual engineering strain can be determined solely by the material thickness and the bend radius. By using the measured material thickness and the designated bend radius, the ductile damage can be obtained on engineering scale according to Equation (6.2.1) or (6.2.2), and the respective results are given in Table 6.1. It can be seen that their differences are less than 6%. Therefore, from the engineering point of view, Equation (6.2.2) can be used to estimate the ductile damage on engineering scale.

As for the damage on true scale, the true strain on the outside surface of strip crest can be obtained by FEA or by Equation (5.4.2) directly. Then the ductile damage can be evaluated on true scale according to Equation (6.3.1) or (6.3.2), and the

results are given in Table 6.2. From this table, it can be concluded that Equation (6.3.2) can be used to evaluate the ductile damage on true scale.

Comparing Tables 6.1 and 6.2, it can be found that there are significant differences between the ductile damage on engineering scale and that on true scale. As discussed in Chapter 3, the engineering strain is a 'length' behaviour, the average strain over a specific gauge length, but the true strain is a 'point' behaviour, the strain at a specific point. Because of this significant difference between their definitions, the true strain is larger than the engineering strain after the specimen is yielded and this difference will become more significant when the specimen is deformed far beyond the necking state and/or a large gauge length is used in obtaining the engineering strain. Therefore, it is more feasible to use the true strain during the stage of necking, because the engineering strain becomes gauge length-dependent after necking occurs. In this research program, the true scale is recommended, but both engineering and true scales are investigated for the purposes of comparison and study.

6.2.2 LCF DAMAGE, D_c

For strip tests, the LCF damage is the damage produced by cyclically loading a strip specimen. Previous work, such as Okamura and Sakai (1979) and Sakano et al. (1996), shows the excellent applicability of linear damage accumulation rule (LDAR), or Miner's rule, in LCF damage. According to this rule, the LCF damage can be defined as follows:

$$D_c = \frac{N_{df}}{N_{vf}} \tag{6.4}$$

where N_{df} is the fatigue life of an actual or damaged strip specimen, in which residual strain or damage exists, and N_{vf} is the fatigue life of a pseudo or virgin strip specimen. A pseudo strip specimen is the same as an actual strip specimen except that it is virgin or undamaged, i.e. no prestrain damage.

For pseudo strip specimens, a power relation can be assumed existing between the damage parameter and their fatigue lives as follows:

$$\Omega = C_1 N_{vf}^{-m} \tag{6.5.1}$$

where Ω is the damage parameter, C_1 and m are constants.

Or on a log-log scale, it can be written as

$$\log \Omega = C - m \log N_{vf} \tag{6.5.2}$$

where C = log C_1 and is a constant and the other parameters are the same as before.

Once a pseudo strip specimen was introduced, the LCF damage can be defined by employing the LDAR. Up to now, two different types of damage, D_m and D_c, have been defined, and the following will discuss how to connect these two different types of damage with the fracture of specimen by DAR.

6.2.3 DAMAGE ACCUMULATION RULE

From the physical point of view, the ductile damage is the nucleation, growth and coalescence of cavities or microvoids, and the LCF damage is the initiation, propagation and coalescence of microcracks. It can be seen that on the scale of cross section, both kinds of damage decrease the net area of cross section, so they can be assumed to be accumulative.

It is known that these two types of damage are accumulated to fracture a strip specimen, but it is unknown which one contributes more to the fracture. Hence, the following generalized rule is postulated:

$$D = (D_m)^{m_m} + (D_c)^{m_c} \tag{6.6.1}$$

where D_m and D_c are defined previously, m_m and m_c are empirical constants.

Furthermore, from the definitions of D_m (see Equation 6.2.1 or 6.3.1) and D_c (see Equation 6.4), it can be seen that both of them are normalized, so the failure criterion can be taken as a unity:

$$D = 1 \tag{6.6.2}$$

By using the definitions of D_m and D_c, DAR (Equation 6.6.1), and failure criterion (Equation 6.6.2), the LCF life prediction model can be developed. The model will

be discussed in Section 6.4 after the damage parameters have been selected in Section 6.3.

6.3 DAMAGE PARAMETERS

To identify an appropriate damage parameter, all test parameters have to be investigated to understand their impacts on the fatigue life so the key parameters can be selected.

6.3.1 EQUIVALENT STROKE RANGE

In strip tests, the totally reversed stroke-controlled method was employed. To distinguish this actually applied stroke from the equivalent stroke, the actually applied stoke is called the nominal stroke henceforward.

Under the cyclic loading of nominal stroke, a strip was repeatedly deformed. Because this stroke is so big that the strip bend was far beyond being plasticized, some irreversible deformations were accumulated in the form of cumulative plastic strain within the strip bend. It had to be mentioned that it was the nominal stroke that produced this cumulative plastic strain within the strip bend, and it was this cumulative plastic strain that fractured the strip specimen. Based on this recognition, the following discussion will focus on the deformation of strip bend.

In strip tests, four parameters were employed to investigate their influences on LCF lives and they were: nominal stroke range, bend angle, bend radius and material thickness. Because the LCF life prediction models will be developed for each material thickness, respectively, the damage parameter can be formulated based on the other three parameters.

From Table 3.7, it can be observed that the LCF life decreases as the nominal stroke range increased, and the nominal stroke range has the greatest impact among the three considered parameters. Hence, the damage parameter should be formulated based on it. Equation (3.6) indicates that the bend angle does not make any contribution to the residual strain, so it will not affect the ductile damage. But this does not mean it has no impact on LCF lives of strip specimens. Table 3.7

clearly shows that the specimens with larger bend angles have much shorter LCF lives. From Chapter 3, it is known that the loading strips or loading plates were welded to strip specimens according to a fixed positioning distance. By analyzing the geometric relation, it can be found that the loading eccentricity depends on the bend angle and a large bend angle will give a small loading eccentricity. Under the cyclic loading of the same nominal stroke, the specimens with small loading eccentricities experienced more cyclic deformations within their strip bends, so they had shorter LCF lives. Moreover, the measurement results show that the loading eccentricity is difficult to be controlled, and it greatly varied. Therefore, its impact has to be counted in the damage parameter.

It can be expected that the nominal stroke range can be used as a damage parameter directly if the tested specimens have the same loading eccentricity. This scenario can be realized by standardizing the strip test by introducing a standard loading eccentricity. Then the equivalent stroke range can be derived from the nominal stroke range and the actual loading eccentricity according to their geometric relationship (see Figure 6.3). In this research program, 70 mm was selected as the standard loading eccentricity based on the consideration of keeping consistent with the previous tests, i.e. Myrholm (2001) and Das (2002). If the strip legs are assumed to be rigid, then the following equations can be obtained:

$$\Delta S_e = H_{sop} - H_{scl} \tag{6.7.1}$$

$$H_{sop} = H_{op} + \frac{\Delta e}{\cos(\theta_{alo}/2)} \sin\left(\frac{\theta_{alop}}{2}\right) \tag{6.7.2}$$

$$H_{scl} = H_{cl} + \frac{\Delta e}{\cos(\theta_{alo}/2)} \sin\left(\frac{\theta_{alcl}}{2}\right) \tag{6.7.3}$$

where, ΔS_e is the equivalent stroke range; $\Delta e = e_o - e_s$, and e_o is the initial loading eccentricity and e_s = 70 mm is the standard loading eccentricity; θ_{alo}, θ_{alop} and θ_{alcl} are the angles between the two actual strip legs when the strip specimen is at the initial state, totally opened and totally closed respectively; H_{op} and H_{cl} are the distances between the two loading hinges when the strip specimen is totally opened and totally closed respectively; and H_{sop} and H_{scl} are the equivalent

distances between the two pseudo loading hinges when the strip specimen is totally opened and totally closed respectively. All these parameters are illustrated in Figure 6.3.

Substituting Equations (6.7.2) and (6.7.3) into Equation (6.7.1), then the following equation can be obtained:

$$\Delta S_e = \Delta S + \Delta e \times \frac{\sin[(\theta_{alo} + \delta\theta_{alop})/2] - \sin[(\theta_{alo} - \delta\theta_{alcl})/2]}{\cos(\theta_{alo}/2)} \qquad (6.8.1)$$

where $\Delta S = H_{op} - H_{cl}$ is the stroke range exerted by the MTS machine; $\delta\theta_{alop} = \theta_{alop} - \theta_{alo}$ and $\delta\theta_{alcl} = \theta_{alcl} - \theta_{alo}$ are the opening rotation and closing rotation of actual strip legs respectively; and the other parameters are the same as before.

If assuming that the actual strip leg rotations can be approximated by the pseudo strip leg rotations, then Equation (6.8.1) can be written as

$$\Delta S_e = \Delta S + \Delta e \times \frac{\sin[(\theta_{alo} + \delta\theta_{slop})/2] - \sin[(\theta_{alo} - \delta\theta_{slcl})/2]}{\cos(\theta_{alo}/2)} \qquad (6.8.2)$$

where, $\delta\theta_{slop} = \theta_{slop} - \theta_{slo}$ and $\delta\theta_{slcl} = \theta_{slcl} - \theta_{slo}$ are the opening rotation and closing rotation of pseudo strip legs respectively, θ_{slo}, θ_{slop} and θ_{slcl} are the angles between the two pseudo strip legs when the strip specimen is at the initial state, totally opened and totally closed respectively; and the other parameters are the same as before. Some of these parameters are shown in Figure 6.3.

The above equations clearly exhibit that the equivalent stroke range combines the effects of both bend angle and nominal stroke range. All parameters in Equations (6.8.1) and (6.8.2) could be determined from strip tests: e_o, θ_{alo} and θ_{slo} were measured before the cyclic nominal stroke was applied, $\delta\theta_{alop}$ and $\delta\theta_{alcl}$ were measured directly by the two RVDTs that were installed on the two strip legs, and $\delta\theta_{slop}$ and $\delta\theta_{slcl}$ could be calculated by using the geometric relationship with e, which was measured by an LVDT, and ΔS was read directly from the MTS machine.

As for the impact of bend radius, it can be observed from Table 3.7 that a specimen with a bend radius of 20 mm endured more cycles than that with a bend

radius of 15 mm. Therefore, the following damage parameter was introduced to count this impact:

$$\Omega = \Delta S_e \big/ R^{m_{br}} \tag{6.9}$$

where Ω is the damage parameter, m_{br} is an empirical constant, and the other parameters are the same as before.

The investigation was conducted by changing the value of m_{br} from 0 to 2. The results showed that the best agreement with test results was obtained when m_{br} = 0, i.e. $\Omega = \Delta S_e$, so it can be concluded that the bend radius does not need to be included directly in the damage parameter. However, this does not mean that the bend radius does not contribute to the damage parameter. Conceptually, the strip bend is the plastic zone of a strip specimen, and it works as a plastic hinge. A strip specimen with big bend radius has large strip bend (or hinge), so it requires a small rotation to absorb the same work exerted by the MTS load than that with a smaller bend radius. Therefore, the impact of bend radius is counted in the damage parameter indirectly by contributing to the rotation of strip legs, which is contained in Equations (6.8.1) and (6.8.2). Based on the above investigations, the equivalent stroke range, ΔS_e, is selected as one of the damage parameters.

6.3.2 ROTATION RANGE

As discussed previously, the failure of strip specimens was caused by the accumulated plastic strain, and this strain was generated by the repeated deformation within the strip bend. Furthermore, this type deformation was the direct result of the rotation of strip legs. Therefore, it can be assumed that this rotation range includes the influences of bend angle, bend radius and nominal stroke range, and it is well reasoned to use the rotation range as the damage parameter. Moreover, it is found that this rotation range almost kept constant during the cyclic loading stage by investigating the test data (see Figure 3.14), and this observation makes using the rotation range as the damage parameter possible. Actually, the rotation range was also included in Equations (6.8.1) and (6.8.2), which are used for computing the equivalent stroke range. However, it was split

into two parts: one was the opening rotation and the other was the closing rotation. Therefore, it can be concluded that the rotation range is more directly related to the failure of specimen than the equivalent stroke range.

The rotation range can be either the rotation of actual strip legs or the rotation of pseudo strip legs. As introduced previously, the former was measured directly by the two RVDTs installed on the strip legs, the latter can be computed by employing the geometric relationship.

6.4 LCF LIFE PREDICTION MODEL

As discussed in Chapter 2, the LCF life prediction model can be developed using different damage parameters. For this research program, two LCF life prediction models were formulated: one was based on the experimental LCF lives, called the life-based model; and the other was based on the tested deterioration rates, named the deterioration rate-based model. Both the equivalent stroke range and rotation range damage parameters are used in each proposed model.

6.4.1 LIFE-BASED MODEL

6.4.1.1 GENERAL DESCRIPTION OF THE LIFE-BASED MODEL

Based on Equations (6.5.1), (6.5.2), (6.6.1) and (6.6.2), the life-based model can be derived as follows:

$$\Omega = C_1 N_{vf}^{-m} \tag{6.10.1}$$

where all parameters are the same as before.

Or on double log scale, it can be expressed as follows:

$$\log \Omega = C - m \log N_{vf} \tag{6.10.2}$$

The pseudo fatigue life can be obtained from the fatigue life of an actual strip specimen as follows:

$$N_{vf} = \frac{N_{df}}{D_c} \tag{6.11.1}$$

where N_{df} is the fatigue life of an actual strip specimen, or simply called the actual fatigue life, and D_c is the LCF damage.

Further, the LCF damage can be derived from the DAR as follows:

$$D_c = \left(1 - (D_m)^{m_m}\right)^{1/m_c} \tag{6.11.2}$$

where all parameters are the same as before.

It can be seen that Equations (6.10.1) and (6.10.2) are the same as Equations (6.5.1) and (6.5.2) respectively, which are the forms of the traditional fatigue life prediction model. In addition, it is called the general model just because Ω is a general damage parameter, which can be any reasonable parameters. In this research program, Ω was either the equivalent stroke range, ΔS_e, or the rotation range, $\Delta\theta$.

6.4.1.2 LCF FAILURE CRITERION

To develop the LCF life prediction model, firstly an appropriate failure criterion has to be selected, and then the fatigue life can be determined from the test data. This research program employed the rupture criterion based on the following three considerations. The first one is to keep consistent with the previous tests, where the rupture criterion was used. The second one is that the rupture criterion can be used to approximately represent the actual failure of full-scale pipes, where the wrinkled pipes are nearly ruptured when the cracks are observed on their outside surfaces (because the cracks mainly propagated from their inside surfaces). The last one is that this criterion is relatively simple and can be easily applied.

6.4.1.3 EQUIVALENT STROKE RANGE BASED MODEL

From the general model, it can be seen that the DAR has to be determined before developing the LCF life prediction model. Generally, this can be done by using the method of trial and error. This research program investigated three types of DAR and they were the LDAR, the square root-square damage accumulation rule (SRSDAR), in which m_m was 0.5 and m_c was 2.0, and the square and square root

damage accumulation rule (SSRDAR), in which m_m was 2.0 and m_c was 0.5. The last two DARs are non-linear. In the following, these three rules were employed to develop the LCF life prediction models respectively.

By employing the DAR and by using the best-fit method, the equivalent stroke range based LCF life prediction model can be developed and the results of C and m are summarized in Tables 6.3 and 6.4.

6.4.1.4 ROTATION RANGE BASED MODEL

Follow the same procedure as that used in developing equivalent stroke range based model, the rotation range based model can be obtained and the corresponding results of C and m are given in Tables 6.3 and 6.4.

6.4.2 DETERIORATION RATE-BASED MODEL

Under the action of LCF, the cross section of a strip specimen was gradually decreased by the initiation, propagation and coalescence of microcracks, and this made the strip specimen gradually lose its load-carrying capacity and energy-absorption capacity. If a relation can be postulated between the deterioration rate of load-carrying capacity or energy-absorption capacity and the damage parameter, then the LCF life can be obtained by integrating the deterioration rate from the initial state to the maximum accepted deterioration level. In the following, the deterioration investigation will be conducted firstly, and then this type model will be developed.

6.4.2.1 DETERIORATION INVESTIGATION

To fully understand the deterioration of strip specimens, three types of deterioration will be investigated and they are the deterioration of axial load, deterioration of bending moment and deterioration of hysteresis loop energy (HLE).

AXIAL LOAD

The deterioration of axial load, which is exerted by the MTS machine, is a phenomenon that the axial load requires to produce a certain stroke magnitude as

the cyclic loading progresses. It indicates the propagation of cracks and the decrease of net cross section area. To investigate this phenomenon, the peak values, the maximum load to open strip specimens, and the valley values, the maximum load to close strip specimens, were first picked out from the axial load spectra. For convenience, those axial loads were normalized by their corresponding peak value and valley value in the first cycle. Finally, the deterioration of these normalized axial loads was obtained by investigating their relation with the loading cycle. The normalized axial load can be expressed as follows:

$$p_{po} = \frac{P_{ipo}}{P_{1po}} \tag{6.12.1}$$

$$p_{vc} = \frac{P_{ivc}}{P_{1vc}} \tag{6.12.2}$$

where, p_{po} and p_{vc} are the normalized peak opening load and the normalized valley closing load, P_{ipo} and P_{ivc} are the peak opening load and the valley closing load in the i^{th} loading cycle respectively, and P_{1po} and P_{1vc} are the peak opening load and the valley closing load in the first cycle respectively.

Typical deterioration diagrams of normalized axial load are given in Figure 6.4. From the figure, the following observations can be made.

Firstly, no plateaus are exhibited and this indicates that there is no obvious crack initiation period. As it was discussed in Chapter 3, it can be explained from two aspects: on one hand, it is known that the residual strain after monotonic bending was far beyond the ultimate strain, so it can be concluded that microvoids formed on the outside surface of strip bend during the monotonic bending stage; on the other hand, the very large compressive strain on the inside surface of strip bend during monotonic bending could generate many micro-wrinkles, and those micro-wrinkles were so sharp that many microcracks occurred.

Secondly, for specimens T8R15A45S30 and T8R15A45S50, their deterioration paths can be approximated by two straight lines and they represent two deterioration periods: the slow deterioration period (SDP), during which the

cracks slowly propagated, and the fast deterioration period (FDP), during which the crack propagation rate was greatly accelerated and made the specimen quickly lose its load-carrying capacity. For specimen T8R15A45S80, the applied stroke was so large that the cracks propagated very fast from beginning and the specimen ruptured very quickly (its life only lasted three cycles), so its deterioration path only consisted of the FDP.

For specimens T8R15A45S30, the normalized opening axial load went up a little bit during the second cycle, and then it decreased gradually and evenly in a rate of about 0.005310; after about 47 cycles, the deterioration rate jumped to about 0.046587, which is about nine times of the deterioration rate during the SDP. However, the normalized closing axial load was deteriorated greatly at first, and then it slowed down in an even rate of about 0.005300, which was almost the same as that of the opening normalized load; after about 57 cycles, the deterioration was accelerated to a speed of about 0.070495, which is about 13.5 times of the deterioration rate during the SDP. Comparing the deterioration path of the normalized opening axial load and that of the normalized closing axial load, it can be found that both of them had an almost same deterioration rate during the SDP, but their totally different behaviour during the first few cycles induced a gap of about 0.18 between them. Another difference is that the normalized opening load entered the FDP earlier than the normalized closing load. The last difference is that the deterioration of normalized opening load was slower than that of normalized closing load during the FDP.

For specimen T8R15A45S50, generally speaking, its deterioration path of normalized opening load and that of normalized closing load showed the same changing trends as those of specimen T8R15A45S30. But the gaps between these two deterioration paths became smaller, especially during the SDP.

For Specimen T8R15A45S80, only the FDP existed. The normalized opening load showed a little greater deterioration rate than the normalized closing load, but the difference was so small that it can be neglected.

BENDING MOMENT

Similarly, it is referred to as the bending moment deterioration that the bending moment required to produce a certain rotation of strip legs decreases as the loading cycle increases, and it also indicates the propagation of cracks and the decrease of net cross section of a strip specimen. And the bending moment deterioration can be investigated by studying the relation between the normalized bending moment and the loading cycle. The normalized bending moment can be expressed as follows:

$$m_{po} = \frac{M_{ipo}}{M_{1po}} \tag{6.13.1}$$

$$m_{vc} = \frac{M_{ivc}}{M_{1vc}} \tag{6.13.2}$$

where, m_{po} and m_{vc} are the normalized peak opening bending moment and the normalized valley closing bending moment respectively, M_{ipo} and M_{ivc} are the peak opening bending moment and the valley closing bending moment in the i^{th} cycle respectively, and M_{1po} and M_{1vc} are the peak opening bending moment and the valley closing bending moment in the first cycle respectively.

Typical deterioration diagrams of normalized bending moment are given in Figure 6.5. By investigating these diagrams, the same observations can be drawn as those for the normalized axial load, so neither description nor discussion is provided here.

HYSTERESIS LOOP ENERGY

The hysteresis loop energy (HLE) in a loading cycle is the area enclosed by its corresponding hysteresis loop, and it indicates the energy absorbed by the strip specimen during this loading cycle. The decrease of HLE shows that the strip specimen loses some of its energy-absorption capability, and the strip specimen is fractured when it loses all of its energy-absorption capability. The peak/valley axial load and the peak/valley bending moment is the value at a specific moment, but the HLE is the value of a whole cycle and it combines the results of opening

and closing a strip specimen once. Therefore, the HLE can more accurately reflect the LCF behaviour of a strip specimen.

The following discussion will only focus on the deterioration of two types of HLE: one is generated from the axial load and stroke hysteresis loops, and the other is produced from the bending moment and rotation hysteresis loops. For simplicity, the former is denoted as the LS HLE, and the latter is written as the MR HLE.

Following the same procedure adopted previously, the normalized HLE can be expressed as follows:

$$u_{LS} = \frac{U_{iLS}}{U_{1LS}} \tag{6.14.1}$$

$$u_{MR} = \frac{U_{iMR}}{U_{1MR}} \tag{6.14.2}$$

where, u_{LS} and u_{MR} are the normalized LS HLE and the normalized MR HLE respectively; U_{iLS} and U_{iMR} are the LS HLE and the MR HLE in the i^{th} cycle respectively; and U_{1LS} and U_{1MR} are the LS HLE and the MR HLE in the first cycle respectively.

Typical deterioration diagrams of normalized LS HLE and normalized MR HLE are presented in Figure 6.6. This figure exhibits that the normalized LS HLE exactly follows the same deterioration path as the normalized MR HLE from beginning to end, and the merging of these two paths indicates that the deterioration of HLE is independent of the type of hysteresis loops, from which the HLE is calculated. However, this merging does not indicate that these two types of HLE are the same. Actually, they have the different amplitudes, and moreover, the sum of LS HLE of all cycles is not equal to that of MS HLE of all cycles. By reviewing the deterioration paths of the normalized axial load and the normalized bending moment (see Figures 6.4 and 6.5), it can be seen that each of them has two paths, the opening path and the closing path, and these two paths deviate from each other. Moreover, the deterioration path of axial load does not merge with that of the bending moment. Based on these comparisons, it can be

concluded that the deterioration of normalized HLE can more precisely describe the LCF damage of strip specimens than that of the normalized axial load and that of the normalized bending moment.

Same as the deterioration paths of the normalized axial load and normalized bending moment, the deterioration path of HLE consists of the SDP and the FDP for specimens tested by small or medium stroke range and only the FDP for specimens tested by large stroke range.

As a summary, the deterioration rates for all specimens tested by typical stroke spectra are given in Table 6.5.

SUMMARY

Generally, the LCF life is the sum of the life of crack initiation and the life of crack propagation up to failure. But based on the above investigation, the life of crack initiation can be neglected, and this conclusion is coincident with the previous work, such as Radhakrishnan (1978) and Bhattacharya and Ellingwood (1998). As for the life of crack propagation, it can be further divided into two parts for the specimens tested by small or medium stroke: one is the life of SDP and the other is the life of FDP. Furthermore, it can be found that the life of SDP dominates the fatigue life. The last conclusion is that the deterioration of normalized HLE can more precisely describe the LCF damage than that of normalized axial load and that of normalized bending moment.

6.4.2.2 GENERAL DESCRIPTION OF THE DETERIORATION RATE-BASED MODEL

Based on the deterioration investigation, the deterioration rate of HLE is constant during SDP. Therefore, if only the life of SDP is concerned, then the LCF life prediction model based on the deterioration rate of HLE can be developed by using the aforementioned two damage parameters.

Assuming a power relation exists between the damage parameter and the deterioration rate of HLE of a pseudo strip specimen, and then the following

equation can be obtained by employing the same procedure as that was used in developing the life-based model and by using the same notations and definitions.

$$\Omega = C_1\left(\frac{du}{dN_v}\right)^m \tag{6.15.1}$$

where du/dN_v is the deterioration rate of HLE of a pseudo strip specimen, and the other parameters are the same as before.

Or on a log-log scale, it can be expressed as follows:

$$\log\Omega = C - m\log\frac{du}{dN_v} \tag{6.15.2}$$

The following relation holds between the deterioration rate of HLE of a pseudo strip specimen, du/dN_v, and that of an actual strip specimen, du/dN_d:

$$\frac{du}{dN_v} = \frac{du/dN_d}{D_c} \tag{6.16}$$

where all parameters are the same as before.

6.4.2.3 EQUIVALENT STROKE RANGE BASED MODEL

By employing the LCF damage, the deterioration rate of HLE of a pseudo strip specimen can be obtained from that of an actual strip specimen, which is given in Table 6.5. And then the equivalent stroke range based models can be obtained by selecting equivalent stroke range as the damage parameter and by using the best-fit method. The results of C and m are given in Tables 6.6. Please note that only the true scale is used here.

6.4.2.4 ROTATION RANGE BASED MODEL

Following the same procedure as that used on above, the rotation range based models can be developed and the results of C and m are shown in Tables 6.6.

6.5 DISCUSSION AND RECOMMENDATION

Because the models were developed by using the best-fit method, so the corresponding statistic parameters can be used to evaluate the reliability of the

models. The following will first introduce three key parameters, and then the models will be evaluated and discussed.

6.5.1 THREE STATISTIC PARAMETERS

6.5.1.1 STANDARD DEVIATION

Standard deviation, s, is defined by

$$s = \sqrt{\frac{\sum_{i=1}^{n}(x_i - x_m)^2}{n-1}} \tag{6.17.1}$$

where x_i is the sample, x_m is the mean of the sample, and n is the size of the sample.

From this definition, it is known that s is small when x_i is close to x_m. In other words, s indicates how far the sample is away from its mean.

6.5.1.2 COEFFICIENT OF MULTIPLE DETERMINATION

Coefficient of multiple determination, R^2, is defined by

$$R^2 = 1 - \frac{\sum_{i=1}^{n}(x_i - p_i)^2}{\sum_{i=1}^{n}(x_i - x_m)^2} \tag{6.17.2}$$

where p_i is the predicted value, and the other parameters are the same as in Equation (6.17.1).

R^2 is a number between 0 and 1, and it reveals that how closely the estimated values from the trendline correspond to the actual data. A trendline is most reliable when its R^2 value is at or near 1.

6.5.1.3 CORRELATION COEFFICIENT

The correlation coefficient, ρ, is defined by

$$\rho = \frac{\sum_{i=1}^{n}(x_i - x_m)(y_i - y_m)}{\sqrt{\sum_{i=1}^{n}(x_i - x_m)^2 \sum_{i=1}^{n}(y_i - y_m)^2}} \tag{6.17.3}$$

where, the parameters are the same as before.

$\rho < 0$ if the trendline of the sample shows a negative slope; and on the contrary, $\rho > 0$ if a positive slope is exhibited. The absolute value of this parameter also varies between 0 and 1 and it indicates how close the relation between these two sets of data is to a linear relation. A linear relation is most reliable when ρ is at or near ± 1.

In a summary, when s is closer to zero, and R^2 and the absolute value of ρ are closer to unity, the regression result is more reliable.

6.5.2 RESULTS, COMPARISON AND DISCUSSION

All results are given in Tables 6.3, 6.4 and 6.6. In those tables, C and m are the regression parameters, and s, ρ, and R^2 are the statistic parameters. For the purpose of comparison, the results of life-based models are given on both true scale, Table 6.3, and engineering scale, Table 6.4. But the results of deterioration rate-based models are only given on true scale, Table 6.6.

6.5.2.1 EFFECT OF DAMAGE ACCUMULATION RULE

For the models based on the true strain scale (Tables 6.4 and 6.6), they were not obviously influenced by the DAR. But for the models based on the engineering scale (Table 6.3), their qualities were improved by using the SRSDAR compared with the other two rules, especially for 11.9 mm thick specimens. This observation indicates that the damage due to the loss of static ductility contributes much more to the failure of those specimens than the LCF damage. In other words, the failure is dominated by the ductile damage. Based on this observation, the SRSDAR is recommended.

6.5.2.2 EFFECT OF DAMAGE PARAMETER

From these tables, it is clear that the quality of model is influenced by the selection of damage parameters. For the fatigue life-based models of 6 mm thick specimens, the equivalent stroke range based models are better than the rotation range based models. But for the other two sets of material, the rotation range based models are better than the equivalent stroke range based models, especially for the deterioration rate-based models. From previous discussions, it is known that the rotation range has a more direct relation with the deformation of strip bend than the equivalent stroke range, so it is not surprising that the rotation range based models behave better than the equivalent stroke range based models. However, it is much easier to determine the equivalent stroke range than the rotation range. Therefore, both rotation range and equivalent stroke range are recommended.

6.5.2.3 EFFECT OF STRESS-STRAIN SCALE

By comparing Table 6.3 with Table 6.4, it can be concluded that the quality of model is independent of the stress-strain scale employed in determining the ductile damage. But for application concern, because the engineering strain becomes gauge length-dependent after necking occurs, the ductile damage has to be evaluated by using the engineering strain and the engineering fracture strain based on the same gauge length. This requirement greatly limits its application, and it is difficult and also impractical to be satisfied. Based on this discussion, the true stress-strain scale is recommended to evaluate the ductile damage.

6.5.2.4 LIFE-BASED VS. DETERIORATION RATE-BASED MODELS

By comparing Table 6.4 and Table 6.6, it can be found that the life-based models are better than the deterioration rate-based models. In the deterioration rate-based models, the deterioration rate of normalized HLE was obtained by computing the HLE in each cycle and then by best-fitting of those data. Although the computation of HLE did not lead to significant errors because it was a direct result of test data, but the best-fit could cause significant errors. In other words,

the deterioration rate models were obtained by best-fitting the test data two times, so it was not surprised that this type of model has relatively poor quality.

However, the deterioration rate-based models have their own specific benefits. The most important one is that it directly relates the deterioration with the fatigue life, so it is very convenient if a deterioration-based failure criterion is employed. Second, by limiting the failure in SDP, it provides more conservative results. Third, like the crack propagation rate-based model that is widely used in fracture mechanics, it works in a more analytic way. Therefore, this type of model is also recommended.

6.5.2.5 PREVIOUS TEST RESULTS

In the previous strip tests and its corresponding coupon tests, which were conducted by Myrholm (2001) and Das (2002), the rotation range, the deterioration rate of HLE, and the true fracture strain and true fracture stress were not included, so only the equivalent stroke range can be obtained and only the engineering stress-strain scale can be employed to evaluate the ductile damage.

Das (2002) tested a total of 16 strip tests. Among of them, eight were 6.0 mm thick and eight were 8.3 mm thick. Because those two sets of thicknesses were also used in this test, they can be compared with this test directly. The results are shown in Figure 6.7. It can be seen that the Das' tests coincide well with the models developed from this test. Based on this observation, the test data from those two tests can be combined together to develop new models, and the results are given in Table 6.7. This table also exhibits that the newly developed models have good qualities.

Myrholm (2001) did eight strip tests on 6.75 mm thick specimens. Because this set of thickness was not used in this test, his test results were re-analyzed separately to develop the same types of models as those from this test. The results are presented in Table 6.7, and it can be seen that the so-developed models have great qualities.

6.5.2.6 FURTHER ANALYSIS AND DISCUSSION

From Tables 6.3, 6.4, 6.6 and 6.7, it can be seen that C and m are almost constants for each type of model regardless of the material thickness, and this observation indicates that a unified model independent of the specimen thickness can be developed by best-fitting all test data. However, because the previous test programs might use different fracture failure criteria, two sets of life-based models will be developed, which are the models based on this test series only and the models based on all tests respectively. The results and their corresponding parameters are also given in these tables.

The results also show very good linear correlation (ρ close to negative unit) and good coincidence between the predicted values from these models and the test results (R^2 close to unit). A comparison with previous tests is also given in Figure 6.8, it can be seen that all data are within a narrow band of the experimental model. So the unified model has very good quality and it is recommended for future use.

6.5.3 RECOMMENDATION

6.5.3.1 DAMAGE PARAMETER

Both the equivalent stroke range and the rotation range are recommended. The equivalent stroke range is much easier to be applied to the full-scale pipes, but the rotation range can give more accurate prediction. Therefore if available, the rotation range is the preferred choice.

6.5.3.2 STRESS-STRAIN SCALE

Because the engineering strain becomes gauge-length dependent after necking occurs and it can not be assured that all obtained engineering strains have the same gauge length and are on the same location, the true stress-strain scale is recommended to compute the ductile damage.

6.5.3.3 DAMAGE ACCUMULATION RULE

Based on the previous discussion, the SRSDAR is recommended although the LDAR is simple and works well in most of cases.

6.5.3.4 CONFIDENCE LEVEL

The confidence level directly relates to the probability that these models fail to give a safe prediction of LCF life. For discussion convenience, this probability is called the fail-to-predict probability. A higher confidence level will give a lower fail-to-predict probability, e.g. a confidence level of 50% corresponds to a fail-to-predict probability of 50% and a confidence level of 97% corresponds to a fail-to-predict probability of 3%.

The models obtained by directly best-fitting the test data only have a confidence level of 50% and this is too low for engineering application. By subtracting two times of standard deviation from these models, new models can be obtained and the so-obtained models give a confidence level of 97.7%. This confidence level is appropriate enough for general engineering application, so this research program recommends a confidence level of 97.7%. Also for discussion convenience, the models with a confidence level of 50% are called experimental models, and those with the recommended confidence level are called the recommended models.

6.5.3.5 SUMMARY

Based on the above recommendations, the corresponding models are collected together in Table 6.8 and they are also shown in Figures 6.9 to 6.12.

6.6 APPLICATION TO FULL-SCALE PIPES

6.6.1 DETERMINATION OF EQUIVALENT STROKE RANGE

To apply the previously developed models to the tested full-scale pipes, the damage parameters have to be properly determined firstly. For strip specimens, the damage parameters are their global behaviour and they can be easily obtained by direct measurement. But for the tested full-scale pipes, they are their local

(wrinkle) behaviour. Because the wrinkle location is unpredictable, it is unknown where to install the instrument. Moreover, the wrinkle is limited within such a small area that it is impossible to install proper instruments to measure the wrinkle rotation, i.e. the rotation range can not be obtained. Therefore, the following will focus on how to determine the equivalent stroke range only.

6.6.1.1 FROM STRIP BEND TO WRINKLE

As that discussed in Chapter 3, the strip bend is a replica of wrinkle head only, but an actual wrinkle consists of one wrinkle head and two wrinkle feet. In the developed models, the equivalent stroke range is the relative axial displacement between two strip legs and it can be easily obtained from the strip test. But for a pipe wrinkle, it is difficult to get the equivalent stroke range because the relative axial displacement of wrinkle head can not be measured directly. In full-scale pipe tests, only the RAD of entire wrinkle can be measured, so the problem becomes to how to determine the equivalent stroke range from this RAD. If a pipe wrinkle is simplified as the mechanism shown in Figure 6.13, the same simplification made by Das (2002), then the following equation can be obtained:

$$\Delta S_e = \frac{e_s}{e_o}\Delta S \tag{6.18}$$

where ΔS_e is the equivalent stroke range, ΔS is the RAD of pipe wrinkle, e_s = 70 mm is the standard loading eccentricity, and e_o is the initial loading eccentricity before the cyclic load being applied.

It has to be mentioned that Equation (6.18) is obtained based on the following geometric relation:

$$\frac{e_{scl}}{e_{cl}} = \frac{e_{sop}}{e_{op}} = \frac{e_s}{e_o} \tag{6.19}$$

where the meanings of e_{scl}, e_{sop}, e_{cl} and e_{op} are illustrated in Figure 6.13.

e_o can be obtained either from the FEA or from the measurement, and the RAD of wrinkle can be measured or estimated, so the equivalent stroke range can be computed from Equation (6.18)

6.6.1.2 FROM LOCAL BEHAVIOUR TO GLOBAL BEHAVIOUR

In the field, it is not practical and also impossible to install a device over the wrinkle to measure its RAD. But the global behaviour of wrinkled pipe can be measured or estimated, so it has practical value to obtain the equivalent stroke range from the global behaviour.

In Chapter 4 and Chapter 5, the relation between the RAD between pivots and the RAD of wrinkle was investigated and the phenomenon of 'deformation localization' was observed. Moreover, it was found that for a fully developed wrinkle, the RAD between pivots approximately equals the RAD of wrinkle.

6.6.2 APPLICATION

6.6.2.1 GENERAL PROCEDURE

The above discussion illustrates how to apply the LCF life prediction models to the full-scale pipes theoretically. But in actuality, the scenario is more complicated and the difficulties arise from two aspects: on one hand, the actual cyclic loads have greatly varied amplitudes, so a counting method has to be employed to determine the number of cycles experienced by each stroke range; on the other hand, an actual wrinkle head is not a perfect curve of circle as the strip bend, so efforts have to be made to determine the wrinkle radius and loading eccentricity before cyclic load can be applied. As discussed in Chapter 5, the wrinkle radius can be determined either from measurement or from FEA, both of them can give satisfactory results. Although the loading eccentricity was not discussed, it can also be determined either by measurement or by FEA.

The procedure to apply the developed models to full-scale pipes can be summarized in the following eight steps:

Step1: Categorize the applied stroke ranges and count the corresponding cycles of each category by selecting a proper counting method, such as the rain flow method (Fisher etc. 1997).

Step 2: Determine the loading eccentricity before the cyclic loading being applied.

Step 3: Calculate the equivalent stroke range of each category.

Step 4: Determine the wrinkle radius.

Step 5: Compute the damage due to monotonic loading.

Step 6: Compute the pseudo fatigue life of each equivalent stroke range category.

Step 7: Compute the fatigue damage of each equivalent stroke range category.

Step 8: Compute the total damage and LCF life.

6.6.2.2 RESULTS AND DISCUSSION

Following the above procedure, D_m and D_c can be computed and the results are given in Table 6.9 and Table 6.10, respectively. By using the recommended DAR, i.e. the SRSDAR, the total damage can be obtained and the results are shown in Table 6.11. It can be seen that the total damage is very close to a unit either for specimen LCF16N1 or for specimen LCF20N, and this indicates that the recommended models work well for the full-scale pipes. By viewing the DAR, it can be found that the damage is dominated by D_m instead of by D_c, so it can be expected that D will be close to a unit if D_m is much larger than D_c, but this observation does not degrade the evaluation of those models. Take specimen LCF20N1 for example, the predicted D_c is 0.2810 and the actual D_c is 0.2136, so the error is 31.55%. From the fatigue point of view, the acceptable accuracy is about 50% to 200% according to Heuler and Schuetz (1986), so this error is within the acceptable range.

6.7 SUMMARY AND CONCLUSIONS

The models developed in this chapter have many forms: the damage parameter can be either rotation range or equivalent stroke range, the model can be based on either fatigue life or deterioration rate, the DAR can be SRSDAR, LDAR, or SSRDAR, and the ductile damage can be evaluated either on engineering scale or on true scale. But the comparisons exhibit that the SRSDAR works better than both the LDAR and the SSRDAR, and the rotation range generates more accurate models than the equivalent stroke range, and the life-based models have better

quality than the deterioration rate-based models. Based on the concern of engineering application, this research program recommends the SRSDAR, both damage parameters, the true scale-based evaluation of ductile damage, and both LCF life prediction models.

Further investigation found that a unified model can give accurate LCF life prediction to all tested specimens and this indicates that the proposed models have great prediction abilities. Finally, the models were applied to the tested full-scale pipes and the results show that the proposed models can predict their LCF lives very well.

Table 6.1: Results of D_m in engineering scale

Material thickmess (mm)	6		8.3		12.64	
Bend radius (mm)	15	20	15	20	15	20
ε_r (mm/mm)	0.1667	0.1304	0.2167	0.1718	0.2964	0.2401
ε_f (mm/mm)	0.2994		0.3054		0.3346	
$D_m^{[1]}$	0.5693	0.4437	0.7288	0.5587	0.9185	0.7601
$D_m^{[2]}$	0.5567	0.4357	0.7096	0.5627	0.8859	0.7176
Difference (%)	-2.22	-1.81	-2.64	0.71	-3.54	-5.59

Note:

1 Material thickness is obtained by measurement;

2 $D_m^{[1]}$ is obtained by Eq.(6.2.1), and $D_m^{[2]}$ by Eq.(6.2.2);

3 Difference= $(D_m^{[2]}-D_m^{[1]})/D_m^{[1]}$ x 100.

Table 6.2: Results of D_m in true scale

Material thickmess (mm)	6		8.3		12.64	
Bend radius (mm)	15	20	15	20	15	20
ε_{tr} (mm/mm)	0.1857	0.1374	0.2436	0.1884	0.3450	0.2801
ε_{tf} (mm/mm)	0.8124		0.7968		1.0030	
$D_m^{[1]}$	0.1922	0.1382	0.2692	0.2035	0.3001	0.2395
$D_m^{[2]}$	0.1865	0.1321	0.2501	0.1889	0.2845	0.2260
Difference (%)	-2.96	-4.40	-7.09	-7.20	-5.20	-5.65

Note:

1 Material thickness is obtained by measurement;

2 $D_m^{[1]}$ is obtained by Eq.(6.3.1), and $D_m^{[2]}$ by Eq.(6.3.2);

3 Difference= $(D_m^{[2]}-D_m^{[1]})/D_m^{[1]}$ x 100.

Table 6.3: Life-based models and its corresponding parameters (engineering scale)

Category	Parameter	SRSDAR		LDAR		SSRDAR	
		ESR	RR	ESR	RR	ESR	RR
t = 6 mm	C	2.1839	0.3107	2.2012	0.3278	2.1864	0.3170
	m	-0.3505	-0.3032	-0.3533	-0.3071	-0.3544	-0.3094
	s	0.0559	0.0552	0.0578	0.0547	0.0604	0.0550
	ρ	-0.9534	-0.9403	-0.9501	-0.9415	-0.9453	-0.9409
	R^2	0.9089	0.8842	0.9026	0.8865	0.8936	0.8852
t = 8.3 mm	C	2.1408	0.3290	2.1724	0.3574	2.1670	0.3486
	m	-0.3314	-0.3276	-0.3283	-0.3229	-0.3176	-0.3104
	s	0.0619	0.0328	0.0617	0.0371	0.0668	0.0491
	ρ	-0.9469	-0.9839	-0.9472	-0.9793	-0.9379	-0.9634
	R^2	0.8966	0.9680	0.8972	0.9591	0.8796	0.9281
t = 11.9 mm	C	2.2304	0.4153	2.2657	0.4493	2.1813	0.3688
	m	-0.3503	-0.3351	-0.3248	-0.3109	-0.2576	-0.2466
	s	0.0775	0.0449	0.0994	0.0744	0.1434	0.1236
	ρ	-0.9516	-0.9814	-0.9191	-0.9481	-0.8227	-0.8490
	R^2	0.9056	0.9631	0.8448	0.8990	0.6768	0.7208
All data	C	2.1568	0.3210	2.1270	0.2916	2.0257	0.1956
	m	-0.3269	-0.3044	-0.2856	-0.2650	-0.2199	-0.2031
	s	0.0676	0.0513	0.0868	0.0737	0.1180	0.1059
	ρ	-0.9525	-0.9677	-0.9203	-0.9320	-0.8468	-0.8535
	R^2	0.9072	0.9364	0.8469	0.8685	0.7171	0.7285

Note:

SRSDAR = Square root and square damage accumulation rule;

LDAR = Linear damage accumulation rule;

SSRDAR = Square and square root damage accumulation rule;

ESR = Equivalent stroke range;

RR = Rotation range;

C, m = Constants in equation $\log\Omega = C + m \log N_{vf}$;

s, ρ = Standard deviation and correlation coefficient respectively;

R^2 = Coefficient of multiple determination.

Table 6.4: Life-based models and its corresponding parameters (true scale)

Category	Parameter	SRSDAR		LDAR		SSRDAR	
		ESR	RR	ESR	RR	ESR	RR
t = 6 mm (This Test Only)	C	2.1235	0.2566	2.1121	0.2469	2.0919	0.2290
	m	-0.3464	-0.2983	-0.3468	-0.2988	-0.3454	-0.2973
	s	0.0552	0.0566	0.0552	0.0564	0.0552	0.0569
	ρ	-0.9545	-0.9373	-0.9545	-0.9376	-0.9545	-0.9365
	R^2	0.9111	0.8785	0.9111	0.8792	0.9111	0.8770
t = 8.3 mm (This Test Only)	C	2.0651	0.2562	2.0568	0.2477	2.0343	0.2256
	m	-0.3300	-0.3278	-0.3304	-0.3280	-0.3300	-0.3278
	s	0.0654	0.0347	0.0649	0.0342	0.0654	0.0347
	ρ	-0.9405	-0.9819	-0.9415	-0.9824	-0.9405	-0.9819
	R^2	0.8846	0.9641	0.8865	0.9652	0.8846	0.9641
t = 11.9 mm (This Test Only)	C	2.1008	0.2911	2.0930	0.2837	2.0679	0.2597
	m	-0.3565	-0.3410	-0.3567	-0.3412	-0.3566	-0.3411
	s	0.0729	0.0376	0.0726	0.0371	0.0728	0.0373
	ρ	-0.9573	-0.9870	-0.9577	-0.9874	-0.9575	-0.9872
	R^2	0.9165	0.9742	0.9172	0.9749	0.9168	0.9745
All data (This Test Only)	C	2.1089	0.2784	2.0985	0.2687	2.0763	0.2479
	m	-0.3546	-0.3314	-0.3542	-0.3310	-0.3545	-0.3313
	s	0.0649	0.0449	0.0641	0.0441	0.0650	0.0453
	ρ	-0.9563	-0.9753	-0.9573	-0.9762	-0.9561	-0.9762
	R^2	0.9145	0.9513	0.9164	0.9529	0.9140	0.9504

Note:

SRSDAR = Square and root-square damage accumulation rule;

LDAR = Linear damage accumulation rule;

SSRDAR = Square and square root damage accumulation rule;

ESR = Equivalent stroke range;

RR = Rotation range;

C, m = Constants in equation $\log\Omega = C + m \log N_{vf}$;

s, ρ = Standard deviation and correlation coefficient respectively;

R^2 = Coefficient of multiple determination.

Table 6.5: Summary of deterioration rate of HLE and the corresponding lives

Specimen	Deterioration rate		Life			Note
	SDP	FDP	SDP	FDP	Total	
T6R15A45S30	N.A.	N.A.			68.50	bad test
T6R15A45S50	-0.004782	-0.139354	15.00	7.75	22.75	
T6R15A45S80	-0.074500	-0.359800	3.00	2.25	5.25	
T6R15A60S30	-0.003479	-0.082998	21.00	12.25	33.25	
T6R15A60S50	-0.038910	-0.208430	5.00	3.75	8.75	
T6R15A60S80	N.A.	N.A.			6.75	bad test
T6R20A45S30	-0.000309	-0.052551	89.00	20.25	109.25	
T6R20A45S50	-0.002875	-0.143837	19.00	7.75	26.75	
T6R20A45S80	-0.059830	-0.221800	5.00	1.25	6.25	
T6R20A60S20	-0.000886	-0.049332	58.00	19.00	77.00	
T6R20A60S30	-0.003912	-0.100758	19.00	10.00	29.00	
T6R20A60S50	-0.036520	-0.209840	5.00	3.75	8.75	
T8R15A45S30	-0.002819	-0.051159	47.00	15.75	62.75	
T8R15A45S50	-0.041303	-0.160877	6.00	5.00	11.00	
T8R15A45S80	N.A.	-0.258000	0.00	3.25	3.25	FDP only
T8R15A60S20	-0.005528	-0.046455	39.00	16.00	55.00	
T8R15A60S30	-0.016317	-0.092567	11.00	8.75	19.75	
T8R15A60S50	-0.108930	-0.235670	4.00	3.25	7.25	
T8R20A45S30	-0.001048	-0.045126	109.00	20.25	129.25	
T8R20A45S50	-0.013475	-0.149868	9.00	5.75	14.75	
T8R20A45S80	N.A.	-0.154350	0.00	3.25	3.25	FDP only
T8R20A60S30	-0.008674	-0.090575	19.00	10.75	29.75	
T8R20A60S50	-0.029080	-0.184351	4.00	4.75	8.75	
T8R20A60S80	N.A.	N.A.				bad specimen
T12R15A45S20	-0.002357	-0.023342	83.00	31.00	114.00	
T12R15A45S30	-0.008846	-0.055813	26.00	12.75	38.75	
T12R15A45S50	-0.056014	-0.115694	6.00	6.75	12.75	
T12R15A45S70	N.A.	-0.264650	0.00	4.00	4.00	FDP only
T12R15A60S12	-0.001430	-0.015140	179.00	47.00	226.00	
T12R15A60S20	-0.007592	-0.038119	39.00	18.00	57.00	
T12R15A60S30	-0.008595	-0.050900	32.00	12.75	44.75	
T12R15A60S50	N.A.	N.A.				bad test
T12R20A45S20	-0.000855	-0.010642	228.00	52.00	280.00	
T12R20A45S30	-0.002831	-0.044196	61.00	17.75	78.75	
T12R20A45S50	-0.012776	-0.103455	16.00	6.25	22.25	
T12R20A45S70	-0.091190	-0.231530	4.00	3.00	7.00	
T12R20A60S12	-0.000364	1.059785	466.00	150.00	616.00	
T12R20A60S20	-0.004078	-0.043545	42.00	18.00	60.00	
T12R20A60S30	-0.035685	-0.091905	9.00	6.00	15.00	
T12R20A60S50	-0.163950	-0.246300	3.00	2.00	5.00	

Note: SDP = slow deterioration period and FDP = fast deterioration period.

Table 6.6: Deterioration rate-based models and its corresponding parameters (true scale)

Category	Parameter	SRSDAR		LDAR		SSRDAR	
		ESR	RR	ESR	RR	ESR	RR
t = 6 mm	C	2.0300	0.2440	2.0363	0.2503	2.0478	0.2618
	m	0.1919	0.1908	0.1917	0.1906	0.1924	0.1913
	s	0.0839	0.0465	0.0840	0.0467	0.0837	0.0461
	ρ	0.8931	0.9628	0.8928	0.9625	0.8936	0.9634
	R^2	0.7976	0.9270	0.7971	0.9265	0.7986	0.9281
t = 8.3 mm	C	1.9537	0.1515	1.9583	0.1564	1.9740	0.1721
	m	0.2179	0.2202	0.2171	0.2196	0.2179	0.2202
	s	0.0876	0.0592	0.0882	0.0601	0.0876	0.0592
	ρ	0.8906	0.9463	0.8888	0.9447	0.8906	0.9463
	R^2	0.7932	0.8954	0.7900	0.8924	0.7932	0.8954
t = 11.9 mm	C	1.9631	0.1638	1.9684	0.1689	1.9875	0.1873
	m	0.2667	0.2575	0.2664	0.2571	0.2666	0.2573
	s	0.0908	0.0562	0.0913	0.0569	0.0910	0.0565
	ρ	0.9330	0.9707	0.9323	0.9699	0.9327	0.9704
	R^2	0.8705	0.9423	0.8691	0.9408	0.8699	0.9417
All data	C	1.9633	0.1616	1.9670	0.1652	1.9845	0.1823
	m	0.2220	0.2155	0.2207	0.2143	0.2225	0.2160
	s	0.1243	0.1053	0.1254	0.1065	0.1240	0.1048
	ρ	0.8262	0.8595	0.8229	0.8560	0.8273	0.8607
	R^2	0.6826	0.7387	0.6771	0.7327	0.6844	0.7408

Note:

SRSDAR = Square root and square damage accumulation rule;

LDAR = Linear damage accumulation rule;

SSRDAR = Square and square root damage accumulation rule;

ESR = Equivalent stroke range;

RR = Rotation range;

C, m = Constants in equation $\log\Omega = C + m \log du/N_v$;

s, ρ = Standard deviation and correlation coefficient respectively;

R^2 = Coefficient of multiple determination.

Table 6.7: Comparison with previous test results: life based models (engineering scale)

Category	Parameter	SRSDAR		LDAR		SSRDAR	
		ESR	RR	ESR	RR	ESR	RR
t = 6 mm (All)	C	2.1961		2.2175		2.2064	
	m	-0.3487		-0.3547		-0.3585	
	s	0.0548		0.0535		0.0534	
	ρ	-0.9430		-0.9456		-0.9459	
	R^2	0.8892		0.8942		0.8947	
t = 6.85 mm (Myrholm)	C	2.2049		2.2097		2.1694	
	m	-0.3037		-0.2829		-0.2458	
	s	0.0158		0.0163		0.0263	
	ρ	-0.9844		-0.9835		-0.9565	
	R^2	0.9691		0.9672		0.9149	
t = 8.3 mm (All)	C	2.1519		2.1846		2.1809	
	m	-0.3376		-0.3348		-0.3239	
	s	0.0465		0.0467		0.0533	
	ρ	-0.9661		-0.9659		-0.9552	
	R^2	0.9334		0.9330		0.9125	
All data	C	2.1829		2.1646		2.0859	
	m	-0.3358		-0.2990		-0.2405	
	s	0.0617		0.0742		0.0990	
	ρ	-0.9586		-0.9397		-0.8898	
	R^2	0.9190		0.8830		0.7918	

Note:

SRSDAR = Square root and square damage accumulation rule;

LDAR = Linear damage accumulation rule;

SSRDAR = Square and square root damage accumulation rule;

ESR = Equivalent stroke range;

RR = Rotation range;

C, m = Constants in equation $\log\Omega = C + m \log N_{vf}$;

s, ρ = Standard deviation and correlation coefficient respectively;

R^2 = Coefficient of multiple determination.

Table 6.8: Summary of models

t (mm)	Expression	
	Experimental	Recommended
6	$\log\Delta S_e = 2.1235 - 0.3464 \log N_{vf}$	$\log\Delta S_e = 2.0131 - 0.3464 \log N_{vf}$
	$\log\Delta\theta = 0.2566 - 0.2983 \log N_{vf}$	$\log\Delta\theta = 0.1434 - 0.2983 \log N_{vf}$
8.3	$\log\Delta S_e = 2.0651 - 0.3300 \log N_{vf}$	$\log\Delta S_e = 1.9343 - 0.3300 \log N_{vf}$
	$\log\Delta\theta = 0.2562 - 0.3278 \log N_{vf}$	$\log\Delta\theta = 0.1868 - 0.3278 \log N_{vf}$
11.9	$\log\Delta S_e = 2.1008 - 0.3565 \log N_{vf}$	$\log\Delta S_e = 1.9550 - 0.3565 \log N_{vf}$
	$\log\Delta\theta = 0.2911 - 0.3410 \log N_{vf}$	$\log\Delta\theta = 0.2159 - 0.3410 \log N_{vf}$
All	$\log\Delta S_e = 2.1089 - 0.3546 \log N_{vf}$	$\log\Delta S_e = 1.9791 - 0.3546 \log N_{vf}$
	$\log\Delta\theta = 0.2784 - 0.3314 \log N_{vf}$	$\log\Delta\theta = 0.1886 - 0.3314 \log N_{vf}$
6	$\log\Delta S_e = 2.0300 + 0.1919 \log(du/dN_v)$	$\log\Delta S_e = 1.8622 + 0.1919 \log(du/dNv)$
	$\log\Delta\theta = 0.2440 + 0.1908 \log(du/dNv)$	$\log\Delta\theta = 0.1510 + 0.1908 \log(du/dNv)$
8.3	$\log\Delta S_e = 1.9537 + 0.0876 \log(du/dNv)$	$\log\Delta S_e = 1.7785 + 0.0876 \log(du/dNv)$
	$\log\Delta\theta = 0.1515 + 0.2202 \log(du/dNv)$	$\log\Delta\theta = 0.0331 + 0.2202 \log(du/dNv)$
11.9	$\log\Delta S_e = 1.9631 + 0.2667 \log(du/dNv)$	$\log\Delta S_e = 1.7815 + 0.2667 \log(du/dNv)$
	$\log\Delta\theta = 0.1638 + 0.2575 \log(du/dNv)$	$\log\Delta\theta = 0.0514 + 0.2575 \log(du/dNv)$
All	$\log\Delta S_e = 1.9633 + 0.2220 \log(du/dNv)$	$\log\Delta S_e = 1.7147 + 0.2220 \log(du/dNv)$
	$\log\Delta\theta = 0.1616 + 0.2155 \log(du/dNv)$	$\log\Delta\theta = -0.0490 + 0.2155 \log(du/dNv)$

Note:

1 All models are based on SRSDAR;
2 ΔS_e = equivalent stroke range;
3 $\Delta\theta$ = rotation range;
4 N_{vf} = pseudo fatigue life;
5 du/dN_v = pseudo deterioration rate of HLE;
6 The experimental models have a confidence of 50% and the recommended models have a confidence of 97.72%.

Table 6.9: Evaluation of D_m of full-scale pipe specimen

Pipe	R (mm)	t (mm)	ε_{tr}	ε_{tf}	σ_{ty} (Mpa)	σ_{tf} (Mpa)	D_m
LCF16N1	10.59	12.42	0.5006	0.9987	489.00	829.52	0.8712
LCF20N1	9.28	6.79	0.3198	0.8084	497.00	830.01	0.8483

Note:

1 ε_{tr} is computed by Equation (5.4.2);

2 D_m is computed by Equation (6.3.2).

Table 6.10: Evaluation of D_c of full-scale pipe specimen

	Category	1	2	3	4	5	6	7	8	9	Sum
LCF16N1	ΔS_i (mm)	6.00	12.50	15.00	16.00	17.00	19.00	26.00	27.00	47.00	
	ΔS_{ei} (mm)	7.97	16.60	19.92	21.25	22.58	25.24	34.54	35.86	62.43	
	N_{di} (cycle)	34.00	2.00	7.00	3.00	4.00	2.00	1.00	0.75	0.50	
	N_{vfi} (cycle)	2313.5	295.2	177.0	147.7	124.6	91.2	37.8	34.0	7.2	
	D_{ci}	0.0147	0.0068	0.0395	0.0203	0.0321	0.0219	0.0264	0.0220	0.0695	0.2534
LCF20N1	ΔS_i (mm)	6.50	10.00	12.00							
	ΔS_{ei} (mm)	11.38	17.50	21.00							
	N_{di} (cycle)	1.00	25.00	29.00							
	N_{vfi} (cycle)	1207.4	348.1	205.7							
	D_{ci}	0.0008	0.0718	0.1410							0.2136

Note:

1 ΔS_{ei} is obtained from Eqation (6.8.2);

2 N_{vfi} is computed from the following models:

$\log\Delta S_e = 2.1008 - 0.3565 \log N_{vf}$ for specimen LCF16N1,

$\log\Delta S_e = 2.1235 - 0.3464 \log N_{vf}$ for specimen LCF20N2;

3 $D_{ci} = N_{di}/N_{vfi.}$

Table 6.11: Evaluation of D of full-scale pipe specimen

Pipe	Dm	Dc	$D = D_m^{0.5} + D_c^2$
LCF16N1	0.8712	0.2534	0.9976
LCF20N1	0.8483	0.2136	0.9667

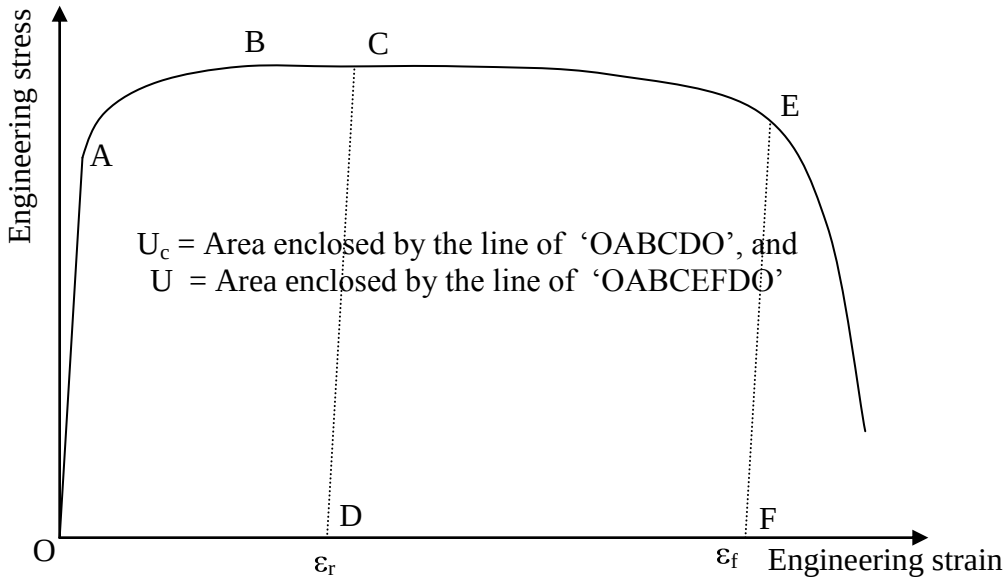

Figure 6.1: Illustration of U and Uc

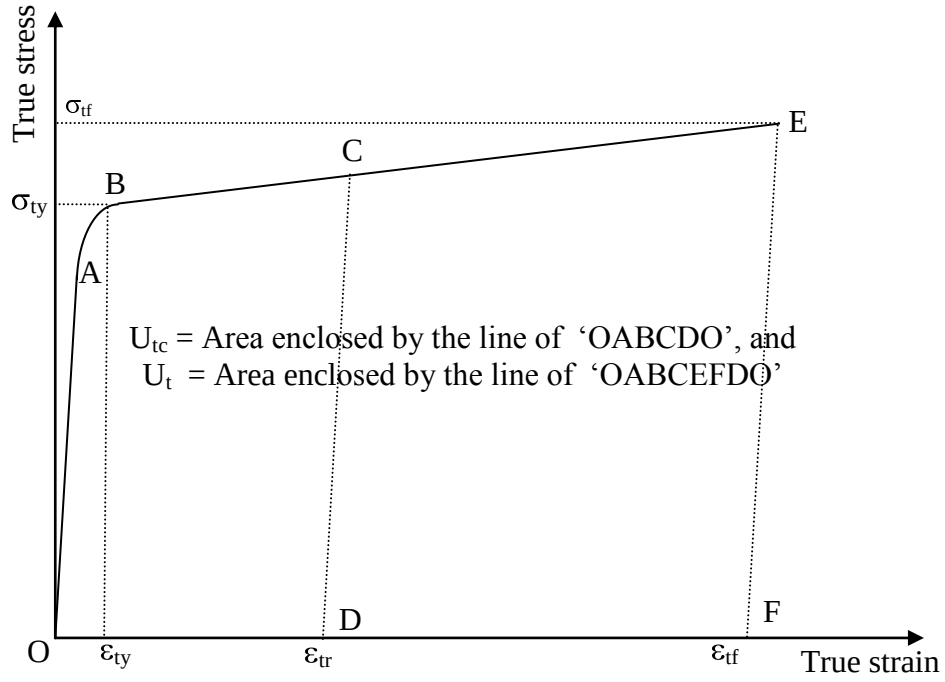

Figure 6.2: Illustration of U_t and U_{tc}

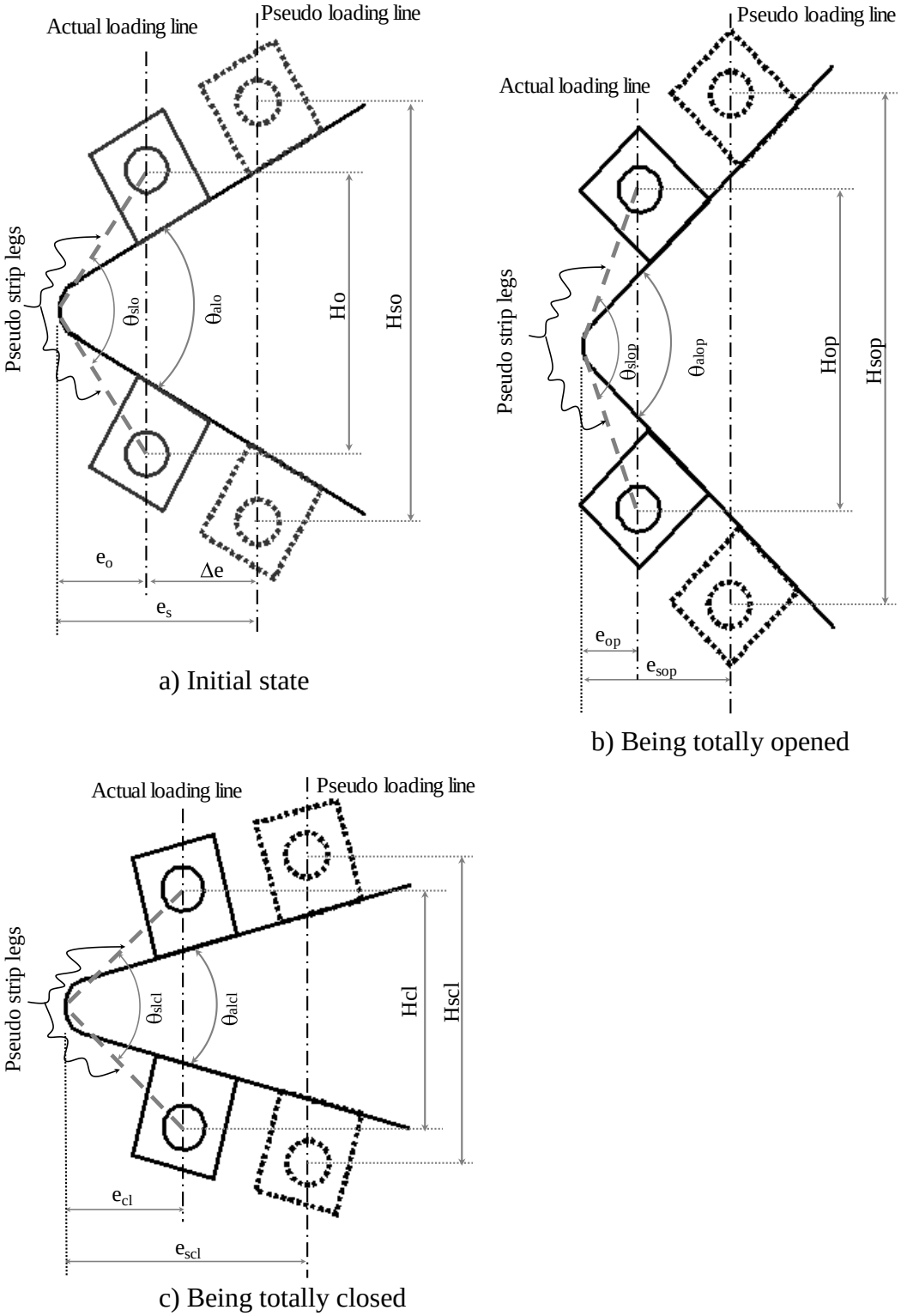

Figure 6.3: Illustration of calculating equivalent stroke range

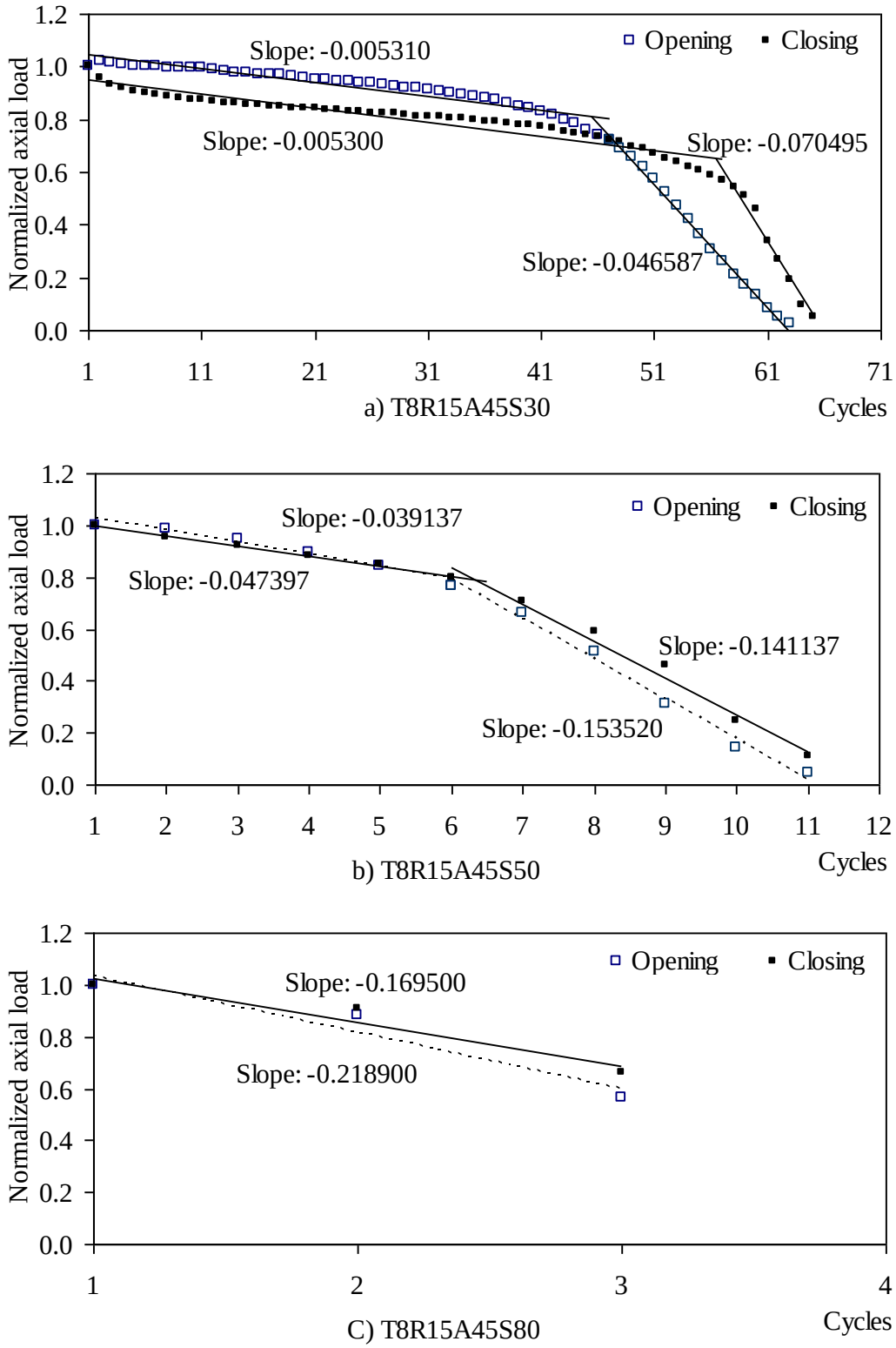

Figure 6.4: Typical deterioration diagrams of normalized axial load

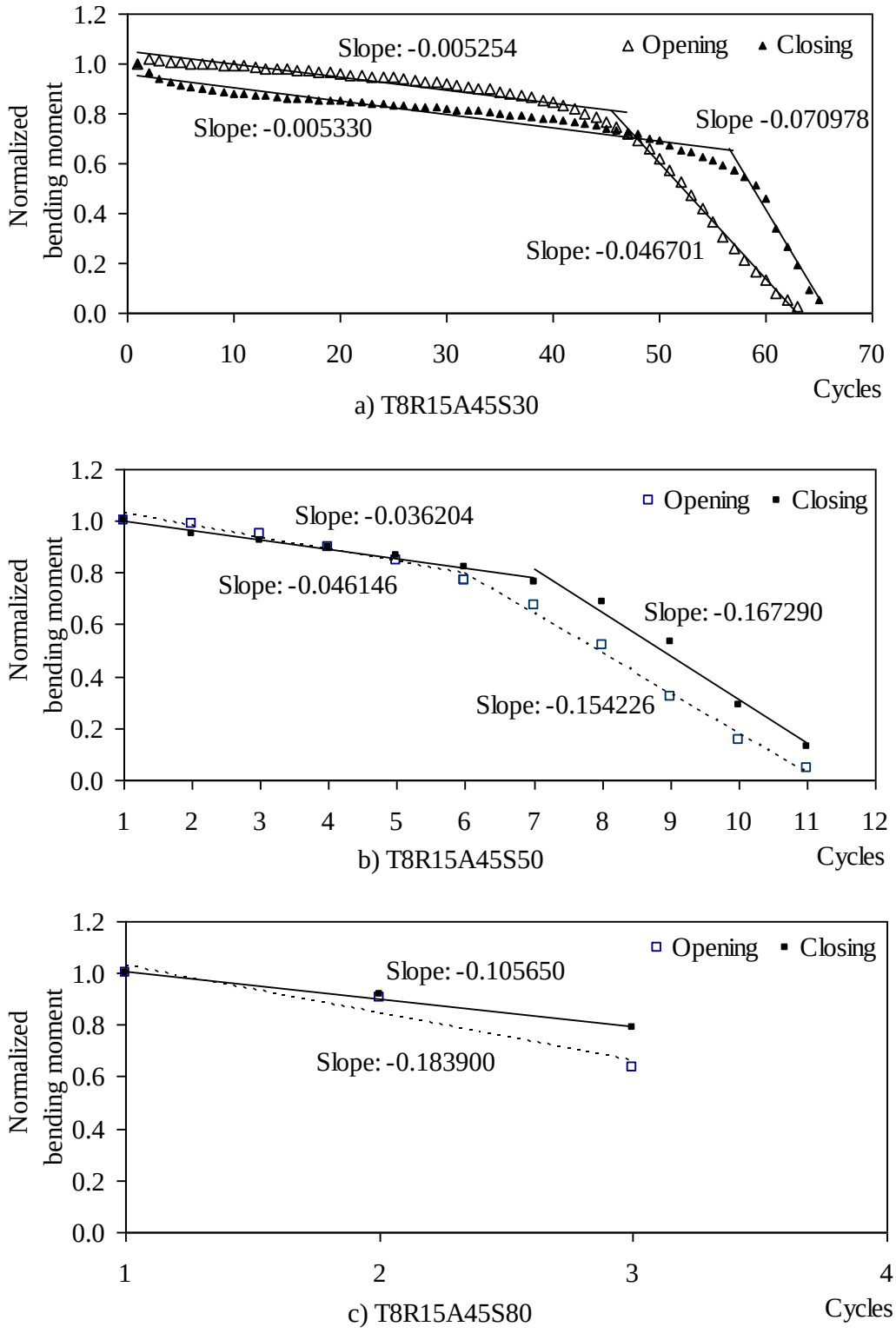

Figure 6.5: Typical deterioration diagrams of normalized bending moment

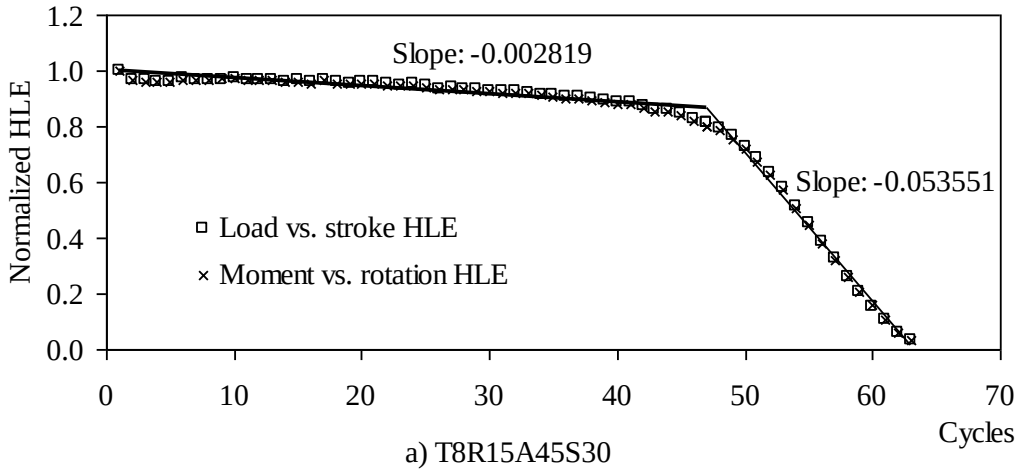

a) T8R15A45S30

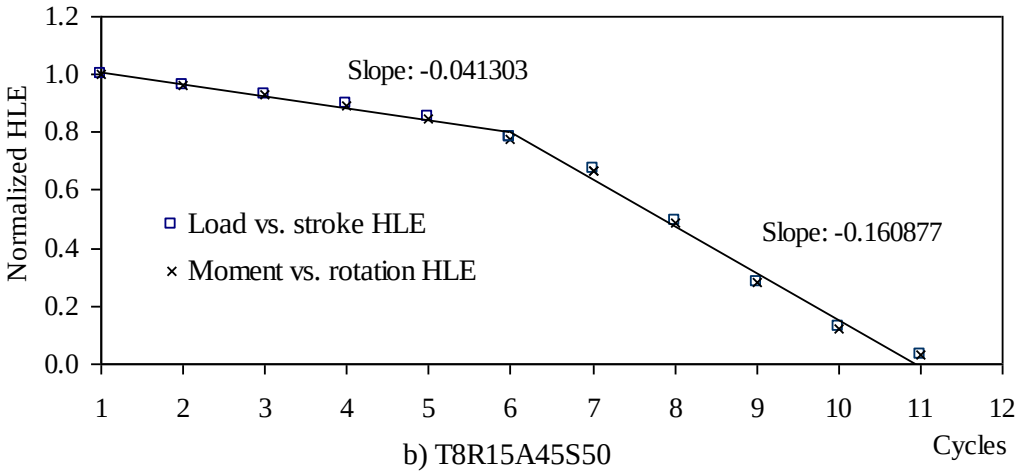

b) T8R15A45S50

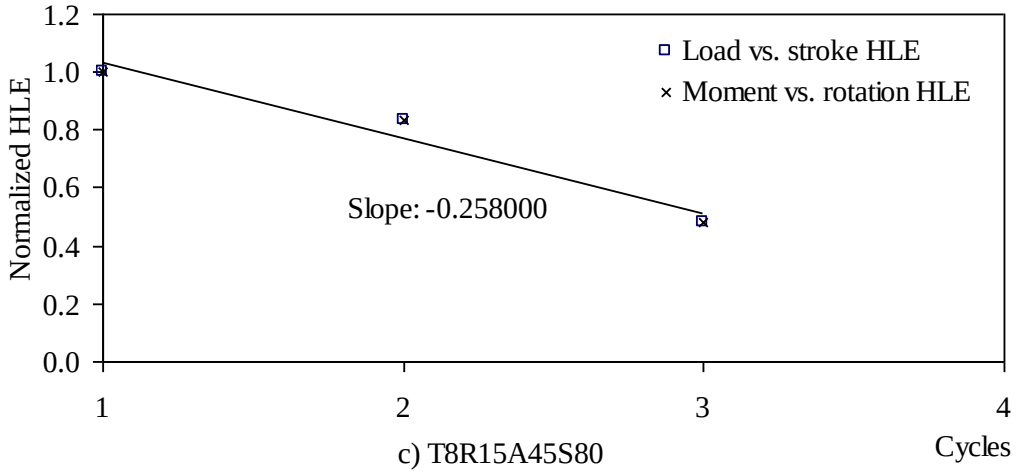

c) T8R15A45S80

Figure 6.6: Typical deterioration diagrams of normalized HLE

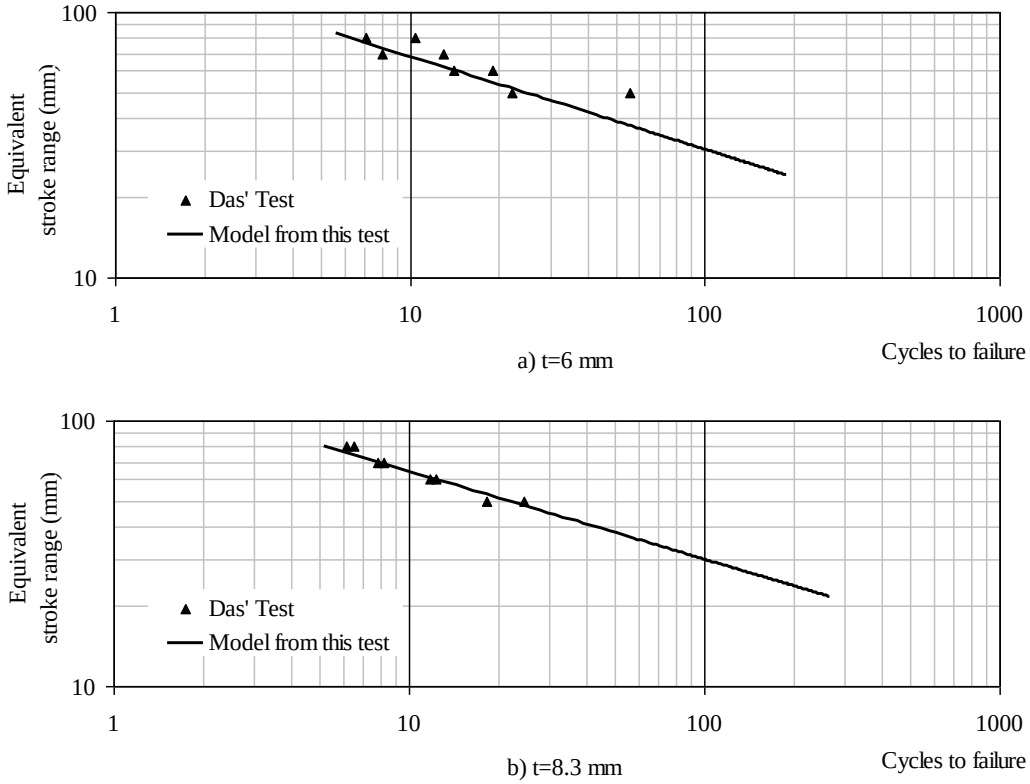

Figure 6.7: Comparison with Das' test

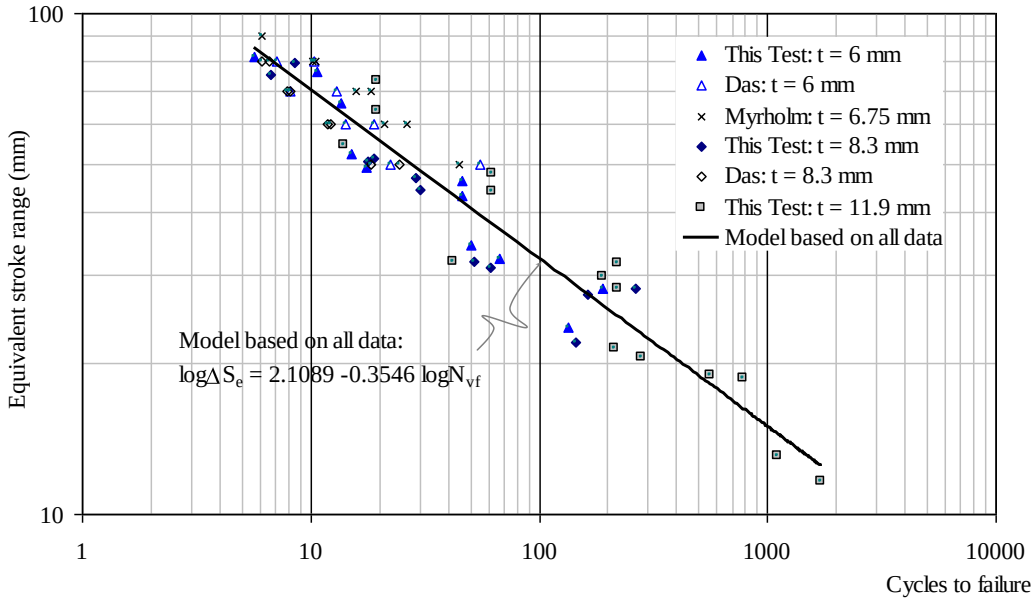

Figure 6.8: Comparison between previous test and this test

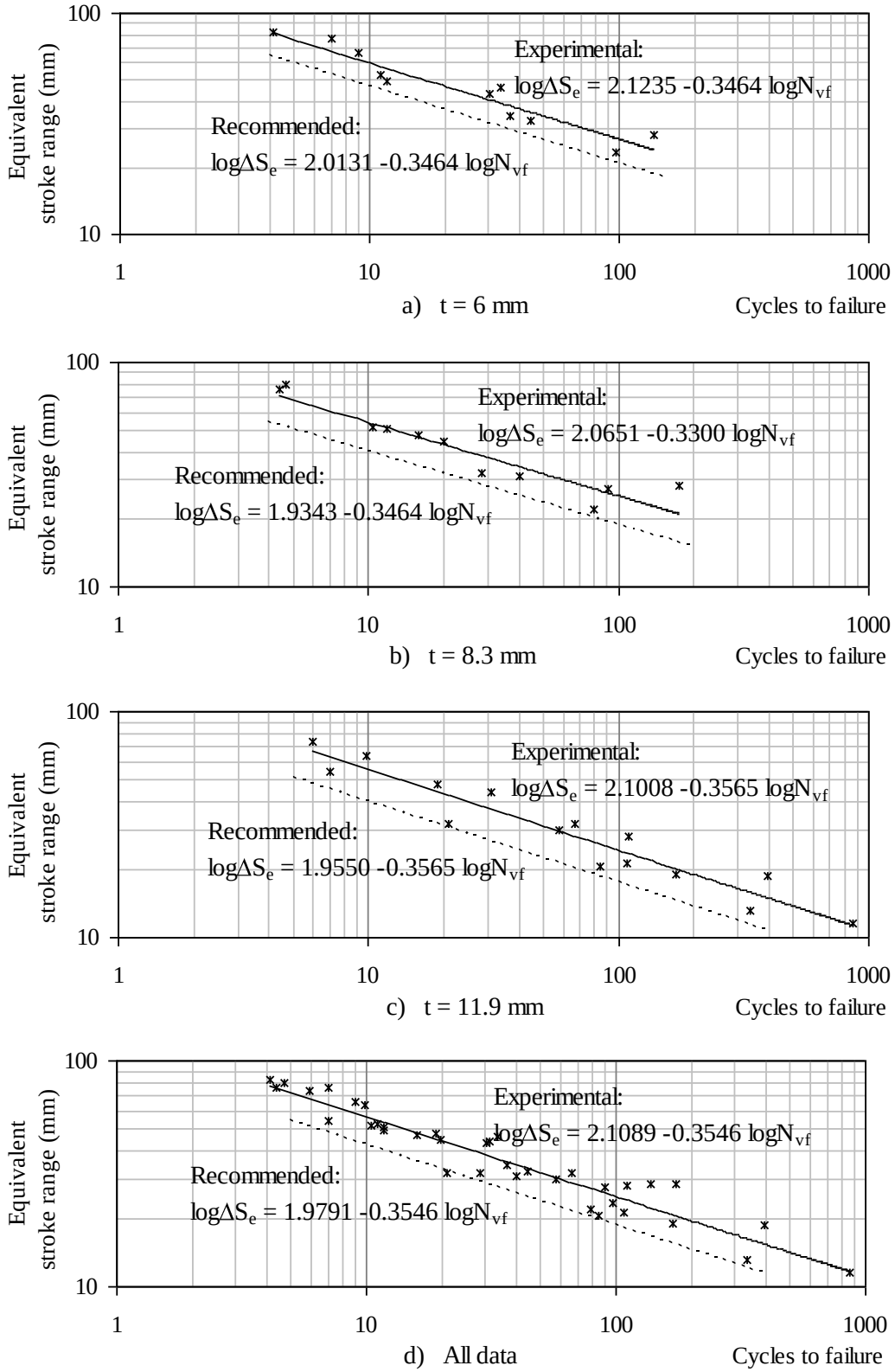

Figure 6.9: Equivalent stroke range and life-based models

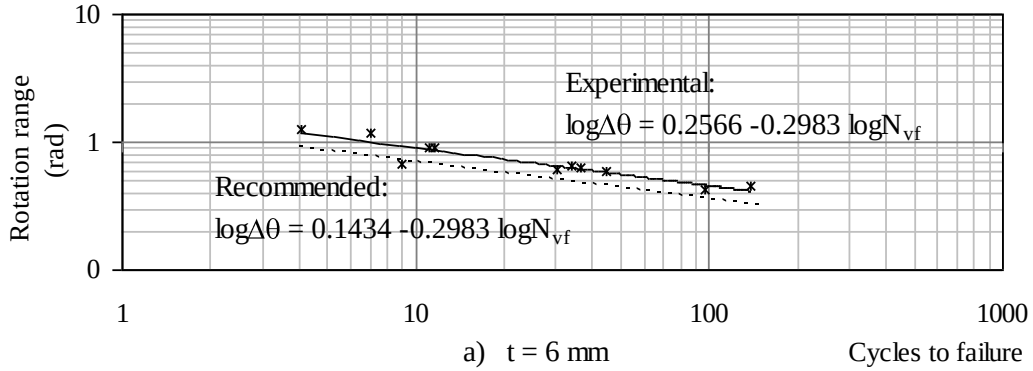

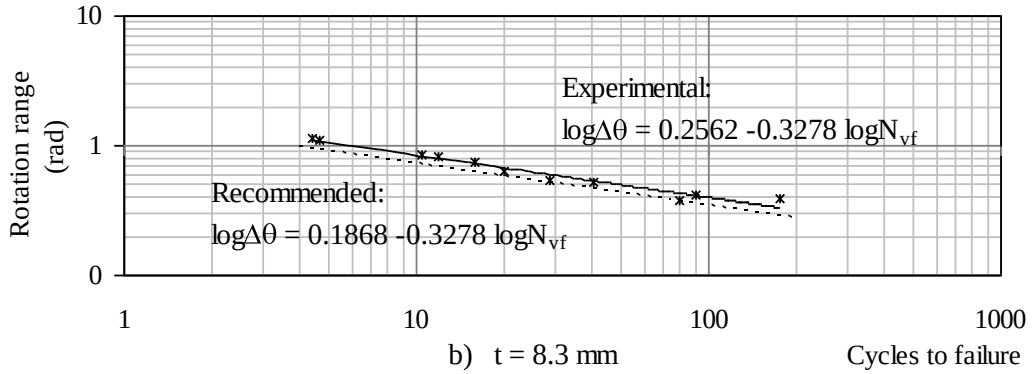

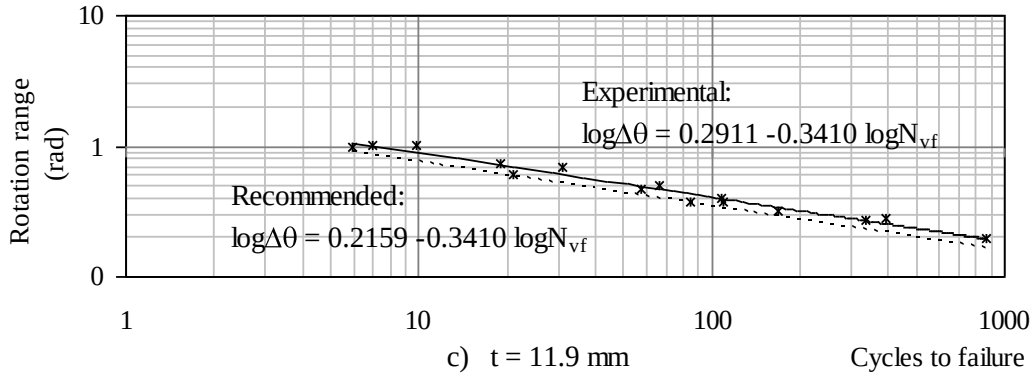

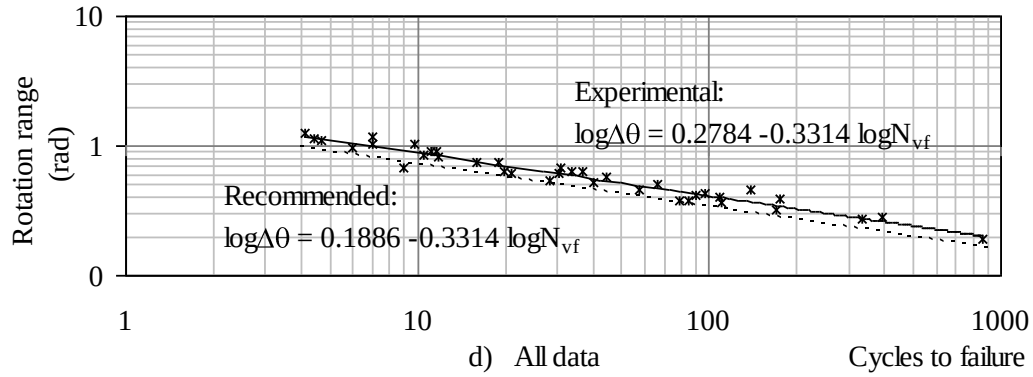

Figure 6.10: Rotation range and life-based models

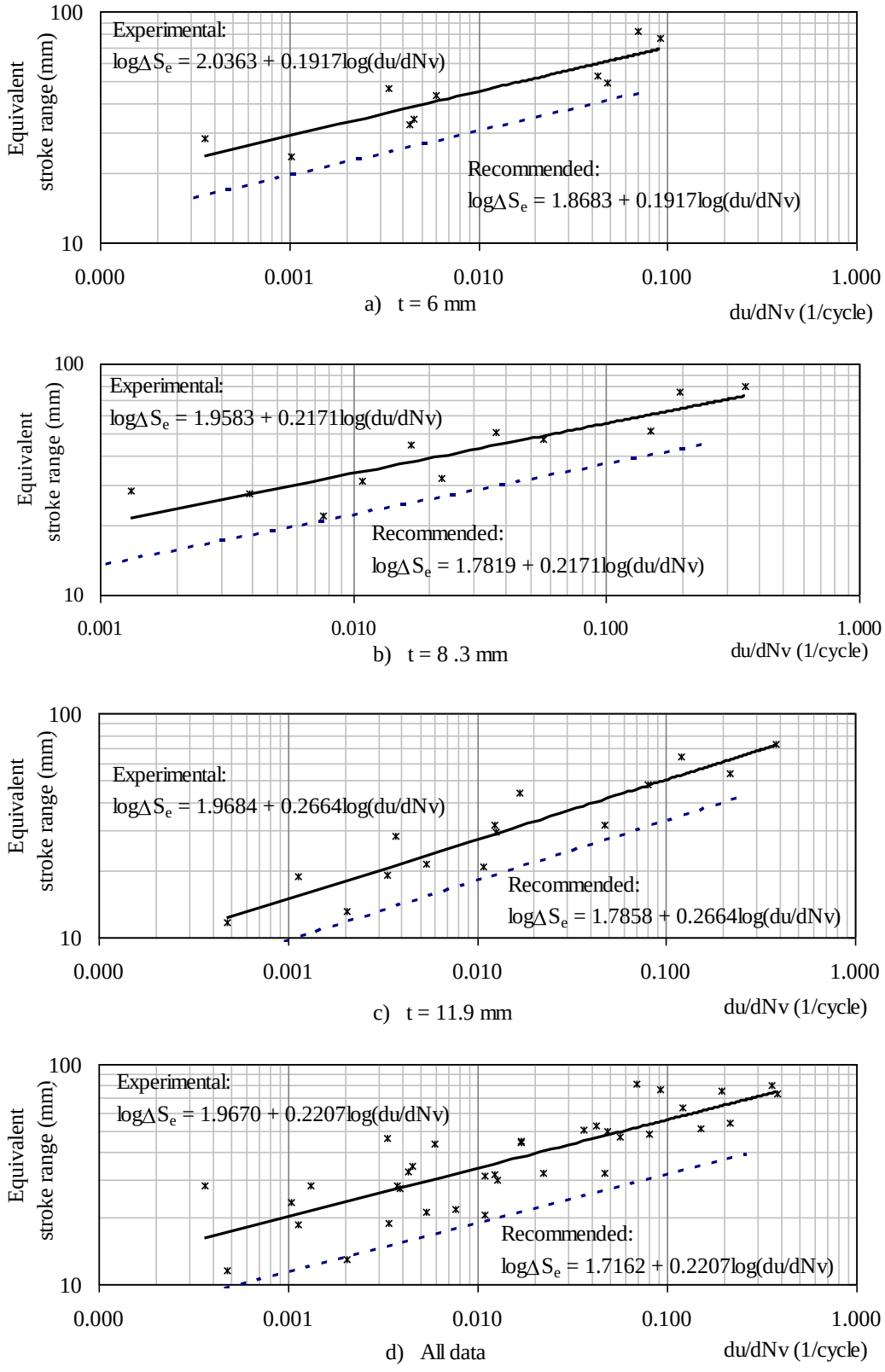

Figure 6.11: Equivalent stroke range and deterioration rate-based models

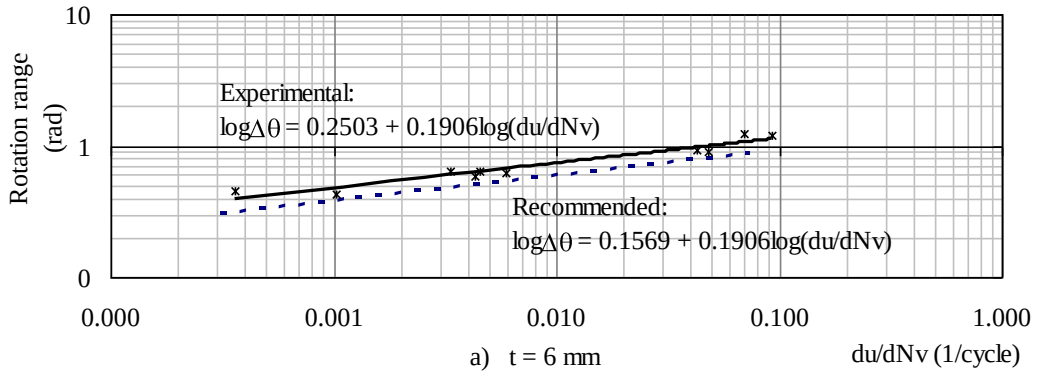

a) t = 6 mm

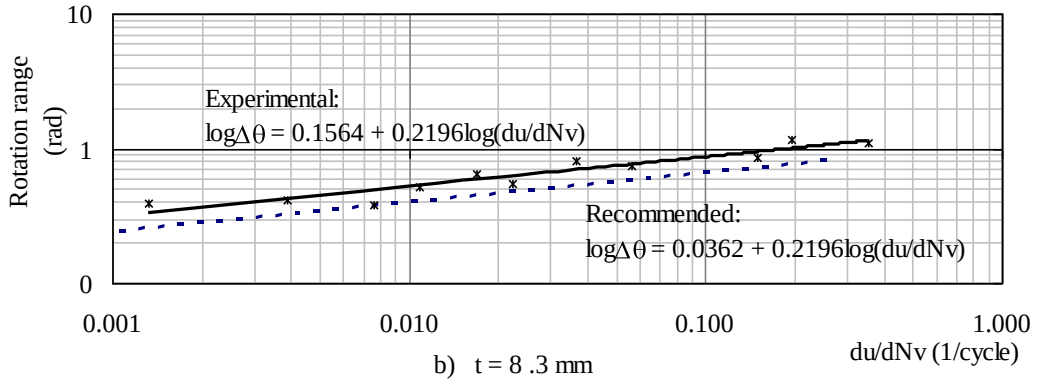

b) t = 8 .3 mm

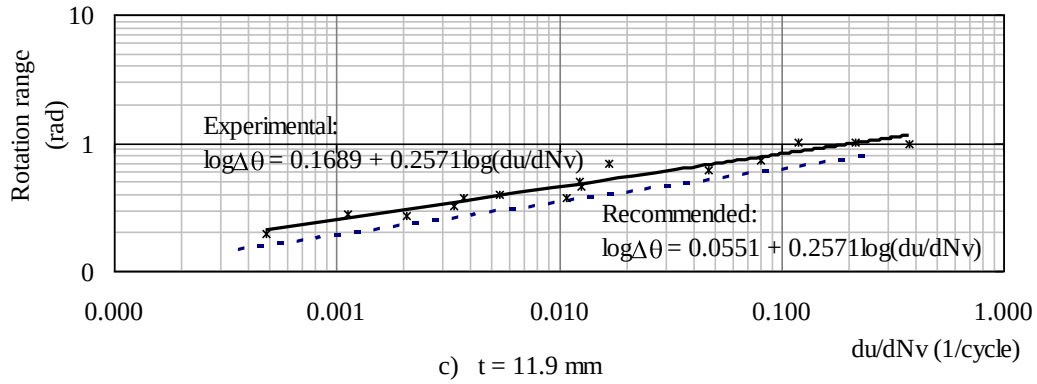

c) t = 11.9 mm

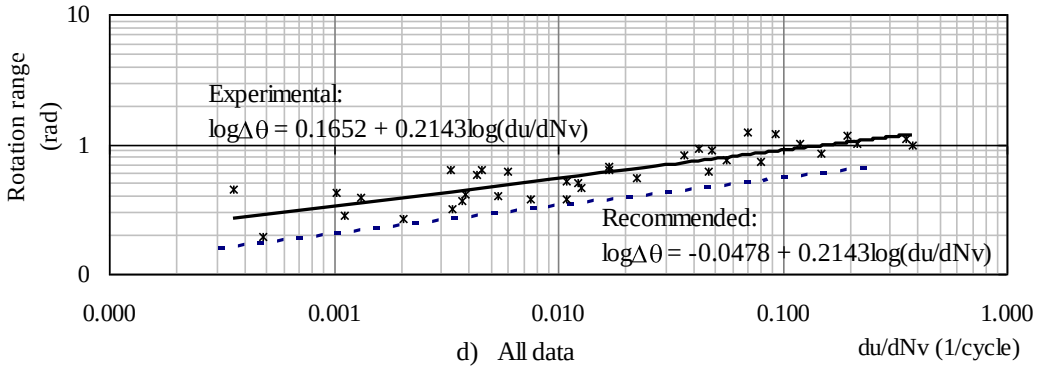

d) All data

Figure 6.12: Rotation range and deterioration rate-based models

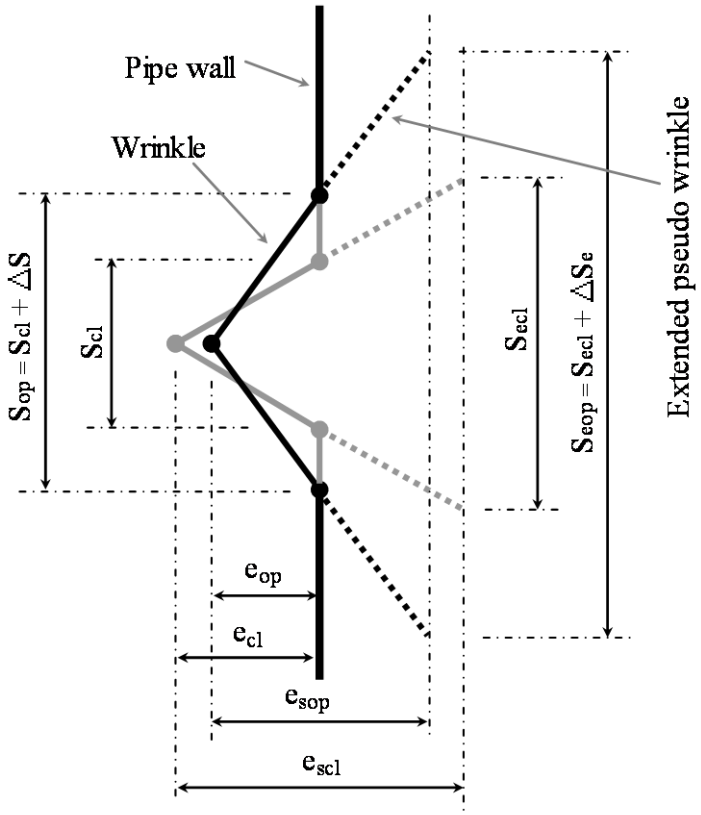

Note:
The dark profile represents a totally opened wrinkle and the light profile indicates a totally closed wrinkle.

Figure 6.13: A simplified pipe wrinkle model

7 SUMMARY, CONCLUSIONS, AND RECOMMENDATIONS

7.1 SUMMARY

Previous work has confirmed that the wrinkled pipes do not lose their safety and integrity under the normal operating conditions if they have good ductility. And the further investigation on limit states has found that the wrinkled pipes can be fractured by either tearing or LCF under specific load conditions. This research program focused on the LCF of wrinkled pipes, and was designed to develop the LCF life prediction models for these wrinkled pipes. It consisted of three phases of work: the strip tests, the full-scale pipe tests and the FEA.

A strip specimen is a replica of a specific pipe wrinkle, and they have the similar LCF behaviour. In the strip test program, a total of 39 strip specimens were tested by a totally reversed stroke-controlled loading method to investigate the impacts of bend angle, bend radius, material grade, and stroke range on their LCF behaviour and finally to develop the LCF life prediction models for the wrinkled pipes.

In the full-scale pipe tests, a complicated loading procedure was developed to form an encircled wrinkle around the pipe by bending and by axial compression and to fracture the wrinkle by LCF. Most of the loading stage was a combination of axial load, internal pressure and bending moment. A total of two specimens were conducted to verify and to validate the LCF models developed from the strip tests.

In the FEA, three models were developed. The first one was the strip model, and it simulated the strip specimens under monotonic bending. By this model, the residual true strain within the strip bend was analyzed. Furthermore, how to evaluate the residual strain was discussed by comparing with the results of measurement, theoretical analysis and FEA. The second one is the half-pipe model, and it was designed to explore the effects of pipe geometry and internal pressure on the wrinkle geometry, especially the wrinkle radius. The last one is the full-scale pipe model, and it was developed to simulate the full-scale pipe

tests, and to provide a numerical solution to the full-scale pipe test. The model provides the basis for applying the LCF life prediction models to full-scale pipes.

Based on the experimental and numerical studies, two LCF life prediction models for winkled pipes, named the life-based and deterioration rate-based models, were developed using both equivalent stroke range and rotation range as the damage parameters. The models were developed from the strip test results and further verified with previous strip test results. The applicability of the prediction model to full-scale wrinkled pipes was developed and verified by the results of the full-scale pipe tests.

7.2 CONCLUSIONS

The following conclusions can be drawn from this research program:

- *Strip Tests:*
  - The results of the strip tests show that the crack initiation life can be neglected and the fatigue life is the crack propagation life.
  - The propagation area is larger from the inside than that from the outside, and this indicates that the opening stroke is more detrimental than the closing stroke.
  - For the strip specimens, punch marks, tackle weld points and scratch lines were the origin of crack initiation, they should be avoided as much as possible in future tests.
  - The residual strain from the initial bending (wrinkling) mainly depends on the R/t ratio of strip bends or pipe wrinkles, and it decreases as the R/t ratio increases. Moreover, it can be approximately evaluated by the proposed formulas.
- *Full-Scale Tests*
  - Under the condition of cyclic axial deformation, the initiative of the failure of full-scale pipes is governed by the seam weld.
  - The similar failure mechanism works for both the strip specimens and the full-scale pipe specimens: cracks initiate from the multi-locations of both

surfaces, and then propagate to the interior, and finally fracture the specimens.

- For specimens with very short lives, such as the specimen T6R15A45S80, the fracture is dominated by the ductile failure mode; for specimens with long lives, such as the specimen T6R20A60S20, the fracture is dominated by fatigue; for specimens with medium lives, such as the full-scale pipe specimens, the fracture is in a combination of fatigue and ductile mode.
- By investigating the variation of local curvature over different gauge lengths, the onset of wrinkling can be approximately captured, and the location of wrinkle can be effectively located.

- *Finite Element Analyses*
  - The three developed FEA models work well, and they can be used for further study.
  - The wrinkle geometry depends on the pipe dimension, global deformation and internal pressure.
  - The wrinkle radius decreases as the D/t ratio increases and/or the internal pressure decreases, and its development can be divided into three zones during the postbuckling stage.
  - The wrinkle length is definition-dependent and a loose definition gives a longer wrinkle length. But the length of wrinkle head is independent of the definition.
  - When the wrinkle is fully developed, the global deformation will be totally localized into the wrinkle area.
- *LCF Life Prediction Models*
  - By investigating the relative statistical and regression parameters, both life-based and deterioration rate-based LCF life prediction models show excellent agreement with the strip test results, including the test results from previous test series.
  - By applying the LCF life prediction models to the full-scale pipe tests, they exhibit good prediction ability.

- A new DAR, called square-root square DAR (SRSDAR), works well when considering the accumulation of the damage due to monotonic loading and the damage due to cyclic loading.
- The damage due to monotonic bending (or winkling) is directly related to the residual strain, and it shortens the LCF lives of strip specimens and wrinkled pipes.

7.3 RECOMMENDATIONS

Based on this research program, the following recommendations can be made for the future work to further the understanding of the LCF behaviour of wrinkled pipes:

- More strip tests are necessary to fill the gap of the fatigue life range between 30 to 100 cycles, especially between 80 to 100 cycles. This will make the LCF test results evenly distributed, so the data base of LCF life prediction models can be consolidated.
- In the field, the cyclic loadings have widely varied amplitudes, and correspondingly, the wrinkled pipes will experience wider fatigue life spans than those studied in this program. Therefore, the domain of LCF life should be extended further to 1000 or more to investigate the validity of the developed models.
- Based on the observation that the opening stroke is more detrimental than the closing stroke, the effects of the mean stroke and the ratio of minimum stroke and maximum stroke on the LCF behaviour should be studied.
- The LCF behaviour of the seam weld should be investigated, and the investigated parameters should include the material grade (especially high strength steel), weld process, and weld geometry.
- Specific research program should be designed to verify or to confirm the crack initiation mechanisms proposed in this research program.
- The loading procedure of the full-scale pipe tests should be improved to more strictly control the cyclic deformation, so the proposed models can be more effectively verified and validated. For example, the full-scale pipe

specimens can be cyclically loaded by rotation instead of by axial deformation.

- Field tests should be planned to investigate the actual loading spectra generated from operational, environmental, and geotechnical effects.

REFERENCES

Ahn, S.-H., Nam, K., Yoo, Y.-S., Ando, K., Ji, S.-H., Ishiwata, M., and Hasegawa, K. 2002. "Fracture Behavior of Straight Pipe and Elbow with Local Wall Thinning." *Nuclear Engineering and Design*, Vol. 211, No. 2-3, pp. 91-103.

ASTM 2005. "ASTM Designation: A 370-05: Standard Test Methods and Definitions for Mechanical Testing of Steel Products." *ASTM*, Philadelphia, PA.

Aydin, M. 2006. *Tearing Fracture of Energy Pipelines under Monotonic Loading Conditions*. Master of Science Thesis, Department of Civil & Environmental Engineering, University of Alberta, Edmonton, Alberta, Canada.

Azizinamini, A., and Radziminski, J.B. 1989. "Static and Cyclic Performance of Semirigid Steel Beam-to-column Connections." *Journal of Structural Engineering*, Vol. 115, No. 12, pp. 2979-2999.

Ballio, G., Calado, L., and Castiglioni, C.A. 1997. "Low Cycle Fatigue Behaviour of Structural Steel Members and Connections." *Fatigue and Fracture of Engineering Materials & Structures*, Vol. 20, No. 8, pp. 1129-1146.

Bhattacharya, B. and Ellingwood, B. 1999. "A New CDM-based Approach to Structural Deterioration." *International Journal of Solids and Structures*, Vol. 36, No. 12, pp. 1757-1779.

Bouwkamp, G. and Stephen, R.M. 1973. "Large Diameter Pipe under Combined Loading." *ASCE Transportation Engineering Journal*, Vol. 99, No. TE3, pp. 521-536.

Calado, L., and Azevedo, J. 1989. “Model for Predicting the Failure of Structural Steel Elements.” *Journal of Constructional Steel Research*, Vol. 14, No. 1, pp. 41-64.

Chan, K. S., and Miller, A. K. 1982. “Prediction of Fatigue Failure in Structural Alloys: Initiation and Crack Propagation.” *Proceedings - International Symposium for Testing & Failure Analysis 1982*, San Jose, California, USA, pp. 272-279.

Chen, H. 2004. *Fatigue Resistance of High Performance Steel (HPS) Details*. Ph.D. Dissertation, Department of Civil & Environmental Engineering, University of Alberta, Edmonton, Alberta, Canada.

Chen, W.F., and Han, D.J. 1985. *Tubular Members in Offshore Structures*. Pitman, Boston, USA.

Coffin, L.F. 1954. “A Study of the Effects of Cyclic Thermal Stresses on a Ductile Metal.” *ASME - Transactions*, Vol. 76, No. 6, pp. 931-949.

Coffin, L.F. 1984. “Low Cycle Fatigue – A Thirty Year Perspective.” *Fatigue 84, Papers Presented at the 2nd International Conference on Fatigue and Fatigue Thresholds*, Birmingham, England, Vol. 3, pp. 1213-1234.

Coppa, A.P. 1966. “Measurements of Initial Geometric Imperfections on Thin Circular Cylindrical Shells.” *AIAA Journal*, Vol.3, No.1, pp. 172-177.

CSA 2002. *CAN/CSA Z245.1-02, Steel Pipe*. Canadian Standards Association, Etobicoke, Canada.

Daali, M.L., and Korol, R.M. 1995. “Low Cycle Fatigue Damage Assessment in Steel Beams.” *Structural Engineering and Mechanics*, Vol. 3, No. 4, pp. 341-358.

Das, S. 2002. *Fracture of Wrinkled Energy Pipelines*. Ph.D. Dissertation, Department of Civil & Environmental Engineering, University of Alberta, Edmonton, Alberta, Canada.

Das, S., Cheng, J.J.R., and Murray, D.W. 2002. “Fracture in Wrinkled Linepipe under Monotonic Loading.” *Proceedings of the International Pipeline Conference*, Sept. 30 – Oct. 3, Calgary, Canada, Vol. B, pp. 1613-1618.

Das, S., Cheng, J.J.R., Murray, D.W., and Zhou, Z.J. 2001. “Wrinkle Behavior under Cyclic Strain Reversal in NPS12 Pipe.” *Proceedings of the International Conference on Offshore Mechanics and Arctic Engineering – OMAE*, Jun. 3 – 8, Rio de Janeiro, Brazil, Vol. 4, pp. 129-138.

Delcol, P.R., Grondin, G.Y., Cheng, J.J.R., and Murray, D.W. 1998. *Behaviour of Large Diameter Line Pipe under Combined Loads*. Structural Engineering Report No. 224, Department of Civil Engineering, University of Alberta, Edmonton, Alberta, Canada.

Dorey, A.B. 2001. *Critical Buckling Strains in Energy Pipelines*. Ph.D. Dissertation, Department of Civil & Environmental Engineering, University of Alberta, Edmonton, Alberta, Canada.

Dowling, N. E. 2007. *Mechanical Behavior of Materials: Engineering Methods for Deformation, Fracture, and Fatigue*. Pearson Prentice Hall, NJ, USA.

Ellyin, F. 1997. *Fatigue Damage, Crack Growth and Life Prediction*. Chapman &Hall, London, UK.

Enami, K. 2005. “Ductile Crack Initiation Behavior in Steels with Compressive Prestrain.” *Journal of Marine Science and Technology*, Vol. 10, No. 1, p 41-52.

Fisher, J.W., Kulak, G.L., and Smith I.F.C. 1997. *A Fatigue Primer for Structure Engineers*. National Steel Bridge Alliance, American Institute of Steel Construction, Chicago, USA.

Galambos, T.V. (Editor) 1998. *Guide to Stability Design Criteria for Metal Structures.* John Wiley & Sons Inc., NY, USA.

Gotoh, K., and Berge, S. 2004. “Low Cycle Fatigue Strength of X65 Pipeline Girth Welds.” *Proceedings of the Biennial International Pipeline Conference,* Oct. 4 – 8, Calgary, Alberta, Canada, Vol. 2, pp. 1653-1660.

Halford,G.R. 1997. “Cumulative Damage Modeling - Crack Nucleation and Early Growth.” *International Journal of Fatigue*, Vol. 19, No. Suppl 1, pp. S253-S260.

Hasegawa, K., Miyazaki, K., Sakata, K., and Kanno, S. 2000. “Low Cycle Fatigue Strength for Pipes with Small Cracks.” American *ASME Pressure Vessels and Piping Division (Publication)*, Vol. 407, pp. 161-163.

Hasegawa, K., Sakata, K., Miyazaki, K., and Kanno, S. 2002. “Fatigue Strength for Pipe with Allowable Flaws and Design Fatigue Curve.” International *Journal of Pressure Vessels and Piping*, Vol. 79, No. 1, pp. 37-44.

Heuler, P., and Schuetz, W. 1986. “Assessment of Concepts for Fatigue Crack Initiation and Propagation Life Prediction.” *Zeitschrift fuer*

Werkstofftechnik/ Materials Technology and Testing, Vol. 17, No. 11, pp. 397-405.

Hibbeler, R. C. 2003. *Mechanics of Materials*. Pearson Education, NJ, USA.

Hibbit, Karlsson, & Sorensen, Inc. (HKS) 2001. *ABAQUS Theory Manual*. Version 6.2. Hibbit, Karlson & Sorensen, Inc., Pawtucket, USA.

Hibbit, Karlsson, & Sorensen, Inc. (HKS) 2001. *ABAQUS/Standard User's Manual*. Vol. I, Version 6.2. Hibbit, Karlson & Sorensen, Inc., Pawtucket, USA.

Hibbit, Karlsson, & Sorensen, Inc. (HKS) 2001. *ABAQUS/Standard User's Manual*. Vol. II, Version 6.2. Hibbit, Karlson & Sorensen, Inc., Pawtucket, USA.

Huang, J.-Y., Li, R.-Z., Chien, K.-F., Kuo, R.-C., Liaw, P.K., Yang, B., and Huang, J.-G. 2001. "Fatigue Behavior of SA533-B1 Steels." *ASTM Special Technical Publication*, No. 1406, pp. 105-121.

Iida, K. 1987. "Very Low Cycle Fatigue Life Influenced by Tensile or Compressive Prestrain." *ASTM Special Technical Publication*, pp. 160-172.

Kuroda, M. 2001. "Extremely Low Cycle Fatigue Life Prediction Based on a New Cumulative Fatigue Damage Model." *International Journal of Fatigue*, Vol. 24, No. 6, pp. 699-703.

Kuroda, M., Yamanaka, S., Komotori, J., and Shimizu, M. 1999. "Consideration on Dominant Factors for Extremely Low Cycle Fatigue Properties." *Technology Reports of the Osaka University*, Vol. 49, No. 2348-2365, pp. 147-154.

Lefebvre, D., and Ellyin, F. 1984. “Cyclic Response and Inelastic Strain Energy in Low Cycle Fatigue.” *International Journal of Fatigue*, Vol. 6, No. 1, pp. 9-15.

Lemaître, J., and Desmorat, R. 2005. *Engineering Damage Mechanics: Ductile, Creep, Fatigue and Brittle Failures*. Springer, NY, USA.

Libertiny, G. Z., Topper, T. H. and Leis, B. N. 1977. “Effect of Large Prestrains on Fatigue.” *Experimental Mechanics*, Vol. 17, No. 2, pp. 64-68.

Mander, J.B., Chen, S.S., and Pekcan, G. 1994. “Low-cycle Fatigue Behavior of Semi-rigid Top-and-seat Angle Connections.” *Engineering Journal*, Vol. 31, No. 3, pp. 111-122.

Manson, S.S., and Halford, G.R. 2006. *Fatigue and Durability of Structural Materials*.
ASM International, OH, USA.

Manson, S.S. 1954. “Behaviour of Materials under Conditions of Thermal Stress.” *National Advisory Committee for Aeronautics Report*, NACA, Washington, DC, USA.

Manson, S.S. 1960. “Thermal Stress in Design, Part19: Cyclic Life of Ductile Materials.” *Machine Design*, Vol. 21, pp. 139-144.

Miyazaki, K., Nebu, A., Ishiwata, M., and Hasegawa, K. 2002. “Fracture Strength and Behavior of Carbon Steel Pipes with Local Wall Thinning Subjected to Cyclic Bending Load.” *Nuclear Engineering and Design*, Vol. 214, No. 1-2, pp. 127-136.

Mohareb, M. 1995. *Deformational Behavior of Line Pipe*. Ph.D. Dissertation, Department of Civil & Environmental Engineering, University of Alberta, Edmonton, Alberta, Canada.

Mohareb, M., Alexander, S.D.B., Kulak, G.L., and Murray, D.W. 1993. "Laboratory Testing of Line Pipe to Determine Deformation Behavior." *Proceedings of the 12th International Conference on OMAE*, Jun. 20 – 24, Glasgow, Scotland, England, Vol. 5, pp. 109-114.

Mohareb, M., Kulak, G.L., Elwi, A., and Murray, D.W. 2001. "Testing and Analysis of Steel Pipe Segments." *Journal of Transportation Engineering*, Vol. 127, No. 5, pp. 408-417.

Myrholm, B.W. 2001. *Local Buckling and Fracture Behavior of Line Pipe under Cyclic Loading*. Master of Science Thesis, Department of Civil & Environmental Engineering, University of Alberta, Edmonton, Alberta, Canada.

Ogiso, S., Sasaki, T., Ooka, Y., Nakamura, H., and Akiyama, H. 1993. "Cyclic Post-Buckling Tests for Low Cycle Fatigue Failure of Buckled Cylinders by Shear and Bending Modes." *Transactions of the 12th International Conference on Structural Mechanics in Reactor Technology*, Aug. 15 – 20, Stuttgart, Germany, pp. 287.

Okamura, H., Sakai, S., and Susuki, I. 1979. "Cumulative Fatigue Damage under Random Loads." *Fatigue of Engineering Materials and Structures*. Vol. 1, No. 4, pp. 409-419.

Park, Y.-S., Park, S.-Journal, Iwai, S., and Kang, S.-H. 2004. "Failure and Damage of Steel Thin-plate Elements and Angle Members due to Very-low-cycle Loading." *Engineering Structures*, Vol. 26, No. 11, pp. 1623-1632.

Radhakrishnan, V.M. 1978. “Cumulative Damage in Low-cycle Fatigue.” *Experimental Mechanics*, Vol. 18, No. 8, pp. 292-296.

Radziminski, J.B., and Azizinamini, A. 1986. “Low-cycle Fatigue of Semi-rigid Steel Beam-to-column Connections.” *Proceedings of the 3rd U.S. National Conference on Earthquake Engineering*, Charleston, SC, USA, Vol. 2, pp1285-1296.

Reemsnyder, H.S. 1982. “Constant Amplitude Fatigue Life Assessment Models.” *Proceedings of the SAE Fatigue Conference*, Society of Automotive Engineers, Dearborn, MI, USA, pp. 119-132.

Sakano, M., Mikami, I., and Nishimura, T. 1994. “Low Cycle Fatigue Life Estimation for Steel Beam-column Joints.” *Technology Reports of Kansai University*, No. 36, pp.149-156.

Sakano, M., Mikami, I., Murayama, H., and Misumi, Y. 1996. “Very-low-cycle Fatigue Behavior of Steel Pier Base Joint.” *Technology Reports of Kansai University*, No. 38, pp. 179-188.

Sarihan, V. 1994. “Energy Based Methodology for Damage and Life Prediction of Solder Joints under Thermal Cycling.” *IEEE Transactions on Components, Packaging, and Manufacturing Technology Part B: Advanced Packaging*, Vol. 17, No. 4, pp. 626-631.

Scavuzzo, R.Journal, Srivatsan, T.S., Lam, P.C., Azzam, T., and Auradkar, R. 1992. “Low Cycle Fatigue of Butt Welded Pipe.” *1992 Pressure Vessels and Piping Conference*, Jun. 21 – 25, New Orleans, LA, USA, ASME, Vol. 235, pp. 157-166.

Schneider, S.P. 1998. “Flexural Capacity of Pressurized Steel Pipe.” *Journal of Structural Engineering*, Vol.124, No.3, pp330-340.

Sleczka, L. 2004. “Low Cycle Fatigue Strength Assessment of Butt and Fillet Weld Connections.” *Journal of Constructional Steel Research*, Vol. 60, No. 3-5, pp. 701-712

Souza, L.T., and Murray, D.W. 1999. “Analysis for Wrinkling Behavior of Girth-Welded Line Pipe.” *Journal of Offshore Mechanics and Arctic Engineering*, Vol. 121, pp. 53-61.

Uemura, T. 1998. “A Fatigue Life Estimation of Specimens Excessively Prestrained in Tension.” *Fatigue and Fracture of Engineering Materials & Structures*, Vol. 21, No. 2, pp. 151-158.

Wang, S.-H., and Chen, W. 2002. “A Study on the Pre-cyclic-load-induced Burst of Creep Deformation of a Pipeline Steel under Subsequent Static Load.” *Materials Science & Engineering*, Vol. A325, pp. 144-151.

Wang, S.-H., Zhang, Y.G., and Chen, W. 2001. “Room Temperature Creep and Strain-rate-dependent Stress-strain Behavior of Pipeline Steels.” *Journal of Materials Science*, Vol. 36, pp. 1931-1938.

Wang, S.-H., and Chen, W. 2002. “Room Temperature Creep Deformation and its Effect on Yielding Behaviour of a Line Pipe Steel with Discontinuous Yielding.” *Materials Science & Engineering*, Vol. A301, pp. 147-153.

Yoon, S., Hong, S.-G., Lee, S.-B., and Kim, B.-S. 2003. “Low Cycle Fatigue Testing of 429EM Stainless Steel Pipe.” *International Journal of Fatigue*, Vol. 25, No. 9-11, pp. 1301-1307

Yoosef-Ghodsi, N., Kulak, G.L., and Murray, D.W. 1995. “Some Test Results for Wrinkling of Girth-Welded Line Pipe.” *Proceedings of 14th Int. Conference on OMAE*, Jun. 18 – 22, Copenhagen, Denmark, Vol. 5, pp. 379-388.

APPENDIX A

SELECTED PHOTOGRAPHS

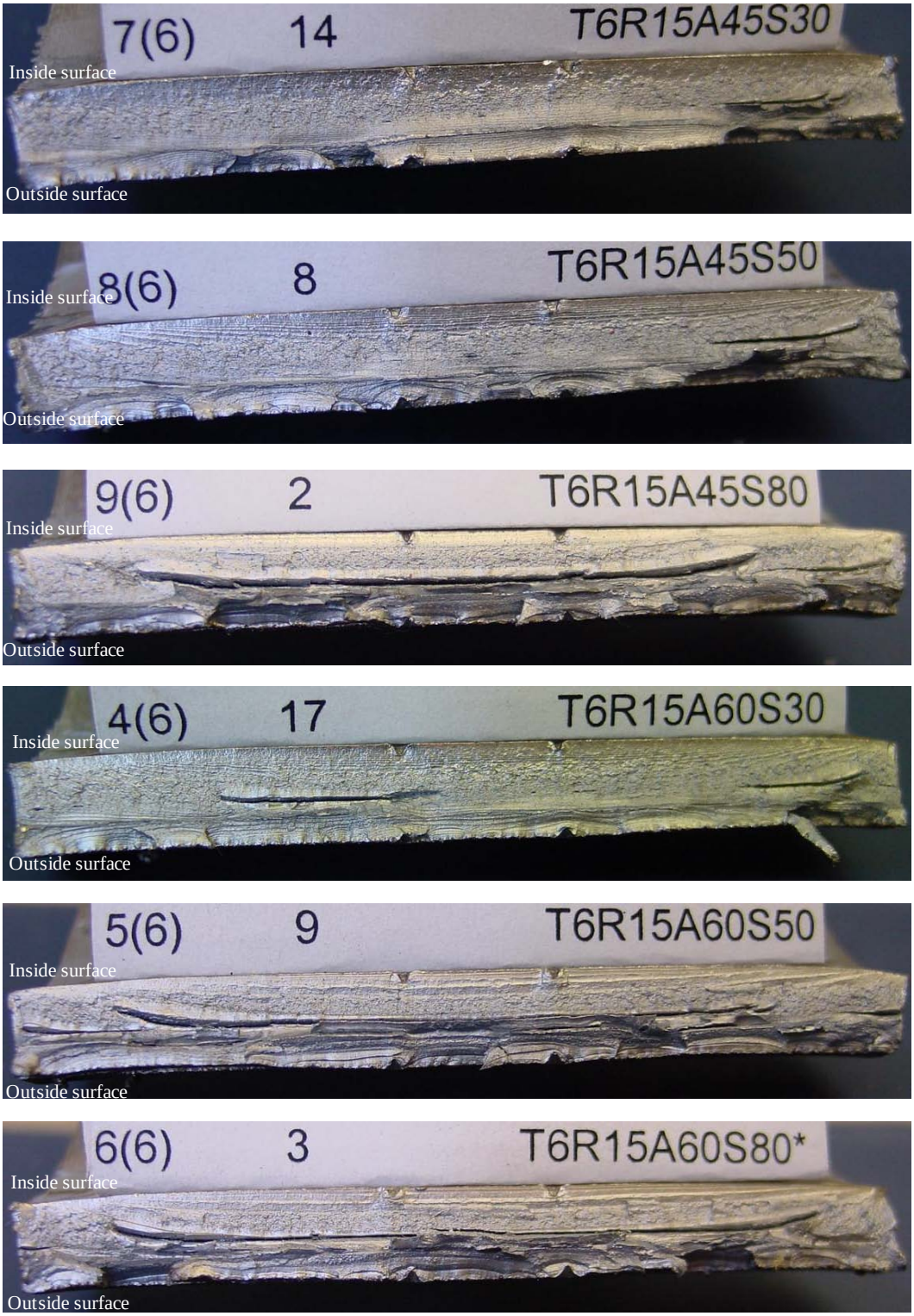

Figure A.1 Pictures of fracture surface: strip specimen series of T6R15

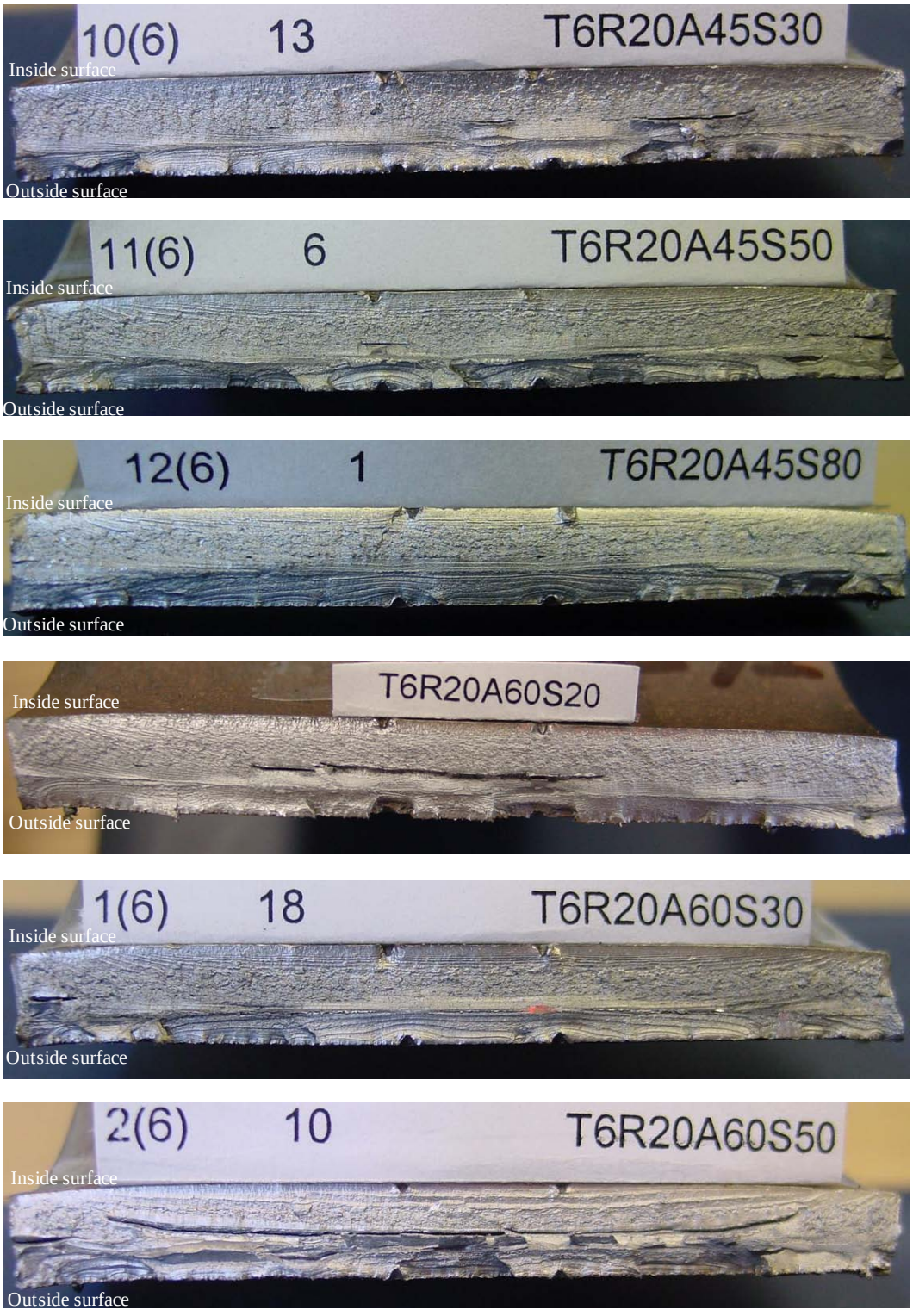

Figure A.2 Pictures of fracture surface: strip specimen series of T6R20

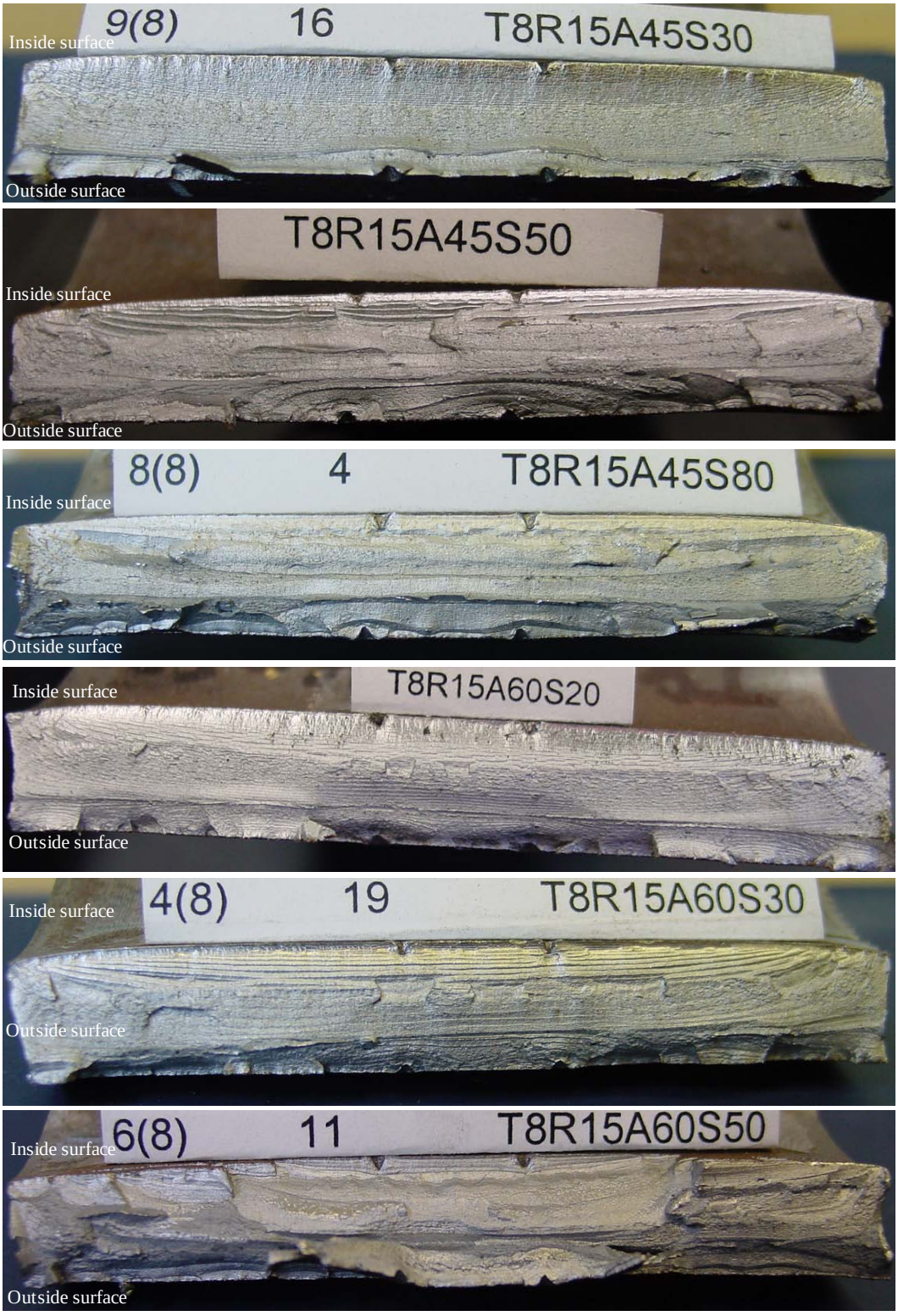

Figure A.3 Pictures of fracture surface: strip specimen series of T8R15

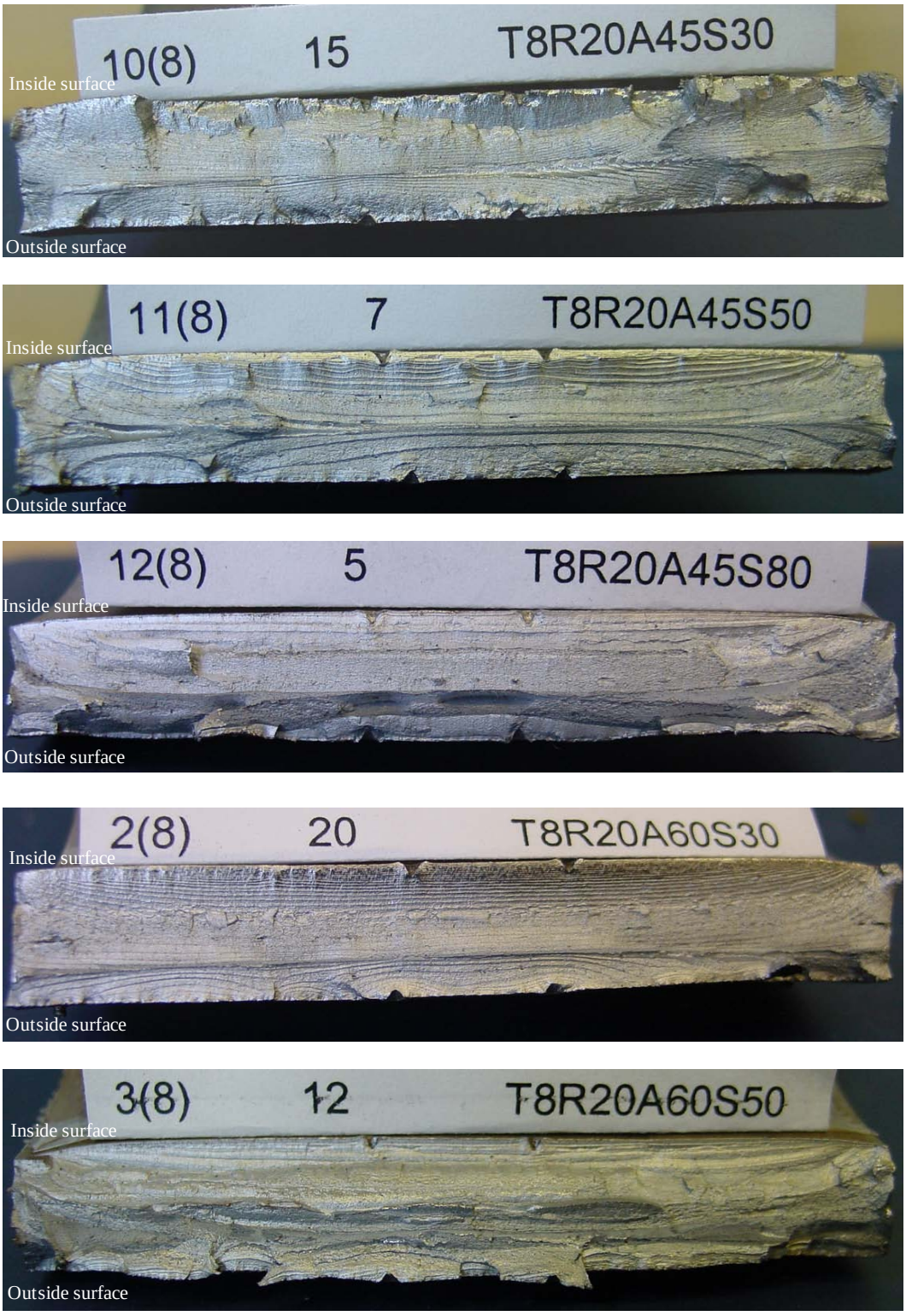

Figure A.4 Pictures of fracture surface: strip specimen series of T8R20

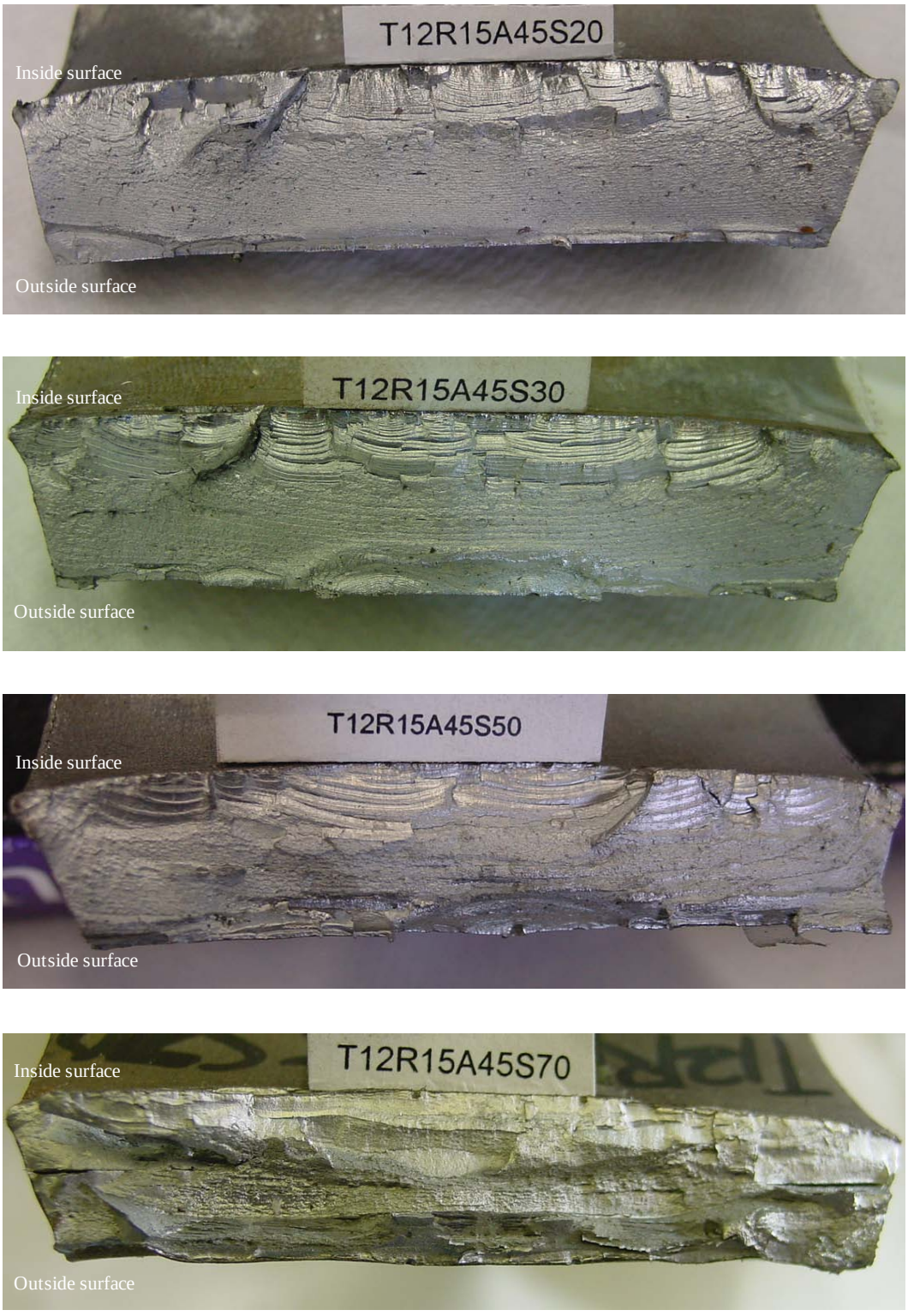

Figure A.5 Pictures of fracture surface: strip specimen series of T12R15A45

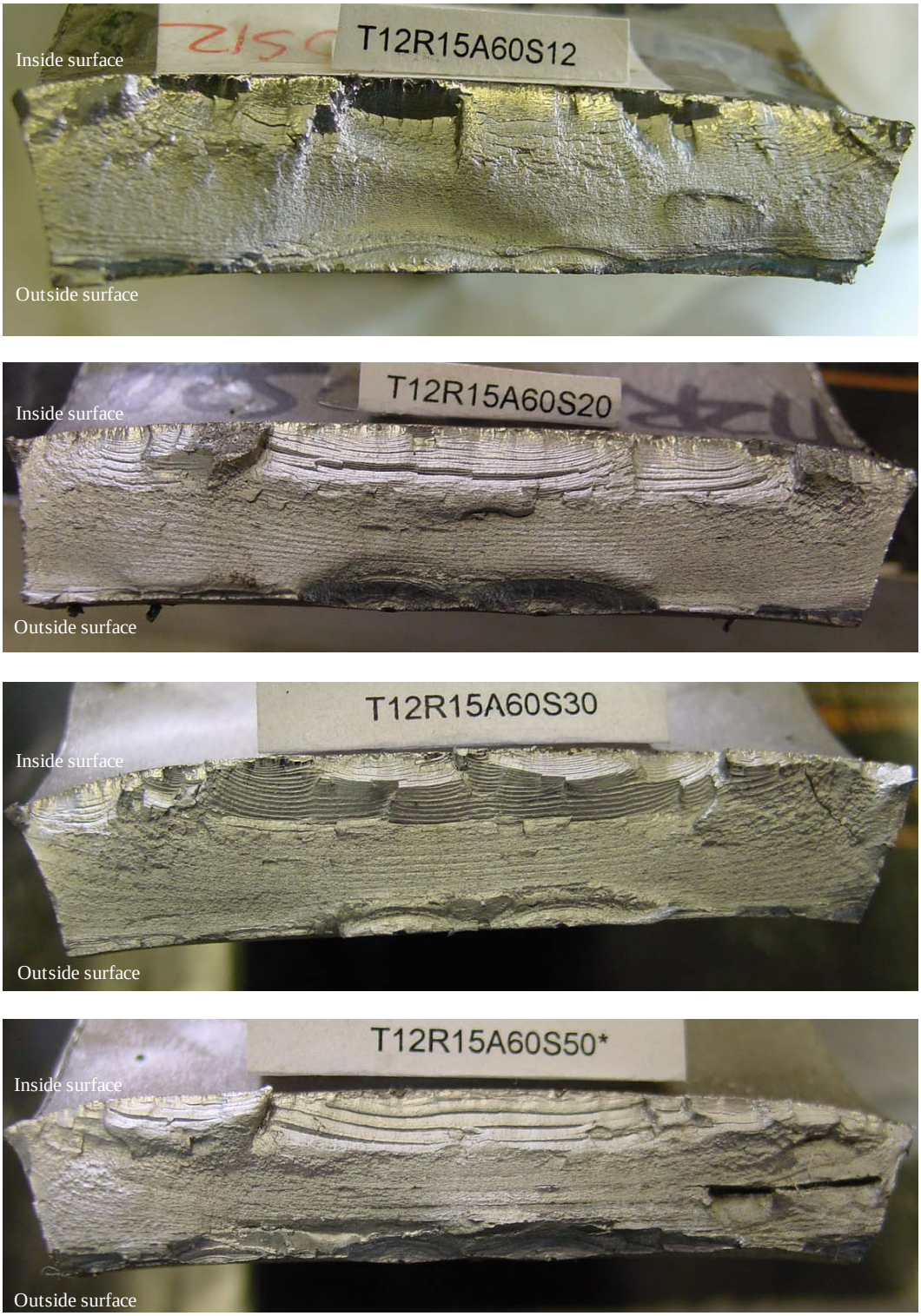

Figure A.6 Pictures of fracture surface: strip specimen series of T12R15A60

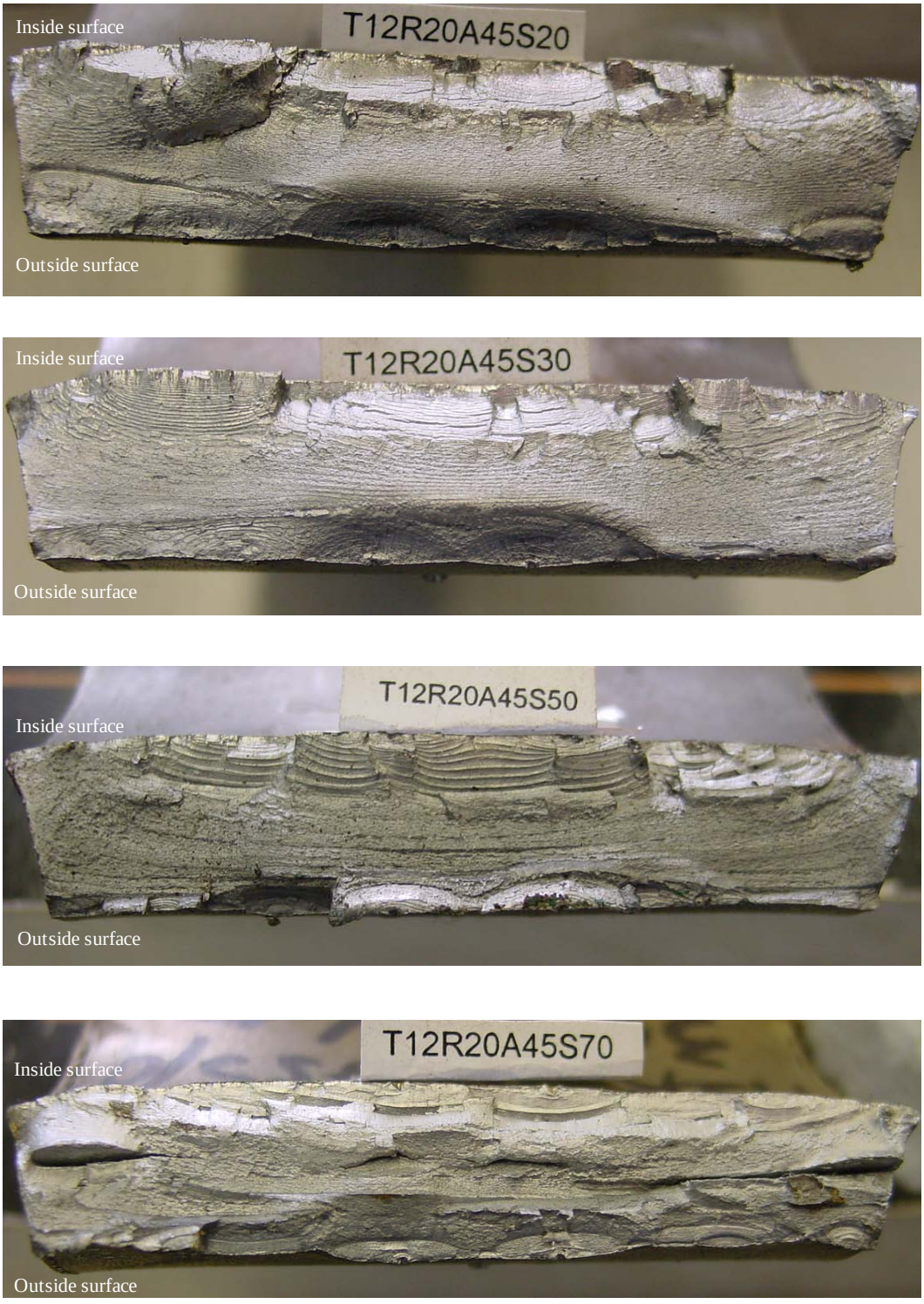

Figure A.7 Pictures of fracture surface: strip specimen series of T12R20A45

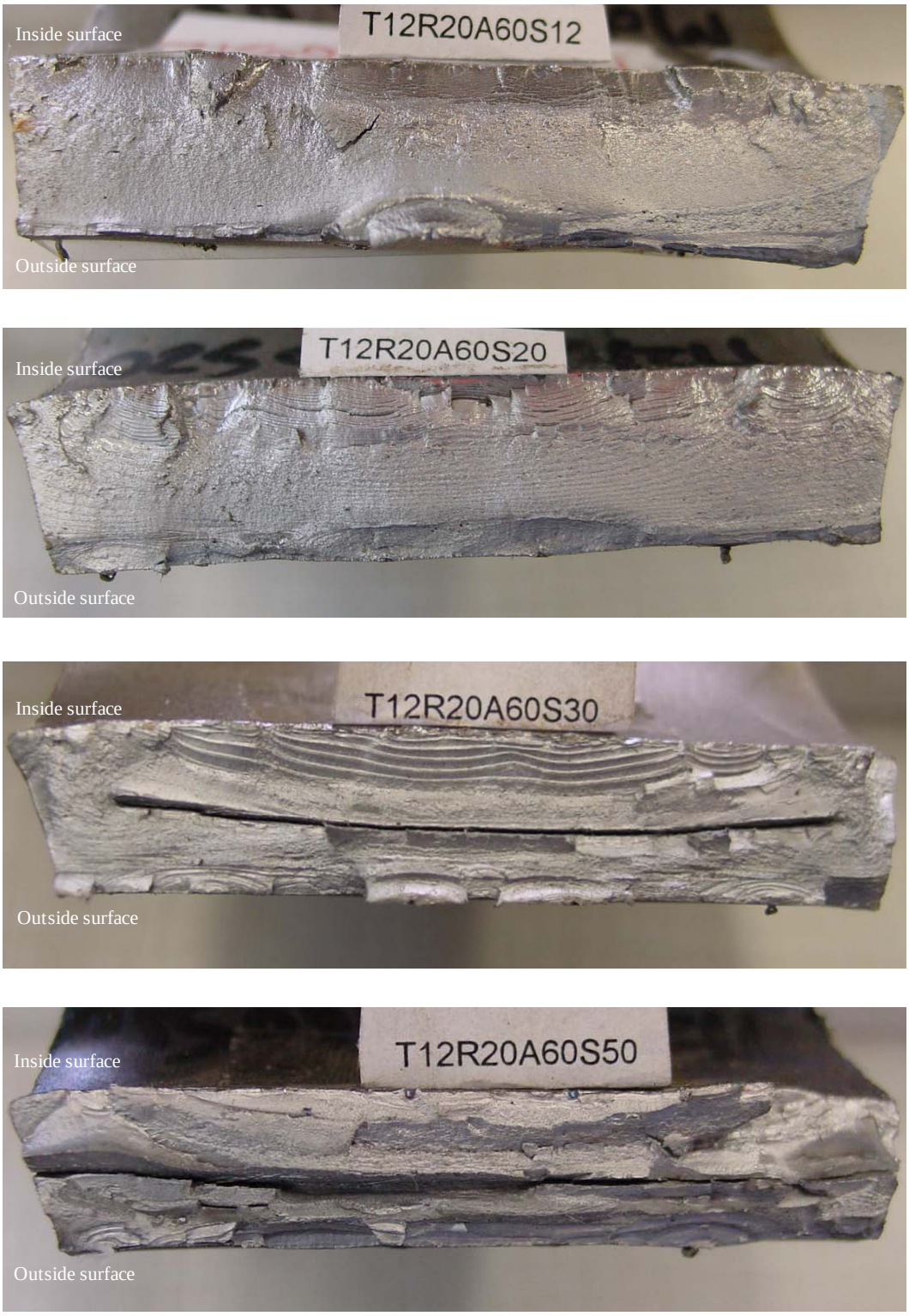

Figure A.8 Pictures of fracture surface: strip specimen series of T12R20A60

APPENDIX B

IMPERFECTION ANALYSIS

In the past decades, both of experimental and theoretical works were done to evaluate the influence of initial imperfections on the buckling load, e.g. Bushnell (1985), Singer (1982), Babcock (1972) and Dorey (2001). Also some researcher explored how to process the measured imperfection data, such Arbocz and Babcock (1969) and Dorey (2001), but none of them can be applied to this research program directly.

In Section 4.1.3.1, the geometric imperfection measurement method used in the U of A was introduced, so the following will focus on the analysis of those measured imperfection data.

B1 SYSTEMATIC ERROR

Although the measuring apparatus can be very advanced and precise, it is impossible to make the axis of central rail and the axis of pipe exactly coincident and the deviation between these two axes does always exist. The reason is that no one knows where the axis of the pipe exactly is before any measurement is done. The deviation can exist in two ways: one is the offset as shown Figure B-1a, and the other is the inclination as shown in Figure B-1b. The errors induced by this deviation are systematic errors and they have to be removed from the measured data.

B2 DATA PROCESS

The geometric imperfection is defined as the deviation from the perfect shape (see Figure B-2, so the imperfection greatly depends on how the perfect shape is defined. For this test, the measured pipe is a cylinder, so the cylinder can be taken as its perfect shape. Now, the problem becomes to how to determine the radius of this cylinder from the measured data. The following will focus on how to get the radius by the least-squares fit of the measured imperfection data.

B2.1 ESTABLISH THE ANALYSIS MODEL

ASSUMPTIONS

Before deriving the relative formulas, the following assumptions will be made at first:

1 The perfect shape of the pipe is a cylinder;

2 The central rail is a perfect straight prism;

3 The central rail is rigid enough to keep its straight shape at any time.

PROBLEM DESCRIPTION AND COORDINATE SYSTEM

The problem can be illustrated in Figure B-3. In this figure, the cylinder is considered as the perfect shape of the pipe, and it has a radius of R. Point 'P_i' is on the inside wall of the pipe, and plane 'i' is vertical to the central rail and is formed by the rotation of the tailor fitted carriage at a specific elevation. Two sets of coordinate system are also shown in this figure: one is the $x_fy_fz_f$ system, and the other is the xyz system. '0_f' is the origin of the $x_fy_fz_f$ coordinate system, and it is located at the center of the bottom cross section of the cylinder; '0' is the origin of the xyz coordinate system, and it is exactly the intersection point of the central rail with the bottom cross section of the cylinder. In the xyz coordinate system, the z axis is normal to the plane 'i', the x axis is parallel to the cross section of the cylinder, and the y axis is determined by the right-hand rule. In the $x_fy_fz_f$ coordinate system, the z_f axis is exactly the axis of the cylinder and has the same positive direction as the z axis, the x_f axis is parallel to the x axis, and the y_f axis is determined by the right-hand rule. Point '1' and point '1_f' are the intersection points when the z axis and z_f axis cross the top surface of the cylinder respectively, and similarly, point 'C_i' and point 'C_{fi}' are the intersection points when the z axis and z_f axis cross the plane 'i' respectively. R_{mi} is the length of line 'C_iP_i', and it can be read from the LVDT; R_i is the length of line '$C_{fi}P_i$', and it can be obtained by using the geometric relations. Then the imperfection at this point is the distance from this point to the surface of the cylinder, and it can be designated as ΔR_i. In plane 'i', θ_{mi} is the radial location recorded by measurement, and θ_0 is

the angle between the zero radial location and the xz plane. Finally, it is necessary to state that the objective of this analysis is determining ΔR_i.

After describing the problem and establishing the coordinate systems, then the problem can be solved step by step as follows.

CONVERSION I: MEASURED DATA TO COORDINATE SYSTEM xyz

The conversion is shown in Figure B-4. From this figure, the following relations can be easily obtained:

$$\begin{cases} x_i = R_{mi}\cos\theta_i \\ y_i = R_{mi}\sin\theta_i \\ z_i = z_{0i} \end{cases} \qquad (A.1)$$

where,

x_i, y_i, z_i = coordinates of point Pi in the xyz coordinate system,

R_{mi} = distance from point 'C_i' to 'P_i',

z_{0i} = z coordinate of point 'C_i', and

$\theta_i = \theta_{mi} + \theta_0$.

(A.1.1)

CONVERSION II: xyz SYSTEM TO $x_f y_f z_f$ SYSTEM

The conversion is shown in Figure B-5. From this figure, the following relations can be obtained:

$$\begin{cases} x_{fi} = x_i + x_{f0i} \\ y_{fi} = y_i\cos\alpha + y_{f0i} \\ z_{fi} = z_i\cos\alpha + R_{mi}\cos\alpha_i \end{cases} \qquad (A.2)$$

where,

x_{fi}, y_{fi}, z_{fi} = coordinates of point Pi in the $x_f y_f z_f$ coordinate system,

α = inclination angle of the z axis from the z_f axis,

α_i = angle formed by the line 'C_iP_i' and its projection on the $x_f y_f$ plane, and it is given by:

$$\alpha_i = \begin{cases} \dfrac{\alpha\theta_i}{\pi/2} & 0 \le \theta_i < \dfrac{1}{2}\pi \\ \dfrac{\alpha(\pi-\theta_i)}{\pi/2} & \dfrac{1}{2}\pi \le \theta_i < \dfrac{3}{2}\pi \\ \dfrac{\alpha(\theta_i-2\pi)}{\pi/2} & \dfrac{3}{2}\pi \le \theta_i < 2\pi \end{cases} \tag{A.2.1}$$

x_{f0i} and y_{f0i} = xf and yf coordinates of point 'Ci', and they are given by:

$$\begin{cases} x_{f0i} = x_{f00} + \dfrac{z_{0i}}{z_{01}}\left(x_{f01} - x_{f00}\right) \\ y_{f0i} = y_{f00} + \dfrac{z_{0i}}{z_{01}}\left(y_{f01} - y_{f00}\right) \end{cases} \tag{A.2.2}$$

In Equation (A.2.2), x_{f00}, y_{f00}, x_{f01}, and y_{f01} are the x_f and y_f coordinates of point '0' and point '1' respectively. z_{01} is the z coordinate of point '1', and z_{0i} is the same as before.

In addition, the inclination angle can be obtained from the following equation:

$$\sin\alpha = \frac{\sqrt{\left(x_{f01} - x_{f00}\right)^2 + \left(y_{f01} - y_{f00}\right)^2}}{z_{01}} \tag{A.3}$$

CYLINDER FITTING

After the above conversions being made, the imperfection at an arbitrary point can be expressed as:

$$\Delta R_i = R_i - R \tag{A.4}$$

where,

$$R_i = \sqrt{x_{fi}^2 + y_{fi}^2} \tag{A.4.1}$$

In the above equations, only R_{mi} and θ_{mi} are knowns, the other parameters are all unknowns. It can be easily identified that there are six independent unknowns, here selecting R, x_{f00}, y_{f00}, x_{f01}, y_{f01} and θ_0. To get those unknowns, the least square rule can be employed as follows.

The summation of the squares of the errors can be given by:

$$ER = \sum_{i=1}^{n} (R_i - R)^2 \tag{A.5}$$

where, n is the size of the sample of measured imperfection data.

Then to minimize ER, its derivative has to be equal to zero, i.e. the partial derivatives of ER with respect to the six independent unknowns have to be zero. By setting those partial derivatives equal to zero, six equations can be got as follows:

$$\frac{\partial ER}{\partial R} = 0 \Rightarrow R = \sum_{i=1}^{n} R_i \Big/ n \tag{A.6}$$

$$\frac{\partial ER}{\partial x_{f00}} = 0 \Rightarrow \sum_{i=1}^{n} x_{fi}\left(1-\frac{z_i}{z_1}\right)\left(1-\frac{R_i}{R}\right) = 0 \tag{A.7}$$

$$\frac{\partial ER}{\partial y_{f00}} = 0 \Rightarrow \sum_{i=1}^{n} y_{fi}\left(1-\frac{z_i}{z_1}\right)\left(1-\frac{R_i}{R}\right) = 0 \tag{A.8}$$

$$\frac{\partial ER}{\partial x_{f01}} = 0 \Rightarrow \sum_{i=1}^{n} x_{fi} z_i\left(1-\frac{R_i}{R}\right) = 0 \tag{A.9}$$

$$\frac{\partial ER}{\partial y_{f01}} = 0 \Rightarrow \sum_{i=1}^{n} y_{fi} z_i\left(1-\frac{R_i}{R}\right) = 0 \tag{A.10}$$

$$\frac{\partial ER}{\partial \theta_0} = 0 \Rightarrow \sum_{i=1}^{n} R_{mi}\left(1-\frac{R_i}{R}\right)(x_{fi}\sin\theta_i - y_{fi}\cos\theta_i) = 0 \tag{A.11}$$

Equation (A.3) and Equations (A.6) ~ (A.11) consist of a set of simultaneous equations. It is obvious that those equations are nonlinear, so numerical method has to be employed. By solving those seven equations, the above mentioned six unknowns and angle 'α' can be obtained. Therefore, the imperfections at the measuring points can be determined from Equation (A.4).

B3 RESULTS AND DISCUSSION

RESULTS

Applying the method developed on above to the full-scale pipes, the imperfections of 16 inch pipe and 20 inch pipe can be obtained and the results are shown in Figures B.6 and B.7 respectively.

DISCUSSION

As introduced previously, the measured data are relative values which indicate the changes of the distance from the intersection point of the central rail and the tailor fitted carriage to the inside of the pipe wall along the carriage. But the data required in the above equations are absolute values, R_{mi}. In this research program, the values of R_{mi} were assumed to the sums of the measured data and the nominal inside radius of the pipe. To check the sensitivity of this assumption to R_{mi}, various values were tried, and the results show that a 100 mm difference in R_{mi} only leads to a maximum error of 0.1 mm. Therefore, it can be concluded that using the nominal inside radius of the pipe can give enough accuracy.

It is also obvious that all unknowns can be found by the least-squares methods from the measured imperfection data, and this brings a couple of benefits. One is that there are no alignment requirements for setting the measurement apparatus, and the other one is that there is no need to conduct additional measurements to get the absolute values of R_{mi}. In addition, the process of data can be carried out in computer automatically by running a pre-developed program. Therefore, this method not only greatly simplifies the measurement, but also waives the manual process of data.

B4 REFERENCES

Arbocz, J. and Babcock, C.D. 1969. "The Effect of General Imperfections on the Buckling of Cylindrical Shells." Transactions of the ASME, *Journal of Applied Mechanics*, Vol. 36, series E, No. 1, pp. 28-38.

Babcock, C.D. 1972. "Experiments in Shell Buckling," in: *Thin-Shell Structures, Theory, Experiments and Design*. Fung, Y.C. and Sechler, E.E., Editors, Prentice-Hall, Englewood Cliffs, NJ, USA, pp. 345-369.

Bushnell, D. 1985. *Computerized Buckling Analysis of Shells*. Martinus Nijhoff, Dordrecht/Boston, USA.

Dorey, A.B. 2001. *Critical Buckling Strains in Energy Pipelines*. Ph.D. Dissertation, Department of Civil & Environmental Engineering, University of Alberta, Edmonton, Alberta, Canada.

Singer, J. 1982. "Buckling Experiments on Shells – a Review of Recent Developments." *Solid Mechanics Archives*, Vol.7, pp. 213-313.

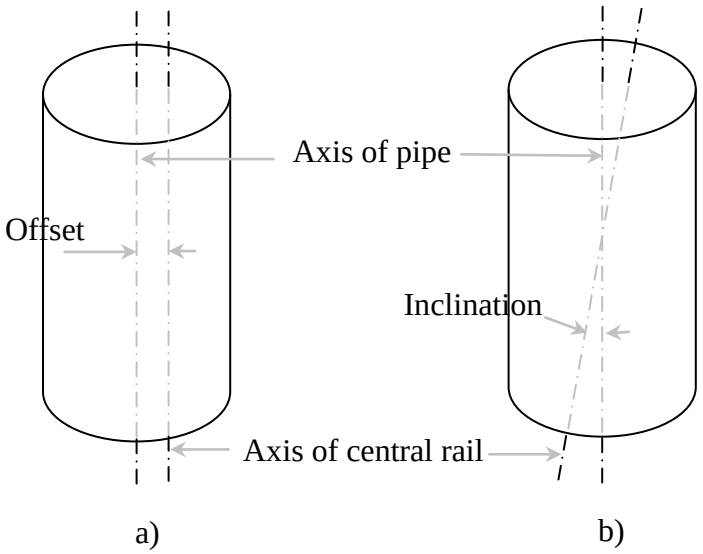

Figure B.1 Deviation of measuring apparatus

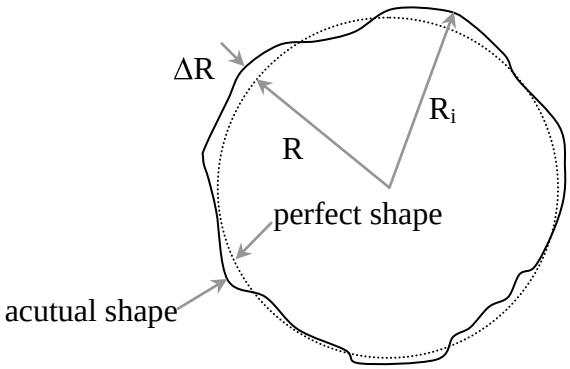

Figure B.2 Illustration of Geometric Imperfection

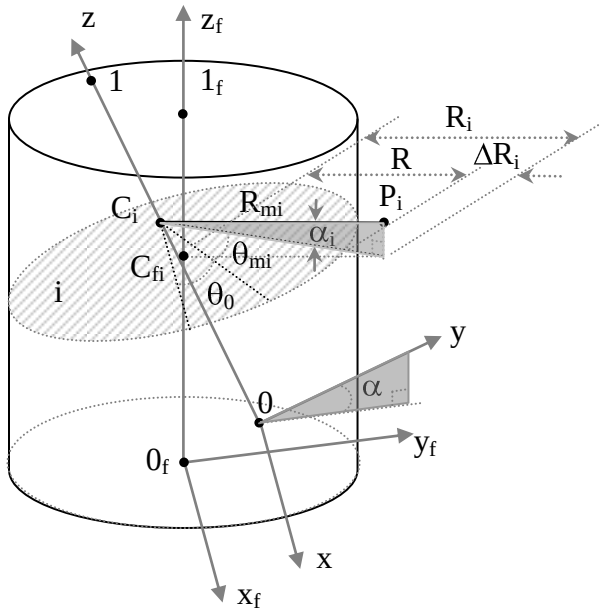

Figure B.3 Schematic illustration of problem and coordinate system

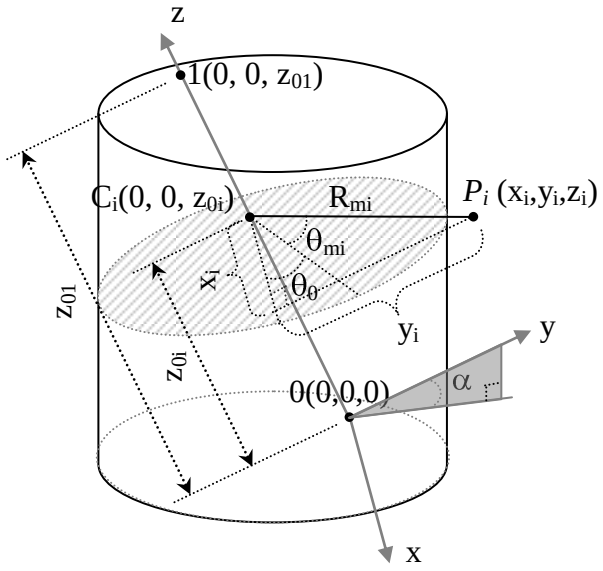

Figure B.4 Schematic illustration of conversion I

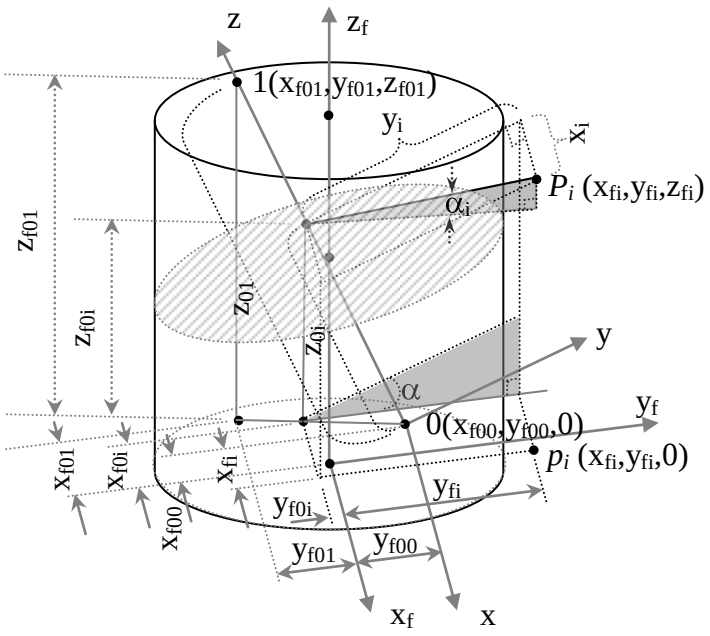

Figure B.5 Schematic illustration of conversion II

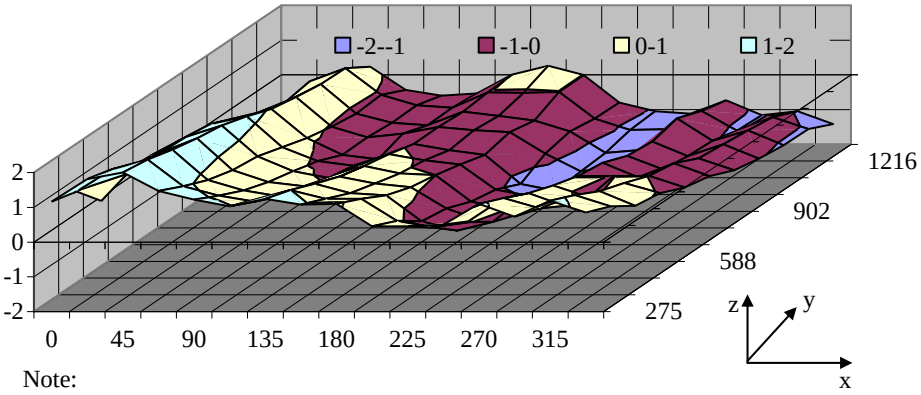

Note:
x = circuferential angle in degree, y = axial distance in m, and z = imperfection in mm.

Figure B.6 Imperfect of 16 inch pipe

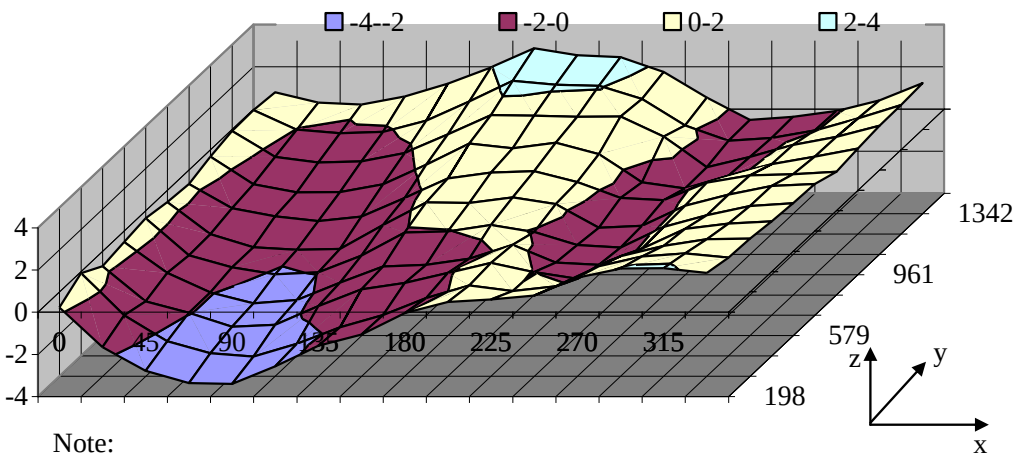

Note:
x = circuferential angle in degree, y = axial distance in m, and z = imperfection in mm.

Figure B.7 Imperfect of 20 inch pipe